Nuclear Cascades and Neutrino Production in the Sources of Ultra-High Energy Cosmic Ray Nuclei

DISSERTATION

zur Erlangung des akademischen Grades
doctor rerum naturalium
(Dr. rer. nat.)
im Fach: Physik
Spezialisierung: Theoretische Physik

eingereicht an der
Mathematisch-Naturwissenschaftlichen Fakultät
der Humboldt-Universität zu Berlin

von

M.Sc. Daniel Biehl

Präsident der Humboldt-Universität zu Berlin:
Prof. Dr.-Ing. Dr. Sabine Kunst

Dekan der Mathematisch-Naturwissenschaftlichen Fakultät:
Prof. Dr. Elmar Kulke

Gutachter: 1. PD Dr. Walter Winter
2. Prof. Dr. Marek Kowalski
3. Prof. Dr. Irene Tamborra

Tag der mündlichen Prüfung: 19.08.2019

Selbständigkeitserklärung

Ich erkläre, dass ich die Dissertation selbständig und nur unter Verwendung der von mir gemäß § 7 Abs. 3 der Promotionsordnung der Mathematisch-Naturwissenschaftlichen Fakultät, veröffentlicht im Amtlichen Mitteilungsblatt der Humboldt-Universität zu Berlin Nr. 126/2014 am 18.11.2014 angegebenen Hilfsmittel angefertigt habe.

Acknowledgements

I wish to express my gratitude to my supervisor Walter Winter for giving me the opportunity to be a part of the NEUCOS project and teaching me to work in research. Throughout the thesis, he supported me not only with his knowledge, but also with his guidance, both scientifically and personally. I acknowledge the support by the European Union's Horizon 2020 research and innovation programme (Grant No. 646623). I would also like to thank Martin Pohl, who, as the leader of the astroparticle theory group at DESY, always created a pleasant atmosphere and good spirit in the department. Special thanks also goes to Marek Kowalski, Irene Tamborra, David Berge and Oliver Benson for agreeing to be available as members of my graduation committee.

I would like to thank Denise Boncioli for all her support and patience with me, her kind and thoughtful way of working and collaborating with each other was always a pleasure for me. Also for proof-reading the entire manuscript of this thesis I am very thankful to her. In this context, I also want to thank Arjen van Vliet for giving valuable comments on the manuscript and being a great colleague. I appreciate the support of Mauricio Bustamante, who also read parts of the thesis and was always available for questions of any kind, in particular for career advice. Thanks to Rasmus Rasmussen for providing comments on the introduction of the thesis and being a great friend and former office mate.

I want to thank my collaborators, Anatoli Fedynitch, Andrew Taylor, Andrea Palladino, Cecilia Lunardini, Jonas Heinze, Leonel Morejon, Tom Weiler and Xavier Rodrigues, for making every project interesting and fun. Without them, this thesis would not have resulted in as many publications, so I thank everyone for their efforts. It was a pleasure to work with them. I also want to thank Kohta Murase, who I had many interesting discussions with, for inviting me for my first plenary talk, which was a really inspiring experience for me, and his support concerning my future career. Further I would like to express my appreciation to work with Iftach Sadeh and Zeljka Bosnjak on follow-up projects of this work. Thanks also to Kathrin Egberts, who since I met her drew my attention on several interesting career options.

I am grateful for the support of our student representatives Juliana Stachurska and especially Maria Haupt, who helped me a lot to resolve issues with my contract as a scientific employee. I wish to thank Ruoyo Liu for being an inspiring colleague and initiating contact to Xiang-Yu Wang for a visit at Nanjing University. I appreciate the invitation of Meng-Ru Wu for a visit at Academia Sinica in Taiwan.

I am glad to have found the best friends I could wish for during my time in Berlin: My colleague Xavier Rodrigues, with whom I had an amazing road trip through the US to get to our first conference and with whom I could share everything as we started and finished the thesis on the exact same days; My former colleague Chun-Sung Jao, who I could connect with on a level which is extremely rare to find and who introduced me to plenty of new things in life, leading to unforgettable memories and experiences; My colleague Leonel Morejon, who has a contagious passion about almost everything and always sees the bright side of life; And last but not least my colleague Shan Gao who I had many interesting coffee breaks and lots of laughs with. I also want to mention Reinaldo Santos de Lima as a good friend and one of the founders of our drinking fridays.

Finally, I want to thank my friends from my hometown, Alex, Jörn, Ox and Matze, for providing distractions whenever I needed them. I also would like to thank Robin Jose for all the useful discussions we had, in particular about future plans. My biggest thanks goes to my family: To my parents, who always supported me in every way, no matter which problem I encountered. To my brother, who I have a deep connection to, without the need of many words. To my grandfathers, of which one sadly passed away during the time I worked on this thesis. And also to Eriko, who is my biggest source of joy and happiness.

Kurzzusammenfassung

Der Ursprung ultra-hochenergetischer kosmischer Strahlung (UHECRs) ist noch immer eine der wichtigsten offenen Fragen der Astrophysik. Gammastrahlenblitze (GRBs) galten als potentielle Quellen, da sie zu den energetischsten Ereignissen im Universum zählen. Konventionelle Szenarien sind jedoch durch die Abwesenheit koproduzierter Neutrinos stark eingeschränkt. Außerdem weisen Messungen der chemischen Zusammensetzung kosmischer Strahlen auf schwere Kerne hin, welche in zu dichten Strahlungsfeldern disintegrieren würden. Um dieses Dilemma zu umgehen deuten neue Studien auf versteckte Beschleuniger wie Sternzerissereignisse (TDEs) oder GRBs niedriger Luminosität (LLGRBs) hin, welche schwer zu detektieren sind.

In dieser Dissertation präsentieren wir neue Ansätze um nukleare Prozesse in astrophysikalischen Quellen effizient und selbstkonsistent zu berechnen. Wir quantifizieren diese Wechselwirkungen anhand der nuklearen Kaskade, welche die Disintegration schwerer Kerne in leichtere Fragmente beschreibt. Wir zeigen wie die Produktion von Nukleonen und Neutrinos in kompakten Objekten durch die nukleare Kaskade gekoppelt ist und dass sich die Kaskade zumindest teilweise entwickeln muss, um die gemessene kosmische Strahlung (und Neutrinos) zu beschreiben. Daher können, im Gegensatz zu den gängigen Annahmen in der Literatur, nukleare Prozesse im Inneren potentieller Quellen nicht vernachlässigt werden.

Auch in umfassenden Quelle-Propagation-Modellen, wie sie in dieser Arbeit entwickelt werden, sind GRBs durch Neutrinodaten unter Druck. Dennoch zeigen wir, dass eine Population von LLGRBs konsistent mit derzeitigen Messungen ist und zugleich auch das Spektrum und die Zusammensetzung kosmischer Strahlung über den Knöchel hinweg sowie Neutrinodaten beschreiben kann. Aus unserer Prozedur können wir zusätzlich weitere Quelleneigenschaften wie die baryonische Ladung oder die Ereignisrate bestimmen.

Weiterhin zeigen wir, dass auch TDEs mögliche Kandidaten eines gemeinsamen Ursprungs der gemessenen kosmischen Strahlung und PeV-Neutrinos sind. Sie können jedoch durch kosmogenische Neutrinos von LLGRBs abgegrenzt werden. Wir präsentieren ein mit experimentellen Daten konsistentes Modell, das sich durch Neutrino-Multiplets testen lässt. Schließlich wenden wir unser Modell auf SGRB 170817A, verbunden mit Gravitationswellenereignis GW170817, an. Wir zeigen für verschiedene Jet-Szenarien, dass der erwartete Neutrinofluss weit unter der Sensitivität derzeitiger Instrumente liegt. Dennoch könnten verschmelzende Neutronensterne die kosmische Strahlung unterhalb des Knöchels erklären.

Abstract

The origin of Ultra-High Energy Cosmic Rays (UHECRs) is still one of the most important open questions in astrophysics. Gamma-Ray Bursts (GRBs) were considered as potential sources as they are among the most energetic events known in the Universe. However, conventional GRB scenarios are strongly constrained by the non-observed but expected co-production of astrophysical neutrinos. In addition, composition measurements by the Pierre Auger Observatory indicate the presence of heavy nuclei, which would disintegrate if the radiation fields in the source were too dense. In order to circumvent this dilemma, recent studies point towards hidden accelerators such as tidal disruption events (TDEs) or low-luminosity GRBs (LLGRBs), which are intrinsically hard to detect and ameliorate the constraints.

In this dissertation, we present novel approaches to efficiently and self-consistently calculate the nuclear processes in astrophysical sources. We quantify these interactions by means of the nuclear cascade, which describes the subsequent disintegration of heavy nuclei into lighter fragments. We will explicitly show how the nuclear cascade links nucleon and neutrino production in compact objects and demonstrate that in order to describe cosmic ray (and neutrino) observations, the nuclear cascade has to at least partially develop. Hence, nuclear processes inside potential sources cannot be neglected, contrary to what is frequently assumed in the literature.

Even in sophisticated source-propagation models, as the ones developed in this thesis, conventional GRBs are in tension with neutrino stacking limits. However, we demonstrate that a population of LLGRBs is not only consistent with current constraints, but can even describe the UHECR spectrum and composition across the ankle as well as neutrino data simultaneously. From our fitting procedure we can further constrain certain source properties, such as the baryonic loading and the event rate.

Furthermore, we show that TDEs are viable candidates for a simultaneous description of cosmic ray and PeV neutrino data too. However, they can be discriminated from LLGRBs by cosmogenic neutrinos. We present a realistic model which is consistent with current constraints, but testable by neutrino multiplets. Finally, we apply our model to SGRB 170817A associated with gravitational wave event GW170817. We show for different jet scenarios that the expected neutrino flux is orders of magnitude below the sensitivity of current instruments. Nevertheless, binary neutron star mergers could in principle support cosmic rays below the ankle.

List of publications

In connection to this dissertation, the following articles were published.

Peer-reviewed publications:

1. *Astrophysical Neutrino Production Diagnostics with the Glashow Resonance*
   Daniel Biehl, Anatoli Fedynitch, Andrea Palladino, Tom J. Weiler, Walter Winter
   JCAP **1701**, 033 (2017) [arXiv:1611.07983]

2. *Cosmic Ray and Neutrino Emission from Gamma-Ray Bursts with a Nuclear Cascade*
   Daniel Biehl, Denise Boncioli, Anatoli Fedynitch, Walter Winter
   Astron.Astrophys. **611**, A101 (2018) [arXiv:1705.08909]

3. *Tidally disrupted stars as a possible origin of both cosmic rays and neutrinos at the highest energies*
   Daniel Biehl, Denise Boncioli, Cecilia Lunardini, Walter Winter
   Sci.Rep. **8**, no.1, 10828 (2018) [arXiv:1711.03555]

4. *Expected neutrino fluence from short Gamma-Ray Burst 170817A and off-axis angle constraints*
   Daniel Biehl, Jonas Heinze, Walter Winter
   Mon.Not.Roy.Astron.Soc. **476**, no.1, 1191-1197 (2018) [arXiv:1712.00449]

5. *Binary neutron star merger remnants as sources of cosmic rays below the "Ankle"*
   Xavier Rodrigues, Daniel Biehl, Denise Boncioli, Andrew M. Taylor
   Astropart.Phys. **106**, 10-17 (2019) [arXiv:1806.01624]

6. *On the common origin of cosmic rays across the ankle and diffuse neutrinos at the highest energies from low-luminosity Gamma-Ray Bursts*
   Denise Boncioli, Daniel Biehl, Walter Winter
   Astrophys.J. **872**, 110 (2019) [arXiv:1808.07481]

Contents

Chapter 1

Introduction

The origin of cosmic rays at ultra-high energies, which are detected at Earth, is one of the major unsolved questions in physics and astronomy. Their energy – tens of million times higher than achievable by terrestrial accelerators – is too high for them to originate from within the Milky Way, as the corresponding gyroradius exceeds the size of our galaxy. Due to their charge, they are significantly deflected by magnetic fields, which leads to time delays of hundreds of thousands of years just by galactic fields alone, making it hard to identify their sources even if they are enormous and powerful objects [1]. The detection rate is extremely low at the highest energies, as just 1 particle is expected per square kilometer and century [2]. Fortunately, modern instruments cover thousands of square kilometers and are therefore able to measure the diffuse flux of ultra-high energy cosmic rays with relatively good statistics [3]. The most important features of the spectrum are a sudden change of slope around $10^{18.5}$ eV, dubbed the ankle, and the cut-off at about $10^{19.5}$ eV [4]. Cosmic ray interactions in the atmosphere trigger air showers of secondary particles of which measurements indicate that the chemical composition gets increasingly heavy at ultra-high energies [5]. This rules out proton only scenarios, which were broadly discussed in the literature until then.

In this dissertation, we contribute to answering the question of the mysterious origin of ultra-high energy cosmic rays by studying how these features of the spectrum and the chemical composition can be addressed. We demonstrate which requirements potential sources need to fulfil in order to be eligible candidates to power the observed diffuse flux while being consistent with experimental constraints. We develop testable scenarios and give quantitative predictions for experimental searches within a fully self-consistent, numerical approach beyond the status quo. By drawing a more complete picture from the results of our studies presented in this thesis, we contribute to improving our knowledge about the Universe outside of our galaxy.

Multi-messenger astronomy provides important concepts to do so by combining knowledge and information from disparate messengers. Spatial and temporal correlation of cosmic rays with electromagnetic radiation may not be possible, yet neutrinos, which are co-produced in nuclear interactions, could serve as a smoking gun signature for cosmic ray acceleration in astrophysical

environments [6]. Neutrinos have extremely small interaction cross-sections, such that they point directly back to their origin. In addition, they travel at almost the speed of light, meaning that correlations with electromagnetic signals should be possible. Depending on the production mechanism, neutrinos come in three different flavors, which they can change during propagation due to flavor mixing . Nevertheless, even the flux at Earth carries the imprint of the way they are produced in cosmic ray interactions, such that neutrino telescopes, which are partially sensitive to the flavor, can constrain the production scenario [7]. Their unique properties and their tight connection to cosmic rays make them the ideal messenger to uncover the sources of ultra-high energy cosmic rays. The detection of the astrophysical neutrino flux in 2013 with the IceCube neutrino detector was a huge step in this direction [8]. Unfortunately, no significant spatial and temporal clustering or correlations with electromagnetic signals have been detected so far, *i.e.*, no high energy neutrino sources have been definitely identified [9]. This is also a consequence of neutrinos reaching Earth from high redshifts, where the Universe is only transparent to neutrinos (and gravitational waves). The reason for this is their extremely large mean free path, while cosmic rays and photons are attenuated much more easily [10].

In the past, conventional source types as for example gamma-ray bursts [11] and active galactic nuclei [12] have been widely considered. Gamma-ray bursts are one of the most energetic electromagnetic outburst class and expected to produce a significant flux of high energy neutrinos if they are baryonically dominated due to cosmic ray interactions with the photons of the prompt emission [13]. However, the absence of correlations in stacking searches of the IceCube neutrino telescope using gamma-ray counterparts puts stringent limits on their contribution to the diffuse astrophysical flux [14]. Thus, neutrinos can efficiently test the paradigm that gamma-ray bursts are the sources of ultra-high energy cosmic rays. Although earlier predictions for the prompt neutrino flux [15] have been updated [16, 17], current neutrino data continues exerting pressure on the allowed parameter space for conventional neutrino emission models [18]. Parameters leading to efficient neutrino production are already excluded [19]. Nevertheless, if the radiation density is low enough, cosmic rays are more likely to escape from the source rather than interacting with ambient photons, such that gamma-ray bursts are still viable.

Not only neutrino production, but also the cosmic ray composition is linked to the radiation density in the source, as interacting nuclei can break up into lighter fragments. Therefore, the behaviour of cosmic ray nuclei in gamma-ray burst jets has been studied mostly in order to determine the necessary conditions for nuclear survival [20, 21, 22]. On the other hand, for compact radiation zones, a cascade of disintegrated isotopes lighter than the primary composition emerges through photo-nuclear interactions in the source [23, 24]. We call this phenomenon the *nuclear cascade* and develop new methods to efficiently and self-consistently compute it at a level of sophistication comparable to state-of-the-art cosmic ray propagation [25], which is a

key novelty of our work. The nuclear cascade as the subsequent feed-down to lower masses is therefore a measure for interactions in the source and, with that, cosmic ray composition and neutrino production.

For the purpose of testing cosmic ray paradigms, a comprehensive source-propagation model is required. In such models, accelerated nuclei are injected into a radiation zone, where secondaries are produced which escape from the source and are propagated through extragalactic space to Earth [26, 23, 27]. In this thesis, we develop combined source-propagation models, which enable us to study the dependence of the resulting diffuse flux of cosmic rays on the injected composition to learn more about the sources. On the contrary, only the ejected composition at the interface between source and propagation has been determined before [4]. Furthermore, an important open question is the determination of the transition energy between lower energy (possibly galactic) cosmic rays and the ultra-high energy component. In the dip model, the ankle is generated by pair-production losses, assuming a pure proton composition. This scenario, in which the transition occurs below the ankle [28], is already constrained by cosmogenic neutrinos [29] and extragalactic diffuse gamma-ray data [30, 31]. Thus, it was considered that the transition occurs at the ankle [23, 32, 33], and generic models can effectively describe the transition to lighter cosmic ray compositions below it due to disintegrated nucleons [27]. We test both of these hypothesis for gamma-ray bursts and demonstrate that the parameter space is largely excluded by neutrino data. Our study naturally points towards low luminosity objects for accommodating the cosmic ray paradigm.

These concepts are in principle applicable to any source class, with dim but abundant sources becoming more popular in the recent years due to the stacking limits strongly constraining conventional source candidates as gamma-ray bursts and active galactic nuclei. One alternative is for example to consider low-luminosity gamma-ray bursts as a distinct population from their high-luminosity counterpart [34, 35, 36, 37]. The stacking bounds do not apply due to their intrinsically low luminosity (limiting the detection of resolved sources) and their much longer duration (such that background suppression is less efficient). They have been postulated as sources of cosmic rays and neutrinos [38, 22, 39, 40, 41], recently also for ultra-high energies including possible injection compositions [42]. As a further consequence of their low luminosity, nuclei would stay mostly intact, addressing the required chemical composition of cosmic rays and implying low neutrino production efficiencies. We go one step further and show by extensive parameter space scans that a simultaneous description of ultra-high energy cosmic ray and neutrino data is possible while being consistent with experimental constraints. We demonstrate the correlation between neutrinos produced in the source and sub-ankle component of the cosmic ray fit and we are able to describe data across the ankle almost perfectly only with a residual power law component. In addition, we give an outlook on a combined source-propagation model

for a dynamically evolving gamma-ray burst. These models, in which the radiation is emitted from multiple zones, provide a high level of complexity and count to the most sophisticated models in the literature. Even in this case, conventional gamma-ray bursts are almost excluded, such that the question of low-luminosity bursts in the dynamical picture naturally arises.

Tidal disruption events, which describe stars torn apart by the gravitational force of a black hole, are another viable alternative. Some of them can launch a relativistic jet [43, 44, 45] where cosmic rays can be accelerated [46, 47] with neutrinos expected as a by-product [48, 49]. Although the sample size is small with only three observed jet-hosting events [50, 51, 52], they are consistent with supermassive black holes disrupting main sequence stars [53] or intermediate mass black holes disrupting white dwarfs [54, 55], for example. They have been discussed as sources of astrophysical neutrinos [56, 57, 58, 59] and ultra-high energy cosmic rays [60, 61], especially because the white dwarf scenario naturally provides mid-to-heavy compositions. So far, a comprehensive study of multi-messenger production in tidal disruption jets has not been performed. By applying our methods to this source class, we are able to give the first consistent calculation of neutrino and cosmic ray production from tidal disruption events. We will show that the population is a viable candidate for a common origin of these particles. We demonstrate that they can potentially be discriminated from other candidates by the non-observation of cosmogenic neutrinos.

Not a single source of ultra-high energy cosmic rays has been identified so far. However, recent breakthroughs as the detection of binary neutron star merger in gravitational waves (GW170817) [62] and electromagnetic radiation (SGRB 170817A) [63] or the potential neutrino event IceCube-170922A coincident with electromagnetic emission from TXS 0506+056 [64] show enormous advances in multi-messenger astronomy. The former has been awarded the Breakthrough of the Year in 2017, and we apply our methods in order to get a better understanding of the source both in the prompt phase as well as for the remnant. We contribute to understanding why no neutrinos are expected from this particular event, as we show that the radiation densities are too low to efficiently produce them. We show that, depending on the evolution of the spectral energy density, a population of binary neutron star mergers can in principle support the cosmic ray flux up to the ankle. As major observatories are either planning or performing upgrades [65, 66, 67, 68, 69], such important detections are expected to happen more frequently in the future. The interplay between experiments and theory will therefore eventually draw a consistent, comprehensive picture of multi-messenger astronomy. By testing conventional scenarios with sophisticated, novel technology as well as providing alternative perspectives and new predictions, this dissertation contibutes to this theoretical picture.

Chapter 2

Cosmic messengers from astrophysical objects

Professional astronomy is nowadays, despite some differences, often used synonymous with astrophysics, and it can be subdivided into observational and theoretical branches that complement each other. The observational branch focuses on obtaining data from analyzing astronomical objects with the means of physics. On the other hand, in theory, analytical and numerical models are developed and computer simulations are performed, seeking to explain the observational results. Such simulations cover, *e.g.*, stellar dynamics, structure formation in the Universe, magnetohydrodynamics (MHD), general relativity, cosmology and astroparticle physics. Although astronomy itself would already qualify as astroparticle physics, as it deals with observing photons from space, usually the term is used when multiple types of particles are involved. Thus, it is tightly connected with multi-messenger astronomy, which provides the framework to interpret observations beyond the electromagnetic spectrum.

In this thesis, theoretical models are developed, applied and interpreted in the context of multi-messenger astronomy. For that purpose, the scientific context including a brief historical overview is presented in this chapter. In the first section, Sec. 2.1, the most important milestones in astronomy combining different types of messenger particles are summarized. The methods developed in this work contribute to exploring potential source scenarios and constraining their respective properties. Then, in Sec. 2.2, an introduction to the state-of-the-art of cosmic ray physics is given, especially focusing on the current status of spectrum and composition at the highest energies. After that, in Sec. 2.3, neutrino astronomy is introduced in the historical context including a review of the status quo, as neutrinos are powerful messengers co-created with ultra-high energy cosmic rays, helping us to understand and identify their sources.

2.1 Milestones in multi-messenger astronomy so far

Electromagnetic radiation from celestial bodies is still the main source of information to date. It can be categorized by the wavelength band of the electromagnetic spectrum in which the measurements are taken. As the instruments are sensitive only to a narrow energy band for

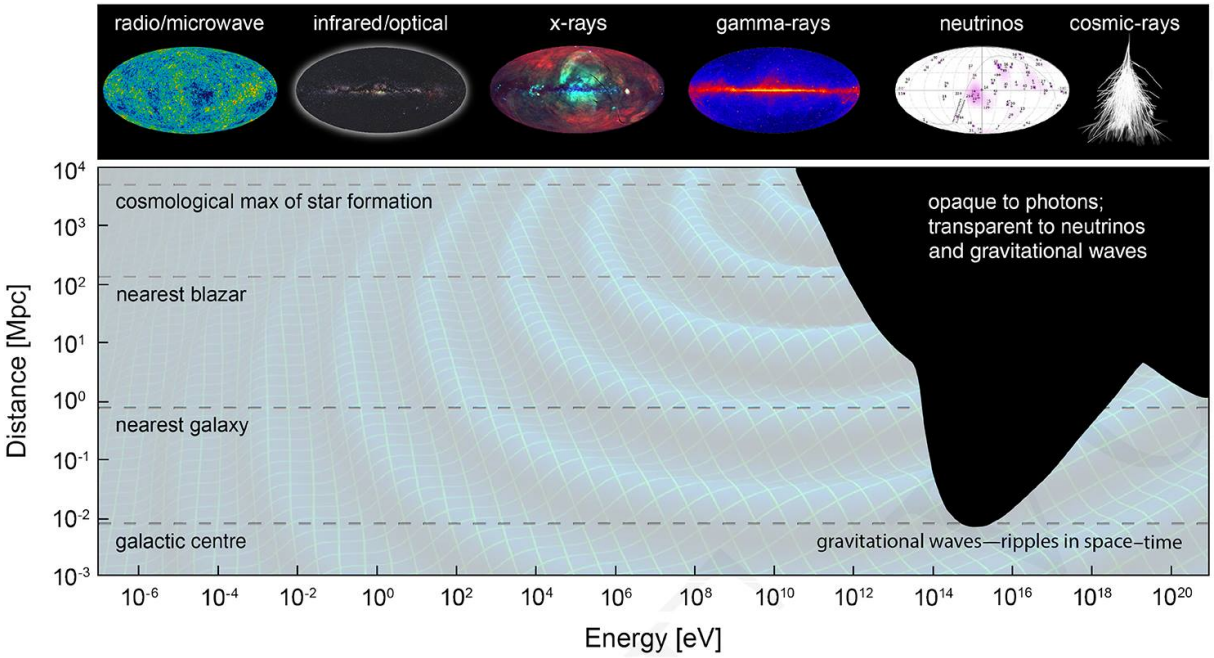

Figure 2.1: Distance after which the Universe becomes opaque to electromagnetic radiation of a certain energy. At the highest energies, $E > 10^{10}$ eV, photons are absorbed after traveling short distances, such that the most energetic cosmic events are obscured, as indicated by the black region. This region is, in turn, accessible by other messengers such as neutrinos and gravitational waves. The top panel depicts how the Universe looks in different wave lengths and messengers. Taken from [10].

which they are optimized, the requirements for different telescopes are diverse. Special attention has to be paid to the construction site for ground based telescopes. Popular examples are the Very Large Array (VLA) radio telescope in New Mexico or the Atacama Large Millimeter Array (ALMA) for observations in the infrared in Chile. X-ray observations, for example, must be performed from balloons, rockets or satellites, as the radiation is absorbed in the atmosphere. For shortest wavelengths, particularly of interest for this work as they are connected with other ultra-high energy messenger particles, measurements are taken with gamma-ray telescopes. A special class of gamma-ray telescopes are the so-called Cherenkov telescopes, such as the High Energy Stereoscopic System (H.E.S.S.) or the Cherenkov Telescope Array (CTA), which do not detect the gamma-rays directly, but indirectly via flashes of Cherenkov light produced by gamma-rays interacting in the atmosphere. The combination of observations in different wavelength bands to obtain a more complete picture is called multi-wavelength astronomy.

However, the Universe becomes opaque for highest energy photons because their energy is high enough to interact with low energy photons of the cosmic background. As shown in Fig. 2.1,

lower energy photons with $E \lesssim 10^{10}$ eV can reach us even from large distances. In contrast, high energy photons are attenuated as they travel through space, such that our view of their origin and, with that, the most powerful events in the universe is obscured. To access the information about far away and very energetic sources, other messengers are needed. Cosmic rays are deflected by magnetic fields and, similar to gamma-rays, interact with the extragalactic background light. Neutrinos have a very low cross section such that they travel through the Universe mostly unattenuated, pointing back straight to their sources. Gravitational waves are ripples in space-time which have to be detected with kilometer-sized interferometers at Earth, which makes the spatial reconstruction harder. Indeed, this region of the parameter space is accessible for neutrinos and gravitational waves [10].

Multi-messenger astronomy is a relatively new field of research, which requires sophisticated instruments to detect disparate messengers. By combining these independent measurements, a more complete picture of their production can be drawn, as they are likely correlated with each other already from the creation in the sources. An example is the so-called $\Delta(1232)$-resonance

$$p + \gamma \to \Delta^+ \to \begin{cases} n + \pi^+ & 1/3 \text{ of all cases} \\ p + \pi^0 & 2/3 \text{ of all cases} \end{cases} , \tag{2.1}$$

which describes an energetic cosmic ray (here: proton) interacting with a photon, for instance in the environment of the source. A Δ-meson is produced which subsequently decays into a baryon plus a charged or neutral pion. The branching ratio is roughly 1/3 for the charged pion channel and 2/3 for producing a neutral pion. These pions decay too, *i.e.*, $\pi^+ \to \mu^+ + \nu_\mu$ or $\pi^0 \to 2\gamma$, respectively. This shows that as soon as there is acceleration of cosmic rays to high energies and sufficiently dense photon fields to interact with, multi-messenger production is possible.

For low energies, multi-messenger observations happened as early as the 1940s, when cosmic rays were measured coinciding with solar flares, which were also observed electromagnetically [70]. In 1987, supernova SN1987A was detected, first with optical telescopes. A few hours later, neutrinos were detected in Kamiokande-II [71], the Irvine-Michigan-Brookhaven (IMB) experiment [72] and Baksan [73]. Often cited as the beginning of the multi-messenger era, a binary neutron star merger was observed in August 2017, first in gravitational waves and shortly after by electromagnetic radiation. The Laser Interferometer Gravitational-Wave Observatory (LIGO) collaboration reported a gravitational wave signal originating from the galaxy NGC 4993, which was later called *GW170817* [62]. A short gamma-ray burst dubbed SGRB170817A was detected by the Fermi Gamma-ray Space Telescope and the INTErnational Gamma-Ray Astrophysics Laboratory (INTEGRAL) 1.7 seconds later [63]. The optical counterpart named AT 2017gfo (originially SSS17a) was detected 11 hours later by the Swope Supernova Survey

(SSS) [74]. In the following, ultraviolet [75], X-ray [76] and radio signals [77] were detected, revealing a brightening of X-ray emissions for about half a year [78]. Strong evidence for a kilonova, in which heavy r-process (rapid neutron capture) nuclei are produced, was reported [79]. Neutrino and cosmic ray production in this event will be reviewed in chapter 6. Only one month later, a very high energy neutrino event with an energy of about 290 TeV named IceCube-170922A was detected by the IceCube collaboration [64]. A few days after, the Fermi-Large Area Telescope (LAT) and the Major Atmospheric Gamma Imaging Cherenkov Telescopes (MAGIC) collaboration reported the detection of gamma-rays from the blazar TXS0506+056, positionally consistent with the neutrino signal [80]. However, it is still controversial if the gamma-rays are correlated to the neutrino event [81]. Note that in multi-messenger astronomy, detection of a messenger and non-detection of another one can constrain production scenarios too.

In order to strengthen the conection between different observatories, networks were created to send out alerts in case of a potential detection, *i.e.*, the observatories share preliminary information on the position of the event, for example. Similarly, archival data is re-investigated to correlate events in different messengers spatially and temporally. The first such network was established in 1999 at Brookhaven National Laboratory and combined multiple neutrino detectors to generate supernova alerts as an early warning system [82]. In 2013, the Astrophysical Multimessenger Observatory Network (AMON) was created, which is a more ambitious project to facilitate multi-messenger observations [83]. Also sub-threshold events can be potentially interesting when looked at with several different instruments. Another automated program to search for astronomical transients is the All Sky Automated Survey for SuperNovae (ASAS-SN).

2.2 Ultra-high energy cosmic rays

After radioactivity was discovered in 1896 by Henri Becquerel, it was widely believed that any ionization of the air was caused by radioactive gases or elements in the Earth's crust and atmosphere [84]. However, in 1909, Theodor Wulf measured higher levels of ionizing radiation on top of the Eiffel Tower than at its base with an electrometer he developed [85]. Domenico Pacini observed similar effects with varying altitude in 1911, concluding that, contrary to the popular belief, there must be a component of ionizing radiation not originating from radioactive isotopes in the Earth's crust and atmosphere [86].

In 1912, high-altitude balloon flights were performed by Victor Hess, where he repeated measuring the ionization rate. He found that the rate increased significantly compared to ground level. To rule out that the Sun is the source of this radiation, Hess made a balloon ascent during a near-total solar eclipse. Finding the same increase of the ionization rate, he concluded that the observations can be best explained by radiation from beyond the atmosphere [87]. Later

balloon flights to higher altitudes in 1913–1914 by Werner Kolhörster confirmed Hess' results. Despite the fact that they were still unidentified, this led to the definitive discovery of cosmic rays, for which Hess was awarded the Nobel Prize in 1936.

It was Robert Millikan who established the name "cosmic rays" for this radiation, since he believed that they were mainly gamma-rays. This theory was disfavored by Jacob Clay in 1927, who found a variation of cosmic ray intensity also with latitude, indicating that cosmic rays are deflected by the geomagnetic field, *i.e.*, must be charged particles [88]. In 1930, Bruno Rossi predicted a difference between cosmic ray intensities arriving from the east and from the west, depending on the charge of the particles. Indeed, this difference was found in three independent experiments, since most particles have a positive charge [89].

Rossi also observed that Geiger counters at ground level simultaneously detect particles (well above the expected background) even if they are widely separated from each other. He realized that this could be an effect of an extensive air shower of particles, generated by the interaction of cosmic rays in the atmosphere [90]. In order to measure the cosmic rays indirectly by detecting these showers, an array of detectors extending over a large area had to be built to deduce the energy of the cosmic ray primary. In 1937, Pierre Auger arrived at the same conclusion, independent from Rossi's earlier findings. He stated that cosmic rays of particularly high energy interact with nuclei in the air, which initiates a cascade of secondary interactions, leading to a shower of photons and electrons at ground level. Auger already concluded that the energy of cosmic ray primaries initiating an extensive air shower is at least 10^{15} eV [91].

Further experiments until 1945 confirmed that primary cosmic rays consist mainly of protons, and that there is secondary radiation produced by interactions in the atmosphere. These secondaries were found to mainly consist of electrons, photons and muons. Homi J. Bhabha and Walter Heitler developed the corresponding theory for secondary production in cosmic ray showers and how they can be measured at ground level, serving as the basis for the modern understanding of air showers [92].

The first cosmic ray particle with an energy exceeding 10^{20} eV was detected at the Volcano Ranch experiment by John Linsley and Livio Scarsi in 1962 in New Mexico [93]. The array covered an area of 9 km^2 and used plastic scintillator surface detectors, a technology which was later used by a number of other extensive air shower detectors, such as Yakutsk in Russia [94], the Haverah Park experiment in England [95] or the Akeno Giant Air Shower Array (AGASA) in Japan [96], the latter with an area of about 100 km^2.

Cosmic rays can also be detected indirectly by observing the Cherenkov light generated by secondary particles from the air shower. Similar to scintillator detectors, arrays of water tanks equipped with photomultipliers are distributed over large areas. When a high energy secondary particle enters the tank, it will emit Cherenkov light since it travels faster than the speed of

light in water. This light is then measured to reconstruct the energy of the particle. Another way to perform a detection is by measuring the fluorescence light which is generated during the longitudinal development of the air shower in the atmosphere. High energy photons produced in the air shower can excite nitrogen molecules in the air, which in turn emit a lower energy, ultraviolet photon upon de-excitation. On Moonless nights, this fluorescence light can be observed. The High Resolution Fly's Eye (HiRes) experiment, operated in Utah, utilizes the atmospheric fluorescence technique.

These detection methods are widely used, for example in the Tunka Advanced Instrument for cosmic ray physics and Gamma Astronomy (TAIGA) [97] or IceTop [98]. The KArlsruhe Shower Core and Array DEtector (KASCADE) operated from 1996 with its extension KASCADE-Grande taking data from 2003 to 2009. They extended measurements of the spectrum up to 200 PeV and studied heavy components of cosmic rays [99, 100]. Currently, the largest cosmic ray detector is the Pierre Auger Observatory (PAO) in Malargue, Argentina. It consists of 1660 water Cherenkov detectors distributed over 3000 km^2 and 24 fluorescence detectors, making it also the first hybrid detector combining both, ground and fluorescence detectors [101]. Another hybrid detector is the Telescope Array (TA) using an array of 507 scintillation surface detectors and 3 fluorescence stations. With a covered area of 762 km^2, TA is smaller than PAO [102]. Since TA and PAO are two of the biggest experiments today, their results will be referred to throughout this thesis. Their findings are discussed in greater detail in Sec. 2.2.1. For both observatories, upgrades (AugerPrime, TAx4) are planned or under development.

Lower energy cosmic rays are measured directly due to the larger flux. There are several satellite based experiments, *e.g.*, the Payload for Antimatter Matter Exploration and Light-nuclei Astrophysics (PAMELA) [103] or the Voyager probes [104]. Some are mounted on the International Space Station (ISS), *e.g.*, the Cosmic Ray Energetics and Mass (CREAM, originally a balloon-borne experiment) [105] or the Alpha Magnetic Spectrometer (AMS-02) [106].

2.2.1 The cosmic ray spectrum and its features

In the recent past, the cosmic ray spectrum has been measured by various experiments, which is shown in Fig. 2.2. The flux spans over 32 orders of magnitude, with the low energy cosmic rays being the most abundant. For energies of about 10^{12} eV, roughly 1 particle can be detected per square meter and second, so direct detection is feasible. However, this rate drops rapidly with increasing energy, such that indirect observation becomes the main detection method. The cosmic ray spectrum follows a power law which changes its slope at several points. The first break happens at the so-called *knee* at about $\sim 10^{15.5}$ eV, where it changes from $E^{-2.7}$ to $E^{-3.1}$. The detection rate at the knee is already only 1 particle per square meter and year, emphasizing

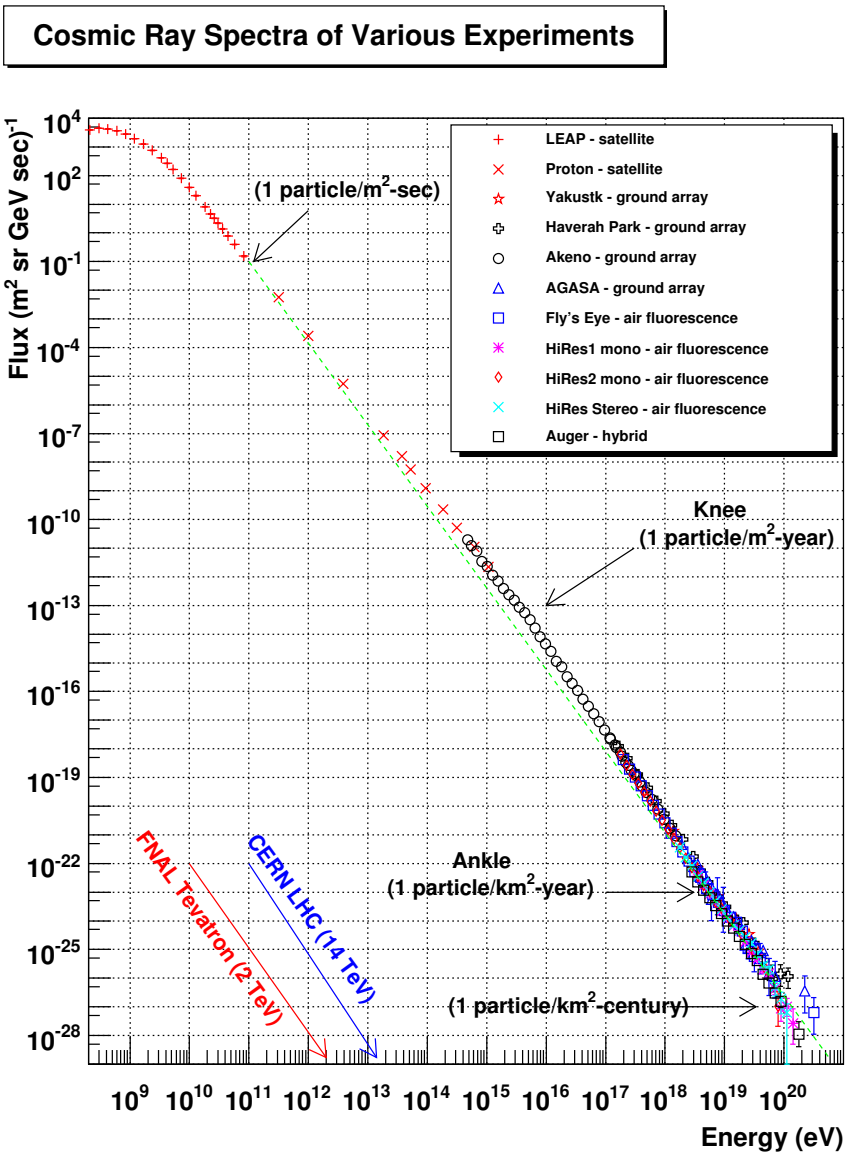

Figure 2.2: All-particle cosmic ray flux as a function of the particle energy as measured by various experiments. Spectral breaks of the spectrum, in particular the *knee* and *ankle*, are indicated with arrows together with approximate detection rates. The maximum energy of terrestrial accelerators is depicted for comparison (red: FNAL Tevatron, blue: CERN LHC). Taken from [2].

the need for huge detector areas. At the second break, called the *second knee* (at $\sim E^{17.7}$ eV not shown in the figure), the power law changes mildly to $E^{-3.2}$. The third feature of the spectrum is the so-called *ankle* at $\sim E^{18.5}$ eV, where the spectrum hardens again to $E^{-2.7}$. At this energy,

it can be expected to detect one particle every year for a detector with a surface area of 1 km^2. At the highest energies around 10^{20} eV, this number further decreases to one particle per square kilometer and century. The highest ever measured cosmic ray energies exceed the maximum energies of terrestrial accelerators, as indicated in the figure for CERN's LHC (blue arrow) or the Tevatron (red arrow) by a factor of several tens to hundreds of millions.

The different breaks in the spectrum have different origins. At the knee, Galactic cosmic rays might reach energies high enough such that their Larmor radius exceeds the size of the galaxy, leading to a depletion in the spectrum [107]. The second knee might indicate the energy above which also Galactic cosmic ray nuclei are depleted [108]. The most important feature of the spectrum for this work is the ankle, whose origin is still debated. Two scenarios which have been considered are energy losses from electron-positron pair production [109] or a transition from Galactic to extragalactic cosmic rays. The idea of a suppression by pair production, the so-called *dip model*, was disfavored by cosmogenic neutrinos in the case of protons interacting with the cosmic microwave background (CMB) $p + \gamma_{\mathrm{CMB}} \to p + e^+ + e^-$, which would exceed neutrino limits [29]. Also the composition be too light in such a scenario (see Sec. 2.2.2).

At the highest energies, a suppression of the spectrum is measured. It is still debated if at energies around $\sim 10^{21}$ eV the accelerators of cosmic rays run out of power or if the cut-off is caused by the interaction of cosmic rays with the cosmic microwave background, as postulated by Greisen, Zatsepin and Kuzmin in 1966 [110, 111]. The so-called *GZK cut-off* is determined by the energy threshold of photo-hadronic interactions as in Eq. (2.1). With the photon energy of the CMB, it can be calculated that this process sets in at energies around $\sim 5 \cdot 10^{19}$ eV, with a mean free path of about 50 Mpc for this interaction. Thus, it is unlikely that protons with higher energies reach the Earth from distances larger than this. This distance is therefore also known as the *GZK horizon*.

While cosmic rays with energies below the ankle could originate from objects in the Milky Way, cosmic rays with higher energies than $\sim 10^{18}$ eV are presumably of extragalactic origin as their Larmor radii exceeds the size of our galaxy [113]. Cosmic rays with energies $E > 10^{18}$ eV are called *ultra-high energy cosmic rays* (UHECRs). A zoom-in on this part of the spectrum, as measured by PAO, is shown in Fig. 2.3, emphasizing the ankle at ~ 5 EeV and the cut-off at ~ 40 EeV [112]. Note that in this representation, the spectrum is multiplied by E^3.

2.2.2 Chemical composition of UHECRs at Earth

The composition of cosmic rays can be deduced from observing the longitudinal profile of air showers with fluorescence detectors. If the incoming cosmic ray primary is a proton, fewer secondary particles are expected compared to an air shower initiated by a heavier nucleus with

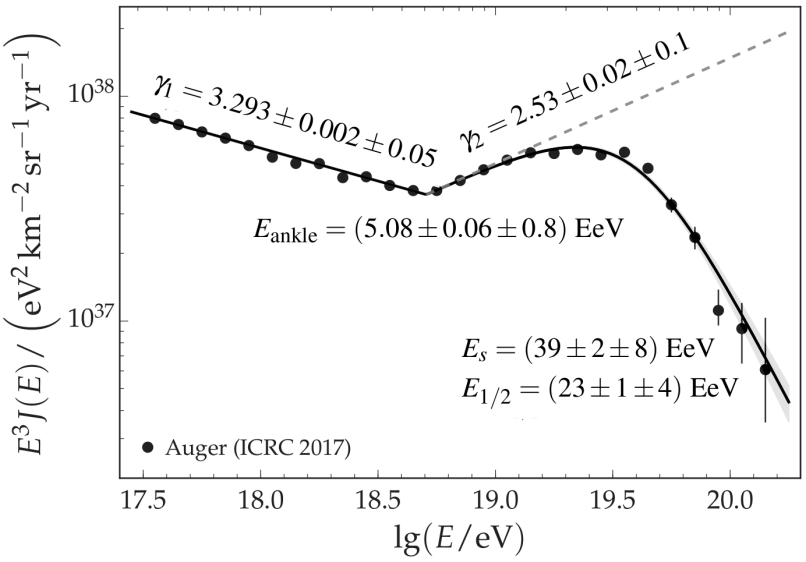

Figure 2.3: Ultra-high energy cosmic ray spectrum as measured by PAO as a function of the energy. The spectral indices of the empirically fitted power laws, γ_1 and γ_2, below and above the ankle at $E_{\text{ankle}} \sim 5$ EeV are added. The energy of the suppression is given by E_S and $E_{1/2}$ represents the energy at which the integrated flux drops by a factor of two below the expectation without suppression. Taken from [112].

the same energy. In addition, the number of secondary particles peaks at a different depth of the shower in the atmosphere. For nuclei primaries, the average depth of the shower maximum is reached earlier, *i.e.*, for higher altitudes than for protons [114].

The corresponding measurement by PAO is shown in Fig. 2.4. Plotted are the first and second moment of the distribution of the shower maximum, $\langle X_{\text{max}} \rangle$ (left panel) and $\sigma(X_{\text{max}})$ (right panel), as a function of the energy. The data points are to be compared to the air shower simulations for protons (red lines) and iron (blue lines), computed with hadronic interaction models EPOS-LHC [115], Sibyll2.3 [116] and QGSJetII-04 [117], as indicated by the legend. The data shows a clear trend towards higher masses for cosmic ray energies beyond the ankle, *i.e.*, $E > 10^{18.5}$ eV. Hence, ultra-high energy cosmic rays do not consist solely of protons, which will become important for the simulations performed in this work.

In contrast to PAO, the composition measurement obtained by TA is compatible with protons for all energies [118]. This triggered a controversy in the community and there is a dedicated joint working group to sort out the differences. Taking into account the different methods in both analyses, the measurements are consistent with each other within their uncertainties [119]. Note that the two observatories are monitoring different parts of the sky, as TA is seeing the northern hemisphere and PAO the southern hemisphere.

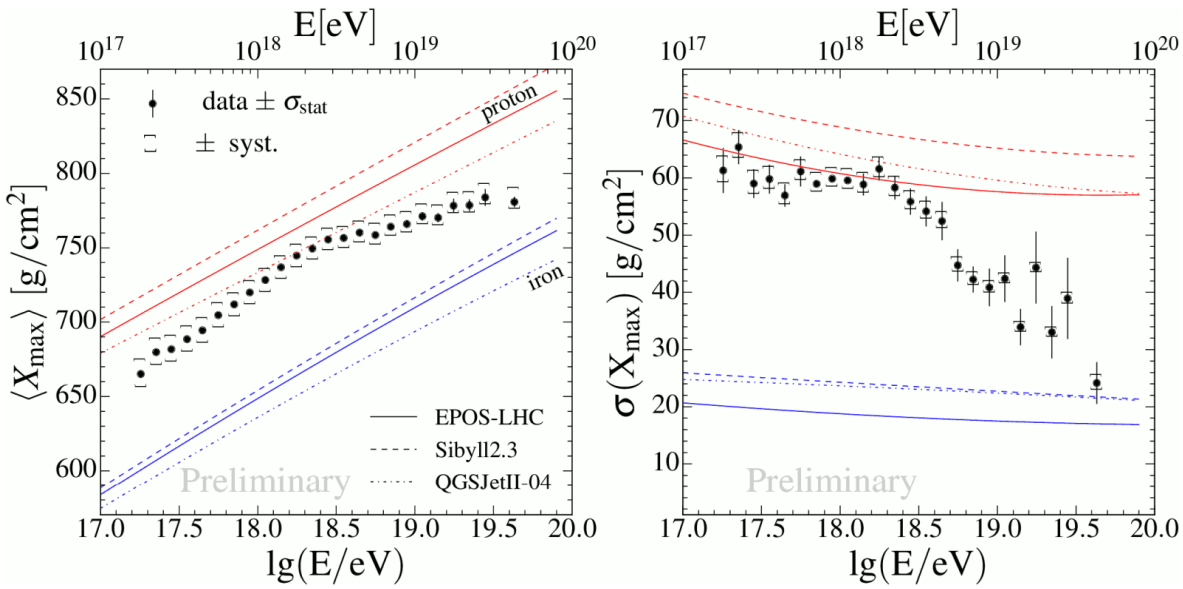

Figure 2.4: Mean atmospheric depth of the shower maximum $X_{\max}$ (left) and standard deviation of $X_{\max}$ (right) as a function of the energy. For comparison, predictions of different hadronic interaction models (solid: EPOS-LHC, dashed: Sibyll2.3, dot-dashed: QGSJetII-04) for pure proton (red) and iron (blue) composition are also shown. Taken from [114].

Results on the arrival direction of ultra-high energy cosmic rays were also published by PAO. The large-scale anisotropy of cosmic rays with energies above 4 EeV was studied in two energy bins, $E \in [4, 8]$ EeV and $E \geq 8$ EeV. A significant dipolar modulation in right ascension was found in the second bin with an amplitude increasing with energy. The direction of the dipole is reported to be consistent with an extragalactic origin at all considered energies. There were no statistically significant quadrupolar components found in the anisotropy [120]. These results can be discussed in the context of model predictions, but arrival directions are not included as a part of the models reported in this thesis.

2.3 Astrophysical neutrinos

Neutrinos are electrically neutral elementary particles which were first postulated by Wolfgang Pauli in 1930 as a way to ensure energy conservation in beta decay, *i.e.*, $n \to p + e + \bar{\nu}_e$ [121]. As neutrinos were not detectable with conventional instruments in that time, it took until 1956 to confirm the existence of neutrinos via inverse beta decay $\bar{\nu}_e + p \to e^+ + n$ by Clyde Cowan, Frederick Reines and collaborators. They used scintillators to detect coincident photons of

about 0.5 MeV, each of which are produced in the annihilation of the resulting positron with a neighbouring electron, giving a unique signature [122].

In 1968, the Homestake experiment to collect and count neutrinos emitted by nuclear fusion in the sun was carried out by Raymond Davis Jr. and John Bahcall. It was a chlorine detector where an incoming neutrino would convert chlorine-37 to argon-37. The argon is separated from the chlorine by purging it with helium gas and the argon atoms can be counted by electron capture radioactive decays. The experiment successfully detected and counted solar neutrinos, however the detected rate turned out to be only about one third of the theoretical prediction [123]. This created the solar neutrino problem. Later it was found that neutrinos, as the leptons in the Standard Model, appear in three generations, which are called flavors. The Homestake experiment was only sensitive to the electron flavor, thus recording only one third of the flux. Later, the two other flavors were discovered, namely the muon-neutrino in 1962 by Jack Steinberger, Melvin Schwartz and Leon Lederman [124], and the tau-neutrino in 2000 by the DONUT ("Direct Observation of the NU Tau") collaboration at Fermilab [125].

The solar neutrino problem was solved when the Sudbury Neutrino Observatory (SNO) in Ontario, Canada, detected neutrino oscillations [126]. Neutrino oscillations are a consequence of them being produced in so-called flavor eigenstates, together with the corresponding lepton. These flavor eigenstates are superpositions of propagation eigenstates (mass eigenstates), such that a neutrino traveling through space will change its flavor depending on the distance, energy and the medium through which it propagates. Different from the predictions of the Standard Model, the neutrino masses are not zero, which has been proven by neutrino oscillations, as they depend on the differences of the mass squares [127]. The neutrino mass is yet undetermined, but can be constrained to very small values. An upper limit obtained by the direct measurement of the beta spectrum ending point in tritium decay is 2 $\mathrm{eV/c^2}$ [128, 129]. It is expected that this limit will be improved by the Karlsruhe Tritium Neutrino Experiment (KATRIN) by one order of magnitude to 0.2 $\mathrm{eV/c^2}$ [130]. The cosmological approach to constrain the neutrino mass predicts a similar limit of 0.2 $\mathrm{eV/c^2}$ for the sum of all three neutrino masses. This estimate is based on the anisotropy of the cosmic background radiation and the parameters of the ΛCDM model. Neutrinos have an impact on structure formation and primordial nucleosynthesis in the Universe, which is where this constraint comes from [131]. Also, the mass hierarchy, *i.e.*, the order of the mass eigenstates, is unknown [132].

Hypothetically, neutrinoless double beta decay can be another option to infer on their mass. If two neutrons of a nucleus decay simultaneously, the two neutrinos can annihilate instead of being emitted. In this case, all the energy is taken by the electrons, such that the electron spectrum has a maximum close to the decay energy. This is, however, only possible, if neutrinos are Majorana particles (in contrast to the Standard Model), *i.e.*, they are their own anti-particles,

otherwise lepton number conservation would be violated. Currently, neutrinoless double beta decays have not been observed [133].

For these light fermions, no right-handed equivalent was observed so far. One possibility to explain this is by the existence of right-handed sterile neutrinos, which interact only via gravitation and are therefore also a candidate for Dark Matter. Sterile neutrinos can, however, mix with active neutrinos of the Standard Model which could be the responsible process to generate their mass. The results of the Liquid Scintillator Neutrino Detector (LSND) experiment, which was running from 1993 to 1998 in Los Alamos, were interpreted as a hint on the existence of sterile neutrinos, but the results are still disputed. Further investigations are currently performed with MiniBooNE since 2007 at Fermilab. See [134] for a recent review.

2.3.1 Neutrino telescopes and the cosmic spectrum

Neutrinos can interact only weakly, mediated by W or Z bosons, with a typical weak cross section of $\sim 10^{-42}$ cm^2, which leads to extremely long mean free paths. Detectors must therefore be very large, such that first ideas of underwater neutrino telescopes were proposed already in 1960 by Moisey Markov. This kind of detectors takes advantage of the Cherenkov radiation produced by a fast, charged particle produced in a neutrino interaction traveling through the medium. This method is one of the most popular nowadays and it can be used to infer on the energy, direction and sometimes flavor of the incident neutrino, as described below. For background suppression of cosmic rays, which are mistakenly identified as neutrinos, lower energy experiments are placed underground such that the instrument is shielded by the earth above. Higher energy experiments often use a "veto" layer surrounding the primary detector, revealing cosmic rays entering the detector and giving a wrong signature.

Popular examples of detectors using this technique are for example the Super-Kamioka Neutrino Detection Experiment (Super-Kamiokande, Super-K) in Japan [135], the Astronomy with a Neutrino Telescope and Abyss environmental RESearch (ANTARES) telescope in the Mediterranean Sea [136] or, with ice as a medium, the Antarctic Muon And Neutrino Detector Array (AMANDA) [137]. AMANDA has been upgraded to the IceCube observatory, which is currently the biggest of its kind with a volume of about 1 km^3 [138]. The next generation deep sea neutrino telescope will be KM3Net with a total instrumented volume of about 5 km^3, for which the first implementation phase started already in 2013 [139]. The Probe Of Extreme Multi-Messenger Astrophysics (POEMMA) is a planned experiment for observing UHECRs via fluorescent nitrogen in extensive air showers and neutrinos through Cherenkov radiation of up-going tau lepton decays [140]. An upgrade for IceCube called IceCube-Gen2 is currently being planned [141].

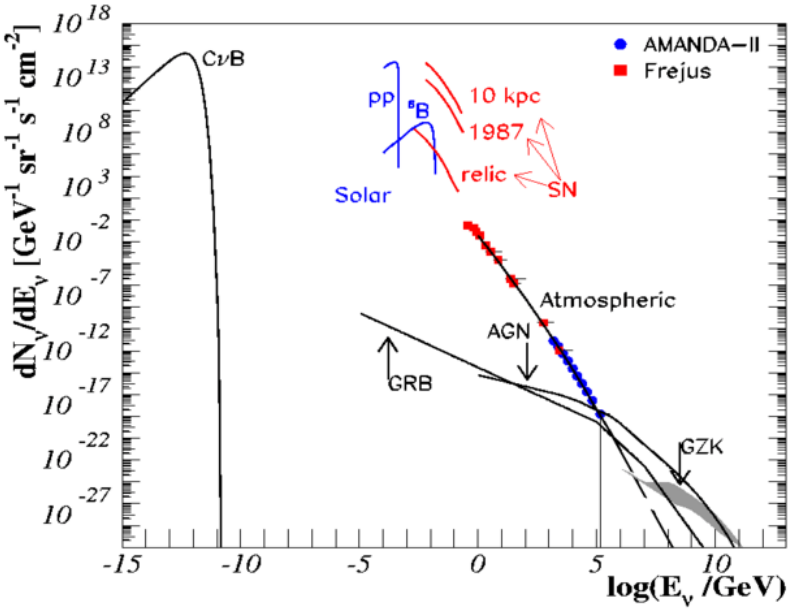

Figure 2.5: Cosmic neutrino spectrum detected at Earth as a function of the energy. The contribution of different components is indicated by the labels: Big Bang (CνB), the Sun (solar), supernovae (SN), atmospheric neutrinos, active galactic nuclei (AGN), gamma-ray bursts (GRB) and cosmogenic neutrinos (GZK). Data points of AMANDA (blue) and the Frejus underground laboratory (red) are shown. Taken from [142].

Radio detection of neutrinos is also possible by using antennas to detect Cherenkov emission from particle showers produced by neutrinos at the highest energies. Because of the high energy, it is especially suited for searches of cosmogenic neutrinos, *i.e.*, neutrinos that are produced by cosmic ray interactions off the CMB during their propagation (also called GZK neutrinos). Next generation detectors considered for construction are, *e.g.*, the Askaryan Radio Array (ARA), which is designed to detect cosmogenic neutrinos with a rate of a few per year [143]. Two of the biggest radio detectors currently planned are the Antarctic Ross Ice-Shelf ANtenna Neutrino Array (ARIANNA), which is planned to cover about 900 km^2 [144], and Giant Radio Array for Neutrino Detection (GRAND), which will have $\sim$ 200,000 antennas in total, if approved [145].

The cosmic neutrino spectrum is shown in Fig. 2.5 for a wide range of energies [142]. At the lowest energies, around 10^{-4} to 10^{-6} eV, there is a contribution from relic neutrinos from the Big Bang. This component is also called cosmic neutrino background (CνB). Since even high energy neutrinos are notoriously difficult to detect, it was not possible to observe these neutrinos so far, but there is strong indirect evidence that this component exists [146]. Next, there are

solar neutrinos with energies of about 0.1 to 18 MeV. Neutrinos from supernovae (see, *e.g.*, [147, 148]), as the ones detected for SN1987A, have similar energies ($\lesssim$ 60 MeV). Atmospheric neutrinos from cosmic ray interactions set in around GeV energies. The highest energy cosmic neutrinos originate from cosmic accelerators or cosmic ray interactions with the CMB on their way to Earth. Their energy can in principle reach up to $\sim 10^{19}$ eV, yet such high energies have not been observed until now [149]. The decay of radioactive elements in the Earth can be an additional component ($\lesssim$ 4 MeV). Other sources of neutrinos are manmade, such as reactor neutrinos ($\lesssim$ 10 MeV) and neutrinos from accelerators ($\lesssim$ 10 GeV).

2.3.2 Astrophysical spectrum and absence of correlations

In 2013, the IceCube neutrino telescope discovered ultra-high energy neutrinos between 30 TeV and 2 PeV, likely of extragalactic origin, with a significance of more than 5σ [8]. As mentioned above, IceCube is currently the largest operating neutrino telescope with an instrumented volume of 1 km^3. It is a Cherenkov detector which uses Antarctic ice as a medium for neutrino interactions, detecting them with photomultipliers buried deep in the ice. These photomultipliers are contained in digital optical modules (DOMs), which are in turn mounted onto a string with a spacing of 17 meters. A total of 86 strings with 60 DOMs each are deployed in $\sim$ 2.5 km deep holes drilled with hot water. In the center of the array, a section of the ice dubbed DeepCore has been more densely instrumented to lower the neutrino energy detection threshold, extending the observable energies below 100 GeV [150].

IceCube can observe different event topologies, of which the main ones are tracks and cascades. The latter can be observed due to neutral-current (NC) interaction of neutrinos of arbitrary flavor, *e.g.*, $\nu_x + N \rightarrow \nu_x + N'$, generating hadronic cascade. Cascades can also be created by charged-current (CC) interactions of electron-neutrinos, *e.g.*, $\nu_e + N \rightarrow e + N'$, resulting in an electromagnetic cascade, *i.e.*, a cascade with a higher electron and photon content. In either case, the signature is localised, approximately spherical and likely to be fully contained within the detector. Thus, the uncertainty in the energy reconstruction is low ($\sim$ 15% above 10 TeV), but the reconstruction of the arrival direction is poor (10° to 40°). For muon tracks it is the opposite: they are observed following a charged-current interaction of a muon-neutrino, *i.e.*, $\nu_\mu + N \rightarrow \mu + N'$, where the resulting muon produces a track of photons along its trajectory. Due to the large mean free path of the muon, the track has a much better angular resolution ($\lesssim 1°$) than cascade events. On the other hand, it is likely that a part of the track is not contained in the detector, which leads to a poorer energy resolution. Tau-neutrinos at PeV energies can be identified via their expected "double bang" topology, *i.e.*, $\nu_\tau + N \rightarrow \tau + N'$, which shows a hadronic cascade at the interaction vertex and a second cascade where the τ-lepton decays

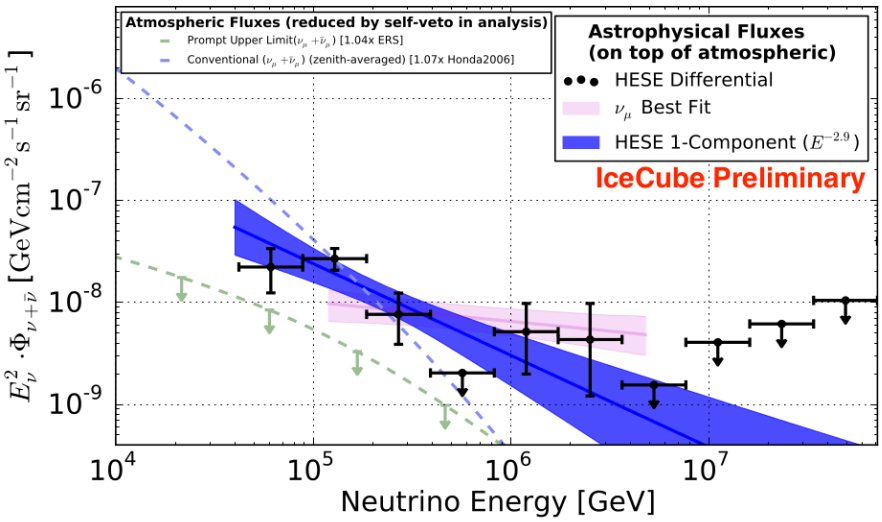

Figure 2.6: Diffuse astrophysical neutrino spectrum (single flavor, combined neutrino and anti-neutrino) as a function of the energy. The black data points with the 1σ uncertainties attached are from the High Energy Starting Events (HESE) data set, with the blue band showing the 1σ uncertainties of a single power-law best-fit to HESE data. The pink band represents the best fit of the through-going muon (TGM) data set. Atmospheric fluxes are also shown (blue: best-fit conventional, green: best-fit upper limit prompt). Taken from [151].

into a tau-neutrino. If only one of the two vertices is contained in the detector, it is called a "lollipop" signature. See [152] for an overview of the event topologies.

Furthermore, incoming electron-antineutrinos can interact resonantly with electrons to create a W boson, *i.e.*, $\bar{\nu}_e + e \rightarrow W$, if their energy is about 6.3 PeV. The obtained signal can be a hadronic cascade or a leptonic cascade or track, depending on the decay channel of the W boson [153]. This so-called *Glashow resonance* will become important in Sec. 3.2.3 since for different production mechanisms in astrophysical objects different flavor ratios are obtained for the neutrinos. This results in different event rates for the Glashow resonance, providing a tool for neutrino production diagnosis.

In 6 years of IceCube data, 82 high energy cosmic neutrinos with energies between 100 TeV and 10 PeV have been detected. The flux of astrophysical neutrinos (per flavor, combined neutrino and antineutrino), as it is known today, is shown in Fig. 2.6 as a function of the energy. There are two main data sets, namely High Energy Starting Events (HESE) and Through-Going Muons (TGM). Fitting the data sets with a single power law yields $E^{-2.9}$ (blue band, including 1σ uncertainties) for HESE and $E^{-2.1}$ (pink band, including 1σ uncertainties) for TGM as a best fit spectral index. Also shown in the figure are the best fit for the conventional atmospheric

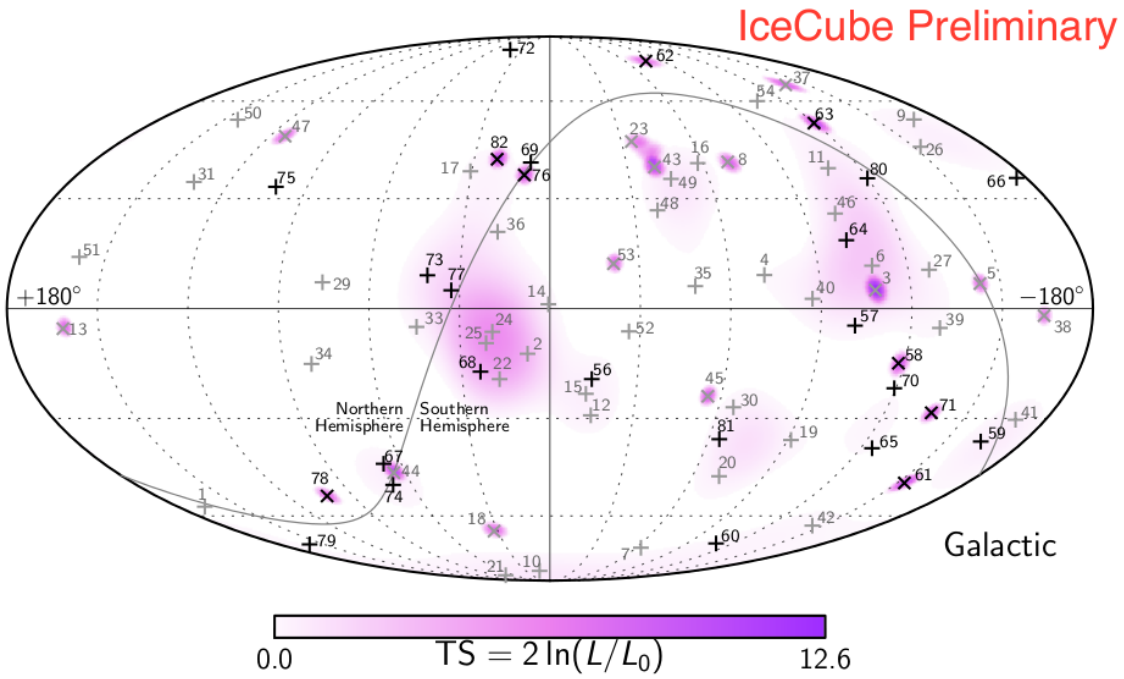

Figure 2.7: Skymap of the arrival direction of detected neutrino events in Galactic coordinates. Shower-like events are indicated by + while track-like events are marked with ×. At each location, the color scale represents the test statistics (TS) for point-source clustering. No significant clustering was found. Taken from [151].

neutrino flux (dashed, blue curve) and the best fit for the prompt atmospheric contribution (dashed, green curve) by cosmic ray interactions in the atmosphere [151]. It has been suggested that the TGM are more representative of the astrophysical flux, possibly because the HESE samples are contaminated with atmospheric events [154].

With the current statistics, it appears that the signal is isotropic, as it shows no significant clustering in the search for point sources, as shown in Fig. 2.7. A maximum-likelihood clustering method with the test statistic (TS) defined as the logarithm of the ratio between maximum likelihood to include a component of a point source and the likelihood for the isotropic null hypothesis was performed. The analysis by IceCube did not find any clustering, *i.e.*, no point sources or hot spots in the sky [151]. Furthermore, the signals are neither coincident with the occurence of gamma-ray bursts [14] nor active galactic nuclei [155] and there is no definite detection of multiple neutrinos from an individual source [156]. This translates into a number of constraints, *e.g.*, the point source limits, stacking bounds or multiplet constraints, which will be discussed in place when they are relevant for the source classes investigated in this thesis.

Chapter 3

Nuclear cascades in combined source-propagation models

As mentioned in Chapter 2, a wide variety of tools including analytical models as well as numerical simulations are used in theoretical astrophysics to tackle a great variety of astrophysical problems. While, in general, the analytical approach enhances the understanding of the physical processes which are involved, it does not always lead to precise results for complex systems. In this case, numerical simulations are needed to perform these calculations with high accuracy in order to obtain meaningful predictions and to study the observational consequences. If the observation is inconsistent with the prediction, the model is adjusted by minimal modifications to fit the data. However, if the inconsistencies are too large, a model representing a certain physical scenario can be disfavored or even ruled out. Following this approach, a numerical simulation will be set up to test source scenarios. By comparing with the data presented in Chapter 2, it is possible to study the properties of potential sources and determine whether they can address the observations.

Neutrinos are, for example, produced in cosmic ray interactions with ambient photons. These processes can be described by providing the corresponding particle densities and cross-sections. While cross-sections are input, the particle densities are determined mainly by the source environment, *i.e.*, how much energy is available and how the source geometry is defined. The idea in this thesis is to set up a fully flexible, deterministic simulation to calculate nuclear processes, which is then applied to certain types of sources. The key novelty of this work is the *nuclear cascade*, which represents the interactions of heavy isotopes and how they break up ("cascade down") due to different radiation processes, leading to neutrino production and altering the cosmic ray composition.

In this chapter, the nuclear cascade is introduced in great detail, along with other ingredients needed to set up a generic model. An overview of the different components is given in Fig. 3.1. In the first step, the progenitor scenario determines the main parameters, *i.e.*, the available energy and volume, and with that the energy densities. Further input obtained from the progenitor is, *e.g.*, the duration of the emission or what the spectral shape of accelerated cosmic rays and target photons looks like. Another important input is the composition of cosmic rays which are

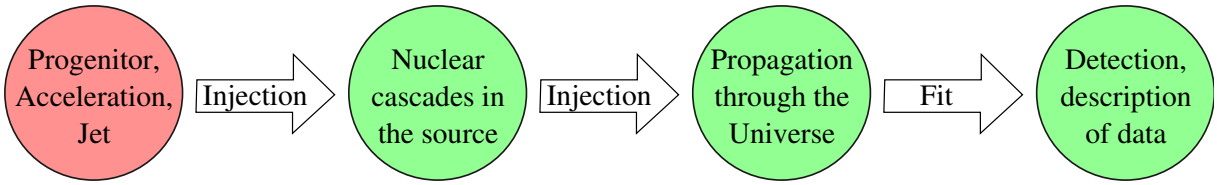

Figure 3.1: Schematic representation of the key components of a generic model. The first ingredient is the progenitor, which determines the source geometry. The densities of accelerated particles and target photons serve then as an input to calculate the nuclear cascade in the radiation zone. Particles escape from the source and propagate through the Universe in the next step, before they are eventually detected at Earth. The colors indicate which components are modeled in this thesis (green) and for which generic assumptions are used (red).

accelerated. Based on this information, the nuclear cascade is calculated in the next step. This yields the particle densities after interactions and energy losses. In this process, neutrinos and gamma-rays are produced and the composition can change because of the gradual disruption of heavy nuclei into lighter fragments. This is the heart of the simulations presented in this thesis, as it is the first fully self-consistent and efficient computation of time-dependent nuclear cascades. A certain fraction of the cosmic rays can escape from the source and undergoes further interactions during propagation through the Universe. These processes can further alter the composition of cosmic rays and produce cosmogenic neutrinos, *i.e.*, neutrinos produced by cosmic ray interactions during propagation. In the last step, the predicted cosmic rays and neutrinos that eventually arrive at Earth are compared to the UHECR spectrum and composition data as well as high energy neutrino data. This will ultimately test the model and with that the source candidates to constrain the origin of UHECRs.

The color of the circles in Fig. 3.1 indicates which components are part of the modeling (green) and for which part certain input assumptions are used (red). In this thesis, the progenitor and acceleration scenarios are not explicitly modeled. Instead, the remaining three components are assembled first and then applied to several source classes which are discussed in the following chapters. Most numerical models in the literature are propagation-only models in contrast to the models developed here, *i.e.*, including only the last two components (see for example [157, 60, 42, 158]). Thus, there are predictions about the composition of cosmic rays at the ejection from the source, after the nuclear cascade developed. However, with including the nuclear cascade as a part of the simulation, the fit to the data can be studied as a function of the injection composition of the source. This is required to uncover the properties of potential

UHECR sources. In addition, different from existing models which take into account the nuclear processes in the source (see for example [23]), the simulations presented in this thesis are efficient, such that parameter scans can be performed.

Now that the signals which are measured at Earth were introduced in the previous chapter, the parts of the model will be presented in this chapter, following the first part in our paper [159]. In Sec. 3.1, it will be described how cosmic rays are accelerated in the source. The second component, namely the nuclear cascade and the radiation modeling will be reviewed in detail. Lastly, it will be discussed how particles can escape from the sources. After that, in Sec. 3.2, the interface to cosmic ray propagation is discussed together with energy budget considerations and cosmological evolution scenarios. Neutrinos do not interact on their way to Earth, but they do oscillate. Flavor mixing and its consequences will be reviewed in detail in the last section of this chapter. The flavor composition can be used to infer on source properties via the Glashow resonance, which will be discusses at the end, based on our paper [160].

3.1 Radiation modeling in collisionless internal shocks

There are two different regimes for which radiation of astrophysical transients is observed: the prompt emission and the afterglow. The principle is depicted in Fig. 3.2 in the case of a black hole engine [161]. In general, it is assumed that the prompt emission is related to the actual event, *e.g.*, a star collapsing to a black hole. The stellar material is ejected with high but different velocities depending on the dynamics of the source. This can happen in the form of a collimated jet, but that is not necessarily the case, as the jet could also be choked or the emission could originate from a cocoon [162, 163]. In a simple picture, spatial over- and under-fluctuations of the matter density with different speeds are represented by shells. These shells collide eventually due to the non-vanishing relative Lorentz factor and so-called *internal shocks* can form. Particles can be further accelerated by scattering off the shock front (see Sec. 3.1.1 for details) and nuclear interactions are triggered if the shock is dense enough.

On the other hand, the afterglow emission happens when the ejected material eventually collides with the ambient medium. External shock waves in the forward (forward shock) and backward (reverse shock) direction are formed which can lead to acceleration and nuclear interactions as well. The afterglow emits radiation over much longer time scales than the prompt phase. In practice, it is therefore more challenging to observe the prompt emission of an astrophysical source, if this part of the sky is not monitored by chance. It is believed that the highest energies are reached during the prompt emission phase, since much more energy is released therein [164, 165]. For that reason, this thesis focuses on modeling the prompt emission

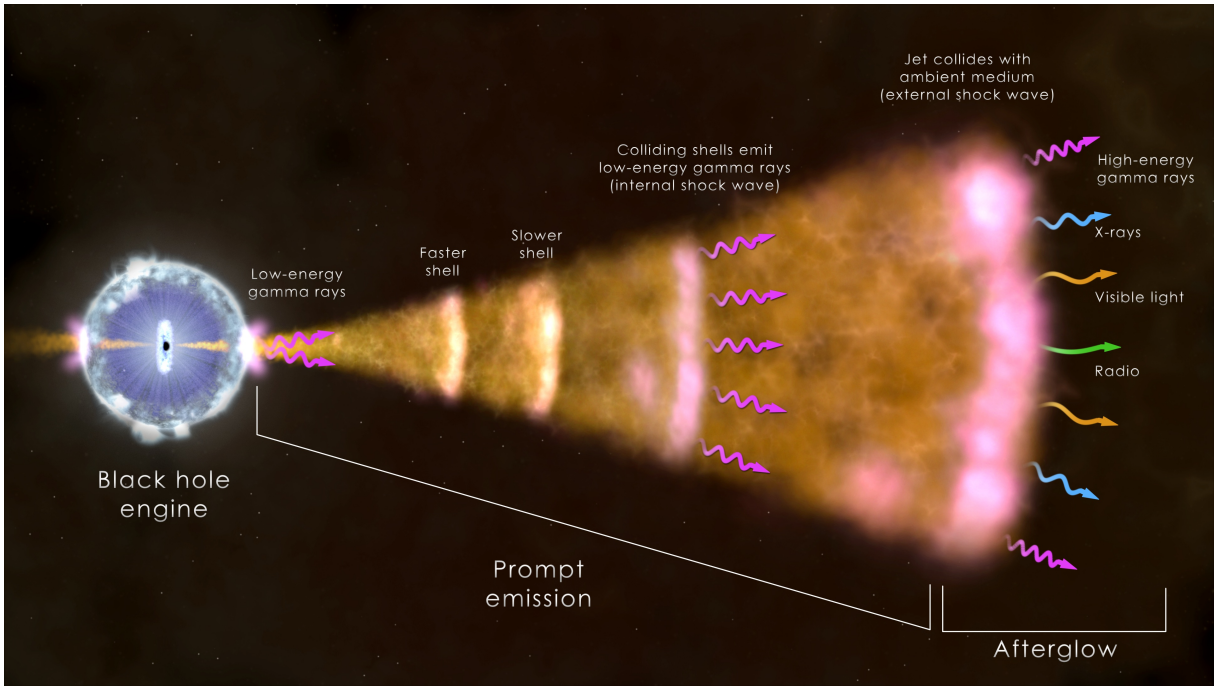

Figure 3.2: Schematic scenario for prompt emission and afterglow of an astrophysical transient. An engine (here: black hole) emits material (not necessarily in a collimated jet) with high velocities. Spatial fluctuations of the matter density, here represented as shells, may collide and internal shocks are formed, leading to particle acceleration, gamma-ray emission and nuclear interactions. Later, further particle acceleration and interactions can happen in external shocks in the afterglow. Taken from [161].

phase in the internal shock model. The main relation of the internal shock model,

$$R = 2\Gamma^2 c \frac{t_v}{1+z} \quad , \tag{3.1}$$

connects the radius at which the shells of plasma collide with the observed variability t_v of the light curve. The variability time scale is also indicative for the shell width $\Delta d' = \Gamma c t_v/(1+z)$, with the shock Lorentz factor Γ and redshift z.

Besides the already mentioned internal shock model, there are two more types of models for the prompt emission phase. One of them are photospheric models, in which the radiation is assumed to originate from thermal electrons inside the plasma. The thermal photons emitted by the electrons can interact again via inverse Compton scattering, pushing them to very high energies. Once the plasma density decreased sufficiently such that the optical depth to Thomson scattering falls below unity, the photons can escape from the plasma. This decoupling can depend on the wavelength of the corresponding photons. Indeed, multi-wavelength observations indicate

a delayed emission of the high energy radiation. In this model, neutrino production is believed to take place near the photosphere, *i.e.*, the transition of the plasma being opaque to transparent. The photospheric radius is typically smaller than the radius at which internal shocks occur, which leads to higher radiation densities. See for example [166, 167] for a review.

The second alternative are jets powered by magnetic reconnection, as for example the Internal Collision Induced Magnetic Reconnection and Turbulence (ICMART) model [168, 169]. In this model, particles are accelerated due to turbulent reconnection of magnetic fields inside the plasma. In contrast to photospheric models, the radius at which photo-hadronic interactions happen, *i.e.*, interactions between photons and nuclei, are expected to be larger than in the internal shock scenario. The advantage of this model is that it describes pulses and the fast time variability of the light curve at the same time by introducing two instead of one characteristic time scale. However, this also means that the interaction rate is suppressed by the ratio of these time scales. Because of this and due to the different model geometry in all three cases the predicted neutrino fluxes can be different.

3.1.1 Fermi acceleration in compact source environments

The primary mechanism by which particles are accelerated in astrophysical sources is the Fermi acceleration, sometimes also called diffusive shock acceleration. It plays an important role in many astrophysical models as particles gain non-thermal energies by being repeatedly reflected at astrophysical shock fronts. There are two different types of Fermi acceleration, namely the first-order Fermi mechanism, which is the acceleration in shocks, and the second order Fermi mechanism, which refers to energy gain in the environment of moving, magnetized gas clouds. Either way, the medium has to be collisionless, *i.e.*, mediated by plasma instabilities, as otherwise frequent collisions with surrounding particles will cause significant energy loss. Thus, it only applies to particles exceeding thermal energies.

Charged particles traversing the shock wave can encounter turbulences in the magnetic field, which can reflect it back through the shock at increased velocity. This process can happen repeatedly, leading to great increases in energy. Assuming that the fractional change in kinetic energy after each crossing of the shock is β, a particle with an initial energy of E_0 will have the energy $E = E_0\beta^n$ after n crossings. Not all particles will return to the shock front as the momentum of the shock itself may carry them away. For P being the probability that the particle remains within the accelerator after each cycle, after n crossings, there will be $N = N_0 P^n$ of the former N_0 particles left in the shock-crossing region. From these expressions, it follows that $N/N_0 = (E/E_0)^k$, with $k = \log P/\log\beta$. In the differential form, a power law $N(E)dE \propto E^{-k}dE$ is recovered. Typically it is expected that $k \gtrsim 2$, but the exact shape depends on the structure

of the shock. Note that this power law shape is already desirable to explain the observed cosmic ray spectrum. For a full theoretical description, see *e.g.* [170, 171].

The acceleration rate assumed in the following is $t_{\rm acc}^{-1} = \eta c/R_L$, where $R_L = E/ZeB$ is the Larmor radius of a particle with energy E and charge number Z in a magnetic field B [172]. The parameter $\eta \leq 1$ is the acceleration efficiency, which is assumed to be 1 in this work, unless noted otherwise. This time scale will be compared to energy loss time scales to determine the maximum energy $E_{\rm max}$ of the accelerated particles. The injected spectrum of particles is then $\propto E^{-2}\exp(E/E_{\rm max})$, normalized to the total energy density in baryons (see also Sec. 4.1). It is assumed that the acceleration and radiation zone, *i.e.*, the region where the particles are accelerated and where they interact, are separated from each other. However, this so-called two-zone model is an approximation as acceleration and interactions could happen simultaneously.

3.1.2 Radiation processes in the nuclear cascade

The calculation of the radiation processes in the nuclear cascade is the main component of the simulations performed in this work. It is based on the *NeuCosmA* code [16, 173], which was implemented to study a pure proton scenario in gamma-ray bursts in [172, 26]. Here, this work is extended by adding heavy nuclei up to iron, motivated by the recent findings of the intermediate mixed composition of UHECRs by PAO. Due to the interaction processes, a subsequent break up of these heavy nuclei into lighter fragments is initiated, which is called the nuclear cascade. See also the complementary description in [24] and our paper [159].

Computing the nuclear cascade is based on a fully deterministic approach to solve the governing system of coupled partial differential equations (PDEs)

$$\frac{\partial N_i'}{\partial t} = \frac{\partial}{\partial E'}(-b'(E')N_i'(E')) - \frac{N_i'(E')}{t_{\rm esc}'} + \tilde{Q}_{ji}'(E') \quad , \tag{3.2}$$

for every particle species i such as nuclear isotopes. The term $b'(E') = E' t_{\rm loss}'^{-1}$ describes energy losses (with loss rate $t_{\rm loss}'^{-1}$) and $t_{\rm esc}'^{-1}$ represents the escape term, *i.e.*, processes which change the particle species or physical escape from the radiation zone. Primed quantities refer to the frame where the shock is at rest, also called shock rest frame (SRF), whereas later the escaping particle fluxes are boosted in the observer's frame. This system of PDEs has to be solved for the differential particle densities N_i' [GeV^{-1} cm^{-3}], with the coupling arising due to the injection term

$$\tilde{Q}_{ji}'(E') = Q_i'(E') + Q_{j\to i}'(E') \quad . \tag{3.3}$$

In Eq. (3.3), the first term $Q_i'(E')$ describes the possible injection from an acceleration zone (typically a power law, see Sec. 3.1.1). The second term $Q_{j\to i}'(E')$ represents the injection from

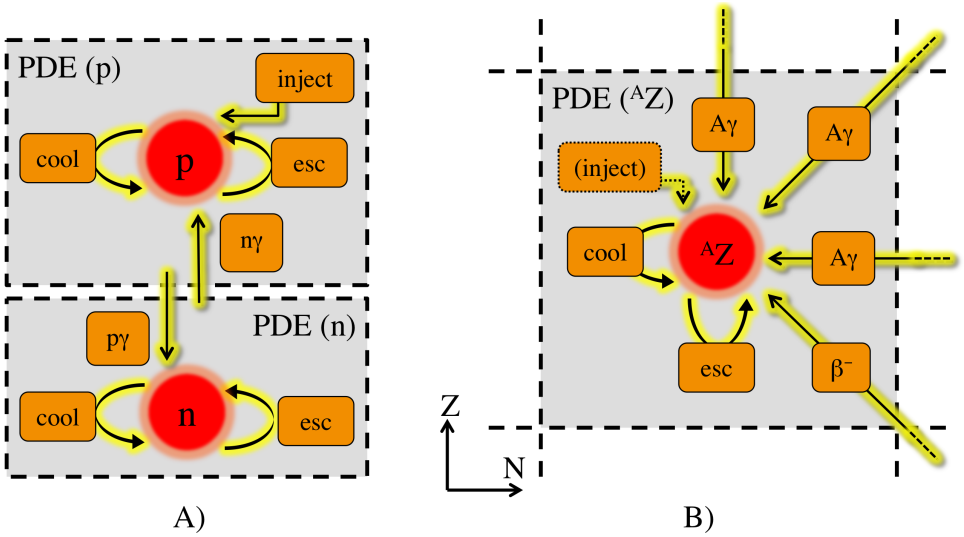

Figure 3.3: Schematic illustration of the terms in the partial differential equation (PDE) leading to the nuclear cascade. On the left hand side (A), the system consists of protons and neutrons which are coupled through photo-hadronic interactions. In the right panel (B), an isotope of the nuclear cascade with mass number A and charge number Z is shown. In both cases, the dashed boxes represent one species (equivalent to one term in the PDE), to which cooling and interaction processes are "attached". Note that there can be an additional injection term from a possible acceleration zone. Taken from [159].

other species, *e.g.*, due to β decays or photo-disintegration, which will be explained below.

In Fig. 3.3, a schematic illustration of every term of the PDE in Eq. (3.2) is shown, where each dashed gray box corresponds to one PDE. In the simulation, cooling and escape (and injection from the acceleration zone Q'_i) act only on a species i itself and are therefore "attached" to it. On the other hand, the injection term $Q'_{j\to i}(E')$ acts on species i (which it is also attached to), but involves another species j. This is represented by the arrows from different dashed boxes corresponding to different species, introducing, for example, decay or disintegration channels.

Example (A) shows computations which have been performed similarly already in [172]. However, this is now extended to optically thick sources by coupling the proton and neutron densities due to $p\gamma$ and $n\gamma$ interactions. In this case, the PDE system consists of only two equations for the nuclear species. Protons are injected from an acceleration zone (*e.g.*, the shock) and are converted efficiently into neutrons by interactions with ambient photons. In contrast to this, in the optically thin regime, interactions hardly occur such that the neutron density would not be populated. Typical cooling processes, which are attached in this case, are synchrotron cooling and adiabatic energy losses. Note that, for $p\gamma$ interactions, not always a neutron is produced

(*cf.* Eq. (2.1)), such that they can also act as a cooling term. Photo-hadronic interactions are escape terms for both species, but only neutrons have an additional, free-streaming escape term, as they are not magnetically confined.

In example (B), the PDE for a nucleus with mass number A and charge number Z, which is potentially coupled to other species, is illustrated. Similar to case (A), cooling processes are attached to it. If not stated otherwise, synchrotron and adiabatic cooling, photo-hadronic energy losses and pair production cooling is included in this work. Escape processes are photo-hadronic interactions and, depending on the actual isotope, decay. Further injection terms can be photo-hadronic $A\gamma$ processes, β decays or spontaneous decays of other isotopes. Note again that escape is to be interpreted as escape from (the density of) the species, such that it corresponds not only to escape from the interaction region, but also conversion into different species.

For setting up the nuclear cascade in the simulation, this procedure has to be repeated for several hundred isotopes entering the PDE system, depending on the injected isotope (or isotopes in the case of a mixed composition). In Fig. 3.4, the full nuclear system including all potentially relevant, known isotopes with $A \leq 56$ is shown up to the heaviest possible injection isotope ^{56}Fe. Each square representing one isotope as a function of the neutron number N and protons number Z refers to one equation in the PDE system, in analogy to Fig. 3.3. The most abundant, stable elements, which are typically considered as injection elements, are shown in dark blue, while less abundant stable elements (with rest frame life times longer than one month) are shown in light blue. Unstable isotopes undergo various decay processes, such as β decays (red) potentially followed by spontaneous emission of nucleons and α particles (white), which can be delayed (light red, delayed by at least 10^{-14} s). This representation is already simplified in the sense that branchings with a probability $< 5\%$ are eliminated. Furthermore, only the leading branches are shown here, because many isotopes have several channels which are taken into account in the computation. By considering up to 481 isotopes in total, around 50,000 channels are initialised. See App. A for the explicit calculation of interaction rates.

The life time of β emitters can range from hours to fractions of seconds. In order to compare it to the characteristic time scale of the system, the dynamical time scale t'_{dyn} of the prompt emission in the SRF, they have to be Lorentz-boosted. If the rest frame life time is short enough, β emitters can play a role for neutrino production (marked by a $\times$ in the figure), although neutrinos from beta decays typically have energies which are roughly 1000 times lower. However, from the figure it is evident that most of these quickly decaying isotopes are relatively far off the main diagonal, meaning that they will be hardly populated. Thus, neutrinos from beta decays are sub-dominant within the sources which are being discussed in the following. Nevertheless, they are included in the calculation.

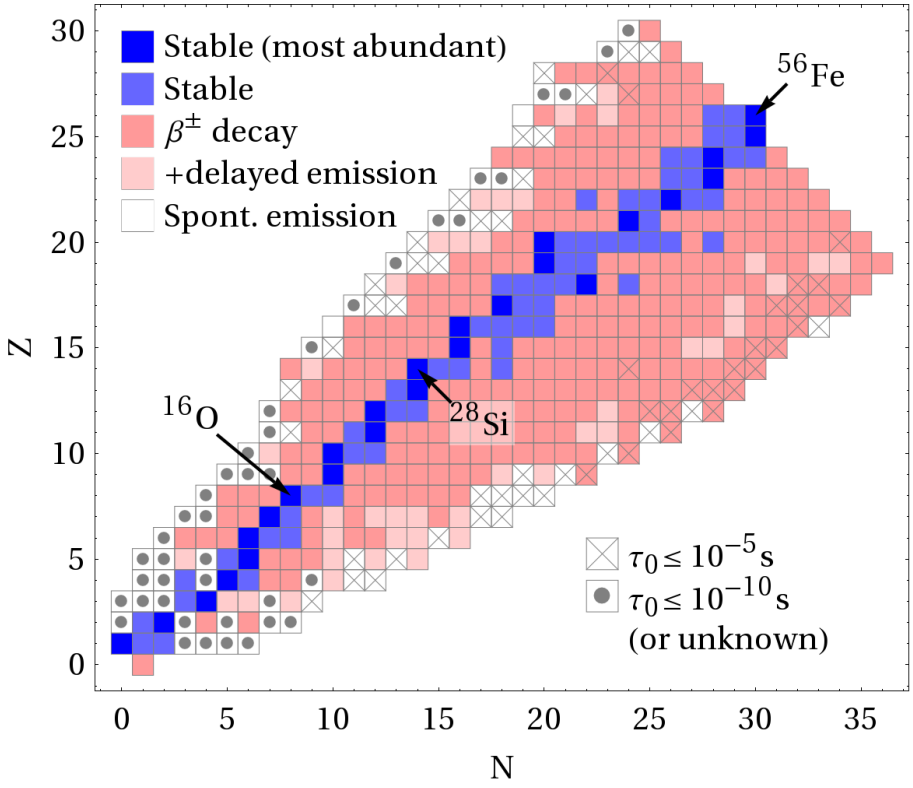

Figure 3.4: All 481 isotopes considered in this work represented in an isotope chart with neutron number N and proton number Z. The heaviest stable isotope is ^{56}Fe. The color coding indicates most abundant stable isotopes (dark blue), stable isotopes (blue), β emitters (red), followed by spontaneous emission of nucleons (light red) and spontaneous emitters of nucleons or α particles (white). Isotope rest frame life times are marked by $\times$ for $\tau_0 \leq 10^{-5}$ s and by $\circ$ for $\tau_0 \leq 10^{-10}$ s, which is small enough to be integrated out even at the highest energies. Taken from [159].

A second class of emitters are proton- or neutron-rich elements, which decay very quickly by the spontaneous emission of nucleons (marked as white boxes with dots in the figure). These processes can be integrated out, *i.e.*, replaced by their daughters, if the life time is short enough, namely shorter than all other radiation processes at the highest energy. Isotopes with unknown life time are also assumed to be of this class. This process mainly affects the light unstable isotopes with $A \lesssim 6$, as isotopes far off the main diagonal are hardly populated. In this process, no accompanying neutrinos are produced.

The disintegration of nuclei by interactions with target photons can be divided into two separate energy scales ϵ_r (photon energy in the nucleus' rest frame). The *giant dipole resonance* (GDR) [174] and other processes can lead to electromagnetic excitation of the nucleus with

the subsequent emission of one or more nucleons or light nuclei for energies between 8 MeV $\lesssim \epsilon_r \lesssim$ 150 MeV. This regime, below the pion production threshold, is referred to as *photo-disintegration* in the following. At higher energies, $\epsilon_r \gtrsim$ 150 MeV, baryonic resonances and higher energy processes dominate the disintegration. These are typically accompanied by meson (and with that neutrino) production and it will be referred to as *photo-meson production* regime.

Since power-law type spectra for the projectile as well as for non-thermal photons are expected, the nuclear cascade will mainly be determined by photo-disintegration above the GDR threshold, requiring that target photons with suitable energies are available as interaction partners. However, this does not hold when low energy cut-offs occur due to synchrotron self-absorption [20, 22]. Following [24], where the photo-disintegration has been discussed from the perspective of nuclear interactions models, the photo-disintegration model in this work is based on cross-section information from CRPropa2 [25] for light nuclei with $A < 12$ and on TALYS 1.8 [175] for heavier nuclei. On the other hand, only few cross-sections are measured and current cross-section models are not always reliable, as the photon absorption is not always well reproduced [24]. Thus, the nuclear cascade and the corresponding uncertainties ultimately depends on our understanding of the interactions. Currently, the lack of cross-section data leads to less reliable predictions for the neutrino production off nuclei [159].

In the energy regime of photo-meson production, a superposition model based on the SOPHIA Monte Carlo generator [176] is used throughout this thesis. The nuclei are treated as a superpositiong of independent nucleons, each with a fraction of the energy of the nucleus $E_{p/n} = E_A/A$. In a photo-hadronic interaction, a photon interacts with only one nucleon which is then ejected from the nucleus. For the residual nucleus, the energy per nucleon is conserved, *i.e.*, $E_{A'} = (A-1)E_A/A$, whereas the energy distributions of the interaction nucleon and secondary pions are computed with SOPHIA. The cross-section $\sigma_{A\gamma} = A\sigma_{p\gamma}$ scales with the mass, with the probability of a neutron interacting given by N/A and Z/A if a proton interacts. Although this superposition model is widely used in astrophysics [21, 22, 25], it has deficits. First of all, the scaling of the cross-section is disputed, as [171] for instance proposes the "Glauber scaling" for the cross-section, $\propto A^{2/3}$. However, a universal cross-section behaviour, *i.e.*, a scaling with A, is suggested by data, but the resonances may smear out [177]. This could happen due to re-absorption processes of nearby neutrons and protons of the nucleus. At higher energies, $E \gtrsim 1$ GeV, the internal structure of the nucleus becomes important, suggesting that the scaling $\propto A^{2/3}$ is more appropriate. Secondly, in the superposition model the probability of ejecting a proton or a neutron is close to 50-50. This may drive the residual nucleus further away from the main diagonal towards less stable elements [178].

Note that in general, photo-disintegration is dominating at the highest energies, but there are cases where photo-meson production becomes more important, for example in tidal disruption

events (see chapter 5) or in gamma-ray bursts with a minimum photon energy cut-off (see chapter 4). We tested the impact of more realistic models for photo-meson production in the sources presented in this thesis. We introduced a universal scaling of the cross-section with A and a transition to the Glauber regime where it scales as $A^{2/3}$. We also allow for multi-nucleon emission instead of only one nucleon per interaction. The overall flux of neutrinos and cosmic rays changes within a factor of 2 and the isotopes populated in the nuclear cascade, which determines the ejection composition of cosmic rays, changes slightly, as more energy is dumped in specific channels along the main diagonal. This is mostly because heavy nuclei can disintegrate faster by skipping intermediate steps. Especially the density of nucleons and ^{4}He increases significantly, while isotopes further off the main diagonal are not populated anymore. See our preliminary results in [177] for details. More refined results, for which I provided the source models to test the impact of the nuclear interaction models, are about to be submitted.

Other than photo-meson production, photo-disintegration and decays, a number of energy loss processes (implemented as continuous energy losses) are taken into account in the simulation as well. At low target photon energies $\epsilon_r \lesssim 8$ MeV, quantum electrodynamics determines $A\gamma$ interactions. Hence, charged particles will produce electron-positron pairs via the Bethe-Heitler process, which is implemented as in [179]. However, this contribution is small for the sources considered in the following, so we do not explicitly show this cooling rate in our plots. Charged particles will also cool via synchrotron radiation, with a corresponding rate

$$t'_{\rm syn}(E') = \frac{9m^4}{4e^4 c B'^2 E'} \quad , \tag{3.4}$$

which is typically also sub-dominant in the sense that it is not the leading process limiting the maximum energy. Still, the energy loss has to be taken into account and in principle it is also possible to encounter scenarios in which synchrotron losses become dominant. Lastly, all species cool adiabatically due to the expansion of the shell, where we assume that the dynamical time scale of the system is also representative for the adiabatic energy losses, *i.e.*, $t'_{\rm ad} \approx t'_{\rm dyn} \propto \Gamma t_v$ [180, 6, 173]. In this expression, t_v is the variability time scale of the observed light curve of an astrophysical transient event.

In addition to nuclei, we also add π^+, π^- and K^+ mesons injected from photo-meson production to the system of PDEs. They lose energy due to synchrotron radiation and adiabatic cooling too, whereas the only escape term is decay. As products of the decay, four muon species are introduced for left- and right-handed μ^+ and μ^-, which means that the helicity dependence is taken into account [181]. Since no tau neutrinos are produced in the source, as the $\tau^\pm$ has a much larger mass than the pion, we further add four neutrino species (ν_e, $\bar{\nu}_e$, ν_μ, $\bar{\nu}_\mu$), which only cool adiabatically.

3.1.3 Cosmic ray escape from dense radiation fields

After acceleration and possibly undergoing interactions in the source (which means setting up the PDE system, computing interaction rates and evolving it in time), particles will eventually leave the source environment and enter the extragalactic medium. While this is not a problem for electrically neutral particles such as neutrons and neutrinos, which simply escape over the dynamical time scale of the system, charged particles as cosmic rays are coupled to the plasma which keeps them confined. Different escape mechanisms have been proposed which all lead to a different shape of the escaping cosmic ray spectra.

Assuming that the particles are distributed isotropically in the radiation zone, *i.e.*, the expanding shell, a fraction of charged particles should be able to escape from the region if the boundary is within reach of their Larmor radius [172]. The fraction of directly escaping particles $f_{\rm esc}$ is therefore defined as the ratio of the escape volume, which is given by a thin shell of thickness $\lambda'_{\rm mfp}$, and the available volume in the source, given by the thickness of the shell $\Delta d'$ in the internal shock model. The fluence of directly escaping cosmic rays can be written as

$$Q' = \frac{N'}{t'_{\rm dyn}} \cdot f_{\rm esc} = \frac{N'}{t'_{\rm dyn}} \cdot \frac{\lambda'_{\rm mfp}}{\Delta d'} = \frac{N'}{t'_{\rm eff,dir}} \tag{3.5}$$

with the effective direct escape time $t'_{\rm eff,dir} = t'_{\rm dyn}\Delta d'/\lambda'_{\rm mfp}$. The mean free path can be defined as $\lambda'_{\rm mfp} = \min[\Delta d', R'_L(E'), ct_{p\gamma}(E')]$, where the first term ensures that $f_{\rm esc} \leq 1$. This means that the ejection is suppressed relative to the in-source density unless the Larmor radius is at least as big as the size of the region. The suppression is either due to low energy particles not being energetic enough to reach the boundary of the radiation zone, or because they will interact before they can reach it. In the latter case, the ejection will be suppressed by the optical thickness, which is defined as the ratio of the photo-hadronic interaction rate and the inverse of the dynamical time scale

$$\tau_n = \frac{t'^{-1}_{p\gamma}}{t'^{-1}_{\rm dyn}} \quad . \tag{3.6}$$

As a consequence of this so-called *direct escape* mechanism, cosmic rays escape with a rate $\propto R_L \propto E'$ and therefore correspondingly hard spectra. This means that they can escape freely if the Larmor radius reaches the shell width $\Delta d'$. It can be shown that the condition for the free-streaming limit is met when the maximum primary energy is determined by the dynamical time scale. Furthermore, it can be shown that even if the shell expands, $f_{\rm esc}$ is invariant [172].

A second scenario, called escape-limited acceleration, was proposed in [182] and has been used in [42]. The shape of the dispersed cosmic ray spectrum is determined by a stationary test-particle approximation. The basic idea is that only cosmic rays close to the maximum

acceleration energy can escape, as they have to pass a threshold or otherwise they remain confined. This threshold is defined by the distance l from the shock beyond which the amplitude of the upstream turbulence becomes negligible. If the diffusion coefficient $D(p)$ as a function of the momentum divided by the shock velocity $u_{\rm sh}$ is smaller than l, the particles are further accelerated, while for $D(p)/u_{\rm sh} \gtrsim l$ the acceleration ceases and the particles diffuse into the far upstream medium. At the end, the spectrum of escaping particles can be approximated by a Delta function. For simplicity, it is often parameterized as

$$Q' = \frac{N'}{t'_{\rm dyn}} \exp\left[-\ln^2\left(\frac{E'}{E'_{\rm max}}\right)\right] \quad . \tag{3.7}$$

The obtained shape is also comparable to the escaping spectra obtained by [23]. Due to the very hard spectral shape, the overlap over different mass groups ejected from the source will be minimized with this scheme. This facilitates the fit to cosmic ray data, as the individual components of the chemical composition can be adjusted more independently from each other (see also Sec. 4.3). Note that at the maximum energy, there is no suppression according to Eq. (3.7), even if photo-hadronic interactions dominate. However, a corresponding term could be added.

The most aggressive assumption which can be made is that the magnetic fields decay quickly enough, such that also charged particles exhibit free-streaming escape over the dynamical time scale. This leads to relatively soft escaping spectra, as also low energy particles can leave from the radiation zone. Also in this case, there is no suppression of the spectrum compared to the direct escape mechanism. This will lead to lower normalization factors and with that, as we will see, lower baryonic loading, which can relax neutrino constraints. This issue will be raised again when the baryonic loading is discussed, see Sec. 4.3.1.

3.2 Combined source-propagation models

Once the particles left the source environment, according to Fig. 3.1, the next step is the propagation through the extragalactic space. On their way, they encounter photon fields such as the cosmic microwave background (CMB) and the extragalactic background light (EBL, ranging from infrared to ultraviolet). In principle, particles can interact with these target photons similar to what happened already in the source, with the energy scale of the process given by the photon energy in the nucleus rest frame. For nuclei, the dominant processes are photo-disintegration on the CMB and EBL, for the highest and intermediate energies, respectively. The threshold for photo-meson production is shifted by a factor A times the threshold of protons. At low energies, nuclei cool adiabatically due to the expansion of the Universe. The dominating energy loss

process for protons at intermediate energies is electron-positron pair production on the CMB. The EBL is not as relevant for interactions of protons as for nuclei, however it is included in our calculations as it provides the majority of low energy cosmogenic neutrinos [183].

Practically, the propagation of ejected cosmic rays is computed by using the *SimProp* propagation code [184]. The photo-disintegration model used in *SimProp* is the Puget-Stecker-Bredekamp (PSB) model [185, 186], which contains one representative isotope for each nuclear mass. The interface to *SimProp* works by grouping the ejected nuclei by mass and summing the corresponding fluxes, choosing a representative mass for each group. For the results presented in this thesis, we use the Gilmore EBL model [187], which is one of the available models in *SimProp*. Note that all results in the following, as for the radiation processes in the source as well, also depend on the choices of these models. See for example [183] for a review of the impact of different models. Our choice of models is motivated by the best fit of PAO data given in [4], which was obtained in the same way.

For the propagation, we assume a certain distribution of sources with redshift, which are all alike in the cosmologically co-moving frame. An order-four tensor is computed for propagating vectors containing the cosmic ray energy spectra of the representative mass ejected from the source to Earth. Neutrinos from the source are already computed by *NeuCosmA* and are propagated by applying a bi-dimensional propagation matrix, weighting the flux according to the chosen source evolution. Cosmogenic neutrinos are computed by *SimProp*, of which the flux at Earth is computed by using equal weights as for the cosmic ray spectra. In the end, the all-particle UHECR spectrum is normalized to the PAO measurements. Out of the normalization, the baryonic loading can be calculated, which is described in the following Sec. 3.2.1.

3.2.1 Cosmic energy budget to power UHECRs

From the measurements of the UHECR energy spectrum and composition, the cosmic energy budget required to power this flux can be deduced, as it was done in [26]. For that purpose, the gamma-ray energy output is characterized mainly by the isotropic equivalent energy $E_{\gamma,\mathrm{iso}}$ per source, the number of observable sources per year $\dot{N}$ and the redshift distribution of the sources. The redshift distribution is typically parameterized as the star formation rate (SFR) given by

$$\mathcal{H}_{\mathrm{SFR}}(z) = \begin{cases} (1+z)^{3.4} & , \quad z < 1 \\ N_1(1+z)^{-0.3} & , \quad 1 \leq z < 4 \\ N_1 N_4 (1+z)^{-3.5} & , \quad z \geq 4 \end{cases} \tag{3.8}$$

with $N_1 = 2^{3.7}$ and $N_4 = 5^{3.2}$ [188, 189, 190], times an additional evolution factor $(1+z)^m$, such that $\mathcal{H}(z) = (1+z)^m \cdot \mathcal{H}_{\rm SFR}(z)$. The parameter m indicates if there are, relative to SFR, more close by ($m < 0$) or far away ($m > 0$) sources, depending on the source type. [1]

Since also weak gamma-ray sources could in principle produce neutrinos and cosmic rays, a threshold correction has to be taken into account for sources whose gamma-ray emission is too faint to be detected. This threshold correction factor

$$f_{\rm thresh} = \frac{\dot{N}}{\dot{N}_{\rm tot}} \leq 1 \tag{3.9}$$

is defined as the ratio between observable events per year $\dot{N}$ and the total number of sources in the observable Universe per year $\dot{N}_{\rm tot}$. The actual value depends on detector characteristics, but in general $f_{\rm thresh} \sim 0.3 - 0.5$ holds [26].

The number of observed sources $\dot{N}$ can be connected to the local event rate $\dot{\tilde{n}}(z=0)$ via a cosmic evolution factor f_z, which describes how representative the local event rate is for the whole population of sources. This means, the stronger the source evolution (larger m), the larger the values of this correction. Note also that the local event rate

$$\dot{\tilde{n}}(z=0) \approx \frac{1}{\rm Gpc^3 yr} \cdot \frac{\dot{N}[{\rm yr}^{-1}]}{968} \cdot f_{\rm thresh}^{-1} \cdot f_z^{-1} \tag{3.10}$$

is already corrected by the beaming factor $\dot{\tilde{n}}(z=0) = \dot{n} / < f_{\rm beam} >$. The number 968 is related to the volume term $4\pi D_H^3 \approx 968$ Gpc^3. See [26] for a detailed description.

With the help of these observables, the required energy output per source which is needed to power the UHECR energy spectrum can be estimated. To do so, the local energy injection rate $\dot{\varepsilon}_{\rm CR}^{[10^{10},10^{12}]}$ is derived in the range between 10^{10} GeV and 10^{12} GeV. This has been done before and it was shown that $\dot{\varepsilon}_{\rm CR}^{[10^{10},10^{12}]} =$ a few $\times\, 10^{44}$ erg Mpc^{-3} yr^{-1}, with little sensitivity to variations of the spectral index of ejected cosmic rays [191, 192, 193]. Hence, the required energy per source is

$$E_{\rm CR}^{[10^{10},10^{12}]} = 10^{53}{\rm erg} \cdot \frac{\dot{\varepsilon}_{\rm CR}^{[10^{10},10^{12}]}}{10^{44}{\rm erg\ Mpc^{-3} yr^{-1}}} \cdot \frac{968{\rm yr}^{-1}}{\dot{N}} \cdot f_{\rm thresh} \cdot f_z \quad . \tag{3.11}$$

Strong source evolution thus requires larger injected energy per source to compensate for the few local sources.

[1] Diffuse fluxes are typically calculated by folding in a luminosity distribution as well. However, for the sake of technical feasibility, luminosity functions are not considered in this work. In turn, we compute representative cases at the peak of the corresponding luminosity distributions, *i.e.*, the results have to be interpreted in terms of such an averaged luminosity. We checked that the impact on the results is small.

From this quantity, we eventually extract the *baryonic loading* ξ_A of the sources, which is defined as the fraction of energy in baryons (integrated over the entire energy range) compared to the energy in gamma-rays (or a certain other wavelength band). However, for UHECR observations, only the energy range $\sim 10^{10} - 10^{12}$ GeV is relevant, which is why this relation has to be modified by a bolometric correction factor $f_{\rm bol} < 1$. This correction is defined as the ratio of energy in UHECRs to the energy in cosmic rays over the whole energy range. In general, the softer the ejected cosmic ray spectrum, the smaller this correction, *e.g.* $f_{\rm bol} = 0.2$ for a spectral index of 2.0 while $f_{\rm bol} = 1.6 \cdot 10^{-4}$ for a spectral index of 2.5. Lastly, we need to correct by the fraction of baryonic energy which is going into cosmic ray production $f_{\rm CR}$, as another part of the energy goes into secondary meson production parameterized by f_π (pion production efficiency). The required energy per source in Eq. (3.11) is then related to the total isotropic energy in gamma-rays as

$$E_{\rm CR}^{[10^{10},10^{12}]} = f_{\rm CR} f_{\rm bol} \xi_A E_{\gamma,\rm iso} \quad . \tag{3.12}$$

These correction factors are implicitly taken into account in our fitting method, yet there is still a certain degeneracy in the interpretation of the baryonic loading due to remaining, poorly constrained parameters. For example, if the population is not well known, low baryonic loadings can be compensated by high event rates and vice versa. For this purpose, we fit with a normalization parameter G defined as

$$G = \xi_A \times \frac{\dot{\hat{n}}(z=0)}{\rm Gpc^{-3} yr^{-1}} \tag{3.13}$$

to address this degeneracy. As the interaction rates scale linearly with the density of baryons in the source, the neutrino flux scales in the same way as the cosmic rays with the baryonic loading obtained from the fit.

3.2.2 Neutrino flavor composition and mixing

Neutrinos do not interact while they propagate through extragalactic space, but they exhibit oscillations between their flavor eigenstates. Due to the high energies and extremely long baselines of astrophysical neutrinos, oscillations decohere such that the flavor conversion can be described by the mean of the oscillation probability, *i.e.*, the oscillatory term averages out such that the conversion probability depends only on the elements of the mixing matrix [194]. We use *tri-bimaximal mixing* (TBM) [195] as a good approximation for flavor mixing over astrophysical distances. The conversion $\nu_i \to \nu_j$, with i and j being any of the three possible lepton flavors,

Table 3.1: Neutrino flavor composition at the source and at Earth, including the fraction of electron anti-neutrinos at Earth for different production scenarios. Neutrinos and anti-neutrinos are combined if the ratios are the same. The TBM model is used for propagation and the kinematics of pion and muon decays are not included. Taken from [160].

	Source flavor comp. $(\phi_e : \phi_\mu : \phi_\tau)$		Earthly flavor comp. $(\phi_e^f : \phi_\mu^f : \phi_\tau^f)$		Earthly $\bar{\nu}_e$ fraction $\xi^f_{\bar{\nu}_e}$ in cosmic neutrino flux
$pp \to \pi^\pm$ pairs	(1:2:0)		(1:1:1)		$9/54 = 17\%$
w/ damped $\mu^\pm$	(0:1:0)		(4:7:7)		$6/54 = 11\%$
	ν	$\bar{\nu}$	ν	$\bar{\nu}$	
$p\gamma \to \pi^+$ only	(1:1:0)	(0:1:0)	(14:11:11)	(4:7:7)	$4/54 = 7.4\%$
w/ damped μ^+	(0:1:0)	(0:0:0)	(4:7:7)	(0:0:0)	0

is then described by the symmetric propagation matrix $\mathcal{P}$ which is given by

$$\mathcal{P}(i \to j) = \sum_k |U_{ik}|^2 |U_{kj}|^2 \quad , \tag{3.14}$$

with U_{nm} being the matrix elemenents of the Pontecorvo–Maki–Nakagawa–Sakata (PMNS) matrix [196, 197]. Adopting the mixing parameters of the TBM model, the propagation matrix can be written as

$$\mathcal{P}_{\text{TBM}}(i \to j) = \frac{1}{18} \begin{pmatrix} 10 & 4 & 4 \\ 4 & 7 & 7 \\ 4 & 7 & 7 \end{pmatrix} \quad . \tag{3.15}$$

By multiplication with this matrix, a vector containing the flavor composition of neutrinos at the source $(\phi_e, \phi_\mu, \phi_\tau)$ will yield the flavor composition at Earth after propagation $(\phi_e^f, \phi_\mu^f, \phi_\tau^f)$. This can be of interest if the event rates for a certain neutrino flavor are relevant.

One such example is the Glashow resonance $\bar{\nu}_e + e^- \to W^- \to$ anything for $E_\nu \approx 6.3$ PeV [153], which was introduced in Sec. 2.3.2. It is sensitive only to the electron anti-neutrino flavor, such that different fractions of electron anti-neutrinos in the Earthly neutrino flux result in different event rates for the Glashow resonance. We showed in our paper [160] that we can still measure a difference in the fraction of electron anti-neutrinos at Earth after propagation. The production mechanism of astrophysical neutrinos is imprinted in their flavor composition, which is accessible with the Glashow event rate. For that purpose, we define the fraction of electron anti-neutrinos at the detector

$$\xi^f_{\bar{\nu}_e} = \frac{\phi^f_{\bar{e}}}{\phi^f_e + \phi^f_\mu + \phi^f_\tau + \phi^f_{\bar{e}} + \phi^f_{\bar{\mu}} + \phi^f_{\bar{\tau}}} \quad , \tag{3.16}$$

on which the event rate will directly depend as shown below. An overview of different production mechanisms along with their flavor composition at the source and on Earth as well as the fraction of electron anti-neutrinos is given in Tab. 3.1. The production scenarios shown therein are $p\gamma$ interactions as described in Eq. (2.1) and pp interactions, which yield

$$p + p \rightarrow \begin{cases} \pi^+ + \text{anything} & 1/3 \text{ of all cases} \\ \pi^- + \text{anything} & 1/3 \text{ of all cases} \\ \pi^0 + \text{anything} & 1/3 \text{ of all cases} \end{cases} . \tag{3.17}$$

The pions will decay again according to $\pi^+ \rightarrow \mu^+ + \nu_\mu$, possibly followed by muon decay $\mu^+ \rightarrow e^+ + \nu_e + \bar{\nu}_\mu$. In the case of π^-, the corresponding anti-particles are produced, while the neutral pion decays into photons. If the muons lose energy very quickly, *e.g.*, in the case of strong magnetic fields and therefore significant synchrotron losses, their decay can be inhibited, which is referred to as *muon damping*. Note that $\bar{\nu}_e$ from neutron decay are not included in these scenarios, as they receive kinematically only a small fraction of the energy, typically much lower than the required Glashow energy [180]. If we now apply the TBM matrix to obtain the flavor composition at Earth, we find that the fraction of electron anti-neutrinos is still different in each scenario by a few percent. In general, more anti-neutrino production is expected for the pp scenario, as π^- are produced in the same amount as π^+. In the $p\gamma$ case, no π^- are expected in the Delta-resonance approximation, leading to only very few anti-neutrinos which can convert into $\bar{\nu}_e$ during propagation. In the case of muon damped sources, the amount of anti-neutrinos is still reduced in both pp and $p\gamma$ production mechanisms, where for the latter one the Earthly fraction of $\bar{\nu}_e$ is even zero. This leads to differences in the expected Glashow event rate and makes these scenarios distinguishable with neutrino telescopes after a certain exposure [160].

3.2.3 Glashow resonance production diagnostics

Following this idea, we now calculate the Glashow event rate and give predictions after how many years of exposure in IceCube certain scenarios can be disfavored, following our paper [160]. My contribution to this work was the numerical computation of neutrino fluxes and flavor ratios for different source properties. The event topology obtained from the $W-$-decay can either be a cascade (hadronic or leptonic) or a muon track (leptonic). The leptonic case cannot be distinguished from a non-resonant event since it necessarily includes an energy loss by the neutrino produced together with the lepton, such that in the following we focus on the hadronic cascade. If we assume a power law for the astrophysical neutrino spectrum, defined by a normalization ϕ_0 and a spectral index α, the number of resonant Glashow events can be

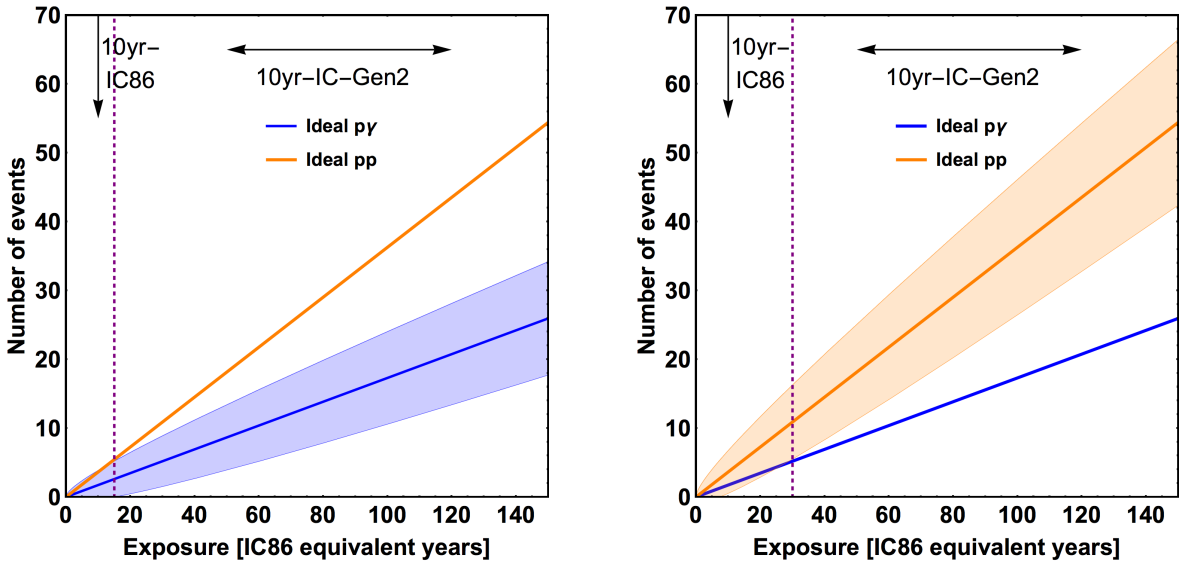

Figure 3.5: Expected number of Glashow events as a function of the exposure for the ideal pp and $p\gamma$ scenario for $\alpha = 2.0$. The bands show the 90% C.L. interval from the uncertainties on the oscillation parameters and the statistical (Poissonian) uncertainty, attached to the assumed "true" scenario ($p\gamma$: left, pp: right). The dashed vertical lines indicate the exposure after which the other scenario can be excluded. The 10 year IceCube-Gen2 equivalent exposure is marked by the horizontal arrow. Taken from [160].

approximated as

$$N^G \approx \xi^f_{\bar{\nu}_e} \times \phi_0 \times T_{\text{exp}} \times 1.071 \times \exp\left(-\frac{\alpha - 2}{0.244}\right) \tag{3.18}$$

as a function of the exposure T_{exp} in units of years using the effective area of IceCube-86 (IC86).[2] Thus, one year of operation corresponds to $T_{\text{exp}} = 1$, and we refer to T_{exp} as IC86 equivalent exposure. Next-generation detectors such as IceCube-Gen2 will have an exposure from 5 to 12 times the exposure of IC86, which we will indicate in our results. The event rate in Eq. (3.18) also depends on the data set we use, as they have different spectral indices and normalization (see Sec. 2.3.2). In our paper, we used $\alpha = 2.0$ and $\phi_0 = 2$ for the through-going muon analysis (extracted from [198]), and $\alpha = 2.5$ together with $\phi_0 = 6.7$ for the high energy starting events (extracted from [199]), which is somewhat outdated now. This shows that the HESE spectrum significantly changes with exposure, while the TGM fit remains almost the same. In the following, we will show results for the TGM sample.

Now we consider the ideal production scenarios for pp and $p\gamma$ interactions, following Eq. (3.17) and Eq. (2.1), respectively. We take into account the energy distributions from secondary meson

[2]The numbers in Eq. (3.18) are obtained from our fitting method to describe the expected number of events and therefore have no physical meaning.

decays assuming a power law pion spectrum as well as realistic flavor mixing angles from [200]. The expected number of Glashow events in the ideal scenarios, obtained with Eq. (3.18), is shown in Fig. 3.5 as a function of the exposure. The bands illustrate the error on the oscillation parameters δ_p and the statistical (Poissonian) error δ_s at the 90% confidence level (C.L.), where we assume that their relative error scales as $\propto 1/\sqrt{T_{\rm exp}}$. In the left panel, it is assumed that the true production mechanism at the source are ideal $p\gamma$ interactions. As illustrated by the vertical dashed line, 15 years of IC86 equivalent exposure are needed to distinguish the source from a hypothetical *pp* scenario. Vice versa, in the right panel the true mechanism is *pp* interactions. About 30 years of exposure is needed to make a distinction among the two cases, which is clearly beyond IC86, but well within reach of IceCube-Gen2, as indicated by the horizontal arrow for 10 years of IceCube-Gen2 exposure. The fact that the Glashow event rate can constrain the production mechanism is often quoted to motivate the IceCube upgrade. However, we will show in the following that this distinction is not possible anymore, if more realistic interaction processes are considered.

For a more realistic description of the *pp* interactions, the usual assumption of isospin symmetry, where π^+, π^- and π^0 are produced in the same amount, does not hold anymore. Because of the power law spectrum of interacting nucleons, the produced secondaries carry a large fraction of the projectile's energy, becoming important for the computation. For typical energies of hundreds of PeV, these large momenta of secondaries lead to valence quark scattering and their subsequent hadronization. Since u valence quarks dominate in protons, the expected pion charge ratio is naturally $\pi^+/\pi^- > 1$ in the forward phase space, *i.e.*, it becomes more similar to the $p\gamma$ scenario. In the following, the *pp* mechanism is computed with hadronic interaction models *Sibyll 2.3* [116], *EPOS-LHC* [115] and *QGSJET-II-04* [117], however the results hardly depend on which of the three Monte Carlo event generators is used. The effect of secondary kaons is small enough to be neglected in this study.

On the other hand, photo-hadronic interactions do not only include the Δ-resonance, but also direct pion production, higher resonances and multi-pion production at high energies. Especially the multi-pion processes are responsible to almost equalize the pion charge ratio, *i.e.* $\pi^+/\pi^- \approx 1$. This intrinsic contamination by π^- with respect to the ideal scenario makes it more similar to the *pp* case. In addition, the resulting secondary pion spectrum depends on the photon spectrum too, such that pion and muon decays are numerically calculated as well in the following, taking into account the re-distribution functions of the secondaries. We pick two representative examples, where the target photons are either provided by a synchrotron spectrum of co-accelerated electrons in active galactic nuclei (called clusters) or by a broken power law which is typical for gamma-ray bursts called (GRB). [3]

[3]The parameters for the clusters are $R \approx 10^{19}$ km and $B \approx 10^{-6}$ G, benchmark point TP8 in [201]. For the

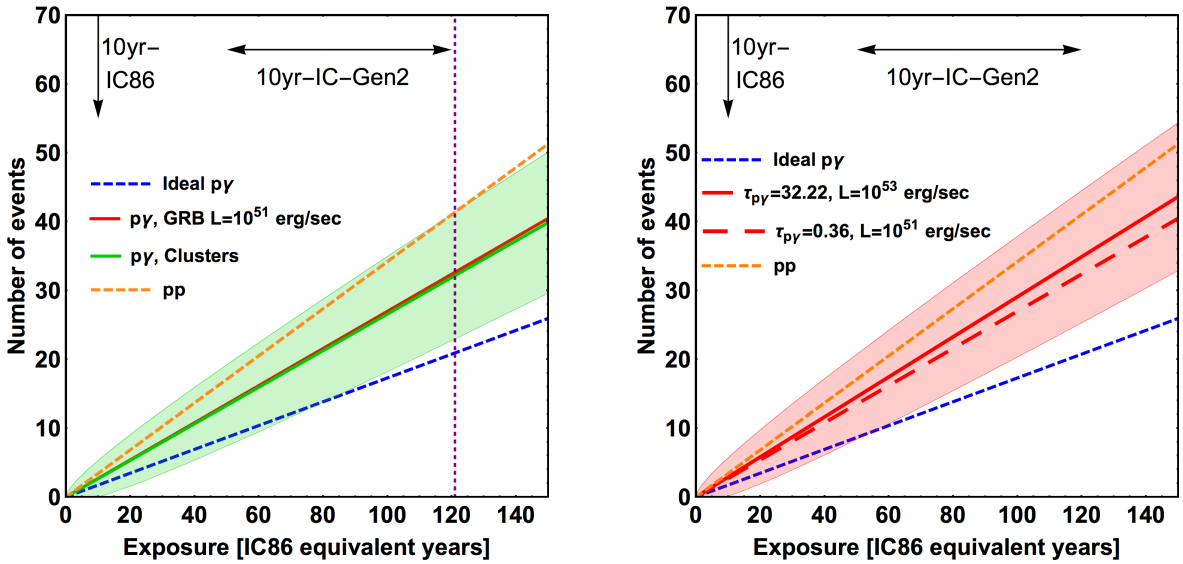

Figure 3.6: Same as Fig. 3.5, but with more realistic interaction models for pp (SIBYLL [116], EPOS-LHC [115], QGSJET [117], giving similar results) and $p\gamma$ (SOPHIA [176]). In the left panel, two different target photon spectra are assumed for the $p\gamma$ case, *i.e.*, a broken power law with spectral indices -1 and -2 and a break at 1 keV (GRB, red), as well as a synchrotron spectrum from co-accelerated electrons (clusters, green). In the right panel, the impact of different luminosities for the broken power law target photon spectrum is shown, *i.e.*, 10^{51} erg s^{-1} (dashed) and 10^{53} erg s^{-1} (solid). Taken from [160].

In Fig. 3.6, we show in the left panel a comparison between the realistic pp and $p\gamma$ scenarios and the ideal $p\gamma$ case. The two different $p\gamma$ sources are very similar despite very different source environments, such that we focus on the broken power law target photon spectrum in the following. Hence, in the more realistic treatment of interactions, the discrimination requires about 120 years of equivalent exposure, which is challenging even in IceCube-Gen2. The ideal $p\gamma$ scenario can, however, be excluded after 81 years of exposure, assuming a true $p\gamma$ source. The contamination of multi-pion processes in $p\gamma$ sources depends on the maximum primary energy. Higher energy protons, for example, have higher center-of-mass energies, where multi-pion production dominates. For a 6.3 PeV neutrino, the parent proton energy has to be at least around 120 PeV. [4] Therefore, sources which produce neutrinos in the Glashow energy range are probably heavily contaminated by multi-pion production.

gamma-ray burst, we choose $L_\gamma = 10^{51}$ erg/s, $t_v = 0.1$ s, $\Gamma = 300$, $z = 2$, and specifically for the broken power law $\varepsilon_b = 1$ keV (SRF), $\alpha = -1$ and $\beta = -2$. Their meaning will become more clear in chapter 4.

[4] The pion takes approximately 20% of the primary energy in Eq. (2.1). In the subsequent decay, all 4 particles roughly get the same amount of energy. Hence, $E_\nu \approx 0.05 E_p$.

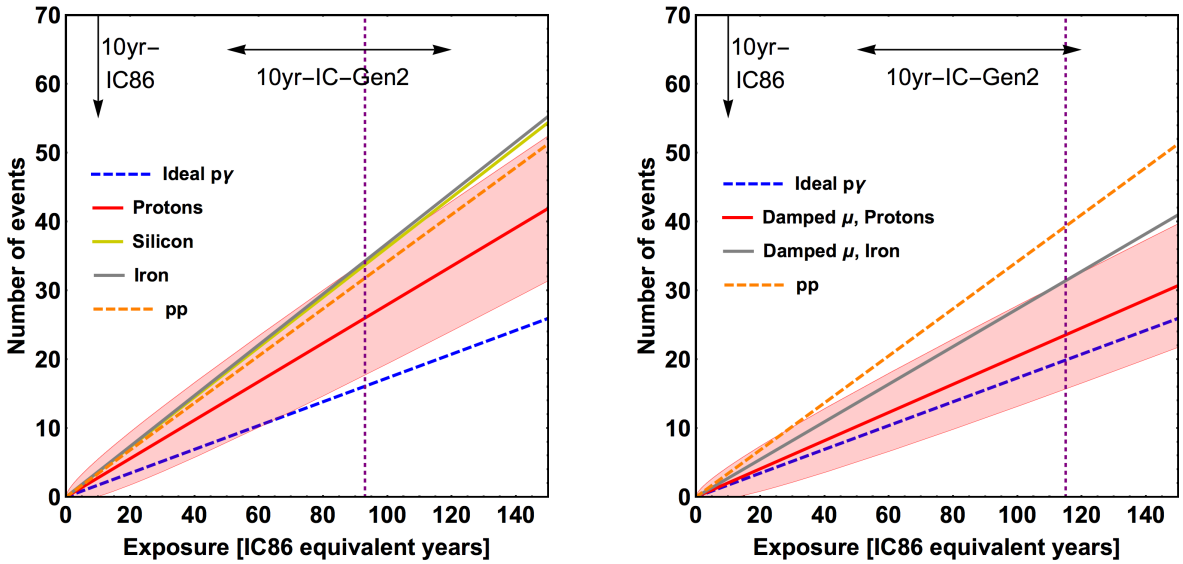

Figure 3.7: Same as Fig. 3.6, but showing the impact of the injected isotope (left panel: protons (red), silicon (yellow), iron (gray)) and of strong magnetic fields (right panel, muons cool faster than they decay in the proton (red) and iron (gray) case) in the $p\gamma$ scenario, compared to the realistic pp and ideal $p\gamma$ case. Taken from [160].

From Eq. (2.1) it is also clear that photo-hadronic interactions produce neutrons. If the source is optically thick to photo-hadronic interactions, *i.e.*, $\tau_n > 1$ (*cf.* Eq. (3.6)), nucleons will rather interact than escape from or cool in the radiation zone. Similar to the Δ-resonance for protons, an isospin-symmetric process exists for neutrons

$$n + \gamma \to \Delta^0 \to \begin{cases} \pi^- + p & 1/3 \text{ of all cases} \\ \pi^0 + n & 2/3 \text{ of all cases} \end{cases} , \tag{3.19}$$

producing mainly π^-. This means, the more interactions happen in the source or the more optically thick it is to photo-hadronic interactions, the more neutrons and with that π^- will be produced, leading to an additional contamination. To increase the optical depth, we increased the radiation density by enhancing the luminosity L_γ, as can be seen in the right panel of Fig. 3.6. Indeed, as the luminosity increases, the neutron to proton ratio in the source increases as well. Since the interactions of neutrons cause significant contamination by π^-, the discrimination becomes impossible even with next generation detectors, as 150 years are not sufficient to distinguish between the realistic pp and $p\gamma$ source.

A similar effect can be observed if heavy nuclei are considered at the source. The disintegration

Table 3.2: Required IC86 equivalent exposure to observe more than 0 events with 90% C.L. Taken from [160].

Dataset	Spectral index	Ideal $p\gamma$	$p\gamma$	pp	Feγ	Damped μ	Opt. thick
HESE [199]	$\alpha = 2.5$	33	22	18	16	32	20
TGM [203, 198]	$\alpha \simeq 2$	15	9.7	7.6	7.1	12	8.9

of heavy nuclei, in which mostly nucleons are produced, contributes significantly to the neutron production. This effect scales with the mass number A of the injected nucleus, as heavier elements become more neutron-rich. The neutron to proton ratio is approximately determined by the neutron-proton-ratio of the primary nucleus. Therefore, as soon as $A \geq 2$, the contamination by π^- strongly increases, making the source more *pp* like in terms of $\bar{\nu}_e$ production. The left panel of Fig. 3.7 shows the expected number of Glashow events in this case. For the injection of silicon or iron, it is not possible to distinguish such an $A\gamma$ source from a *pp* scenario. However, as the $A\gamma$ scenario is almost independent of the actual composition as long as $A \geq 2$, it can be discriminated from a proton composition after about 95 years of exposure, which is within reach of IceCube-Gen2. The inverted case, *i.e.*, distinguishing a true $A\gamma$ source from a $p\gamma$ scenario, takes more time (about 124 years). However, if the source is known to have high radiation densities, the Glashow resonance can serve as a smoking gun signature for primary nuclei.

This discrimination power also holds for muon damped sources, where pions can decay but the muon decay is inhibited, *e.g.*, by strong magnetic fields. Examples of possible source candidates for muon damping are gamma-ray bursts [180], microquasars [202] and tidal disruption flares [59, 48]. [5] In the damped $\pi^+ \to \mu^+\nu_\mu$ mode, no anti-neutrinos are produced at all. However, in the presence of a π^- contamination, the produced $\bar{\nu}_\mu$ will contribute to the electron anti-neutrino fraction after flavor mixing. We illustrate the results for the muon damped scenario in the right panel of Fig. 3.7, again for proton and iron injection. For protons, the results are comparable to the ideal $p\gamma$ scenario, while iron is closer to the *pp* case due to the intrinsic presence of neutrons at the source. The relative distance between the $A\gamma$ and $p\gamma$ scenario hardly changes compared to the whole pion decay chain, such that the two scenarios are still distinguishable after about 115 years. In this case, additional measurements are needed to confirm the muon damping.

Also the non-observation of Glashow events can be instructive as conventional scenarios can get under tension after long enough exposures. We list in Tab. 3.2 the value of $T_{\rm exp}$ needed to exclude zero events, which is when the low edge of the shaded region exceeds zero events. The

[5] In our examples, we achieve muon damping by decreasing the variability time scale by one order of magnitude, *i.e.*, $t_v = 0.01$ s.

Table 3.3: Required IC86 equivalent exposure for the discrimination between different neutrino production scenarios at the 90% C.L. for a spectral index of $\alpha = 2.0$. Exposures which could potentially be covered by IceCube-Gen2 (less than 120 years) are in bold, whereas the symbol ∞ is used for exposures larger than a few hundred years. "Damped μ" refers to the proton damped muon scenario and "opt. thick" denotes to the $p\gamma$ case with $L_\gamma = 10^{53}$ erg/s. Taken from [160].

Data →	$\alpha = 2$					
Theory ↓	Ideal $p\gamma$	$p\gamma$	pp	Feγ	Damped μ	Opt. thick
Ideal $p\gamma$	·	**81**	**32**	**26**	∞	**55**
$p\gamma$	**53**	·	156	**93**	144	∞
pp	**16**	121	·	∞	**28**	∞
Feγ	**12**	**66**	∞	·	**20**	122
Damped μ	∞	∞	**48**	**37**	·	**104**
Opt. thick	**33**	∞	∞	162	**72**	·

results are shown for two different spectral indices obtained from the data sets, whereas the non-observation would become not indicative if the spectral index is softer (as it tends to be in the updated HESE analysis). For a hard spectrum, the Feγ, $p\gamma$, pp and optically thick scenarios can be constrained in the case of no detections.

Our results on the discrimination power among different production scenarios are summarized in Tab. 3.3 in terms of years of IC86 equivalent exposure. It clearly illustrates that IC86 has no chance to use the Glashow resonance as a source diagnostics tool with ten years of data. Even for IceCube-Gen2 the discrimination between pp and $p\gamma$ scenario remains challenging, but it can potentially discriminate other production mechanisms if the neutrino spectrum is not too soft. One of the most promising applications may be the discrimination between $p\gamma$ and $A\gamma$ scenarios, *i.e.*, the presence of heavy nuclei in the source.

Chapter 4

Gamma-ray bursts as multi-messenger sources

Gamma-Ray Bursts (GRBs) are among the most energetic events observed in the Universe [11]. They were accidentally discovered in the late 1960s by the U.S. Vela satellites, which were originally launched to enforce the Nuclear Test Ban Treaty. The treaty, signed by the United States and the Soviet Union in 1963, banned tests of nuclear weapons in the atmosphere, in outer space and under water. Still, the U.S. suspected that the Soviet Union might conduct secret nuclear tests, so the satellites were suited to detect pulses of gamma radiation from nuclear weapons. On July 2, 1967, a flash of gamma-rays was detected by Vela 3 and 4 which looked different from any known nuclear weapons signature and was therefore not given attention. After launching additional satellites with better instruments, the team at the Los Alamos National Laboratory, led by Ray Klebesadel, continued to find bursts of gamma-rays in the data. They were able to roughly determine the positions in the sky, ruling out a solar or terrestrial origin. In 1973, after detecting 16 of such events, the discovery was declassified and published in [204].

Early theories about GRBs predicted that the sources are positioned within the Milky Way. In that case, the radiation should be concentrated around the galactic plane, which was tested from 1991 by the Compton Gamma-Ray Observatory (CGRO) with its Burst and Transient Source Explorer (BATSE), a highly sensitive detector for gamma-rays. BATSE, which is senstitive in the energy range of $\sim$ 25 keV to 2 MeV, detected more than 2700 bursts of different duration, light curve and luminosity, providing strong indication that the distribution of GRBs is isotropic [206]. In Fig. 4.1, examples for light curves as measured by BATSE are shown, stressing that the profiles can look very different, with high variations in intensity and duration.

Based on these observations, BATSE data suggested that GRBs can be divided into two populations depending on their duration [207]: Around 30% of the detected bursts correspond to short-duration bursts with durations of 2 seconds or less. Long-duration bursts, accounting for roughly 70% of the observations, can have durations up to tens or hundreds of seconds. There is possibly a third population of rare ultra-long bursts which last for $10^3 - 10^4$ seconds or more [208, 209]. Short GRBs, which are currently believed to occur as a result of the merger of compact objects [210], typically show a harder gamma-ray spectrum than long GRBs.

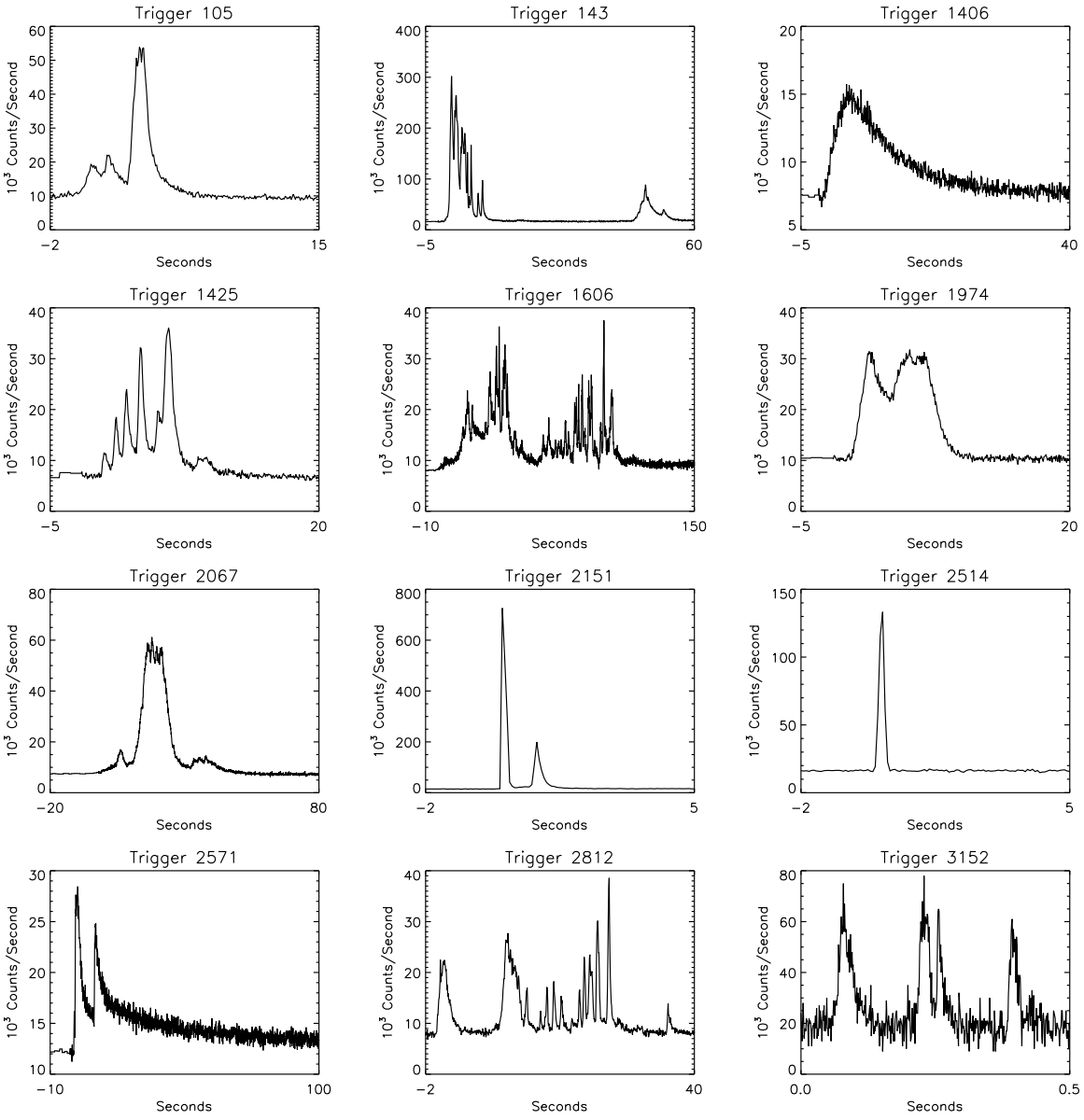

Figure 4.1: Examples for GRB light curves as recorded by BATSE. Shown is the photon count as a function of the duration of the burst. Taken from [205].

Long-duration bursts, on the other hand, have been observed in association with core-collapse supernovae [211].

After BATSE, a number of other satellites were launched, as for example BeppoSAX (1996–2003), which observed in X-ray in the energy range from 0.1 to 300 keV and contributed significantly to confirming the extragalactic origin of GRBs [212]. The Swift Gamma-Ray Burst

Mission (*Swift*, 2004–), which is still one of the main instruments for the detection of GRBs today, observed the afterglow of short-duration GRBs for the first time [213]. Besides Swift, the Fermi Gamma-ray Space Telescope (*Fermi*, 2008–), hosts two of the most important instruments for GRB observations nowadays, namely the Gamma-ray Burst Monitor (GBM) as well as the Large Area Telescope (LAT). GBM is sensitive in the energy range from 200 keV to 40 MeV while LAT is sensitive between 20 MeV and 300 GeV [214].

Because of their high energy output, ranging from $10^{47} - 10^{53}$ erg s^{-1} and more, GRBs were believed to be one of the prime candidates for UHECR sources. However, due to neutrino observations, this so-called GRB-UHECR paradigm is under strong tension, as no accompanying neutrinos were detected although they are co-produced in cosmic ray interactions. IceCube demonstrated that GRBs contribute at most around 1% to the diffuse flux of astrophysical neutrinos. Although, strictly speaking, only the most simple models are excluded by this analysis, absence of correlations of neutrino events with GRBs observed in electromagnetic radiation makes these so-called stacking bounds stronger with increasing exposure, such that also more sophisticated models begin to be constrained. On the other hand, there are mechanisms to get out of this dilemma, *i.e.*, if the source was mostly optically thin to photo-hadronic interactions or if the electromagnetic emission is somehow obscured.

Despite the stacking bounds, understanding how GRBs work is still of high interest for the community. One of the more recent highlights was the discovery of a short GRB accompanying the neutron star merger observed in gravitational wave event GW170817 [63]. It was confirmed that compact merging objects can trigger short GRBs and that heavy elements can be produced in GRBs via r-process nucleosynthesis [79], for example. Furthermore, in January 2019, a GRB was detected at sub-TeV energies for the first time by MAGIC, shortly after being triggered by a Swift alert [215]. As we will see, it might also be promising to look for GRBs with future, ground-based Cherenkov telescopes, such as CTA.

This chapter discusses the possibility that GRBs are the sources of UHECRs, starting with conventional GRBs and then investigating sub-populations and different models. In Sec. 4.1, we review the energetics of GRBs and give details on the input used for this source class to set up the model. After that, in Sec. 4.2, we present a sophisticated analysis of conventional GRBs based on our paper [159], where we classify GRBs based on the development of the nuclear cascade. These results are processed in Sec. 4.3, where the propagation is calculated and the fit to cosmic ray data is performed. Therein, we discuss the impact of the injection composition in the source on the results. My contribution to this project was the implementation of the gamma-ray burst source model and calculation of the nuclear cascades. I performed the parameter space scans and corresponding classification and studied the dependence of the neutrino flux on the composition. I developed the interface to SimProp, provided qualitative estimators and performed cross-

checks of the model. In Sec. 4.4, we investigate the sub-population of low-luminosity GRBs as a possible way to circumvent the stacking limits, following our paper [216], where I again provided the source model including different escape mechanisms as well as parameter space scans and classification similar to earlier works. In the end, in Sec. 4.5, we show how the predictions of the static, one-zone approach change with considering a dynamical model for GRB evolution, *i.e.*, including multiple emission zones, for which a project is ongoing.

4.1 Energetics of gamma-ray bursts

From the structure of a GRB's light curve, the variability time scale t_v can be deduced, which is one of the main parameters for the model. Within the internal shock scenario, we can relate the size of the region to this time variability by assuming that the engine emits shells which collide at a radius R according to Eq. (3.1). Note that by applying the internal shock model, we place ourselves in the prompt emission scenario in the following, which is assumed to be the main emission channel for most GRBs since the photon densities are much higher than in external shocks with the circumburst medium. The width of the shock is given by $\Delta d' = R/2\Gamma$ with the shock Lorentz factor Γ, which is typically between 100 and 1000 for conventional GRBs. This shock or shell width defines the characteristic time scale of the system, *i.e.*, the dynamical time scale $t_{\rm dyn} = \Delta d'/c$, which corresponds to the variability time scale boosted back into the SRF. In the static burst approximation or one-zone model, we assume that in total N such collisions happen which are all alike in the SRF. The number of collisions is given by $N \simeq T_{90}/t_v$, *i.e.*, the ratio of the duration of the burst T_{90}, during which 90% of the emission is observed, and the variability time scale. This averaged picture of a GRB yields reliable results in most cases, but we will discuss the impact of dynamical models for GRBs, which includes multiple, different emission zones, too.

The target photon spectrum assumed for GRBs follows observations and can typically be described as a broken power law

$$N'_\gamma(\varepsilon') = C'_\gamma \cdot \begin{cases} (\varepsilon'/\varepsilon'_{\gamma,\rm br})^{-\alpha} & \varepsilon'_{\gamma,\rm min} \leq \varepsilon' < \varepsilon'_{\gamma,\rm br} \\ (\varepsilon'/\varepsilon'_{\gamma,\rm br})^{-\beta} & \varepsilon'_{\gamma,\rm br} \leq \varepsilon' < \varepsilon'_{\gamma,\rm max} \\ 0 & \text{else} \end{cases} \tag{4.1}$$

with the photon break energy $\varepsilon'_{\gamma,\rm br}$ and two spectral indices α and β. In the following, we choose $\varepsilon'_{\gamma,\rm br} = 1$ keV, $\alpha = 1.0$ and $\beta = 2.0$, unless noted otherwise. The minimum and maximum photon energies, $\varepsilon'_{\gamma,\rm min}$ and $\varepsilon'_{\gamma,\rm max}$, are chosen as small and large enough such that nuclei will always find interaction partners for disintegration at the GDR. However, we studied the impact of the

photon field on the neutrino and cosmic ray fluxes in [159] and [177], showing that there is a small effect, but we will not consider this in the following. The factor C'_γ is the normalization of the photon spectrum, which will be obtained from matching the photon density in the SRF

$$u'_\gamma = \int \varepsilon' N'_\gamma(\varepsilon') d\varepsilon' = \frac{L_\gamma \Delta d'/c}{\Gamma^2 V_{\rm iso}} = \frac{L_\gamma}{4\pi c \Gamma^2 R^2} \tag{4.2}$$

with measured quantities. The observed isotropic equivalent luminosity L_γ has to be boosted back into the SRF by dividing with Γ^2 and converted to an energy by the characteristic time scale of the collision $t_{\rm dyn}$. The energy density is then obtained by dividing by the isotropic volume $V_{\rm iso} = 4\pi R^2 \Delta d'$. The integration limits are determined by the Fermi-GBM energy range.

In the following, Eq. (4.2) will become important as it clearly shows how the radiation density scales with the parameters of the model: It scales linearly with the luminosity $\propto L_\gamma$ and is strongly dependent on the radius $\propto R^{-2}$, which directly comes from the volume of the radiation zone. In the same way it scales $\propto \Gamma^{-2}$, which is however fixed in our calculations to a typical value for conventional GRBs, *i.e.*, $\Gamma = 300$. Note that there is a degeneracy between collision radius R, Lorentz factor Γ and variability time scale t_v on account of the internal shock model Eq. (3.1). Therefore, varying the collision radius implicitly varies t_v. It is possible to fix one of the other parameters as well, vary Γ instead and compute the remaining one in the internal shock scenario.

A pure or mixed composition of nuclei is injected into the radiation zone with a spectrum following the expected power law of Fermi shock acceleration

$$Q'_i(E'_i) = C'_i \cdot \begin{cases} E'^k_i \cdot \exp\left[-(E'_i/E'_{i,\rm max})^p\right] & E'_i \geq E'_{i,\rm min} \\ 0 & \text{else} \end{cases} \tag{4.3}$$

with a spectral index $k \simeq 2.0$ and an exponential cut-off function with $p = 2.0$ for every species i. The cut-off function will have a small impact on the neutrino spectra shown in the following, while the cosmic ray fit is more sensitive to it. The maximum energy $E'_{i,\rm max}$ is obtained by balancing the energy gain with the energy loss processes, *i.e.*,

$$t'^{-1}_{\rm acc}(E'_{i,\rm max}) = t'^{-1}_{\rm dyn} + t'^{-1}_{\rm syn}(E'_{i,\rm max}) + t'^{-1}_{e^+e^-}(E'_{i,\rm max}) + t'^{-1}_{A\gamma}(E'_{i,\rm max}) \quad , \tag{4.4}$$

where the rate for photo-hadronic interactions includes both, photo-meson production and photo-disintegration. For the computation of these rates, we calculate the magnetic field by

$$u'_B = \frac{B'^2}{8\pi} = \frac{\epsilon_B}{\epsilon_e} u'_\gamma \quad \Rightarrow \quad B' = \sqrt{8\pi \frac{\epsilon_B}{\epsilon_e} \frac{L_\gamma}{4\pi\Gamma^2 R^2}} \quad , \tag{4.5}$$

where we typically assume that the fraction of energy in the magnetic field ϵ_B is in equipartition with the fraction of energy in gamma-rays ϵ_e, *i.e.*, $\epsilon_B = \epsilon_e$. With typical magnetic field strengths $B \sim 10^2 - 10^5$ G and sizes $R \sim 10^7 - 10^{12}$ km, GRBs fulfill the Hillas criterion $E_{\max} = \Gamma Z e B R$, which uses the argument that the size of UHECR sources has to be at least the Larmor radius of the accelerated particles [217].

The normalization factor C_i' is determined by normalizing the total energy per isotope

$$\int_0^{10E'_{i,\max}} E_i' Q_i'(E_i') dE_i' = \xi_{A,i} \cdot u'_\gamma \cdot \frac{c}{\Delta d'} \tag{4.6}$$

to the energy density in photons times a baryonic loading factor $\xi_{A,i}$, which is assumed to be 10 as this is a typical value for GRBs [13]. It will, however, be adjusted a posteriori by the cosmic ray fit, which is no problem as the model is linear in baryonic loading. The additional factor $c/\Delta d'$ originates from the conversion from density to flux according to Eq. (3.5).

Based on the primary injection spectrum, we can give a simple estimate for the predicted neutrino fluence $E_\nu^2 \phi_\nu$ by using the relation

$$E_\nu^2 \phi_\nu = \frac{1}{4} f_{p\gamma} E_p^2 \frac{dN_p}{dE_p} / (4\pi d_L^2(z)) \quad , \tag{4.7}$$

where $E_p^2 dN_p/dE_p$ denotes the primary injection spectrum in [GeV] in the source, integrated over the volume. The factor $f_{p\gamma} = t_{\rm dyn}/t_{p\gamma}$ is called pion production efficiency, as it describes the ratio of the photo-hadronic interaction rate to the dynamical time scale. Here, it is defined for protons, but there are scaling relations for nuclei as well [22]. Assuming the Δ-resonance approximation, it is possible to derive an analytical expression for the pion production efficiency

$$f_{p\gamma} \simeq \frac{L'_\gamma}{\varepsilon'_{\gamma,\rm br} \Gamma^2 R} = \frac{L'_\gamma}{\varepsilon'_{\gamma,\rm br} \Gamma^4 t_v} \quad , \tag{4.8}$$

similar to our radiation density in Eq. (4.2).[1] Neutrinos produced by pion decay get about 25% of the energy of the pion, thus the factor 1/4 in Eq. (4.7). Dividing by $4\pi d_L^2(z)$ boosts the spectrum in the observer's frame by distributing the energy on a sphere with the luminosity distance $d_L(z)$ as radius.

In fact, by similar considerations it is possible to place an upper bound on the diffuse neutrino flux from astrophysical sources, independent from the model and whether those sources are detected or not. From Sec. 3.2.1, we know that the energy injection rate of cosmic rays is a few $\times 10^{44}$ erg Mpc^{-3} yr^{-1} for a cosmologically distributed source. The present-day diffuse flux of

[1] The difference between the pion production efficiency and the photon density in Eq. (4.2) is a factor $\Delta d'/c$ originating from the definition of $f_{p\gamma}$ relative to the dynamical time scale.

muon neutrinos (combined ν_μ and $\bar{\nu}_\mu$) can then be estimated via

$$E_\nu^2 \phi_\nu = \frac{1}{4} f_{p\gamma} \xi_z t_H \frac{c}{4\pi} E_{\rm CR}^2 \frac{dN_{\rm CR}}{dE_{\rm CR}} \approx \text{a few} \times 10^{-8} \xi_z \text{GeV cm}^{-2}\text{s}^{-1}\text{sr}^{-1} \quad . \tag{4.9}$$

With respect to Eq. (4.7), this equation includes not only the energy in cosmic rays per source and primary, but the injection rate of the whole population $E_{\rm CR}^2 dN_{\rm CR}/dE_{\rm CR}$. The factor $t_H \approx 10^{10}$ yr is the Hubble time and ξ_z is a factor of order unity taking into account possible unobserved contributions to UHECRs from high redshift sources. This bound is named after Waxman and Bahcall who first derived it [218]. It cannot be exceeded by any source, however for GRBs the stacking limits due to the non-observation of correlated neutrinos are stronger by now.

4.2 Nuclear cascade source classes

In order to describe cosmic ray and neutrino production in the source, we introduce three qualitatively different cases in terms of development of the nuclear cascade in this section: The *Empty Cascade*, meaning that the nuclear cascade barely develops and most nuclei stay intact due to the low efficiency of photo-hadronic interactions. As a consequence, in this case the neutrino production is low. In the case of the *Populated Cascade*, the nuclear cascade develops while disintegration and photo-meson production are efficient for heavy masses. Nuclei will be able to survive partially and neutrino production is moderate. Lastly, in the *Optically Thick Case* the source is opaque to all nuclear species, implying efficient neutrino and nucleon production with a fully developed nuclear cascade. The transition between these source classes is continuous, however we first discuss three benchmarks in the following, where we fix $R \simeq 10^{8.3}$ km and $\Gamma = 300$, such that the radiation density depends only on the L_γ. In the first step, we inject a pure ^{56}Fe composition in the source. After that, we show parameter space scans and how the parameter space can be separated into regions of these source classes.

4.2.1 Development of the nuclear cascade in GRBs

The Empty Cascade source class is defined as the case that is optically thin to $A\gamma$ interactions of the primary injected isotope and thus also for all lighter isotopes including nucleons, since the cross section scales with the mass number A. This source class requires low radiation density, hence low luminosities or large radii. In Fig. 4.2, we show a benchmark for this class with a luminosity of $L_\gamma = 10^{49}$ erg s^{-1}. In the top left panel, the rates of the dominant processes for the injected primary are shown, including the photo-meson production for protons $t'^{-1}_{p\gamma}$ for comparison. For the sake of simplicity, Bethe-Heitler pair production is included but not shown as it is sub-dominant in all the examples we show. One can clearly see that the source is

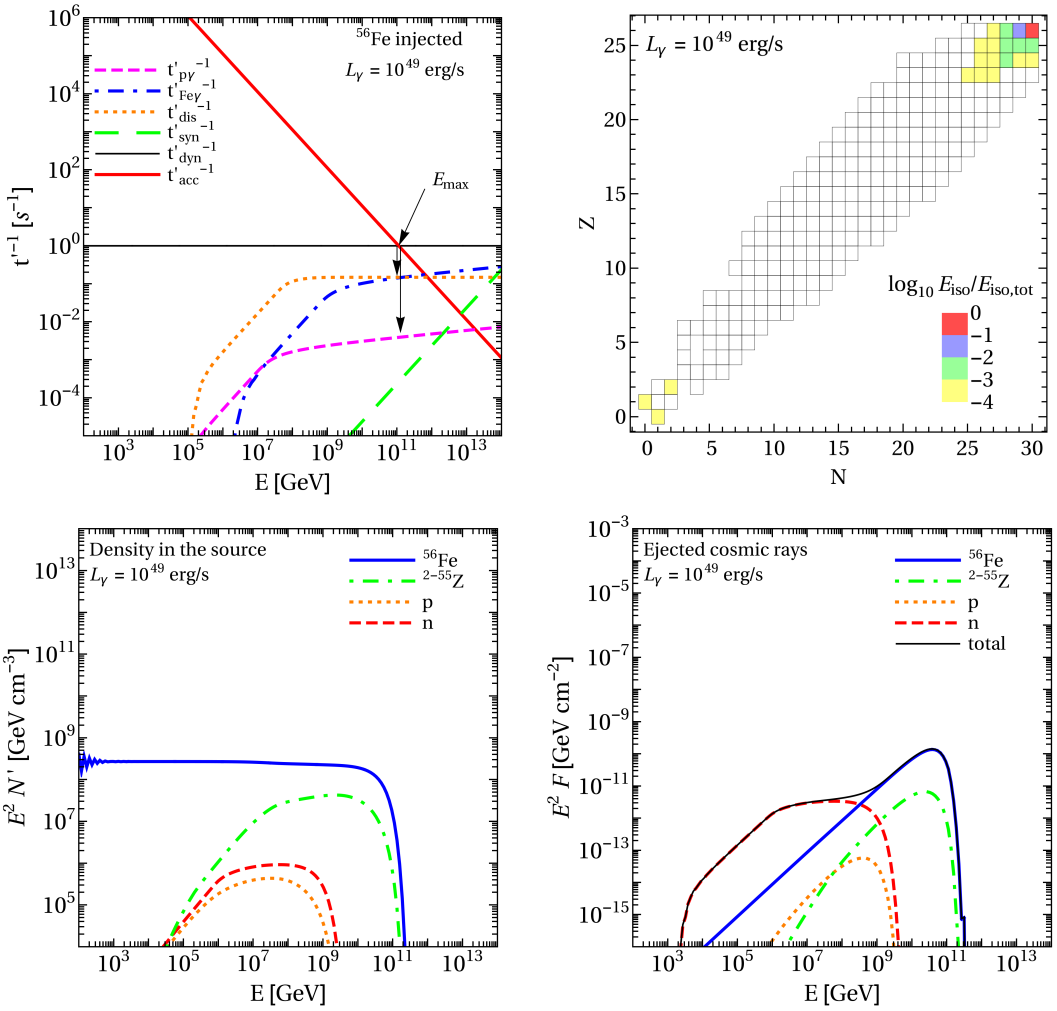

Figure 4.2: Benchmark for the *Empty Cascade* source class with isotropic luminosity $L_\gamma = 10^{49}$ erg s^{-1} and pure ^{56}Fe injection: Interaction rates (top left, for iron, $p\gamma$ also included), the nuclear cascade (top right), particle densities in the source (bottom left) and ejected cosmic ray fluence per shell (bottom right, without interactions on EBL and CMB) as a function of the energy in the observer's frame. The color code in the nuclear cascade shows the fraction of energy stored in each isotope, relative to the total isotropic equivalent energy $E_{\rm iso,tot}$ (white: fraction smaller than 10^{-4}). Different curves in the bottom panels correspond to different isotopes according to the legend. The other GRB parameters are $R \simeq 10^{8.3}$ km, $\varepsilon'_{\gamma,\rm br} = 1$ keV and $z = 2$. Taken from [159].

optically thin to photo-hadronic interactions by comparing $t'^{-1}_{\rm dis}$ and $t'^{-1}_{A\gamma}$ to $t^{-1}_{\rm dyn}$, as indicated by the arrows. The maximum energy is dominated by adiabatic losses, such that cosmic rays

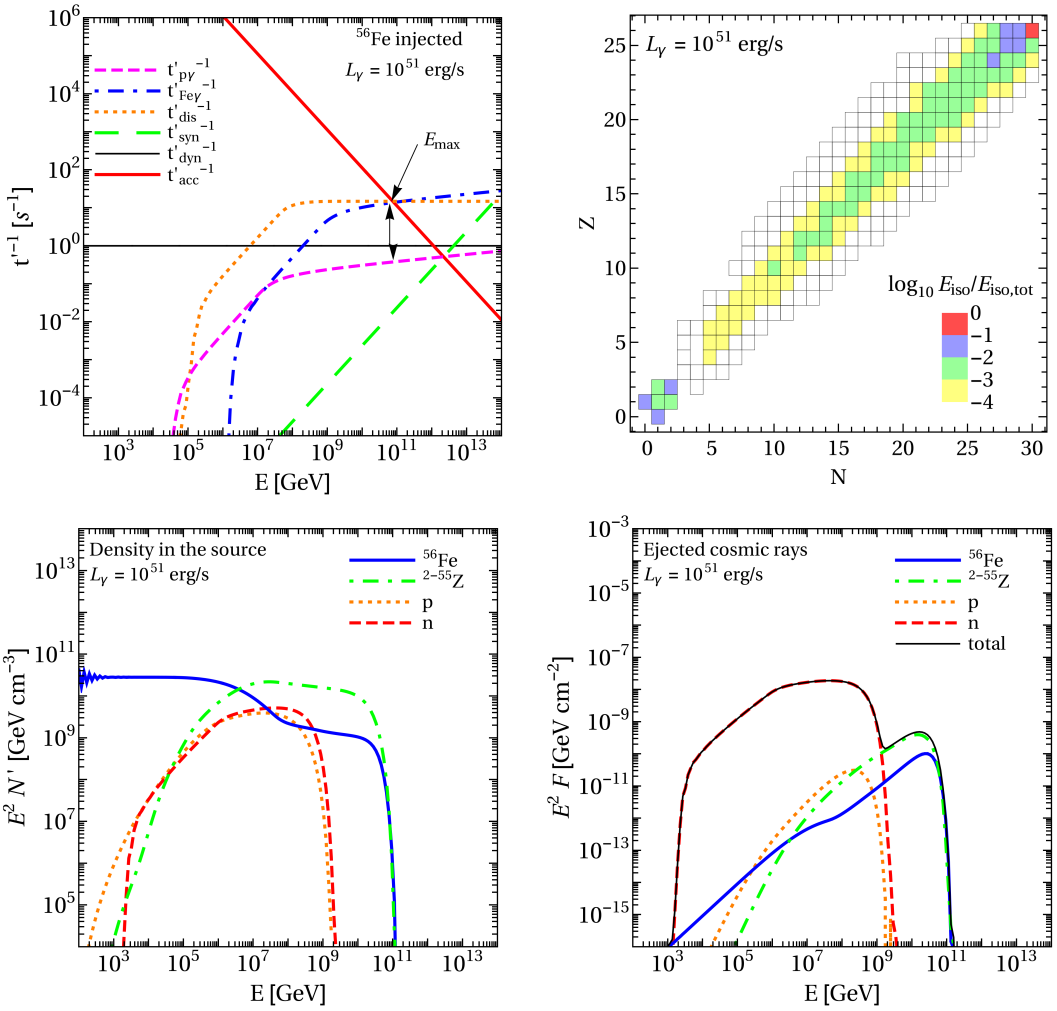

Figure 4.3: Same as Fig. 4.2 but for the *Populated Cascade* source class with isotropic luminosity $L_\gamma = 10^{51}$ erg s^{-1}. Taken from [159].

rather cool than interact. However, a small fraction will still interact, such that the nuclear cascade (shown in the top right panel) will be populated around the injected isotope and a few nucleons and ^{4}He will be produced. The color shows the integrated energy per isotope relative to the total injection energy, where white boxes represent energy fractions smaller than 10^{-4}.

The (quasi-)steady state particle densities in the source are shown in the lower left panel of Fig. 4.2. Since the source is optically thin, the injected spectrum $\propto E^{-2}$ of ^{56}Fe is hardly modified and extends up to the maximum energy. Nucleons and secondary nuclei are suppressed and their maximum energies follow Lorentz factor conservation. The ejected cosmic ray spectra, depicted in the lower right panel as the fluence at Earth including adiabatic losses only, show

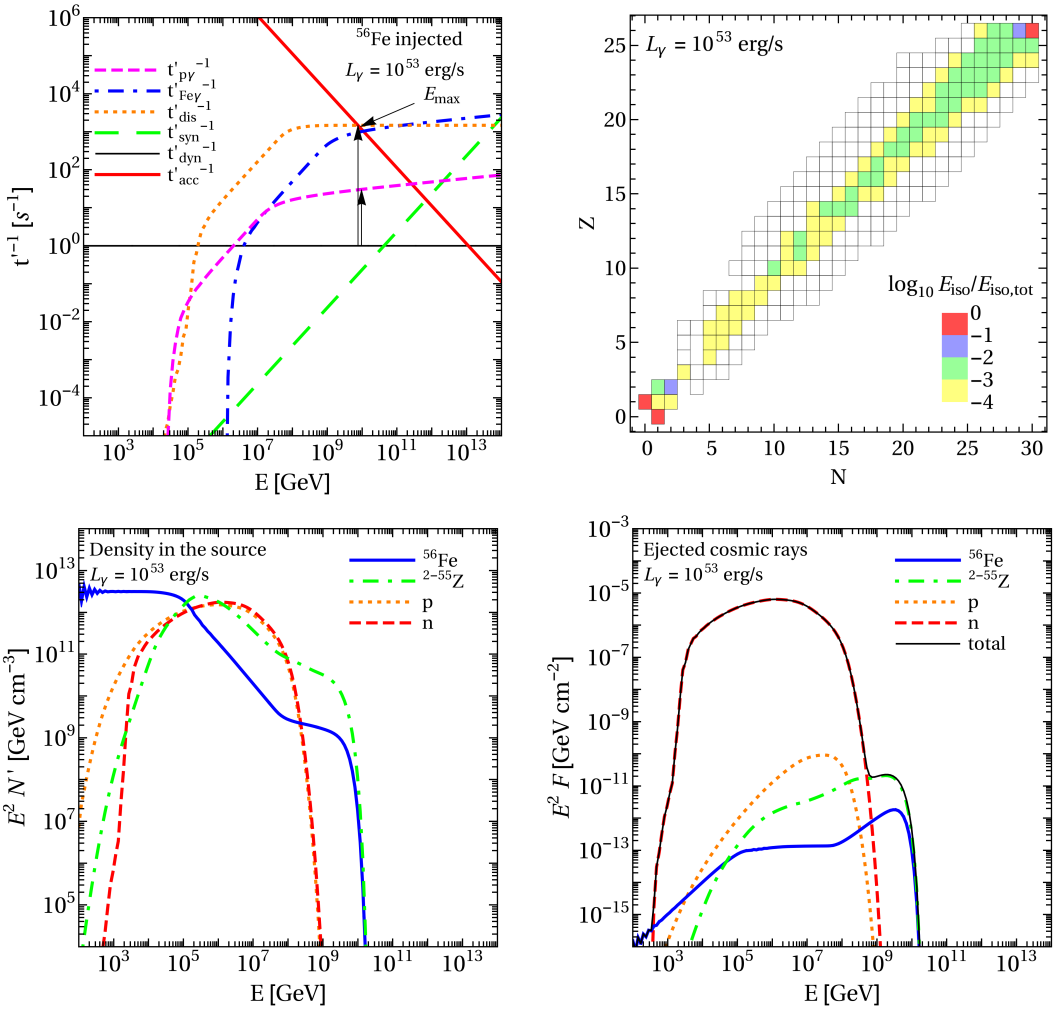

Figure 4.4: Same as Fig. 4.2 but for the *Optically Thick Case* source class with isotropic luminosity $L_\gamma = 10^{53}$ erg s^{-1}. Taken from [159].

harder spectra $\propto E^{-1}$ because of the direct escape mechanism, see Sec. 3.1.3. However, neutrons are not magnetically confined, so they soften the overall spectrum as they decay and convert to protons on their way to Earth. The characteristics of the Empty Cascade are that the ejected cosmic rays are dominated by the hard spectrum of injected primaries, while only few nucleons are produced, making the composition heavy. Nevertheless, compared to the density in the source, the contribution of neutrons, especially at low energies, is more substantial than expected, due to the additional suppression of the escape mechanism at the highest energies.

In the case of the Populated Cascade, which is obtained for $L_\gamma = 10^{51}$ erg s^{-1}, the source is optically thick to $A\gamma$ interactions of the injected primary which will disintegrate and populate

the cascade. At the same time, the source is still transparent to photo-hadronic interactions of nucleons, such that proton and neutron fluxes will be hardly affected by these interactions. This source class is encountered for intermediate radiation densities, *i.e.*, intermediate luminosity and radii. The example for this source class is shown in Fig. 4.3. From the interaction rates, it is clear that at the maximum energy, photo-meson production and disintegration are now the limiting processes for the injected ^{56}Fe. However, nucleons (and light nuclei) are still limited by adiabatic cooling. The nuclear cascade is well populated with integrated energies in nucleons and helium between 1% and 10% of the total energy, similar to isotopes close to the injection.

The densities in the source show now a clear depletion of the E^{-2} spectrum beyond the disintegration threshold, while the peak density of secondaries are comparable to the primary density. The densities of neutrons and protons do not reach this level yet, still the ejected cosmic ray spectrum is already dominated by neutrons. The reason is that the ejected spectra are suppressed by the optical thickness in the escape mechanism. The Larmor radius of the cosmic rays reaches only about 1/30 the size of the region at the maximum energy, so particles which are not contained in this thin layer on the outside of the shell take too long to escape. The effective cosmic ray escape spectrum is therefore relatively soft because of the neutron component, which can be controlled by the luminosity or, more general, by the radiation density.

If we further increase the luminosity, the source will become optically thick even to nucleons (and consequently all other isotopes), which defines the Optically Thick Case as shown in Fig. 4.4. This requires extremely high luminosities $L_\gamma = 10^{53}$ erg s^{-1} which drives up the interaction rates, such that adiabatic cooling is sub-dominant for all species. The nuclear cascade appears to be less populated off the main diagonal, which is because of the strong disintegration, *i.e.*, intermediate isotopes efficiently interact and most of the energy is dumped into nucleons, which are now occupied at a similar level as the primaries. The densities of heavy nuclei in the source are strongly suppressed beyond the photo-disintegration threshold, while protons and neutrons are populated at a level comparable to the injection. The density of nucleons peaks at the photo-meson threshold as they cascade down in energy due to multiple interactions. The ejected cosmic rays are dominated by neutrons as the heavy nuclei are strongly suppressed because of the small Larmor radii. In fact, the strong $A\gamma$ interactions make it complicated to reach ultra-high energies at all.

In Fig. 4.5 we show the all-flavor neutrino fluence per shell for the different source classes. In each panel, the total flux is shown (thin black curve) as well as the decomposition of this total flux according to the contribution of primary nuclei (solid, blue), secondary isotopes (dot-dashed, green) and nucleons (dashed, red). For the Empty Cascade source class, the dominant contribution to the neutrino flux are photo-hadronic interactions of the injected isotope. On the other hand, for the Populated Cascade, the dominant contribution is given by $A\gamma$ interactions

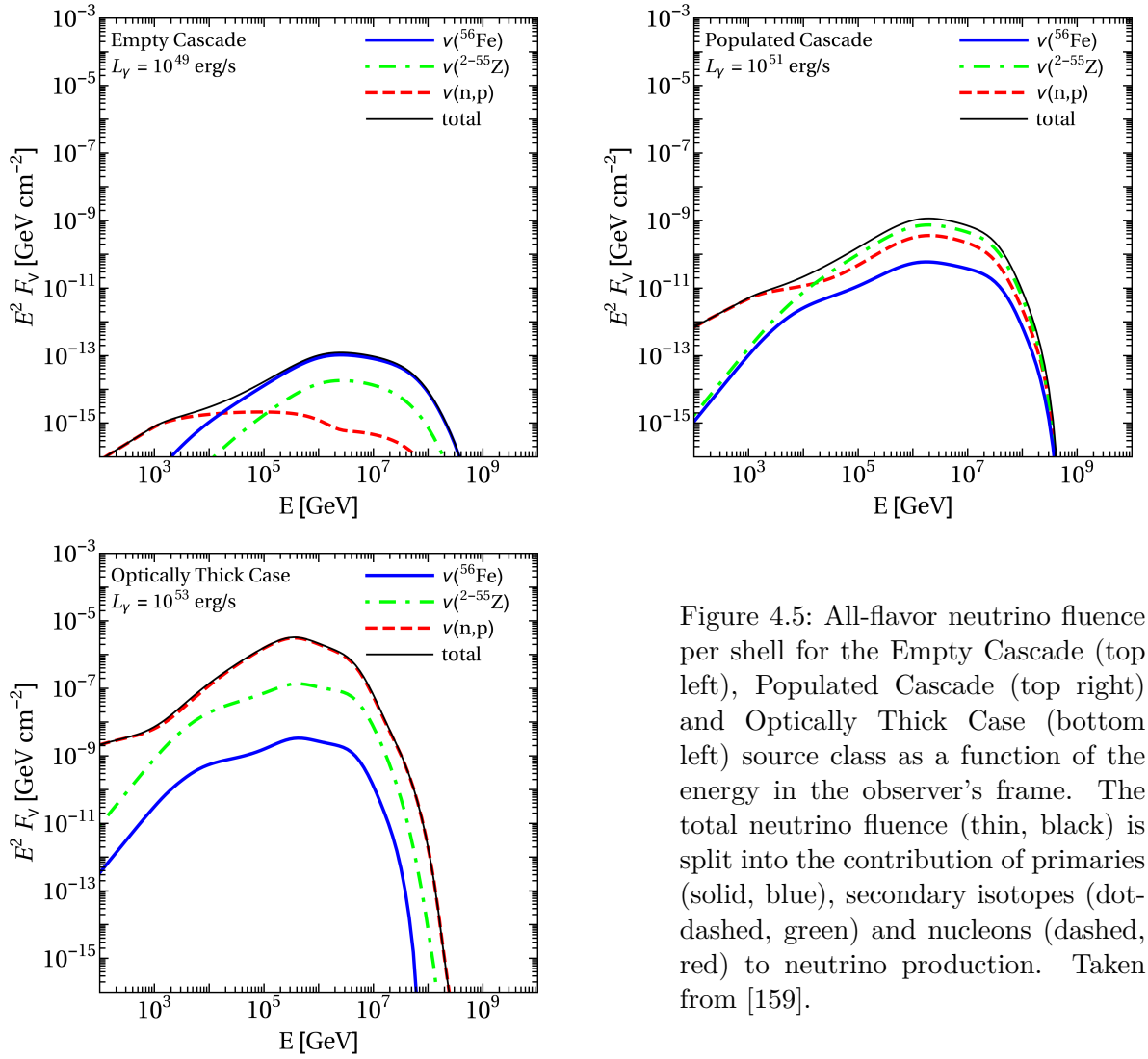

Figure 4.5: All-flavor neutrino fluence per shell for the Empty Cascade (top left), Populated Cascade (top right) and Optically Thick Case (bottom left) source class as a function of the energy in the observer's frame. The total neutrino fluence (thin, black) is split into the contribution of primaries (solid, blue), secondary isotopes (dot-dashed, green) and nucleons (dashed, red) to neutrino production. Taken from [159].

off the secondary nuclei. In the Optically Thick Case, photo-meson production of protons and neutrons has the largest contribution. Neutrinos from beta decay are included and visible as a bump in the nucleon contribution at low energies, *i.e.*, it is sub-dominant at the peak. By increasing the luminosity, the neutrino fluence grows quadratically as the photon and the baryon density both scale with luminosity.

As mentioned in Sec. 3.1.2 as well as in Refs. [24] and [177], photo-meson production is relatively well understood in the case of nucleons. However, predictions for photo-meson production off nuclei rely typically on a superposition model with an implicit scaling of the cross section (here: $\propto A$). This implies that the neutrino prediction for the Optically Thick Case is robust,

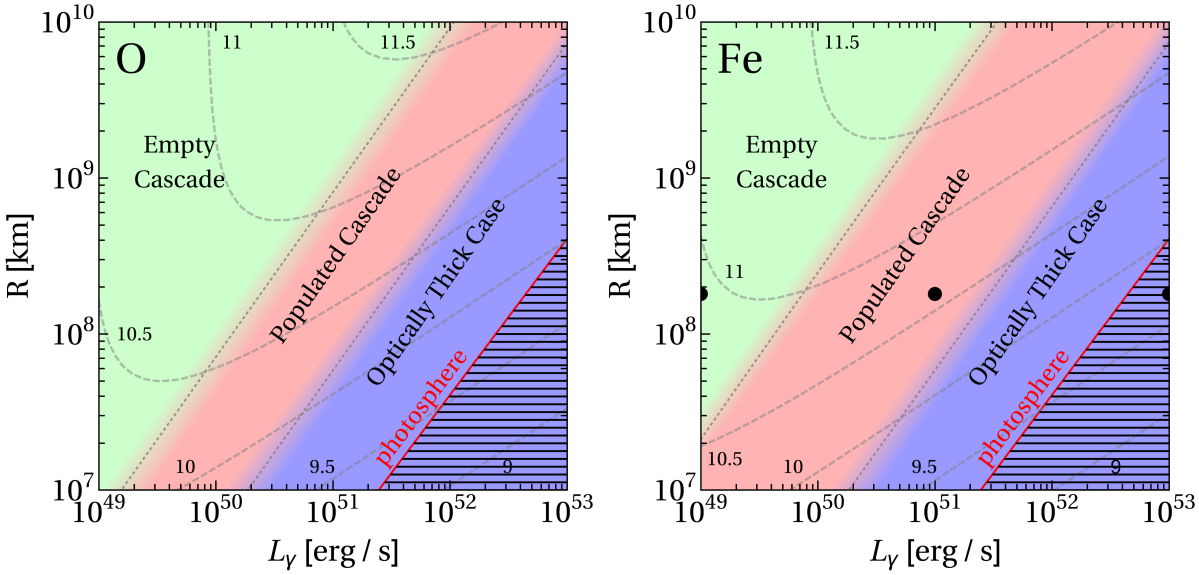

Figure 4.6: Parameter space scan showing the regions for the different nuclear cascade source classes as a function of luminosity L_γ and collision radius R in the internal shock scenario. The injection composition is pure ^{16}O (left) or ^{56}Fe (right). We fix $\Gamma = 300$ and scale $t_v \propto R$ according to Eq. (3.1), the other parameters are the same as in Fig. 4.2. Black dots in the right panel represent the benchmarks shown in Sec. 4.2.1. The gray dashed contours indicate the maximum energy $\log_{10}(E_{i,\mathrm{max}}[\mathrm{GeV}])$ in the observer's frame while the gray dotted line indicates the transition from one region to another. Below the photosphere (red solid line), gamma-rays cannot escape from the source due to electron-positron pair production. Taken from [159].

whereas the other classes (where the fluence is however low) could carry large uncertainties which will only be quantified in the future. Improved models as in [177] show that the contribution of nucleons may be also dominating in the Populated Cascade, but in the superposition model these predictions are less reliable because of the poorly understood cross sections.

4.2.2 Classification of parameter space regions

Following the classification of sources depending on the radiation density in the previous section, we show in Fig. 4.6 the parameter space divided into three regions as a function of the luminosity L_γ and collision radius R for pure ^{16}O injection (left) and ^{56}Fe (right). The transition between these regions is continuous, however we show the transition from optically thin to optically thick to primaries and nucleons as gray dotted lines. In the case of iron, the black dots represent the benchmarks shown in the previous chapter. Furthermore, we show the sub-photospheric region (hatched), where photons cannot escape because of Thomson scattering. Below the photosphere,

our model is not valid anymore because the target photon spectrum changes. For details on the calculation of the photosphere, see App. B.

The alignment of the Optically Thick region (and the photosphere) in the lower right corner is evident since high luminosities and small radii mean high photon densities. On the other hand, radiation densities are low in the upper left corner, where the Empty Cascade region is encountered. The maximum primary energy in the observer's frame, depicted by the gray dashed contours, is typically determined by adiabatic cooling (upper left) or $A\gamma$ interactions (lower right). Their shape can be understood by comparing the interaction rates $t'^{-1}_{A\gamma} \propto u'_\gamma \propto L_\gamma/R^2$ and $t'^{-1}_{\rm dyn} \propto 1/R$ with the acceleration rate $t'^{-1}_{\rm acc} \propto B'/E' \propto \sqrt{u'_\gamma}/E' \propto \sqrt{L_\gamma}/(E'R)$. The maximum primary energy is then constant along $R \propto \sqrt{L_\gamma}$ in the $A\gamma$ dominated region, while the dependence on R cancels in the region dominated by adiabatic losses. The adiabatic cooling limited scenario corresponds to a rigidity dependent maximum energy (Peters cycle), which roughly coincides with the Empty Cascade case.

The transition between the Empty Cascade and the Populated Cascade depends on the injected isotope since the photo-hadronic interaction rate scales with A, which can be seen by comparing the two panels. In turn, the transition between adiabatic dominated and interaction dominated maximum energy shifts because the transition from Populated Cascade to Optically Thick Case is independent from the injection composition. Thus, the smaller the injected mass, the smaller the Populated Cascade region will be, as it directly scales with A and approaches the $p\gamma$ rate more and more.

4.3 The conventional GRB-UHECR paradigm

In order to connect the nuclear cascade source classes with cosmic ray data, we now assume a cosmological distribution of identical GRBs with a fixed duration of $T_{90} = 10$ s. This implies that the emission per GRB is produced in $N = T_{90}/t_v$ individual collisions which were discussed in the benchmarks in the previous section. We perform a fit to PAO data of UHECR spectrum and composition, combining the modeling of the interactions in the source and the propagation as computed with SimProp with the Gilmore EBL and PSB cross section model. We take into account extensive air showers in the atmosphere of the Earth for which EPOS-LHC is used[2]. The GRBs are assumed to follow a redshift evolution according to the star formation rate and we assume pure ^{28}Si injection in the source described by a power law with spectral index $k = 1.8$ and a cut-off power $p = 2.0$, *cf.* Eq. (4.3). These parameters are chosen a priori but fixed in the following.

[2]Although differences between nuclear interaction models could matter in this context, a detailed study on air shower models is meaningless with a fixed injection composition.

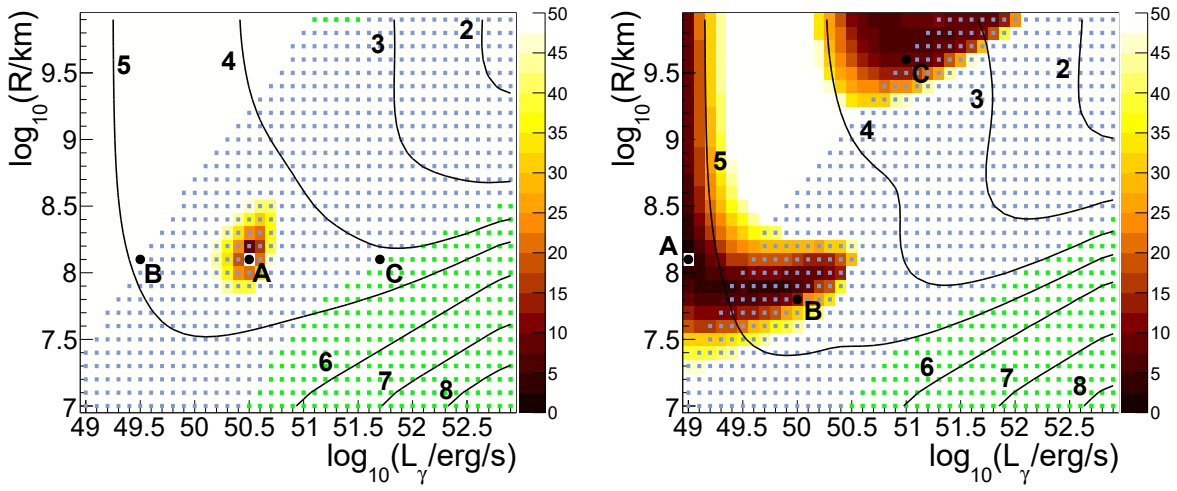

Figure 4.7: Parameter space scan for the mixed composition dip (left, fit above 10^{18} eV) and ankle (right, fit above 10^{19} eV) model in the internal shock scenario. The color bar shows $\sqrt{\chi^2 - \chi^2_{\text{min}}}$ as a function of luminosity and radius for the fit to cosmic ray data obtained by PAO [219, 5]. Pure ^{28}Si is injected into the source with a spectral index of $k = 1.8$ and the sources are distributed over $z = 0$ to 6 following the star formation rate. Blue squares mark the excluded region by IceCube according to the GRB stacking analysis from muon tracks in the northern and southern sky at 90% C.L. [199, 18]. Green squares correspond to the 90% C.L. for the IceCube-excluded region from the cosmogenic neutrino analysis [221], taking into account $\nu_\mu + \bar{\nu}_\mu$. The black contours indicate the baryonic loading $\log_{10} \xi_A$. Taken from [159].

We perform the fit by using the combined spectrum [219] and composition [5] in a procedure similar to [220] and [4]. Again, we scan the parameter space in luminosity and production radius and calculate the fluxes for each set of parameters. Together with the cosmic rays, prompt and cosmogenic neutrino fluxes are calculated following [26]. For prompt neutrinos, the exposure for muon neutrinos is obtained by summing the exposure relative to different IceCube analyses, considering a total of 1014 GRBs observed in the Northern Hemisphere [199, 18] and 664 GRBs which occured in the Southern Hemisphere [18]. The total number of bursts of this combined sample is compared with an assumed 667 bursts per year in [26]. The corresponding exposure for cosmogenic neutrinos is taken from [221]. In the scan, we show excluded regions by neutrino data at 90% C.L. assuming both analyses are free of background.

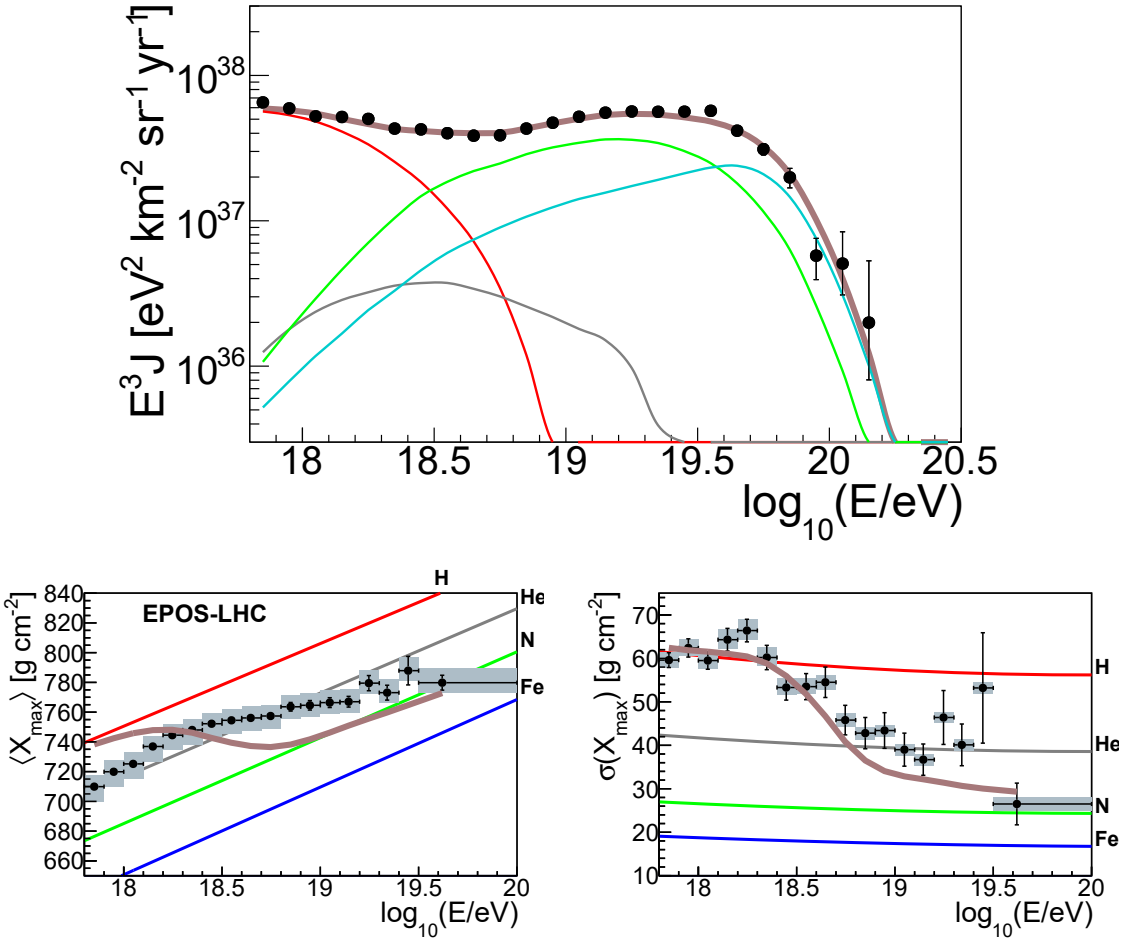

Figure 4.8: Cosmic ray spectrum (top, multiplied by E^3) and composition (bottom) obtained for the best fit in the mixed composition dip model, corresponding to Fig. 4.7 point A. Spectra at Earth are grouped according to $A = 1$ (red), $2 \leq A \leq 4$ (gray), $5 \leq A \leq 22$ (green), $23 \leq A \leq 28$ (cyan) and total (brown). The average and standard deviation of the $X_{\max}$ distribution is predicted assuming EPOS-LHC [115] for UHECR-air interactions. Pure compositions ^{1}H (red), ^{4}He (gray), ^{14}N (green), ^{56}Fe (blue) and data from [222] are shown for comparison. Taken from [159].

4.3.1 UHECR fit with mixed composition models

After calculating the propagated spectra, we perform a fit to the UHECR spectrum and composition as measured by the PAO in the following, assuming injection of pure ^{28}Si with a spectral index of $k = 1.8$. Furthermore, we assume a distribution of GRBs according to the SFR [190] between redshifts $z = 0$ to 6. We distinguish between two scenarios, the *mixed composition dip*

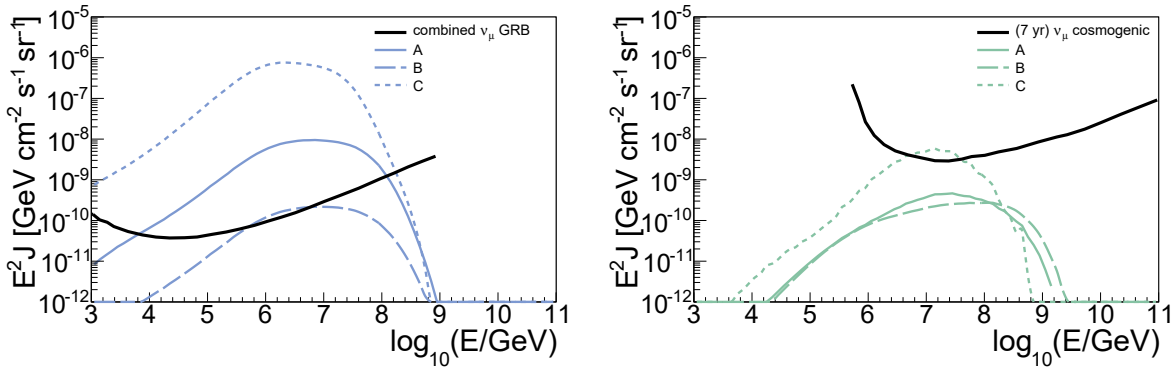

Figure 4.9: Prompt (left) and cosmogenic (right) neutrino flux (muon flavor) obtained for selected points in the parameter space according to Fig. 4.7 for the mixed composition dip model. The fluxes are compared to the differential (as defined in [26]) limits obtained from [18] (northern + southern exposure) and [221]. Taken from [159].

model and the *mixed composition ankle model*. For the former, we include the ankle region in the energy range as we fit above 10^{18} eV while for the latter, we fit above 10^{19} eV. The result of the fits are shown in Fig. 4.7 for both models, where the quality of the fit is represented by the color bar illustrating $\sqrt{\chi^2 - \chi^2_{\mathrm{max}}}$ as a function of luminosity and radius. Parameter combinations which are marked with blue squares are excluded by the IceCube prompt GRB analysis [18], whereas green markers refer to cosmogenic neutrino limits [221], both at 90% C.L. The black contours depict the baryonic loading $\log_{10} \xi_A$ needed to address the flux of UHECRs.

From the left panel, we infer that the best fit point named A is found for intermediate luminosities and radii. The corresponding cosmic ray spectrum and composition observables at Earth are shown in Fig. 4.8. The ankle can be well reproduced without the need of additional components, as the nuclear cascade in the source produces a light component at lower energies. On the other hand, a sufficient amount of heavy nuclei survive at the highest energies, which reproduces the feature. For the composition observables, the trend to heavier masses can be reproduced, but the energy dependence of this effect is not matched. In this study, we want to investigate the impact of source properties rather than the injection composition. It is not optimized to give the best possible description to data, as a mixed injection composition and a shift in the energy scale would need to be included. The baryonic loading roughly follows the maximum energy contours, confirming the results of [26] and a value of 3×10^4 at the best fit.

The mixed composition dip model best fit point coincides with the Populated Cascade region, where the dominating contribution to the prompt neutrino flux is photo-meson production of secondary nuclei. This region is excluded by the GRB stacking limits, as shown in the left panel

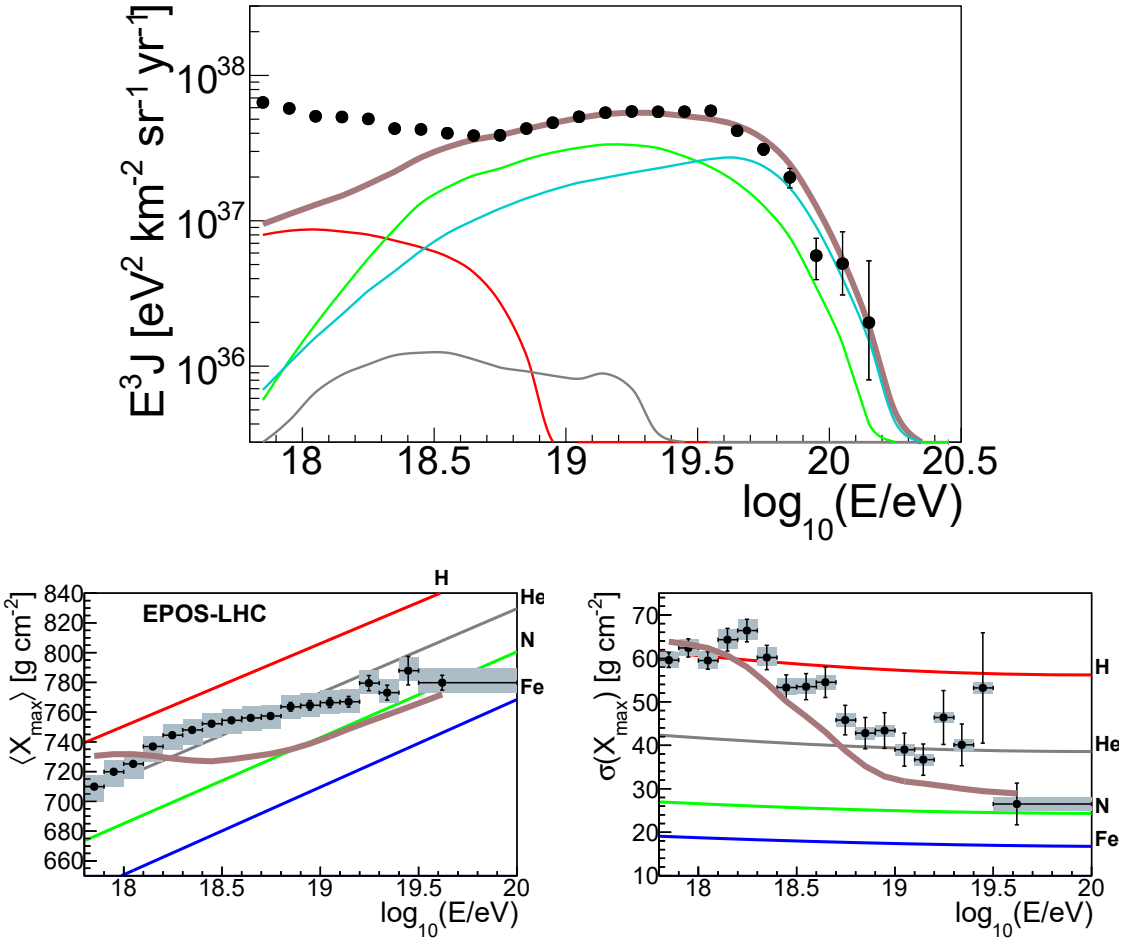

Figure 4.10: Same as Fig. 4.8 but for the mixed composition ankle model. Taken from [159].

of Fig. 4.9. The corresponding cosmogenic fluxes are illustrated in the right panel together with the differential limit. In both cases, the flux of muon neutrinos is shown at Earth for different points in parameters space corresponding to Fig. 4.7. It is possible to see how the prompt neutrino flux scales with the radiation density, as point B is an example at the transition from Empty Cascade to Populated Cascade while point C is at the border to the Optically Thick Case. All examples are excluded by prompt neutrinos, whereas only the most extreme case, point C, violates the cosmogenic limit. This is mainly because of the extraordinarily high flux of nucleons injected into the extragalactic space. The amount of neutrinos is also indicative for the amount of nucleons produced in the nuclear cascade, controlling the sub-ankle component. See our paper [159] or Sec. 4.4 for the illustration of this feature.

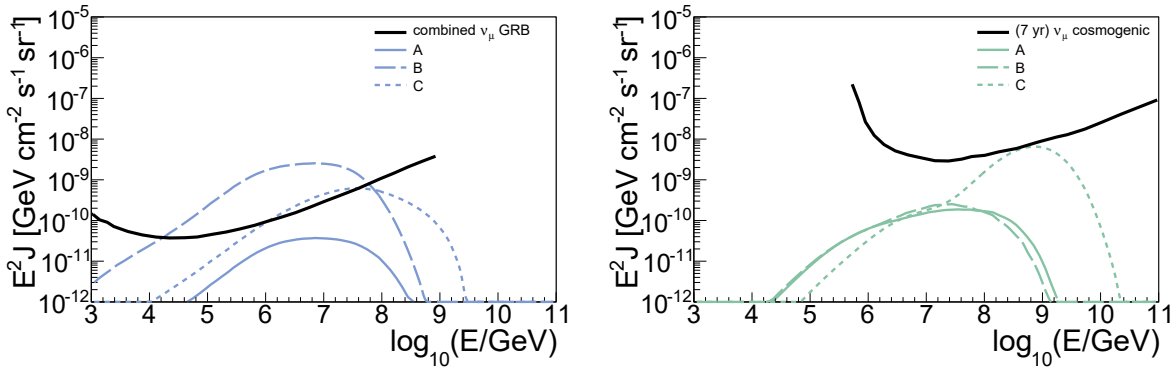

Figure 4.11: Same as Fig. 4.9 but for the mixed composition ankle model. Taken from [159].

The best fit for the mixed composition ankle model, which is indicated by point A in the right panel of Fig. 4.7, is found for similar radii but very low luminosities compared to the mixed composition dip model. The UHECR spectrum and composition at the best fit are shown in Fig. 4.10 for this model. Here, the fit is performed for energies above 10^{19} eV, including a penalty for overshooting the flux at lower energies. The overall quality of the fit is better than in the mixed composition dip model, however it is at the border of the scanned parameter space. This is because in the Empty Cascade region, the overshooting of the flux at lower energies can be naturally avoided. However, this also shows the impact of the chosen energy range for the fit: When the starting energy is lower, the flux at lower energies has to be enhanced, pushing the best fit towards the Populated Cascade region. Since the best fit parameters belong to the Empty Cascade case, the protons in the energy spectrum at Earth come mainly from interactions during propagation, as nucleon production in the nuclear cascade is inefficient. The transition towards heavier isotopes at the highest energies is flatter than in the previous case, but it can not address the exact behaviour either for the same reasons.

The best fit in the mixed composition ankle model is not excluded by neutrino limits, as can be seen in Fig. 4.11. We also show again two examples, point B and C, which are in or at the border to the Populated Cascade region, respectively. Point B reproduces the UHECR spectrum in a reasonable way with the transition in composition being slightly sharper (not shown). However, enhancing the luminosity results in the violation of the stacking limits. The cosmogenic neutrino flux does not change substantially from point A to B. Point C represents an example with intermediate luminosity and high collision radius, such that the disintegration in the source is barely efficient. Thus, high maximum primary energies can be reached at the source, which leads to very high energy protons at Earth from interactions during propagation and, with that, a high cosmogenic neutrino flux.

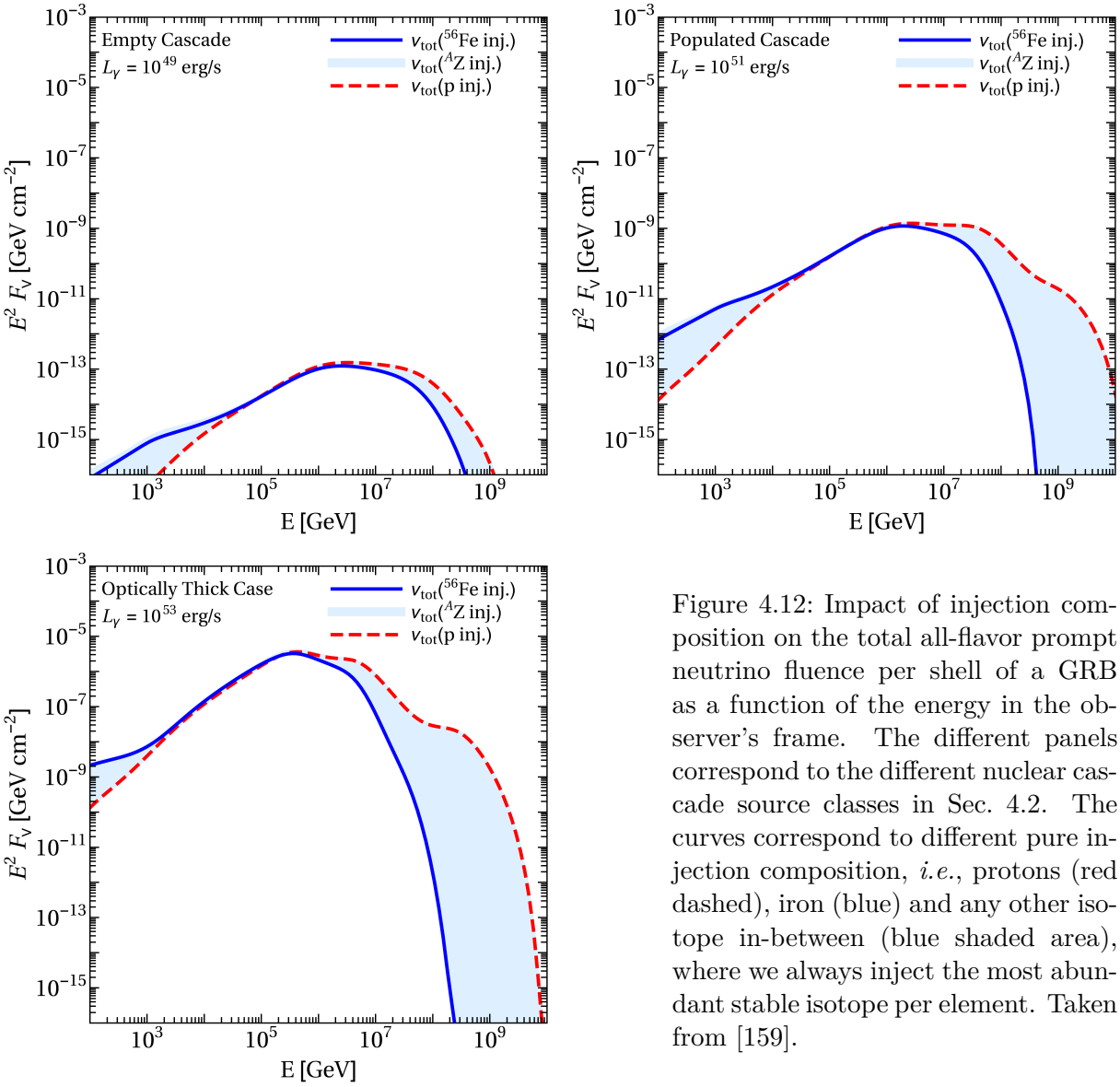

Figure 4.12: Impact of injection composition on the total all-flavor prompt neutrino fluence per shell of a GRB as a function of the energy in the observer's frame. The different panels correspond to the different nuclear cascade source classes in Sec. 4.2. The curves correspond to different pure injection composition, *i.e.*, protons (red dashed), iron (blue) and any other isotope in-between (blue shaded area), where we always inject the most abundant stable isotope per element. Taken from [159].

4.3.2 Impact of the injection composition

In this section, we study the dependence of prompt neutrino production and cosmic ray fit on the injected source composition. For every possible element (identified by its charge number Z), we pick the most abundant stable isotope, compute the nuclear cascade and calculate qualitative estimators for the cosmic ray fit. When the nuclear cascade develops, prompt neutrinos are produced, which is depicted in Fig. 4.12. The figure shows the total prompt muon neutrino fluence for three different luminosities corresponding to the benchmarks from Sec. 4.2.1 as a

function of the observed energy. The blue curve represents the fluence obtained for a pure iron injection composition (same as total in Fig. 4.5), while the dashed red curve corresponds to pure proton injection. The blue shaded area in-between both curves contains the neutrino fluences of all other injected elements from hydrogen up to iron. The most important result is that the peak of the fluence hardly depends on the injection composition. This is a consequence of Lorentz factor conservation in the disintegration, the E^{-2} spectrum conserving the energy per decade, the photo-meson interaction rate being almost flat beyond the threshold and strong magnetic field effects on secondary mesons, which determine the maximum energy cut-off. This becomes clear if the nucleus is treated as a superposition of nucleons. Rewriting the secondary production in terms of nucleons (see, *e.g.*, [223]) leads to almost the same result as before if the primary flux times the interaction rate roughly scales as E^{-2} and the photo-meson cross section $\sigma_{A\gamma} \simeq A\sigma_{p\gamma}$. Due to Lorentz factor conservation, disintegration does not affect this result, as there is hardly any energy lost.

The high-energy cut-off of the neutrino spectrum is higher for lighter masses as the maximum primary energy does not follow the Peters cycle (rigidity-dependent maximum energy) in the Populated Cascade and Optically Thick Case. Therefore, the maximum energy per nucleon, which affects maximum neutrino energy, decreases. This effect becomes visible if it is stronger than the cut-off from magnetic field effects. At low energies, the neutrino fluence from nuclei is higher because of decaying neutrons produced in the nuclear cascade.

Now, we will illustrate why ^{28}Si is a good example for the fit to data and qualitatively explain the values of the best fit parameters in the previous section. The discussion is based on four different estimators:

- Spectral shape. The ejection spectrum is roughly described by a single power law with a spectral index determined by the peaks of the heavy ($A > 1$) and light ($A = 1$) component.
- Maximum energy. Determined by the equilibrium between acceleration rate and energy loss rates, the ejected spectrum will have a characteristic maximum energy $E_{\rm max}$.
- Composition at $E_{\rm max}$. To describe the trend towards heavy masses observed in the $X_{\rm max}$ measurements at Earth, the composition at the maximum energy is relevant.
- Transition energy $E_{\rm trans}$. The energy at which the composition gets heavier.

The estimators are shown for different luminosities as a function of Z in Fig. 4.13. In each panel, the estimated preferred ranges are illustrated by the shaded band. The zig-zag pattern in some of the curves originates from the mass pattern of the most abundant stable injection isotopes as a function of charge Z. Note that R is fixed in these figures.

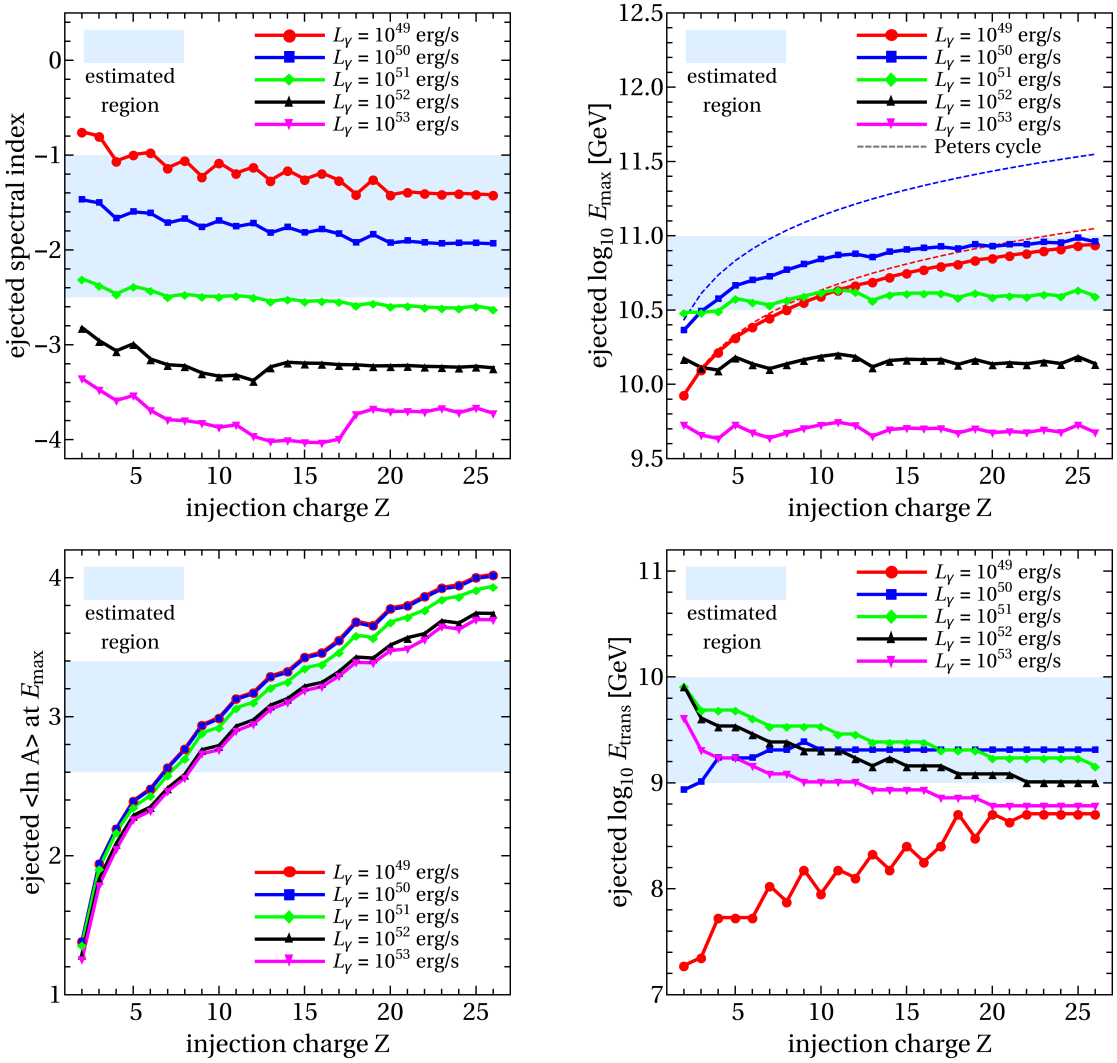

Figure 4.13: Qualitative estimators to show the impact of the injection composition on the UHECR fit as a function of the charge number Z of the injected isotope: Spectral index at the ejection from the source (top left), maximum energy (top right), ejected composition in $< \ln A >$ at the maximum energy (bottom left) and energy at which the composition shows a transition from light to heavy (bottom right). The different curves correspond to different luminosities as defined by the legend. Estimates are taken from [29, 4, 224]. Taken from [159].

The spectral index, shown in the upper left panel, hardly depends on the injection composition, but rather on the luminosity. While in the Optically Thick Case the resulting spectra are too soft, luminosities between 10^{49} erg s^{-1} and 10^{53} erg s^{-1} are favored, which is compatible with our mixed composition models. Furthermore, it is in agreement with the results presented by

the PAO, where the spectra at injection are comparable to the ones ejected from the source in our model [4].

From the upper right panel, it can be seen that the maximum energy tends to be too low for high luminosities, as it becomes strongly limited due to $A\gamma$ interactions. Almost all the other cases lead maximum energies in a reasonable range (if $Z \geq 8$ for the Empty Cascade). In this panel, we also show the deviation from the often assumed Peters cycle (as in [4]), *i.e.*, the scaling of the maximum energy with rigidity. This is true in the Empty Cascade regime, when the maximum energy is limited by adiabatic losses, as for 10^{49} erg s^{-1}. The dashed curves represent an ideal Peters cycle. However, as the maximum energy is limited by other energy loss processes such as photo-hadronic interactions, the scaling with Z is much more mild. Already for 10^{50} erg s^{-1}, significant deviations are expected.

The ejected composition at the maximum energy has to be at least as heavy as the composition measured by the PAO at the highest energies. The lower left panel shows that, besides the obvious strong scaling of the ejected composition with Z, the $< \ln A >$ at the highest energies also depends mildly on the luminosity. This is because the average mass is reduced for higher luminosities due to the development of the nuclear cascade and with that efficient disintegration and production of nucleons. From this panel it is also evident that injection charges between 7 (nitrogen) and 14 (silicon) may provide reasonable results.

From these three estimators, we can qualitatively explain the fit range between 10^{49} erg s^{-1} and 10^{53} erg s^{-1} for the mixed composition ankle model. In the context of the mixed composition dip model, the best fit is determined by an isotropic luminosity for which the transition energy is allowed, as depicted in the bottom right panel of Fig. 4.13. For the Empty Cascade, the injected primary dominates at the highest energies, leading to a smooth transition at low energies which increases with Z. In the case of the Populated Cascade, the transition energy hardly depends on the injection composition, but slightly decreases for increasing Z. The transition itself happens suddenly but becomes smoother again for higher luminosities, because the nuclear cascade is populated mainly by lighter isotopes in the Optically Thick Case.

Note that this discussion is aimed to give a qualitative understanding of the fit results, but it is in general difficult to compare the injected composition to theoretical expectations, as many other effects can have an influence on it. For example, if the jet originates within a Wolf-Rayet star, significant contributions of helium, oxygen and carbon are expected. On the other hand, if the event is connected to a supernova, high levels of silicon or iron may be expected. Even heavier nuclei than iron could be produced by r-process nucleosynthesis (rapid neutron capture) in the jet, as for example studied in [225]. The approach presented in this section follows the opposite direction, *i.e.*, tracing back the observed UHECR composition to the acceleration zone and identify the injection and source properties needed in order to describe UHECR data.

4.4 Low-luminosity gamma-ray bursts

In this section, we assume that GRBs can be sub-divided into two distinct populations: Conventional or high-luminosity GRBs with luminosities $\geq 10^{49}$ erg s^{-1}, which were discussed above, and low-luminosity GRBs (LLGRBs) with luminosities $\leq 10^{49}$ erg s^{-1}. With a local event rate of about 300 Gpc^{-3} yr^{-1}, they are much more abundant than high-luminosity bursts (≈ 1 Gpc^{-3} yr^{-1}) [34, 35, 36, 37]. Hence, LLGRBs have been proposed as sources of cosmic rays and neutrinos [38, 22, 39, 40]. More recently, LLGRBs were studied in the context of UHECRs including models for the injection composition in the source [42]. As a consequence of the low luminosity, most nuclei can escape from the sources without interacting, leading to the chemical composition measured by the PAO after propagation [5]. On the other hand, if the nuclear cascade does not develop, neutrino production may be too weak to address the astrophysical diffuse flux at the same time in a one zone model.

Our study of conventional GRBs points already towards low luminosities to explain the non-observation of correlated events. The advantage of LLGRBs over their high-luminosity counterpart is that the neutrino stacking bounds do not apply due to their much lower luminosity, which limits the detection of resolved sources, and their much longer duration, leading to inefficient background suppression. Following this idea, we study if nuclear cascades can develop in LLGRBs and whether they can power the diffuse flux of neutrinos and cosmic rays at the same time, using similar methods as in Secs. 4.2 and 4.3. We show that the UHECR spectrum and composition can be described in an energy range across the ankle by controlling the sub-ankle component with the nuclear cascade, as mentioned in [27, 32, 159]. Our analysis is based on a combined source-propagation model starting with nuclear compositions reasonable to be found in jets of GRB progenitors [226, 42]. Our results were published in [216].

We assume the same acceleration zone as in the previous scenario, except for the injection of a mixed composition of 60% ^{16}O and 40% ^{28}Si in the jet. Typical Lorentz factors for LLGRBs are much lower than for conventional ones, *i.e.*, we fix $\Gamma \simeq 10$ in this case [227]. We vary the radius between 10^8 km and 10^{12} km, such that according to the internal shock model $R \simeq 2\Gamma^2 ct_v$ the variability time scale changes from 1 to 10000 seconds. Thus, the duration is of the order of 10^5 s, which is a bit longer than the durations typically observed ($10^3 - 10^4$ s). On the other hand, such long durations are expected from the view of progenitors for long GRBs, *e.g.*, blue supergiants or young stars [228, 229]. There may be also observational biases, as for example only the peak of the light curve may be observable [230]. Otherwise, if the duration is too short, the jet may not be able to break out and it is choked [231]. Such unsuccessful jets are not expected to emit UHECRs as the cooling in the environment is too strong, but they could possibly produce high energy neutrinos [232]. In the following, the chosen parameters are

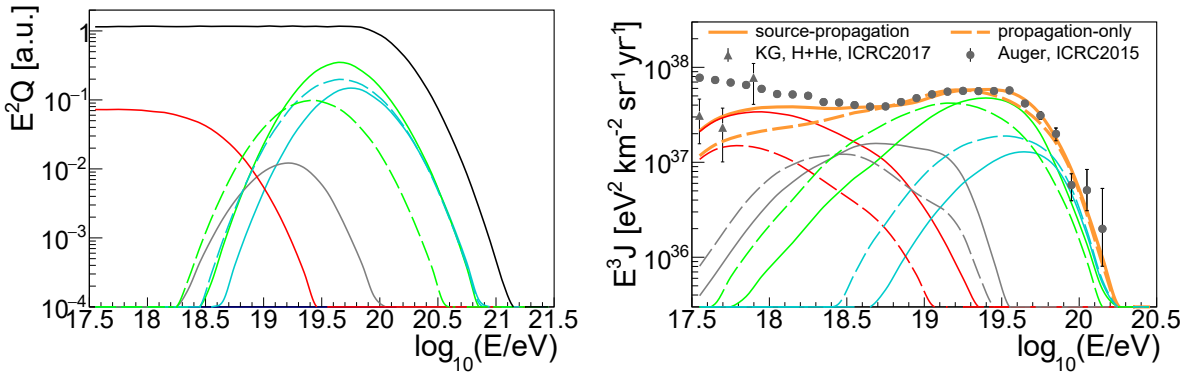

Figure 4.14: Difference of a combined source-propagation model (solid), which includes the nuclear cascade in the source, compared to a propagation-only model (dashed), computed with the same injection composition and parameters. In the left panel, the cosmic rays escaping from the source, multiplied by E^2 are shown. Dashed curves are the assumed escape spectra in the propagation-only model which are not explicitly computed: $A = 16$ (green) and $A = 28$ (cyan). The solid curves show groups of isotopes generated by the nuclear cascade: $A = 1$ (red), $2 \leq A \leq 4$ (gray), $5 \leq A \leq 24$ (green), $25 \leq A \leq 28$ (cyan), while the black curve represents the power law injection spectrum $\propto E^{-2} \exp(-E/E_{\rm max})$ (sum of 60% ^{16}O and 40% ^{28}Si). The right panel shows these fluxes multiplied with E^3 after propagation (same colors, orange: total) fitted to UHECR data from PAO [219]. Data points of KASCADE-Grande are shown for comparison [233]. Taken from [216].

consistent with jet formation and survival [227]. In contrast to the conventional GRBs, here we assume that only particles at the highest energies can escape, such that the ejected spectra are described by $\propto \exp[-\ln^2(E/E_{\rm max})]$, as derived in [182] and used in [23, 42]. The cosmological distribution of LLGRBs is assumed to follow the SFR as $(1+z)^m \times \mathcal{H}_{\rm SFR}(z)$ with $0 \leq m \leq 1$ [188].

The fit procedure is slightly adjusted with respect to the previous section, *i.e.*, we fit the UHECR spectrum [219] and composition [222] above the ankle. After that, we model the end of the sub-ankle component (which may be of Galactic origin) at lower energies as an additional power law. In the end, we re-fit the relative weights of the super- and sub-ankle components considering the energy range above 10^{18} eV. The additional power law is defined by a spectral index α and a normalization $f_{\rm gal}$ in terms of percentage of the total flux, determined at a fixed energy $E = 10^{17.5}$ eV. From the fit, we determine the baryonic loading ξ_A again, assuming $\dot{\tilde{n}}(z=0) = 300$ Gpc^{-3} yr^{-1}, consistent with [35].

In Fig. 4.14, we show a comparison between the propagation-only model corresponding to [42] (dashed curves), and the source-propagation model (solid curves), which includes the nuclear

cascade in the source. As a consequence, in the propagation-only model, it is argued that the nuclei survive, such that the escaping composition directly represents the injected composition. There is no secondary production and especially no production of nucleons, which is important for the extragalactic sub-ankle component. This is the reason why, for the same injection, in the source-propagation model also lighter mass groups are present in the left panel of the figure, as we allow not only for the survival but also for the interaction of nuclei. Note that the light component of the escaping spectra is softer compared to the other ones as it includes neutrons which are not magnetically confined. For comparing both computations, we first normalize the propagated fluxes and then show the spectra at the source with the proper normalization. Since for the propagation-only model, a depletion of nucleons is found due to the lack of interaction in the source, such a model could eventually require stronger source evolution in order to compensate for that. This can be fundamental for describing UHECR data, as also pointed out in [234, 27, 32]. Furthermore, the neutrino production in the source cannot be computed directly in a propagation-only scenario.

The classification of the parameter space in terms of the different nuclear cascade source classes is shown in the left panel of Fig. 4.15 as a function of the X-ray luminosity L_X and collision radius R for pure ^{28}Si injection. In the right panel, the result of the fit to cosmic ray data is shown. Similar to the cosmic ray fit for conventional GRBs, its contours follow the maximum energy, which is here about $10^{18.7}$ eV in the SRF. We superimpose the region where the source neutrino flux corresponds to the IceCube flux in the 1σ region [151], which shows that a moderate amount of disintegration is needed to account for the astrophysical flux as it coincides partially with the Populated Cascade. Our best fit point A, marked by a star, lies within the neutrino band, *i.e.*, it is possible to address UHECR data and the diffuse neutrino flux simultaneously. For comparison, we also show the point Z for the parameter combination which was studied in [42].

The results of the fit are illustrated in Fig. 4.16. With this parameter set it is possible to describe the UHECR spectrum and composition as well as the IceCube neutrinos at the same time. The shape of the neutrino spectrum does not fit exactly, but this could be an effect of limited statistics or additional components in the neutrino flux, for instance a Galactic component [154]. The fit yields a baryonic loading of about $\xi_A \sim 10$, which is a typical value found for GRBs in the literature [13]. It is considerably smaller than the baryonic loading obtained for high luminosity GRBs, however, it is degenerate with the duration and local rate of GRBs, meaning that there is room for interpretation depending on how well constrained the parameters are. Still, our best fit is consistent with current observations and constraints.

The effect of the radiation density in the source on the neutrino and cosmic ray spectra is shown in Fig. 4.17, where we show the fluxes of points A, B and C corresponding to Fig. 4.15.

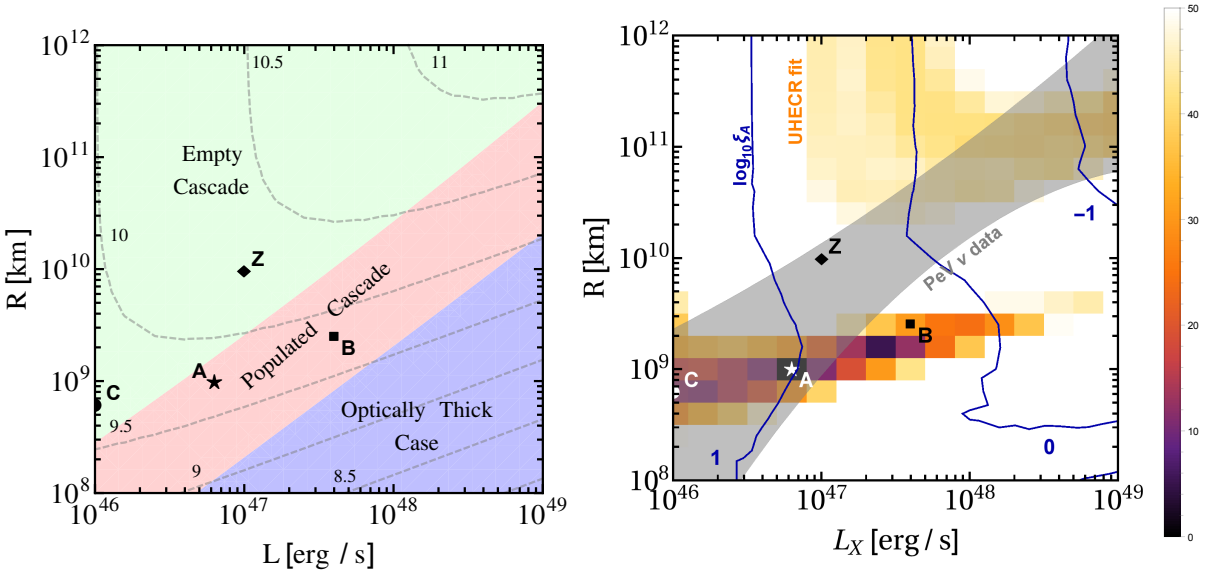

Figure 4.15: Parameter space scan as a function of X-ray luminosity L_X and collision radius R. The left panel shows the different regions in terms of development of the nuclear cascade as in Fig. 4.6 for pure silicon injection. The gray contours show the primary $\log_{10}(E_{\rm max}/{\rm GeV})$ in the SRF. The right panel shows the fit to UHECR data by the color scale representing $\chi^2 - \chi^2_{\rm min}$. PeV neutrino data is illustrated by the gray-shaded band, including the uncertainties of the flux. The blue contours indicate the baryonic loading $\log_{10}\xi_A$ obtained from the fit. In both panels, point A is the best fit point which we compare to fit results of [42] depicted by point Z. Points B and C show additional benchmarks discussed in the text. Taken from [216].

All these parameter sets are chosen to have about the same maximum energy, such that the cosmic ray spectra exhibit similar cut-offs at the highest energies. The best fit point A can be compared to an example with higher (point B, dotted) or lower (point C, dashed) radiation density. This serves as a good illustration how the nuclear cascade controls the prompt neutrinos and the sub-ankle component in the cosmic ray fit. Due to the enhanced radiation density in the source, the efficiency of photo-hadronic interactions is increased, producing a large flux of light elements, which is preserved even after propagation to Earth (left panel, red lines). The neutrinos produced in these interactions (right panel) are strictly related to the nuclear cascade. Combined source-propagation models break the degeneracy between different interpretations of cosmic ray data. Both, parameter set A and B, reproduce the cosmic ray spectrum above the ankle, but the corresponding neutrino fluxes are considerably different from each other. This discrimination power is, however, lost in cosmogenic neutrino fluxes, as the parameter sets chosen here have similar maximum energies.

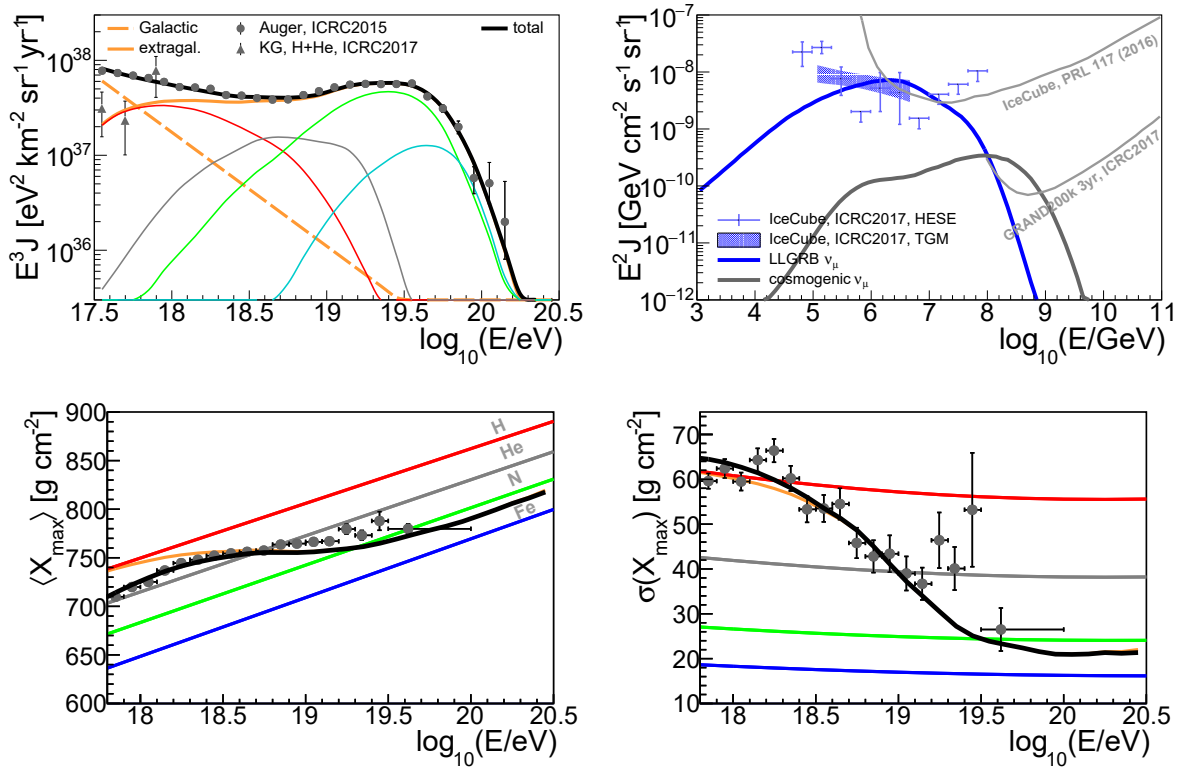

Figure 4.16: Cosmic ray spectrum (top left), neutrino spectrum (top right) and cosmic ray composition (bottom panels) as a function of the energy in the observer's frame, corresponding to the best fit point A in Fig. 4.15. The UHECR spectrum, multiplied by E^3, shows the same mass groups and data points as in Fig. 4.14. The dashed orange curve represents a sub-ankle component (possible of Galactic origin), while the solid orange curve depicts the (total) extragalactic component. The prompt and cosmogenic muon neutrino fluxes from LLGRBs are to be compared to the HESE and TGM data [235] and to the cosmogenic limits from IceCube [221] and GRAND [145], respectively. The lower panels show the predictions (extragalactic only: orange, sub-ankle and extragalactic: black) and data [222] of the first and second moment of the distribution of $X_{\max}$, assuming EPOS-LHC [115] as interaction model for UHECR-air interactions. Taken from [216].

The interpretation of the cosmic ray spectrum across the ankle is a controversial issue. As we have shown for conventional GRBs, it is in principle possible to reproduce the spectrum above EeV energies with only one population of sources. However, the observed composition cannot be described by models with a prevailing light component at low energies. The production of nucleons in the nuclear cascade on the other hand is a natural way to achieve a lighter composition at lower energies. Here, we argue that a fading Galactic cosmic ray population

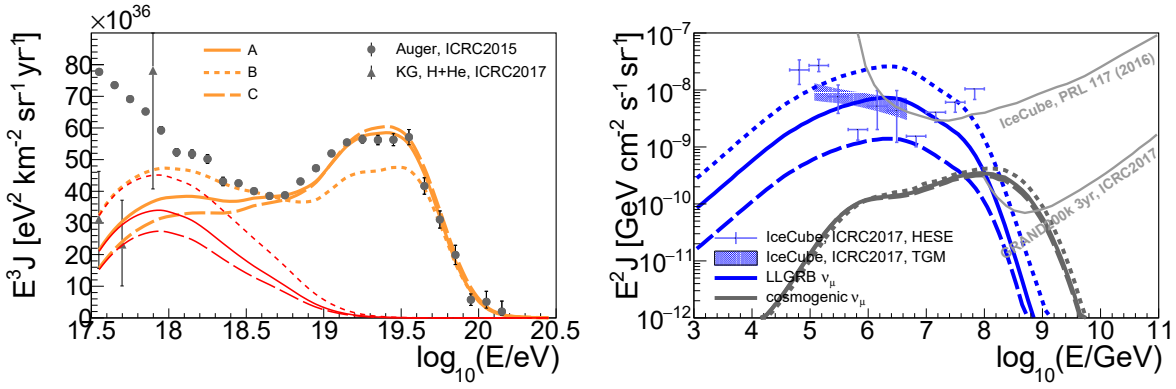

Figure 4.17: Cosmic ray (left, multiplied by E^3) and muon neutrino fluxes (right, multiplied by E^2) at Earth as a function of the energy in the observer's frame. In both panels, the fluxes are shown for points A, B and C in Fig. 4.15. While the maximum energy is similar, the difference between the points is the development of the nuclear cascade. In the left panel, the total cosmic ray flux (orange) is shown on a linear scale together with the nucleon component (red). Taken from [216].

can account for a fraction of the flux around $\sim$ EeV, similar to [234, 27, 32, 4]. With such a component, the spectrum can be described above EeV energies and the composition at these energies becomes heavier than in the case of protons only. If we fix the chemical composition of the Galactic component to silicon too, we find a spectral index of $\alpha = 4.2$ and the percentage of the flux at $10^{17.5}$ is about 78%. As already pointed out in [32], the slope and fraction of this component is also influenced by the redshift evolution. We choose $m = 1$ which is closer to the GRB source evolution in [189] than to the SFR, which corresponds to $m = 0$. For $m = 0$, the fit results are not qualitatively affected, but due to the lower flux of nucleons at $\sim$ EeV, a larger $f_{\rm gal}$ is needed. Furthermore, the cosmogenic neutrino flux would be lower by a factor ~ 2 if SFR was used. Vice versa, if $m > 1$, the percentage of the sub-ankle component would decrease, but the composition is getting too light since nucleons are dominating. Note that the source evolution for LLGRBs is yet unconstrained, however the evolution used in this work is consistent with the diffuse gamma-ray background [33].

In our study about LLGRBs, the cosmogenic neutrino flux is within reach of next generation neutrino telescopes such as GRAND [145]. As already pointed out in [29, 4, 236], there is an anti-correlation between the spectral index of the ejected cosmic rays and the value of m. The stronger the evolution, *i.e.*, the bigger the value of m, the more interactions will happen during propagation because far away sources dominate. This will break up nuclei such that it naturally softens the spectrum, which allows to have hard escape spectra at the source. If the direct escape mechanism was assumed ($\propto E^{-1}$), the source evolution would need to be

correspondingly weaker, *i.e.*, with local sources dominating. Thus, cosmogenic neutrinos can potentially discriminate between two sources which could both account for the UHECR and PeV neutrino data (see *e.g.* [237] for a study on the discrimination power of GRAND).

We tested that for the target photon spectrum we use in this work, gamma-rays even beyond PeV energies could be trapped due to annihilation processes (see App. B). In order to get a rough estimate for the detection potential of LLGRBs, we calculated the gamma-ray cascades from escaping EeV photons from π^0 decays. Since the density of neutral pions is not explicitly included in our source model, we made a rough approximation taking into account the spectrum of charged pions and the corresponding branching ratio. With this rough estimate, we find that indeed high energy gamma-rays can be expected in an energy range from MeV to TeV at Earth, which is for example suitable for CTA. However, further investigation is needed to determine whether the expected sensitivity above 10 GeV can be reached in CTA [238], as it depends on the low energy target photons, which are experimentally unconstrained.

The energy scale uncertainty of the cosmic ray measurements has not been taken into account here, *i.e.*, our model reproduces UHECR data even at the energy calibration face value. However, model parameters as the acceleration efficiency (here: $\eta = 1$) are degenerate with the energy shift, such that solid conclusions on these parameters cannot be obtained from this study. Moreover, we tested the impact of a luminosity distribution as it is defined in [35]. The results are very similar to Fig. 4.16, as our best fit is close to the peak of the distribution. Therefore, we do not explicitly take it into account here.

4.5 Multi-zone emission models for GRBs

In this section, instead of calculating $N = T_{90}/t_v$ identical internal shocks as in the static burst model above, we allow for the dynamical evolution of the burst. As the burst expands, collisions will occur at different radii, providing different shock parameters [239, 240]. Every shock is then computed as in the one zone model. In the end, the total ejected spectra are calculated as the sum of all individual collisions. As a consequence of the dependence on the radius, a GRB can for instance efficiently produce neutrinos (at low radii) and still eject a heavy composition (at large radii) at the same time. This model is based on [241] where it was introduced for protons only. In this work, I expanded it to treat the nuclear cascade as well up to iron. A significant amount of time was invested to cross-check the results with [23], which is a different approach using different assumptions, such that it required a high effort. However, we successfully cross-checked it to the level where we understand most of the differences. A project about fitting the injection composition in a combined source-propagation model using [242] is ongoing. Here, selected methods and results of our model are presented.

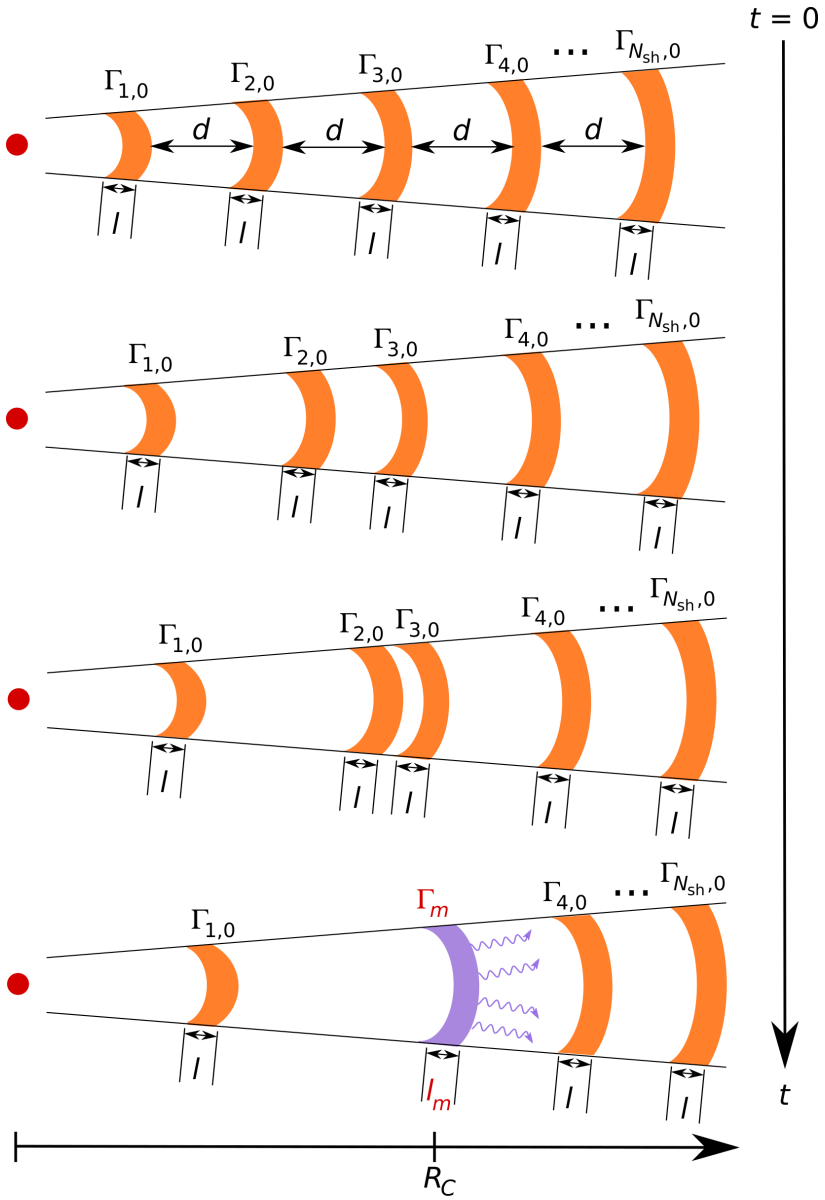

Figure 4.18: Time evolution of the dynamical GRB model. Initially (top), a number of $N_{\rm sh}$ shells of identical thickness l and varying Lorentz factor $\Gamma_{i,0}$ is separated by a distance d from each other. Due to the velocity differences, shells will collide as time progresses, creating a shock at a collision radius R_C (relative to the central emitter) where particle acceleration and interactions occur. The merged shell is reinjected into the system and may collide again. The simulation finishes either when all shells reach the circumburst medium or when they are ordered with increasing speed from inner to outer shells. Taken from [241].

The dynamical evolution of the burst is depicted in Fig. 4.18. In the beginning, the burst is initialised as $N_{\rm sh}$ shells with identical thickness l and different Lorentz factors $\Gamma_{i,0}$, which are separated from each other by a distance d. The first shell is placed at a radius $R_{\rm min}$ from the central emitter (*e.g.*, a collapsing star), which has little impact on the distribution of collision radii in the following, as they all travel outwards with an average Lorentz factor and collide much further than $R_{\rm min}$. As time progresses, fast shells will catch up with slow shells due to the difference in velocity, and eventually collide at a radius R_C. Internal shocks are formed as in the one zone model and they are computed in exactly the same way. The two colliding shells merge, their shell properties are re-calculated and the merged shell is re-injected in the system at the collision radius. Shells can collide multiple times and the simulation finishes when either all of them are ordered according to increasing velocity from inner to outer shells or all of them reach the circumburst medium, defined by $R_{\rm max}$, where external shocks start. Other collision models are possible too, *e.g.*, the shells do not merge but reflect from each other [243]. Such dynamics can be tested with this model, however the large amount of parameters complicate getting meaningful results. In the following, we treat the collisions as independent from each other, *i.e.*, ejected particles do not interact with other regions of the burst.

One of the most important components of this model is the initial Lorentz factor distribution. As long as it yields reasonable Lorentz factors $\Gamma \simeq 100 - 1000$ (for conventional GRBs), it is experimentally unconstrained. Especially the shape can have a large impact on the results, see *e.g.* [241] where different benchmarks are discussed. A frequently assumed distribution is

$$\Gamma(n) = \begin{cases} \left(\frac{\Gamma_{\rm max}}{2} + 50\right) - \left(\frac{\Gamma_{\rm max}}{2} + 50\right) \cos\left(\frac{\pi n}{0.4 N_{\rm sh}}\right) & n \leq 0.4 N_{\rm sh} \\ \Gamma_{\rm max} & \text{else} \end{cases} \tag{4.10}$$

used in [23] (with $\Gamma_{\rm max} = 600$), where n is the index of the current shell and which represents a disciplined engine emitting slow shells first and fast shells afterwards until a plateau is reached. We used the same distribution to compare the results to our model, however we were interested in how a stochastic engine influences the result. This is also motivated by the more realistic light curve obtained when a stochastic engine is assumed. In this case, the light curve clearly shows the expected time variability which is missing for disciplined engines. However, smooth light curves are also observed for some bursts. The distribution of initial Lorentz factors we use is shown in Fig. 4.19, where we inject the typical number of 1000 shells in the system. Since the stochasticity term influences the distribution of collisions, we reduced the maximum Lorentz factor $\Gamma_{\rm max} = 400$ in order to get a comparable average collision radius. On top of Eq. (4.10), we add a stochastic term which draws from a log-normal distribution with an exponent $a_\Gamma = 0.1$ controlling the amplitude.

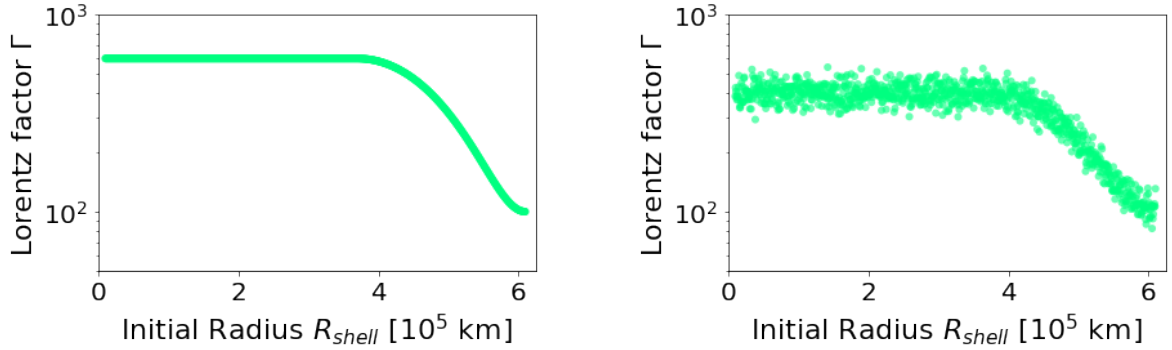

Figure 4.19: Initial Lorentz factor distribution as a function of the distance from the central emitter. Each dot represents one shell at a certain radius and its corresponding Lorentz factor. The left panel corresponds to the distribution in Eq. (4.10), while in the right panel, we added a stochastic term (log-normal distribution with exponent $a_\Gamma = 0.1$) to the disciplined engine.

The energy content of the burst is controlled by the initial bulk kinetic $E_{\mathrm{kin},k}$ energy. Together with the Lorentz factor distribution, a mass

$$m_k = \frac{E_{\mathrm{kin},k}}{\Gamma_k c^2} \tag{4.11}$$

is assigned to each shell. Another possible scenario is that the mass is equally distributed to the shells, *i.e.*, the initial bulk kinetic energy is different for all shells. In order to obtain the radiation density for the nuclear interactions out of the collision model, we define the mass density of a shell

$$\rho_k = m_k / V_{\mathrm{iso},k} \quad \text{with} \quad V_{\mathrm{iso},k} = 4\pi r_k^2 l \quad , \tag{4.12}$$

which we will need in the following. In the case of a collision of a fast (f) shell with a slow (s) shell, the dissipated energy

$$E_{\mathrm{diss}} = (\Gamma_f - \Gamma_m) m_f c^2 + (\Gamma_s - \Gamma_m) m_s c^2 \tag{4.13}$$

is equal to the difference in kinetic energy before and after the collision. In this formula, the Lorentz factor of the merged shell is calculated as

$$\Gamma_m \simeq \sqrt{\frac{\Gamma_f m_f + \Gamma_s m_s}{m_f/\Gamma_f + m_s/\Gamma_s}} \quad . \tag{4.14}$$

The merged shell is assumed to instantly cool by prompt emission of its internal energy given

by Eq. (4.13). The width of the merged shell is calculated as

$$l_m \simeq l_s \frac{\beta_{\rm fs} - \beta_m}{\beta_{\rm fs} - \beta_s} + l_f \frac{\beta_m - \beta_{\rm rs}}{\beta_f - \beta_{\rm rs}} \quad , \tag{4.15}$$

where $\beta_{\rm fs/rs} = \sqrt{1 - \Gamma_{\rm fs/rs}^{-2}}$ is the speed of the forward / reverse shock with Lorentz factors

$$\Gamma_{\rm fs/rs} = \Gamma_m \sqrt{\frac{1 + 2\Gamma_m/\Gamma_{s/f}}{2 + \Gamma_m/\Gamma_{s/f}}} \quad . \tag{4.16}$$

In order to calculate the mass of the merged shell, we assume that the merged shell obtains the average density

$$\rho_m \simeq \frac{l_s \rho_s + l_f \rho_f}{l_m} \quad . \tag{4.17}$$

Thus, we get the mass and, with that, the kinetic energy of the merged shell according to

$$m_m = \frac{E_{{\rm kin},m}}{\Gamma_m^2 c^2} = V_{{\rm iso},m} \rho_m \quad \text{with} \quad V_{{\rm iso},m} = 4\pi R_C^2 l_m \quad . \tag{4.18}$$

The energy densities will be provided to *Neucosma* to calculate the nuclear interactions of each collision, assuming a static broken power law target photon field and accelerated particles from diffusive shock acceleration as in the one-zone approach, until the evolution of the burst is finished. The complexity of the system now scales with the injected mass number due to the nuclear cascade, such that a whole burst will take about 8 hours[3] to compute for iron injection (for protons it is significantly faster and the results of [241] have been reproduced as a cross-check). These methods are different from the ones used in [23], where the burst is for example parameterized in terms of a total wind luminosity $L_{\rm wind}$, resembling rather one propagating shock than many shell collisions. If accounting for the different collision model and other differences, as the acceleration model, the target photons or using the length scale of the turbulence for particle escape from the shock for example, it is possible to get comparable results with our model. However, in the following we focus on more general, qualitative results to show the potential of the model.

The optical thickness $\tau_{p\gamma}$ to photo-hadronic interactions and the maximum energy $E_{\rm max}$, both for protons, are depicted in Fig. 4.20 for all collisions in the burst assuming a stochastic engine. According to the plot, about 500 collisions are optically thick to photo-hadronic interactions of protons, *i.e.*, represent the Optically Thick Case (red dots), while the other 500 correspond to the Empty and Populated Cascade scenario (blue cirlces), where protons can escape. A

[3]The computation time is a rough value obtained on a single Intel(R) Core(TM) i5-6500T CPU @ 2.50GHz.

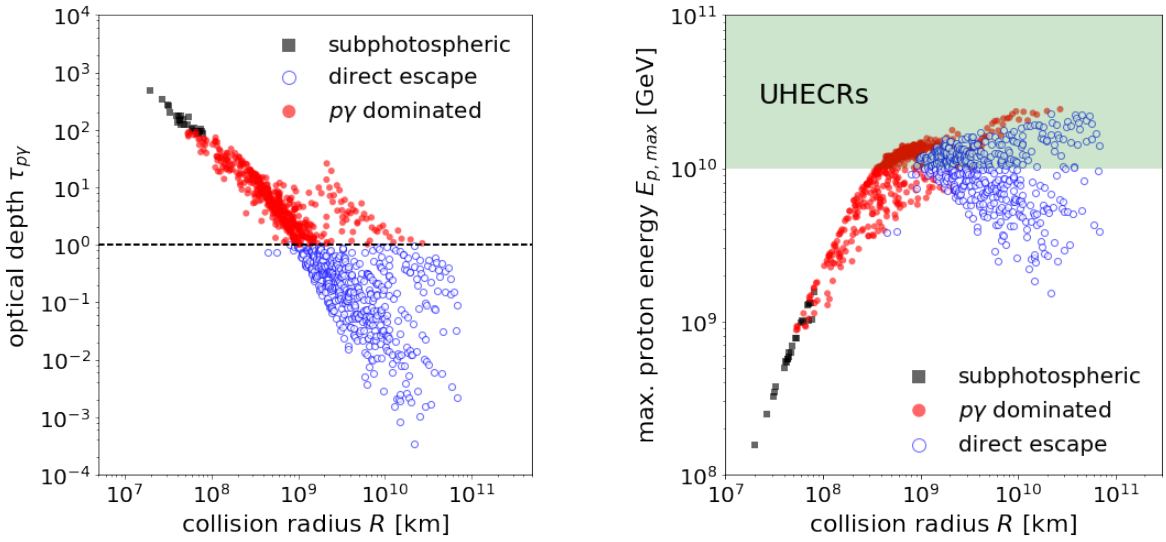

Figure 4.20: Optical depth to photo-hadronic interactions (left) and maximum energy in the observer's frame (right) for protons as a function of the collision radius R. In both panels, sub-photospheric collisions are marked by black squares, while red dots represent collisions dominated by $p\gamma$ interactions and blue circles indicate the escape-limited case. In the left panel, the transition from opaque to transparent is depicted by the black dashed line at $\tau_{p\gamma} = 1$. On the right hand side, the green region shows the UHECR regime with energies $> 10^{19}$ eV. Note that the maximum energie for nuclei can be higher.

small amount of collision in this example is sub-photospheric (black squares), *i.e.*, the collision radius is smaller than the photospheric radius (see App. B). When summing over all collisions, sub-photospheric collisions are typically not taken into account, since our model is not valid to account for the photon fields below the photosphere. For nuclei, a similar graph can be produced, where the optical depth would shift by the mass number A of the desired nucleus. In general, collisions become more transparent with increasing radius as the radiation density drops with $\propto R^{-2}$. Note that in the multi-zone picture, the radius and the thickness are not related to each other anymore.

A closer look on the distribution of the points in the scatter plot reveals two components: For the first component, collisions become optically thin at a radius of $\sim 2 \cdot 10^9$ km, while the second component shows $p\gamma$ dominated collisions even above this radius up to $\sim 3 \cdot 10^{10}$ km. Such features are often related to the details of the initial Lorentz factor distribution. In this case, the first component could represent collisions of shells which are initially close to each other, *i.e.*, collide with neighboring shells. These collisions would happen early in the burst evolution, meaning already at low radii, where the radiation density is large. Collisions

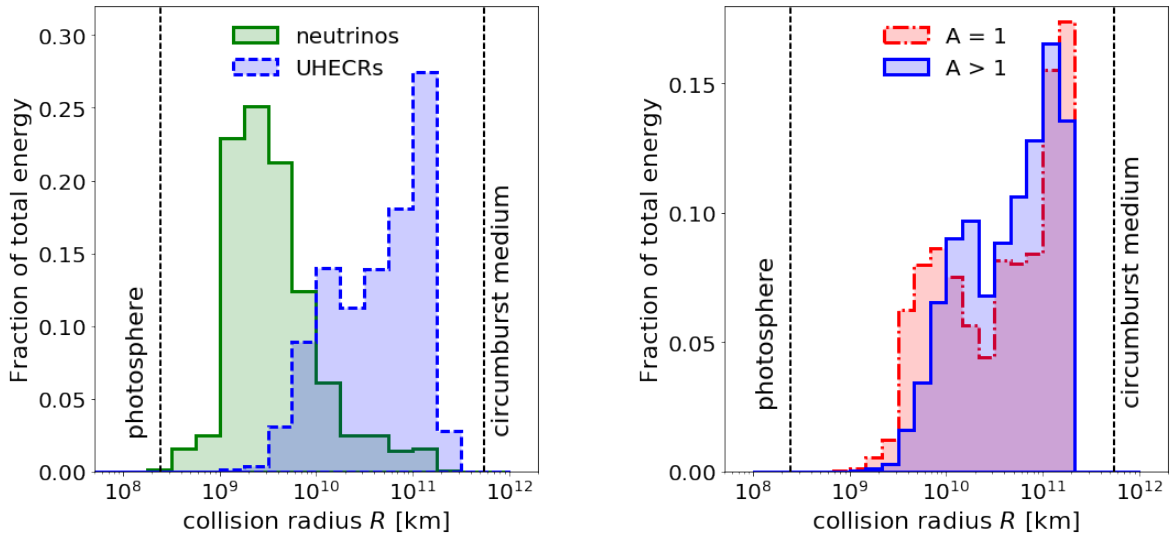

Figure 4.21: Energy output per particle type (left) and per mass group (right), both normalized to the respective total energy, as a function of the distance from the central emitter. Here, the photosphere is defined as the minimum radius of super-photospheric collisions, while the circumburst medium is placed at the maximum radius.

from the second component happen further outside, which may correspond to shells which are initially far separated and catch up with each other late in the evolution (probably after several other collisions), but still have a high difference in Lorentz factor due to the behaviour of the engine. Although the densities dropped already, high shock Lorentz factors can lead to efficient photo-hadronic interactions.

In general, the maximum energy is the largest at intermediate radii, where the acceleration is not limited by strong energy losses and the magnetic field (which also scales with the density) is still strong enough to accelerate the particles to high energies. For nuclei, the maximum energy will be higher as what is shown in the figure by up to a factor corresponding to the charge number Z (in the adiabatically limited case). Here, the second component is also visible at the largest radii, where protons still reach ultra-high energies, while the maximum energy of the first component falls below 10^{19} eV again.

The energy output of the burst can now also be spatially resolved and even decomposed in different particle types and mass groups, as shown in Fig. 4.21. In the left panel, the energy output of neutrinos and UHECRs is shown, both normalized to the total energy in neutrinos and UHECRs, respectively. Neutrinos are typically produced at low radii in collisions close to the photosphere. On the other hand, cosmic rays at ultra-high energies with the right composition are produced more in outer collisions where the maximum energy is high and nuclei can at least

partially survive. Because of this spatial separation of neutrino and cosmic ray production, the collision model (including the engine behaviour) gives a direct handle on controlling the fluxes: A strong engine with a long downtime for example will emit shells with high Lorentz factors but large separation. If it is rather disciplined than stochastic, the relative Lorentz factor will be small such that most of the collisions will happen far outside, producing mostly cosmic rays and few neutrinos. On the other hand, a stochastic engine with low downtime will lead to many early collisions, such that many neutrinos will be produced and fewer cosmic rays.

A similar train of thought in general applies to the energy output per mass group, shown in the right panel, where the nucleon component and the heavy component are both normalized to their respective total energy again. However, the difference is not as drastic and the transition from light to heavy emission is more continuous over radius. In this particular example, a mixed composition is injected, carrying also a significant fraction of protons. This leads to an overlap of both components also at high radii. The total dissipated energy is usually less than 15% of the kinetic energy of the shocks for this collision model. Note that for the sake of better illustration, a different simulation has been chosen to plot these histograms with respect to Fig. 4.20, *i.e.*, the radii are not directly comparable. The picture changes with a different collision model and Lorentz factor distribution, however in most cases the picture is similar. Gamma-rays can also be included in this picture, but they are not explicitly calculated in nuclear interactions.

The total ejected cosmic ray spectrum is shown in Fig. 4.22 along with the contribution of different mass groups (thick curves). For neutrons, protons and the group $Z = 21 - 26$, the contribution of all individual collisions is plotted too (thin curves). Due to summing over spectra with different maximum energies and normalizations, the total spectrum per mass group can have a different shape from the single collision ejection spectra. This leads, for example, to a softening of the summed spectrum with respect to the escape-limited scenario, where only particles at the maximum energy can escape. The neutron spectra is significantly softer because they can escape freely as they are not coupled to the plasma. The relative normalization of the different mass groups to each other depends on the nuclear cascade in the individual collisions, but largely also on the injected composition in the source. Currently, the composition is fixed and identical for all shells. A merged shell does not change its composition, since the bulk mass is only slightly affected by the radiation processes. However, also other scenarios are possible, *e.g.*, distributing the composition depending on the radius, which could be motivated by the onion structure of stars. Once they collapse, the outer material could be ejected first, leading to an increasingly heavy composition for shells closer to the engine. For an ongoing study, we take advantage of the fact that the burst scales with the injection composition in a linear way. This means that we compute bursts with pure injection composition and then fit superpositions of these compositions, *i.e.* an effective mixed composition, in order to describe cosmic ray data for

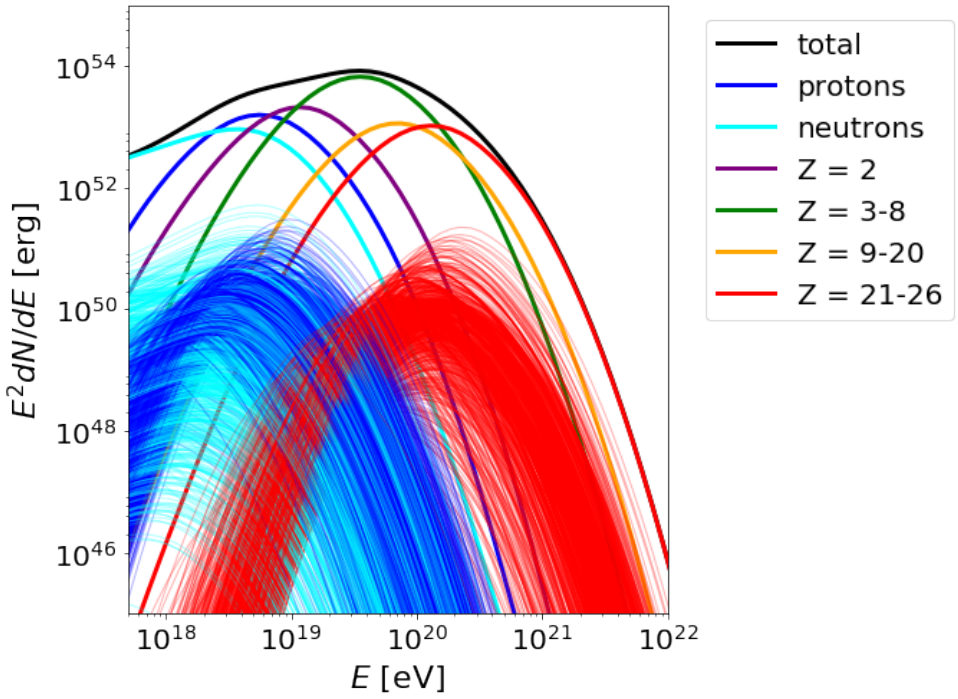

Figure 4.22: Total ejected energy from the source (black) split up to show the contribution of different isotope groups (thick curves) as a function of the energy in the observer's frame. The thin curves for neutrons, protons and the group $Z = 21 - 16$ illustrate the contribution of individual collisions (not shown for other groups).

every point in parameter space. With this strategy, instead of trying all possible compositions for one parameter set, we simply fit 6 independent components to obtain a better description of cosmic ray data and constrain the composition of the source and not only the composition at the ejection.

Chapter 5

Tidal disruption events as UHECR and neutrino sources

Traditional candidates for UHECR and neutrino emission like GRBs but also AGNs are disfavored to be the dominant source of the diffuse flux of IceCube neutrinos by stacking analyses [18, 155], which challenge also the paradigm that they are the sources of UHECRs. This has stimulated research on alternative origins [244, 245] with tidal disruption events (TDEs) being one such alternative scenario. Tidal disruption events are processes in which a star is torn apart by the strong gravitational force of a black hole, which is illustrated in Fig. 5.1. A typical assumption is that half of the star's debris is accreted onto the black hole, forming an accretion disk. If the mass accretion rate is high, a relativistic jet can form [43, 45, 44, 246], which potentially can accelerate baryons to ultra-high energies [46, 47] with neutrinos as a by-product [56, 49].

In this chapter, we will introduce the physics along with the observations and a population model of tidal disruption events in Sec. 5.1. After that, we will apply our methods to this class of sources, such that we can identify nuclear cascades in TDEs in Sec. 5.2. We present a joint description of neutrino and cosmic ray data at the highest energies, based on our paper [248]. For this project, I implemented a tidal disruption source model and performed the parameter space scan and classification similar to our previous works. Further I contributed with a study of the injection composition and considerations about two-photon annihilations, as presented in App. B in more detail. Lastly, we discuss the model in the context of neutrino multiplet constraints.

5.1 Physics of tidal disruption events

The basic principles of tidal disruption of stars by SMBHs were first discussed in the 1970s and 1980s [43, 45, 44, 246], whereas this description follows [59]. As the star approaches the SMBH, it can be deformed and eventually destroyed by tidal forces. This happens at a distance r_t from the black hole called the tidal radius, where the force on a mass element inside the star due to self-gravity is equal to the gravitational force of the black hole on the same mass element. If the

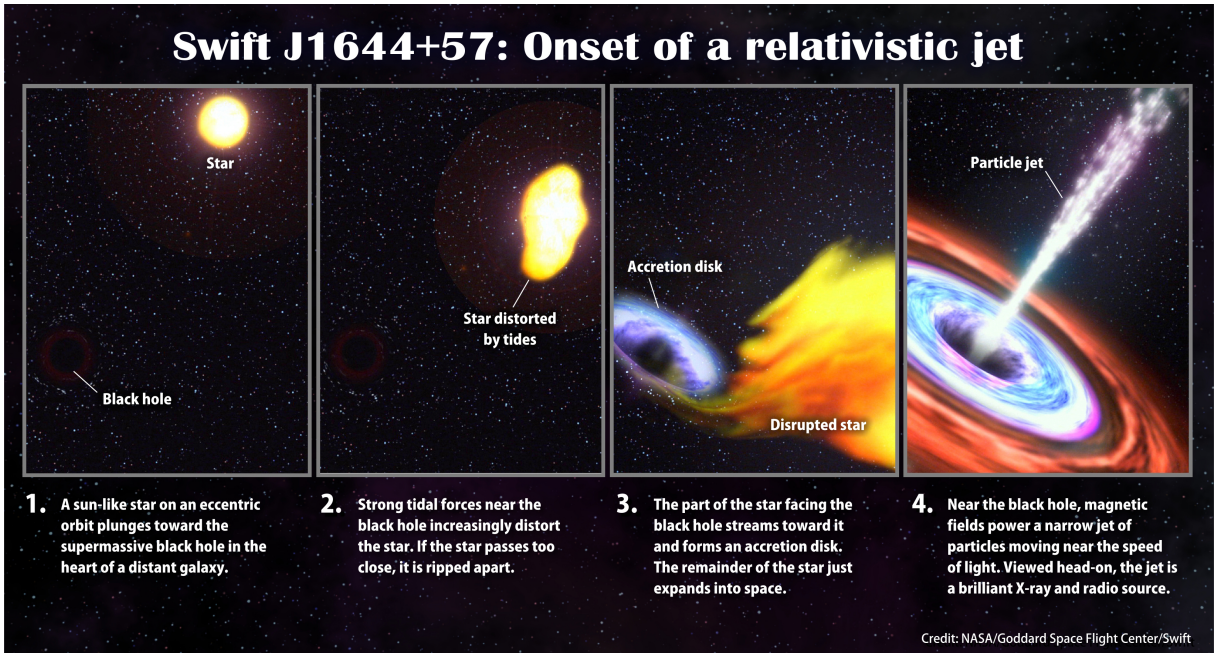

Figure 5.1: Schematic illustration of a tidal disruption event. A star approaching a black hole begins to feel its gravitational force and is tidally distorted. If it gets too close, it is ripped apart and a fraction ($\sim 50\%$) of the stellar material is accreted by the black hole. In some cases ($\sim 10\%$), a relativistic jet is launched. Taken from [247].

star is of mass m and radius R and M denotes the mass of the SMBH, the tidal radius is given by

$$r_t = \left(\frac{2M}{m}\right)^{1/3} R \simeq 8.8 \times 10^{12}\mathrm{cm} \left(\frac{M}{10^6 M_\odot}\right)^{1/3} \frac{R}{R_\odot} \left(\frac{m}{M_\odot}\right)^{1/3} \quad . \tag{5.1}$$

The corresponding orbital period τ_t at the tidal radius is determined via

$$\tau_t = 2\pi \left(\frac{r_t^3}{2MG}\right)^{1/2} \simeq 10^4\mathrm{s} \left(\frac{R}{R_\odot}\right)^{3/2} \left(\frac{m}{M_\odot}\right)^{-1/2} \quad . \tag{5.2}$$

These quantities can be compared to the Schwarzschild radius

$$R_s = \frac{2MG}{c^2} \simeq 3 \times 10^{11}\mathrm{cm} \left(\frac{M}{10^6 M_\odot}\right) \tag{5.3}$$

of the SMBH and the corresponding time scale

$$\tau_s \sim 2\pi R_s/c \simeq 63\mathrm{s} \left(\frac{M}{10^6 M_\odot}\right) \quad . \tag{5.4}$$

Here, τ_s is a good approximation of the orbital period at the innermost stable circular orbit (ISCO), which is the smallest stable circular orbit in which a particle can orbit a massive object [249]. In black hole accretion disks, this marks the inner edge of the disk. Comparing Schwarzschild radius and tidal radius shows that the star can be swallowed as a whole if $M \gtrsim 10^8 M_\odot$. In this case, no prior disruption occurs. However, we will choose a smaller value of M in the following, *i.e.*, the star will be disrupted and about $\sim 1/2$ of the stellar mass is accreted onto the black hole [45]. Therefore, the maximum energy released in this event is

$$E_{\max} \sim M_\odot c^2/2 \cdot (R_s/R) \simeq \begin{cases} 10^{54}\text{erg} & \text{for } R = R_s \\ 10^{52}\text{erg} & \text{for } R = r_t \end{cases} \tag{5.5}$$

as a rough ball-park scale, assuming that the change in the internal energy of the SMBH is negligible. The infall of the tightest bound debris takes $\mathcal{O}(10)$ days, during which the event is initially dark. Thereafter, rapid accretion of matter on the SMBH begins. Depending on the dynamics of the stellar debris, a flare with super-Eddington luminosity[1] that declines with time as $t^{-5/3}$ can be generated if the mass infall rate is sufficiently high [250, 251]. When the infall rate drops below the Eddington rate, the flare vanishes rapidly after a time $\Delta T \sim \mathcal{O}(0.1 - 1)$ yr.

5.1.1 Swift J1644+57: best observed jetted TDE

If a relativistic jet is launched, highly super-Eddington flares are expected. So far, three jet-hosting ("jetted") TDEs have been identified of which Swift J1644+57 is best observed [50, 51, 52]. Swift J1644+57, which is believed to be a SMBH activated by the tidal disruption of a passing star, was discovered on March 28 in 2011 at a distance of 1.2 Gpc. The X-ray flare had an isotropic equivalent luminosity $L_X \simeq 10^{47.5}$ erg s^{-1}, which is well beyond the Eddington luminosity of 10^{44} erg s^{-1}. This requires a strongly anisotropic radiation pattern, *i.e.*, a relativistic jet pointed towards Earth. The total energy in X-rays of this event was $E_X = 10^{53.5}$ erg over $\Delta T = 10^6$ s. The energy E_X is therefore well below the maximum energy in Eq. (5.5), which still needs to be corrected by the beaming factor $2\Gamma^2$. The observed spectral energy distribution can be described by a broken power law with indices $\alpha = 2/3$ and $\beta = 2$ with a break at 1 keV. The light curve shows a minimum variability time of 100 s and the Lorentz factor was deduced to be ~ 10 [50]. This particular event will serve as a motivation for the parameters chosen for our model in the following. The parameters of Swift J1644+57 are considered typical and are similar to other observations of jetted TDEs, such as Swift J2058.4+0516 [51].

[1] The Eddington luminosity is the maximum luminosity a star can achieve while an equilibrium between the radiative pressure acting outwards and the gravitational force acting inwards is maintained.

The observations are consistent with a supermassive black hole (SMBH, $M > 10^5 M_\odot$) disrupting a main sequence star [53]. Another viable explanation of current data is the disruption of smaller and denser stars, such as white dwarfs (WDs) by intermediate mass black holes (IMBH, $10^3 M_\odot > M > 10^5 M_\odot$) [54, 55]. The latter case has the advantage to motivate the presence of intermediate mass isotopes, which is suitable for the fit of the cosmic ray composition. ONeMg white dwarfs have been considered originating from past supernovae or explosive nuclear burning [60]. Another class of progenitors are carbon-oxygen white dwarfs (CO-WD), which we will use in the following as a motivation to inject pure nitrogen in the jet. This choice is further motivated by the observation of nitrogen emission lines in TDEs. Other scenarios are possible as well, *e.g.*, tidal forces triggering the burning of elements which would normally not happen due to the mass of the star [54].

Recently, TDEs have been considered as sources of astrophysical neutrinos [56, 57, 58, 59] and UHECRs [60, 61]. Notably, it has been considered that the mixed nuclear composition of UHECRs observed at the PAO can be provided by TDEs if the disrupted stars have intermediate to heavy nuclear compositions [54, 60, 5]. However, a consistent study of the joint production of neutrinos and cosmic rays in TDEs has not been performed before. It was discussed that the internal shock scenario faces the difficulty of nuclei disintegrating in the jet in this case, leading to neutrino and secondary production in the nuclear cascade [60]. In order to circumvent these difficulties, it has been assumed that UHECRs originate from regions with low radiation densities where interactions are negligible, *i.e.*, the nuclear cascade does not develop.

Since we are able to calculate the nuclear cascade including all relevant cooling and interaction processes in the source, we present the first consistent calculation of UHECR and neutrino production in TDE jets in the internal shock model, based on our paper [248]. In the following, we will demonstrate that TDEs can power both, the UHECR and astrophysical PeV neutrino flux, if an appropriate nuclear injection composition is assumed.

5.1.2 The population of jetted tidal disruption events

The cosmological distribution of TDEs $\dot{\rho}(z, M)$ is the product of the black hole mass function $\phi(z, M)$, defined as the number of black holes per unit mass and per comoving volume at redshift z, the rate of TDEs per black hole $\dot{N}_{\rm TDE}$ and the so-called occupation fraction $f_{\rm occ}(M)$, which represents the probability of a black hole being located at the center of a host galaxy [59]:

$$\dot{\rho}(z, M) = \dot{N}_{\rm TDE} f_{\rm occ}(M) \phi(z, M) \quad . \tag{5.6}$$

The black hole mass function is calculated in [252, 253] for $M \geq 10^5 M_\odot$, where it is found that it declines with z roughly as $(1 + z)^{-3}$ and scales with mass as $M^{-3/2}$ for all z between

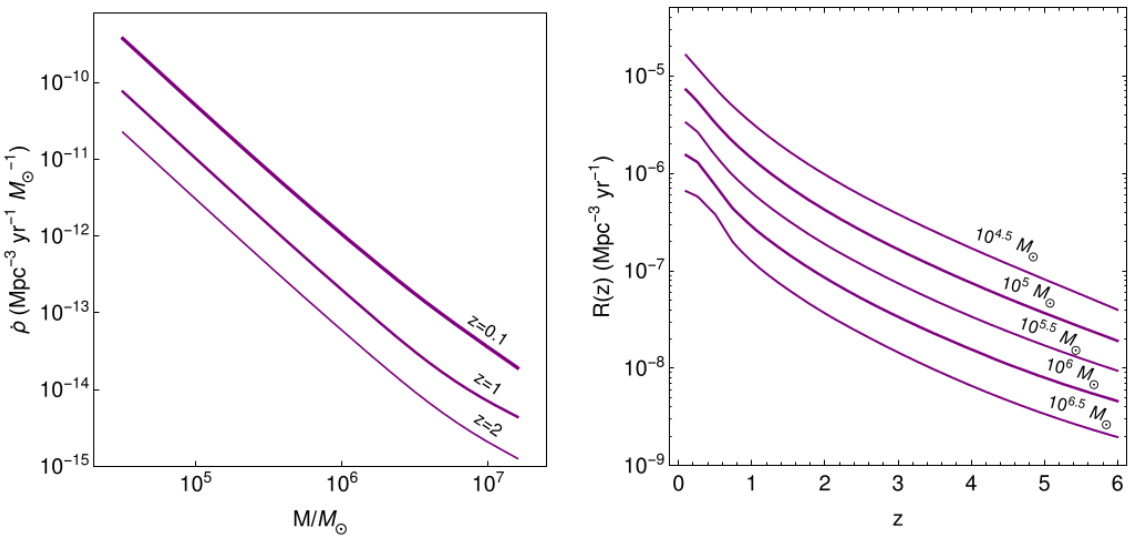

Figure 5.2: Differential rate $\dot{\rho}(z, M)$ of TDEs (left, jetted and non-jetted) as a function of the black hole mass for selected values of z and total volumetric rate $R(z)$ of TDEs as a function of redshift for different values of $M_{\rm min}$. Taken from [59].

$10^5 M_\odot \lesssim M \lesssim 10^{7.5} M_\odot$. Compared to GRBs, the source evolution is negative, *i.e.*, close sources dominate, which will have a significant impact on the secondary production during propagation. The occupation fraction $f_{\rm occ}(M)$ is represented approximately by a step function, *i.e.*, $f_{\rm occ} = 0$ ($f_{\rm occ} = 1$) below (above) a minimum black hole mass $M_{\rm min}$. This takes into account that low mass SMBHs are likely to be ejected from their host galaxies, thus not triggering any TDEs [254, 255]. Per black hole, the rate of TDEs decreases weakly with increasing mass as $\dot{N}_{\rm TDE} \simeq 10^{-3.7} (M/10^6 M_\odot)^{-0.1}$ yr^{-1}, which is close to the upper limit obtained by ASAS-SN data [256].

The differential TDE rate $\dot{\rho}(z, M)$ and the total rate $R(z) = \int_{M_{\rm min}}^{M_{\rm max}} \dot{\rho}(z, M) dM$ are shown in Fig. 5.2. The dependence of the differential rate on the mass is about $\dot{\rho}(z, M) \propto M^{-1.6}$ in the left panel and the total rate is dominated by the lowest $M_{\rm min}$, decreasing by a factor ~ 4 when $M_{\rm min}$ is increased by a factor 10. In order to obtain the effective rate of observable jetted TDEs, the beaming factor $1/(2\Gamma^2)$ and the fraction η of TDEs producing a jet has to be taken into account, *i.e.*, $\tilde{R} = R\eta/(2\Gamma^2)$. Typical assumptions are $\Gamma \simeq 10$ and that about 10% of all TDEs launch a relativistic jet [50], leading to observable jetted TDE rates $\tilde{R}(0) \simeq 0.1 - 10$ Gpc^{-3} yr^{-1} depending on $M_{\rm min}$.

The expected local rate for jetted TDEs can be compared to constraints from IceCube data [257, 258, 259]. Rare but powerful transients with a rate $\tilde{R}(0) < 10$ Gpc^{-3} yr^{-1} can be excluded if they are the dominant contribution to the observed astrophysical neutrino flux. This constraint

however applies only to short transients like GRBs, and relaxes for longer lived sources like TDEs. Nevertheless, it indicates that the neutrino flux from TDEs must be dominated by the low mass part of the black hole mass function to avoid these constraints. Next generation neutrino telescopes which are able to identify dim but frequent sources could place a bound as strong as $\tilde{R}(0) < 10^3$ Gpc^{-3} yr^{-1} [141], meaning that the TDE scenario is clearly testable. We stress that the model we present in the following is consistent with current data, as we will discuss in Sec. 5.2.2.

5.2 Identification of nuclear cascades in TDEs

The model is based on parameters that are consistent with the Swift J1644+57 observation and based on *Neucosma* [159] to calculate the nuclear interactions in the jet as in Chapter 4. We assume direct escape of cosmic rays from the sources, which then propagate through extragalactic space that is simulated with *SimProp* [184]. Again, we assume that all TDEs are identical in the cosmologically co-moving frame and that they evolve negatively with redshift, *i.e.*, $\propto (1+z)^{-3}$, following mainly the black hole mass function [253]. Finally, we fit the UHECR spectrum and composition data beyond 10^{19} eV in order to assess the compatibility with observations. The energy scale is shifted by 20% to account for uncertainties of the PAO experiment [260]. The energy shift is treated as systematics and is degenerate with the acceleration efficiency η, which is set to 1 in the following, and the nuclear injection composition (as higher Z reach higher maximum energies). The fit is performed by using a maximum likelihood method with three fit parameters as before: the production radius R, the X-ray luminosity L_X and a normalization parameter G. The latter, defined as

$$G = \xi_A \times \frac{\tilde{R}(0)}{0.1\mathrm{Gpc}^{-3}\mathrm{yr}^{-1}} \quad , \tag{5.7}$$

takes into account the degeneracy between the baryonic loading ξ_A and the local apparent rate $\tilde{R}(0)$ of jetted TDEs. The value of the local apparent jetted TDE rate is the rate of WD-IMBH disruptions inferred from observations, $\tilde{R}(0) \sim 0.01 - 0.1$ Gpc^{-3} yr^{-1}, which is in agreement with theoretical arguments [55, 58, 60]. Note that the rate is lower with respect to Sec. 5.1.2 as different black hole masses are relevant here.

The results of the fit in the parameter space are shown Fig. 5.3. In the left panel, the filled contours represent the confidence level for the fit to cosmic ray data as a function of L_X and R after marginalizing over G. The region where the predicted neutrino flux addresses the two PeV data points in IceCube within 1σ is superimposed as a gray band. The blue curves show the isocontours of $\log_{10} G$. As in the case for LLGRBs, we find again that the region of the cosmic

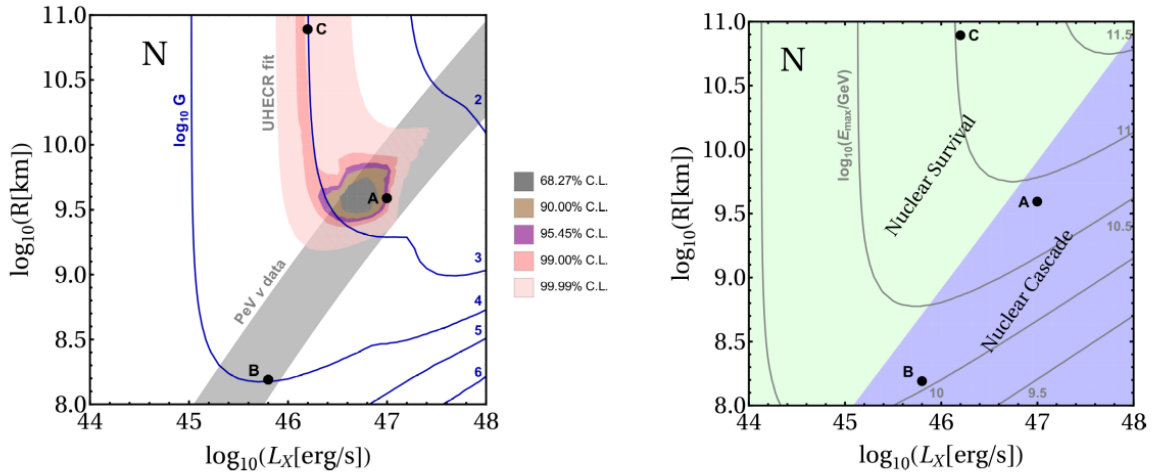

Figure 5.3: Parameter space of the cosmic ray fit (left panel) and the nuclear cascade (right panel) as a function of luminosity L_X and radius R. The UHECR fit results are shown as shaded contours (C.L. as indicated by the legend) and the region to simultaneously describe neutrino data is represented by the gray band, which corresponds to the 1σ region of the data. The blue curves show isocontours of $\log_{10} G$ obtained from the fit, including an energy shift of -20% to account for the uncertainty of the energy scale. For the nuclear cascade, only the nuclear survival (Empty Cascade) and nuclear cascade (Populated Cascade and Optically Thick Case) are shown (shaded regions). The black curves show the maximum energy $\log_{10}(E_{\max}/\mathrm{GeV})$ in the observer's frame. Point A is the best fit, point B and C are marked for comparison (not shown here, see [248] for details). Taken from [248].

ray fit and description of PeV neutrino data overlap, meaning that a simultaneous description of both of them is possible. This is indicated by point A, while point B and point C correspond to the individual neutrino and cosmic ray best fit, respectively. In the right panel, the different regimes of the nuclear cascade are shown, where we distinguish only between nuclear survival (Empty Cascade) and nuclear cascade (Populated Cascade and Optically Thick Case). The maximum energy of the cosmic rays in the observer's frame is shown by the black contours. The C.L. of the cosmic ray fit follow the maximum energy at around $E_{\max} \simeq 10^{10.8}$ GeV, which indeed reproduces the ultra-high energy range of observed cosmic rays at Earth. As a certain amount of disintegration is required to produce neutrinos, the PeV neutrino data band coincides with the nuclear cascade region. At point C, the UHECR spectrum and composition can be well reproduced, but neutrino production is inefficient due to low radiation densities, resulting in a too low neutrino flux. In turn, at point B, neutrino production is efficient but the maximum energy of the cosmic rays is too low in order to describe the ultra-high energy range.

For the best fit point A, the value of the normalization is $G \simeq 540$, which can be interpreted as WD disruptions with a local rate of $\tilde{R}(0) \simeq 0.1$ Gpc^{-3} yr^{-1} and a baryonic loading of $\xi_A \sim 500$. As a sanity check, it can be calculated that for a WD with $m \sim M_\odot$ and $\Gamma \sim 10$, a baryonic loading of $\xi_A \approx 0.15 \times 2\Gamma^2 mc^2/E_X \simeq 525$ is obtained, with the factor $2\Gamma^2$ correcting for the beaming and assuming that 15% of the disrupted star's mass is reprocessed into non-thermal baryons. The corresponding accretion rate is approximately $L_{\rm accr} \sim 0.15 \times mc^2/\Delta T \simeq 10^{47}$ erg s^{-1} for a jet duration of $\Delta T \sim 10^6$ s, which can be compared to the Eddington luminosity of the black hole $L_{\rm Edd} \sim 10^{43}(M/10^5 M_\odot)$ erg s^{-1}. Considering the uncertainty of the Lorentz factor, the ratio is roughly consistent with simulations [261]. The same normalization factor G can be obtained assuming a lower baryonic loading at the expense of a higher local rate. For points in the upper right of the allowed region, the value of G will also be slightly lower. Note that a lower value for the normalization is required if the spectral injection index from acceleration is harder than E^{-2}.

5.2.1 Joint description of UHECRs and neutrinos

The cosmic ray and neutrino observables at the best fit point A are shown in Fig. 5.4. The UHECR spectrum (upper left) and composition (lower panels) beyond $10^{18.7}$ eV and PeV neutrino data (upper right) are well reproduced. The UHECR flux is also showed in the neutrino panel to illustrate that both of them are at a comparable energy level. The upper limit at 6 – 10 PeV is obtained by the non-observation of the Glashow resonance assuming an ideal *pp* source, *i.e.*, an equal flux of neutrinos and anti-neutrinos at Earth [8]. However, this does not hold for $p\gamma$ sources [160, 262], which could be even muon damped, relaxing the constraint by a factor $\sim$ 4–5. The expected number of Glashow events in IceCube for the flavor composition at our best fit is ~ 1.2 in 6 years of operation. This is consistent with a non-observation within the uncertainties. However, recently a 5.9 PeV event was observed, which might be a candidate for a resonant event [263]. Neutrinos at lower energies cannot be described with this model, such that we invoke an additional flux which might originate from multiple components [154], from choked jets correlated with type II supernovae [232] or Dark Matter decays [264], for instance.

In Fig. 5.5, the interaction rates (top left), neutrino fluence (top right), particle densities in the source (bottom left) and the ejected cosmic ray fluence (bottom right) are shown for the best fit point A. As a consequence of the broken power law target photon spectrum, the photo-disintegration rate peaks at about $10^{7.5}$ GeV and then kinks off, such that the maximum energy is limited by photo-meson production. This is a suitable benchmark to test the impact of more realistic photo-meson models, which is why it was chosen as a benchmark in [177]. The neutrino fluence is shown per flavor in the observer's frame for a source at redshift $z = 0.001$. Neutrinos

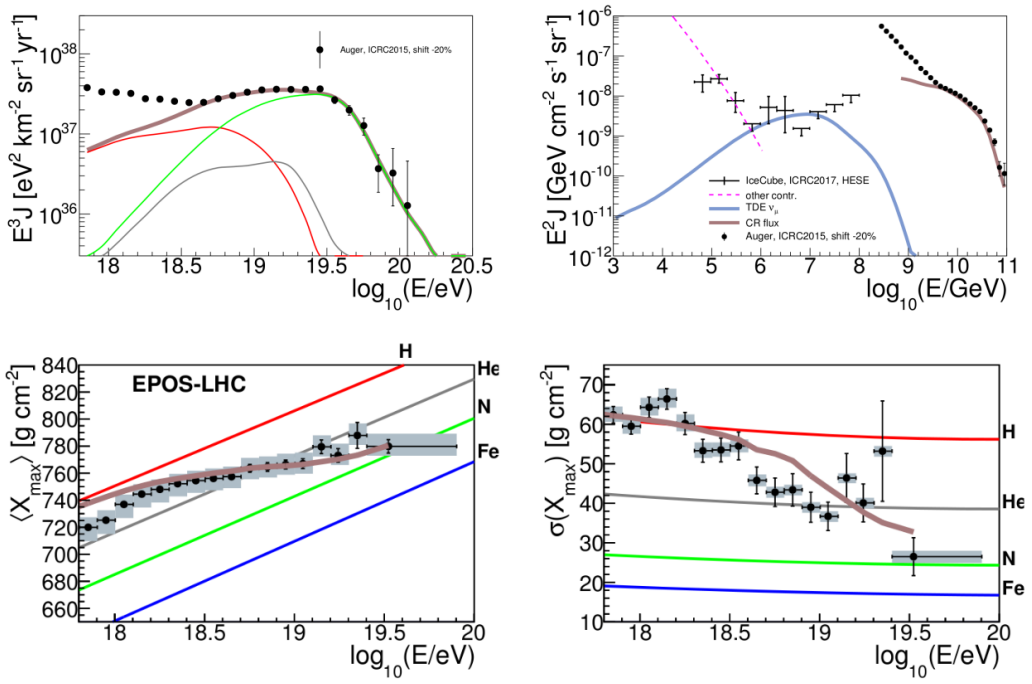

Figure 5.4: Cosmic ray and neutrino observables corresponding to the combined best fit point A in Fig. 5.3 with $G = 540$. The UHECR energy spectrum multiplied by E^3 is shown together with the PAO data points [219] in the upper left panel. The contribution from different mass groups is shown (thin curves, same color as lower panels). In the upper right panel, the predicted muon neutrino flux from TDEs is shown compared to the HESE data points of IceCube [235]. The total flux of UHECRs is depicted in the same panel for comparison. The lower panels show the prediction and data [222] of the average (left) and standard deviation (right) of the $X_{\max}$ distribution. Straight lines correspond to predictions of the EPOS-LHC interaction model [115] for UHECR-air interactions. A shift of -20% is applied to take into account energy scale uncertainties. Taken from [248].

from beta decays are shown as a separate curve, indicating that they are only relevant at low energies. The nitrogen spectrum in the source shows a depletion at the highest energies (with respect to the injection spectrum, which is shown for comparison), which is where disintegration becomes efficient and secondary isotopes produced in these processes dominate the spectrum. The ejected cosmic ray spectra are harder because of the direct escape mechanism, which assumes that particles can only escape if they can reach the edge of the region within their Larmor radius. Here, the escape is moderately efficient, as even at the highest energies the Larmor radius does not reach the size of the region. This is because the source is optically thick to photo-hadronic interactions, *i.e.*, the maximum energy is not limited by the dynamical time scale. The escaping

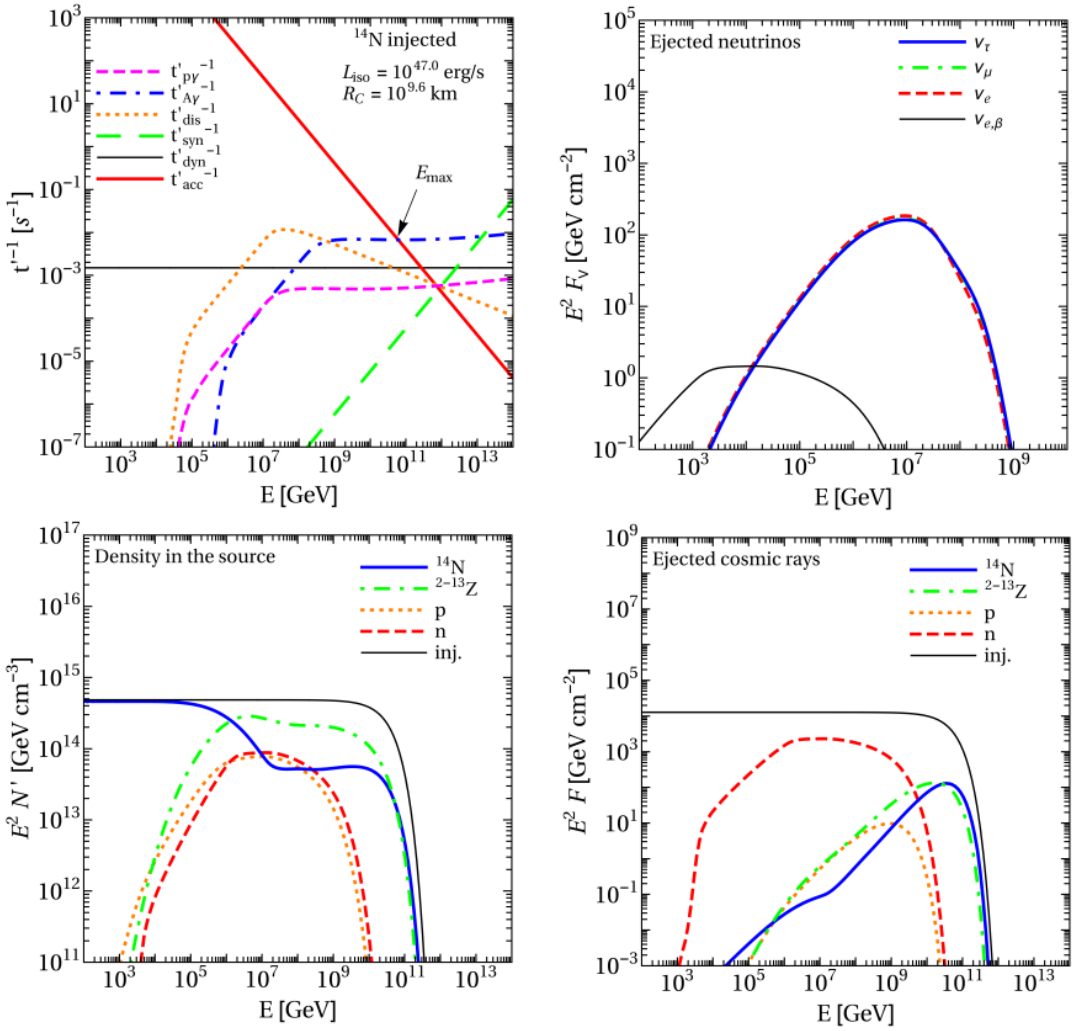

Figure 5.5: Interaction rates (top left), neutrino spectra per flavor (top right), isotope densities in the source (bottom left) and ejected cosmic ray spectra (bottom right, adiabatic cooling only) for best fit point A in Fig. 5.3 as a function of the energy in the observer's frame. The TDE parameters are $L_X = 10^{47}$ erg s^{-1}, $R = 10^{9.6}$ km, $\Gamma = 10$, $\varepsilon'_{\gamma,\mathrm{br}} = 1$ keV and $z = 0.001$ for pure ^{14}N injection. The ejected fluences do not take into account interactions during propagation. The injected spectrum ('inj') is shown in the bottom panels for comparison. Taken from [248].

fluence is correspondingly suppressed even at the highest energy. Neutrons, on the other hand, are electrically neutral and not bound to the plasma, such that they can escape freely. The ejected neutron spectrum follows the density in the source.

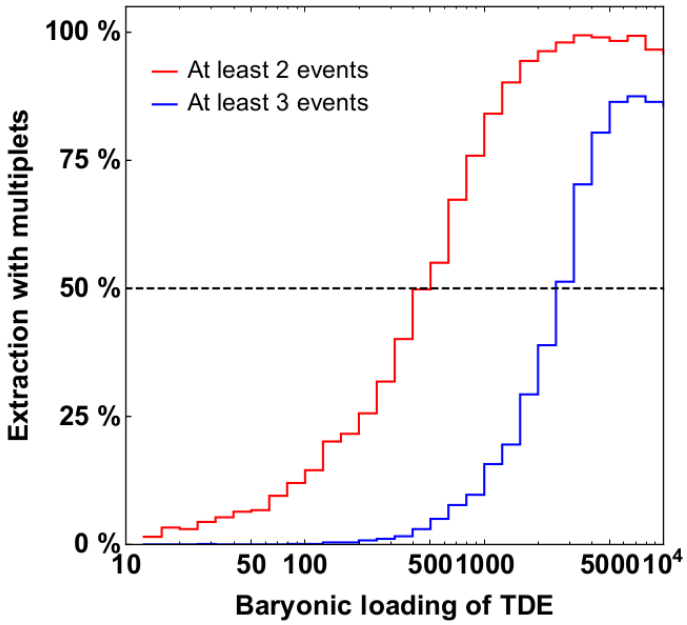

Figure 5.6: Probability to observe multiplets from the same TDE as a function of the baryonic loading. The red curve corresponds to two events and the blue curve to three events from the same source. The probabilities have been calculated with an IceCube exposure of 5.7 years. Taken from [154].

5.2.2 Constraints and testability with neutrino multiplets

Observational constraints must be considered, of which the lower limits on the apparent local rate from the non-observation of neutrino multiplets [259, 257, 258] may be the most constraining one, as mentioned already above. This constraint cannot be avoided by increasing the rate and decreasing the luminosity, as such a population is constrained by X-ray observations [265]. Large baryonic loadings are ruled out as well, as with $\xi_A \gtrsim 1000$ Swift J1644+57 would have been observed in neutrinos. Furthermore, high baryonic loading factors imply a total energy of more than 10^{54} erg in the TDE, which violates the energetics argument [266]. However, with a baryonic loading of ~ 500, which is found in this study, only 0.3 events are expected. Thus, if TDEs are the dominant source of PeV neutrinos, about 10 TDEs are needed to account for the 3 PeV events which have been measured so far. Roughly estimating the chance to get a multiplet by drawing 3 events from 10 TDEs gives a probability $\sim 28\%$.[2] A more detailed study on multiplet constraints, using our exact TDE flux at the best fit, has been carried out in [154]

[2]The probability P to obtain at least one multiplet is given by $P = 1 - \frac{n!}{(n-k)!}\frac{1}{n^k}$ for $n = 10$ and $k = 3$, assuming identical sources at the same distance.

and is shown in Fig. 5.6. With respect to the simple estimate, the probability is higher, but still only around 50%. Nevertheless, neutrino multiplets will be able to further constrain this model.

Another potential limitation of our model is the assumed redshift evolution of TDEs, which follows the IMBH number density here. Recent studies consider that small and intermediate mass black holes were more abundant in the past, as they may have merged into more massive black holes until today [267]. This points towards a less negative or even positive redshift evolution of the TDE rate, *i.e.*, distant sources have a larger contribution to the UHECR and neutrino flux, making the combined description more challenging. Also the fact that the input parameters are fixed inspired by Swift J1644+57 may be a limitation. For example, ultra-long GRBs might be caused by the disruption of WDs [266] with GRB111209A being a candidate. Compared to this study, these bursts have different X-ray spectra and a shorter duration and variability time scale. The tidal disruption of neutron stars, which may be associated to gravitational wave events as for instance GW170817, can be an alternative scenario. The observed short GRB in the follow-up of this event may be interpreted as a representative of a new population of jetted TDEs [63]. In general, multiple classes of sources may be considered to contribute to the total UHECR and neutrino fluxes.

Chapter 6

Binary neutron star merger associated with GW170817

A recent milestone in multi-messenger astronomy was the observation of a binary neutron star merger associated with gravitational wave event GW170817, as mentioned in Chapter 2. On the 17th of August 2018, LIGO detected a gravitational wave signal which was promptly followed by electromagnetic radiation about 1.7 seconds later [62]. The electromagnetic counterpart was first observed in gamma-rays [63] and eventually also in the X-ray [268, 269] and radio bands [77, 270]. Observations across the UV, optical and near-infrared spectrum have been interpreted as a kilonova [271, 272, 273] with evidence for nucleosynthesis of r-process elements [79, 274]. The signal was determined to originate from the galaxy NGC 4993 at a redshift of $z = 0.008$, which corresponds to roughly 40 Mpc. In total, more than 70 observatories participated to obtain data in the follow-up campaign. An overview of the many multi-messenger and multi-wavelength observations can be found in [275], while [276] gives a theoretical overview.

In this section, we will investigate neutrino and cosmic ray production in this specific event, based on our works [277] and [278], respectively. In Sec. 6.1, we use the information on the spectral energy distribution as measured by *Fermi*-GBM along with other inferred parameters of the SGRB to predict the expected neutrino fluence and argue why no neutrino observations are expected. We consider two different jet scenarios, a low-luminosity structured jet and an off-axis top-hat jet, in order to explain the low luminosity of this event. We demonstrate that the fact that the event was visible in gamma-rays implies that there is a maximum baryonic loading and show that the highest achievable neutrino fluence is well below the limits. My contribution to this project was the implementation of the short GRB model caused by the neutron star merger including the different jet scenarios. I worked on the scaling relations and the photospheric limit in order to numerically compute the maximum possible neutrino fluxes. Furthermore, I ran a parameter space scan to constrain observation angle and Lorentz factor. On the other hand, in Sec. 6.2, we consider cosmic ray production of a population of remnants of binary neutron star mergers. We discuss constraints of the magnetic field of the remnant arising due to the lack of a cooling feature in the observed synchrotron spectrum. Non-thermal electron losses are then calculated in different magnetic field scenarios to obtain the resulting spectral

energy distribution. For strong fields, we show that photo-disintegration can be efficient within a bottleneck period of days to weeks after the merger. We find that this class of sources can in principle support the population of cosmic rays below the ankle. My main contribution was to set up the model in order to calculate the interaction rates and determine the bottle-neck in the optical thickness of the neutron star merger remnant.

6.1 Neutrinos from short gamma-ray burst 170817A

Due to the low observed luminosity, it was considered whether the emission of this event is viewed off-axis. In such a case, the observed parameters need to be boosted back in the jet frame first, where the interactions take place. Following our paper [277], we take into account two different jet models in the following, a structured low-luminosity jet and a uniform top-hat jet which is observed off-axis (similar to the simple and advanced model in [279, 280]), as illustrated in Fig. 6.1. In the following, we have to distinguish between the Lorentz factor Γ and the Doppler factor

$$D(\theta) = \frac{1}{\Gamma(1 - \beta \cos\theta)} \approx \frac{2\Gamma}{1 + \theta^2\Gamma^2} \tag{6.1}$$

for the boost from the jet rest frame to the observer's frame. The Doppler factor depends on the angle θ under which the emission is observed, which means that for the on-axis case the Doppler factor is $D(0) = 2\Gamma$. The effect of the cosmological redshift is negligible because of the small value of z at which the event was observed.

In the case of the structured jet (A), the jet is structured in the sense that different characteristics as energy E and Lorentz factor Γ are measured when observed under different angles. If we happen to observe the emission along an axis that has low luminosity, this naturally explains the dimness of the GRB. However, the observer is also exposed to the off-axis emission of other axes in the jet, which are illustrated by Γ' and Γ'' in the figure. Although they are suppressed by their Doppler factor, they can overshoot the dim on-axis radiation if the gradient in luminosity is too high. Thus, the Lorentz factor and luminosity must not change too rapidly under different angles. The structured jet can be treated as a low-luminosity top-hat jet observed on-axis as long as these variations are small. Hence, its predictions are similar to conventional GRB neutrino fluence predictions for low luminosity. A trivial version of the structured jet case is a uniform emission in all directions. This scenario could be further motivated by the fact that the probability to observe the emission on-axis is relatively small. Other alternatives as choked jets or cocoon emission are not discussed here. See [281] for a discussion of alternative jet scenarios.

In the off-axis scenario (B), we consider a uniform top-hat jet for which the observed luminosity is suppressed by the Doppler factor which depends on the angle between the edge of the jet and

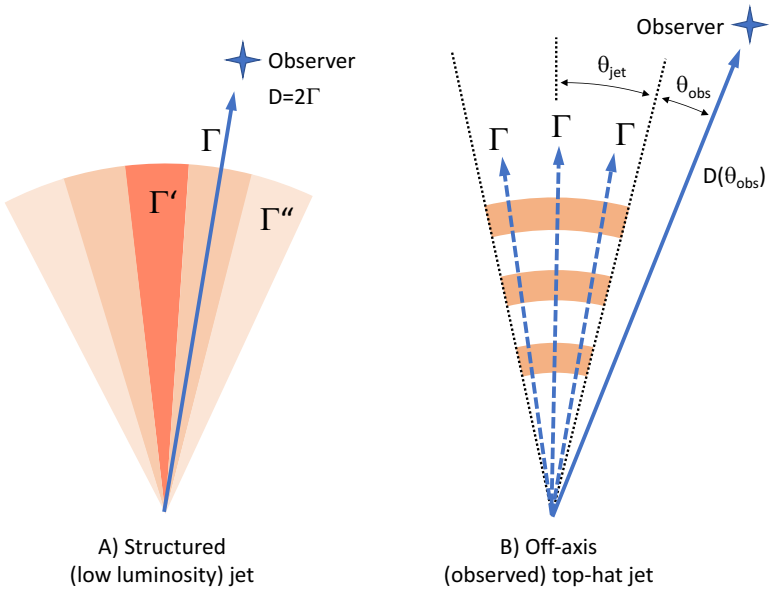

Figure 6.1: Illustration of the different jet geometries and corresponding angles considered in this section. The structured (low-luminosity) jet (A) has different characteristics depending on the angle under which it is observed. In the off-axis (top-hat) jet case (B), the jet is uniform within the opening angle, but observed off-axis and therefore Doppler boosted. Taken from [277].

the observation axis $\theta_{\rm obs}$. Due to the observed geometry, there is a transition in the luminosity scaling around $\theta_{\rm obs} = \theta_{\rm jet}$, where the latter is the jet opening angle (as measured to the jet axis). We do not impose any direct constraint on $\theta_{\rm jet}$ and it is not inferable from observations, but we will use $\theta_{\rm jet} \simeq 1/\Gamma$ to show this transition.

In either case, we assume the internal shock scenario as in Sec. 4.1. For an on-axis observer, the jetted emission is not distinguishable from a sphere expanding into full solid angle, allowing us to treat the emission in the isotropic-equivalent picture. Thus, for the structured jet, we can take the observed parameters at face value, whereas for the off-axis interpretation the quantities have to be transformed to the on-axis frame as a function of $\theta_{\rm obs}$ and Γ. For $\theta_{\rm obs} = 0°$, both scenarios coincide by construction. We emphasize that the neutrino production in the off-axis scenario is usually larger with increasing observation angle if the observations are fixed. As the observed gamma-ray fluence has to be de-boosted by the Doppler factor, the photon density and with that the neutrino production efficiency will be much higher as in the structured jet case. The boost back into the observer's frame can typically not compensate for that, such that the expected neutrino fluence will be higher for larger off-axis angles due to this re-scaling.

In the following, our calculations are based on *Fermi* measurements. The duration of the burst was measured to be $T_{90} = 2.0 \pm 0.5$ s with a minimum variability time scale of $t_v = 0.125 \pm 0.064$ s [282]. Combining the information on the redshift $z = 0.008^{+0.002}_{-0.003}$ and the gamma-ray flux $F_\gamma = (5.5 \pm 1.2) \times 10^{-7}$ erg s^{-1} cm^{-2} [282], the luminosity is estimated to be about $L_\gamma \simeq 10^{47}$ erg s^{-1}. This yields a similar total energy $E_\gamma = 2 \times 10^{47}$ erg as in [63]. The spectral energy distribution can be described as a Comptonized spectrum, corresponding to the best fit to observations in [63]. For this purpose, we use the 256 ms time integrated selection from T0–0.192 s to T0+0.064 s, with a spectral index $\alpha = 0.14 \pm 0.59$ and a peak energy $E_{\rm peak} = 215 \pm 54$ keV [282]. The results shown in the following depend slightly on the energy band and time interval chosen to determine these parameters. The Lorentz factor Γ and observation angle $\theta_{\rm obs}$ are not constrained by observations, but they can be constrained by the time delay between gravitational wave and electromagnetic signal [283, 284]. In the following, we compare our results to this constraint adopted to our geometry.

6.1.1 Off-axis transformations and photospheric constraint

As before, the main parameters influencing the neutrino production efficiency are the isotropic equivalent gamma-ray luminosity L_γ and the dissipation radius, which in the internal shock model is given by $R \simeq 2\Gamma^2 c t_v$. The radius and the Lorentz factor in this formula are given in the source frame, whereas t_v is given by the on-axis observation. Radiation from such internal shocks can only be directly observed if the photospheric radius $R_{\rm ph}$, defined as the radius where the shells become optically thin to Thomson scattering, is smaller than the collision radius. The photospheric radius is given by [285]

$$R_{\rm ph} \simeq \left(\frac{\sigma_T}{4\pi m_p}\right)^{1/2} \left(\frac{\xi_A E_{\rm iso,on}}{\varepsilon \Gamma T_{90}/t_v}\right)^{1/2} \quad , \tag{6.2}$$

where ξ_A is the baryonic loading defined as the ratio between energy in protons and photons in the *Fermi* GBM energy band from 10 to 1000 keV. The conversion efficiency of kinetic energy to total dissipated energy is called ε, which is set to 25% as corresponding values were found in [286, 241], and $E_{\rm iso,on}$ is the total isotropic equivalent energy in gamma-rays observed on-axis. See App. B for the derivation of this formula. Note that too small values for ε are not compatible with afterglow observations, whereas higher efficiencies are difficult to obtain since it requires that the Lorentz factors of the colliding shells are largely different. As the photospheric radius scales with ξ_A/ε, smaller efficiencies correspond to a lower baryonic loading for fixed $R_{\rm ph}$. Demanding $R \gtrsim R_{\rm ph}$ can thus be used to constrain the baryonic loading in internal shocks.

An estimate for the maximum R for SGRB 170817A can be derived from the time delay $t_{\rm delay}$ between the gravitational wave and the electromagnetic signal [63]. Assuming that the emission originates from the collision of two shells with Γ_1 and Γ_2, where $\Gamma_2 > \Gamma_1$ and that the first shell is emitted at the time of the merger, the distance covered by the time that the second shell catches up is $R \approx 2\Gamma_1^2 c t_{\rm delay}$. Hence, for $\Gamma \lesssim 100$, the upper bound for the collision radius is about $R \sim 10^{9.5}$ km. In the following, we typically obtain radii between 10^7 and 10^8 km, which are well below and thus consistent with this limit.

For a relativistic shell, the observed quantities have to be Doppler shifted depending on the Lorentz factor Γ and the observation angle $\theta_{\rm obs}$, defined relative to the edge of the jet. Thus,

$$t = D(\theta_{\rm obs})^{-1} t' \quad \text{and} \quad E = D(\theta_{\rm obs}) E' \tag{6.3}$$

for the transformation of times and energies, respectively (primed quantities refer to the SRF). These transformations are valid for observed quantities that do not depend on the shell geometry, *e.g.*, the peak energy of the photon spectrum $E_{\gamma,\rm peak}$. On the other hand, the isotropic equivalent energy $E_{\rm iso}$ and the variability time t_v for instance have to be integrated over the geometry of a single shell and the scaling will be different. In the case of $E_{\rm iso}$, this is due to the fact that it is defined as observed spectral flux F_ν in (erg s^{-1} cm^{-2} Hz^{-1}) integrated over time, area and frequency. Therefore, it scales differently depending on whether the observer is inside or outside of $\theta_{\rm jet}$. A full derivation can be found in [287], which yields

$$E_{\rm iso}(\theta_{\rm obs}) \propto \begin{cases} \text{const.} & \text{for } \theta_{\rm obs} \lesssim 0 \\ D(\theta_{\rm obs})^2 & \text{for } 0 < \theta_{\rm obs} \lesssim \theta_{\rm jet} \\ D(\theta_{\rm obs} + \theta_{\rm jet})^3 & \text{for } \theta_{\rm jet} < \theta_{\rm obs} \end{cases} . \tag{6.4}$$

These three regimes have a different geometrical interpretation:

- $\theta_{\rm obs} \lesssim 0$: The observer is within the jet opening angle, *i.e.*, the jet is indistinguishable from isotropic, spherical emission. Angles close to the viewing axis contribute most to the observed radiation.

- $0 < \theta_{\rm obs} \lesssim \theta_{\rm jet}$: The observer is outside of the jet opening angle, but only at a small angle from the edge of the jet. Hence, the jet geometry still contributes and the observed flux has to be integrated over the observable part of the jet close to the edge.

- $\theta_{\rm jet} < \theta_{\rm obs}$: The observer sees the emission under a large angle, such that all regions of the jet have approximately the same Doppler factor. As a consequence, the jet looks like a point source to the observer.

Now that these regimes and transformations are defined, we can derive relationships between quantities in the on- versus off-axis frame. Note that even if the observation happens on-axis, the quantities need to be boosted by $D(0)$ from observer's to shock rest frame in order to compute the proper radiation densities. We define

$$b = \begin{cases} D(0)/D(\theta_{\rm obs}) & \text{for } 0 \leq \theta_{\rm obs} \lesssim \theta_{\rm jet} \\ aD(0)/D(\theta_{\rm obs} + \theta_{\rm jet}) & \text{for } \theta_{\rm jet} < \theta_{\rm obs} \end{cases} \tag{6.5}$$

with $a = D(2\theta_{\rm jet})/D(\theta_{\rm jet})$ in order for b to be continuous in $\theta_{\rm obs}$. With this, we can express the on- to off-axis ratio of the isotropic equivalent energy as

$$\frac{E_{\rm iso,on}}{E_{\rm iso,off}} = \begin{cases} b^2 & \text{for } \theta_{\rm obs} < \theta_{\rm jet} \\ b^3 & \text{for } \theta_{\rm jet} < \theta_{\rm obs} \end{cases} \tag{6.6}$$

while the peak energy is just Doppler shifted as it is independent from the jet geometry. Similar to $E_{\rm iso}$, the variability time scale has to be integrated over the shell geometry because the radiation from different parts of the shell surface is delayed depending on $\theta_{\rm obs}$. Following [287], the scaling holds

$$\frac{t_{v,\rm on}}{t_{v,\rm off}} = \begin{cases} b^{-1} & \text{for } \theta_{\rm obs} < \theta_{\rm jet} \\ b^{-1/2} & \text{for } \theta_{\rm jet} < \theta_{\rm obs} \end{cases} . \tag{6.7}$$

The scaling of the duration T_{90} is controversial. While in [63], it is implied that the duration scales with b depending on the observation angle as well, in [288] it is argued that the observed burst duration does not change with observation angle since it is defined in the source frame, which is at rest relative to the observer. In the following, we choose to not re-scale T_{90} with off-axis angle, implying a larger number of interaction regions $N \simeq T_{90}/t_v$ in the on-axis frame. The physical picture is that peaks in the light curve observed on-axis are smeared out off-axis, similar to the discussion in [288], which effectively leads to a slower variability time if observed off-axis. However, the number of collisions N drops out from the computation to a first approximation and the smaller on-axis time variability only slightly increases the neutrino production efficiency as the width of the shell is estimated from it. We compared our results to the case where we include the re-scaling of T_{90} and concluded that it does not change the qualitative picture.

The secondary radiation calculated in the SRF has to be boosted back off-axis in order to predict observations, however there is still a net-effect. In the following analytical discussion, we focus on the case of small angles $\theta_{\rm obs} < \theta_{\rm jet}$ for the off-axis transformations. The gamma-ray peak energy is shifted towards higher energies as $E'_{\gamma,\rm peak} \propto b$ in the SRF, which implies that the neutrino production threshold is lower. As $E'_{\nu,\rm peak} \propto 1/E'_{\gamma,\rm peak}$, the observed neutrino spectrum

will scale $E_{\nu,\mathrm{peak}} \propto b^{-2}$. The neutrino production efficiency f_ν, which is defined as the fraction of energy the proton primaries dump into neutrino production, scales with the particle densities in the shell and thus with the luminosity and collision radius. Similar to the pion production efficiency in Sec. 4.1, it can be estimated as

$$f_\nu = \frac{E_{\nu,\mathrm{iso}}}{\xi_A E_{\gamma,\mathrm{iso}}} \propto \frac{L_\gamma}{\Gamma^4 E_{\gamma,\mathrm{peak}} t_v} \tag{6.8}$$

in the on-axis case if the synchrotron cooling of the secondaries is neglected. For small angles $\theta_{\mathrm{obs}} < \theta_{\mathrm{jet}}$, the product of the peak energy and variability time is invariant under the observation angle and f_ν transforms proportional to luminosity $L_\gamma = E_{\gamma,\mathrm{iso}}/t_v$ as $f_\nu \propto b^3/\Gamma^4$. Together with the scaling of the neutrino peak $\propto b^{-2}$, the approximate scaling of the observed neutrino fluence F_ν in (GeV^{-1} cm^{-2}) can be written as

$$F_{\nu,\mathrm{off}}(E_\nu) \approx \frac{b^5}{\Gamma^4} F_{\nu,\mathrm{on}}(b^2 E_\nu) \quad . \tag{6.9}$$

This means that the expected neutrino fluence is higher when the observation is interpreted as off-axis emission, with the peak shifted to lower energies.

The scaling of the isotropic equivalent energy $E_{\mathrm{iso}} \propto b^2$ has an additional implication for baryonically loaded jets: Since the baryon density scales with the energy density, the shells are less transparent to gamma-rays if the same flux is observed off-axis. Based on Eq. (6.2), the scaling is then

$$R_{\mathrm{ph}} \simeq \left(\frac{\sigma_T}{4\pi m_p}\right)^{1/2} \left(\frac{\xi_A E_{\gamma,\mathrm{iso,off}}}{\varepsilon T_{90}/t_v}\right)^{1/2} \left(\frac{b^2}{\Gamma}\right)^{1/2} \quad . \tag{6.10}$$

This condition limits the observation angle θ_{obs} and the Lorentz factor Γ for a fixed baryonic loading if the emission originates from the dissipation of internal shocks beyond the photosphere. Vice versa, it can be used to estimate the maximum possible baryonic loading for which $R \gtrsim R_{\mathrm{ph}}$ as

$$\frac{\xi_A}{\varepsilon} \lesssim \frac{4\pi m_p}{\sigma_T} \frac{T_{90}/t_v}{E_{\gamma,\mathrm{iso,off}}} \frac{4\Gamma^4}{b^4} \tag{6.11}$$

if the internal shock relation for R is substituted for the photospheric radius. For larger baryonic loadings, the radius at which internal shocks occur will be below the photosphere, where gamma-rays cannot escape. Thus, we would not have observed the event electromagnetically at all. The neutrino fluence computed for the maximum baryonic loading corresponds to the maximum possible neutrino fluence too.

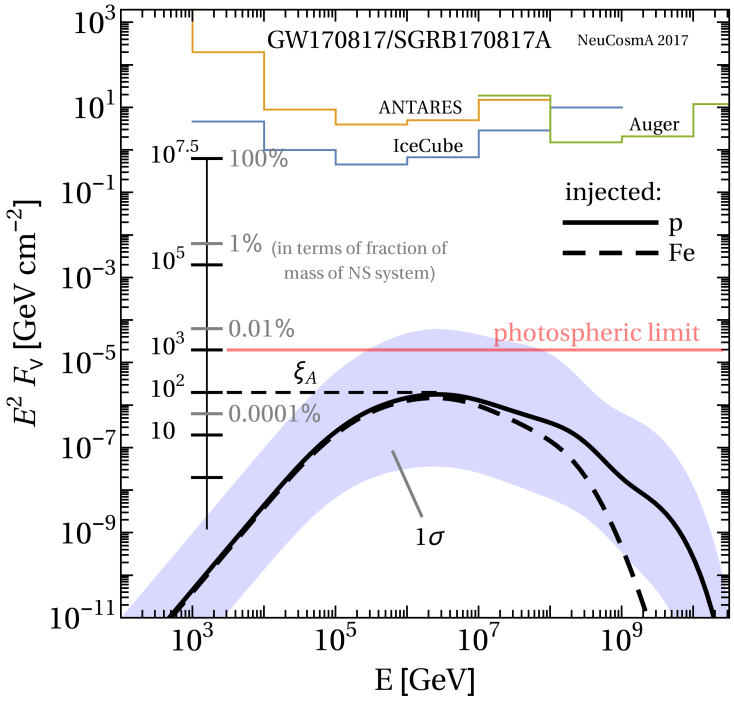

Figure 6.2: Neutrino fluence ($\nu_\mu + \bar{\nu}_m u$) expected for SGRB 170817A assuming pure proton (solid) or iron (dashed) injection. The parameters are $z = 0.008$, $L_X \sim 10^{47}$ erg s^{-1}, $t_v = 0.125$ s [275, 282] and $\Gamma \approx 30$. The blue shaded region corresponds to the 1σ uncertainties of these parameters. The black scale represents the scaling of the fluence with the baryonic loading ξ_A, with the gray percentage indicating the fraction of the total mass of the NS merger. As the photosphere scales with the baryonic loading, the emission would be sub-photospheric for $\xi_A > 10^3$ as illustrated by the horizontal red line. Neutrino limits are taken from [289]. Taken from [277].

6.1.2 Predictions for structured and off-axis jet scenarios

First, we assume a structured (low-luminosity) jet where the Lorentz factor is fixed to $\Gamma = 30$. Fig. 6.2 shows the predicted muon neutrino fluence for pure proton injection modelling SGRB 170817A. As shown also in chapter 4, the peak neutrino fluence is not affected by injecting nuclei heavier than protons in GRBs, however the cutoff shifts to lower energies. In this example, an initial baryonic loading of $\xi_A = 100$ was used for the computation, as indicated by the scale on the left hand side of the plot. The blue band includes the 1σ uncertainties on the measured duration T_{90}, variability time scale t_v, redshift z, gamma-ray fluence F_γ, spectral index α and peak energy $E_{\rm peak}$ of the target photon spectrum. The gray scale indicates the fraction of the total mass of the binary neutron star system translated into the baryonic loading, with which the

neutrino fluence directly scales. Demanding super-photospheric emission translates into the red horizontal line, as the photosphere also scales with baryonic loading. According to Eq. (6.11), the maximum baryonic loading is $\xi_{A,\mathrm{max}} \sim 10^3$, meaning that the neutrino fluence can be up-scaled by a factor 10 at most in this scenario to obtain the maximum possible neutrino fluence for this SGRB in the structured jet internal shock model.

The left panel of Fig. 6.3 shows the impact of the Lorentz factor on the muon neutrino fluence. The red curve corresponds to the case of $\Gamma = 30$ as in Fig. 6.2 with the solid curves showing the fluxes for the initial baryonic loading $\xi_A = 100$. The figure illustrates how the fluxes scale with Γ according to Eq. (6.9) without imposing any constraints. For large shifts, there is an additional damping of the tail of the spectrum due to fast secondary cooling, which was not considered in the simple analytic estimate. Low values of Γ correspond to efficient neutrino production as the collision radius decreases. On the other hand, the photospheric radius increases, such that low Lorentz factors $\Gamma \lesssim 20$ lead to sub-photospheric collisions. This is indicated by the thin solid curves, whereas the dashed curves represent the maximum neutrino fluence under the photospheric constraint for each case. The fluence for cases with $\Gamma < 20$ are scaled down to be in agreement with the photosphere, while in the case of $\Gamma > 20$ the fluence is up-scaled as much as it is allowed by the photosphere. Even in the most optimistic case, the neutrino fluence is still three orders of magnitude below the sensitivity of neutrino telescopes, meaning that a neutrino detection of SGRB 170817A was very unlikely in the structured jet scenario.

In the off-axis scenario, the observation angle θ_{obs} enters as an additional parameter which has an impact on neutrino production and photospheric radius. In the right panel of Fig. 6.3, the dependence of the neutrino fluence on the observation angle is shown with $\Gamma = 30$ fixed. Also in this case, the solid curves show the unscaled fluences with the initial baryonic loading of 100, while the dashed curves represent the maximum possible neutrino fluence corresponding to the maximum baryonic loading determined by the photospheric constraint. For this particular choice of Γ, the collisions become sub-photospheric already for $\theta_{\mathrm{obs}} \gtrsim 2°$. For large observation angles, the fluence will be highly suppressed, making a neutrino detection even less likely than in the structured jet case. The neutrino fluence peaks at a few $\times 10^{-5}$ GeV cm^{-2} and a baryonic loading $\xi_{A,\mathrm{max}} \approx 10^3$.

In the left panel of Fig. 6.4, we demonstrate how the observation angle θ_{obs} and the Lorentz factor Γ are constrained by requiring super-photospheric emission. The parameter scan shows the maximum possible baryonic loading such that the collision is just super-photospheric in the internal shock model, as indicated by the contours. We take into account the change of the scaling of the parameters from Eq. (6.5) for large observation angles with the assumption $\theta_{\mathrm{jet}} = 1/\Gamma$, depicted by the white dashed curve. In addition, we show the constraint on these parameters obtained by the time delay $t_{\mathrm{delay}} = 1.7$ s as calculated in [284], adapted to our parameters.

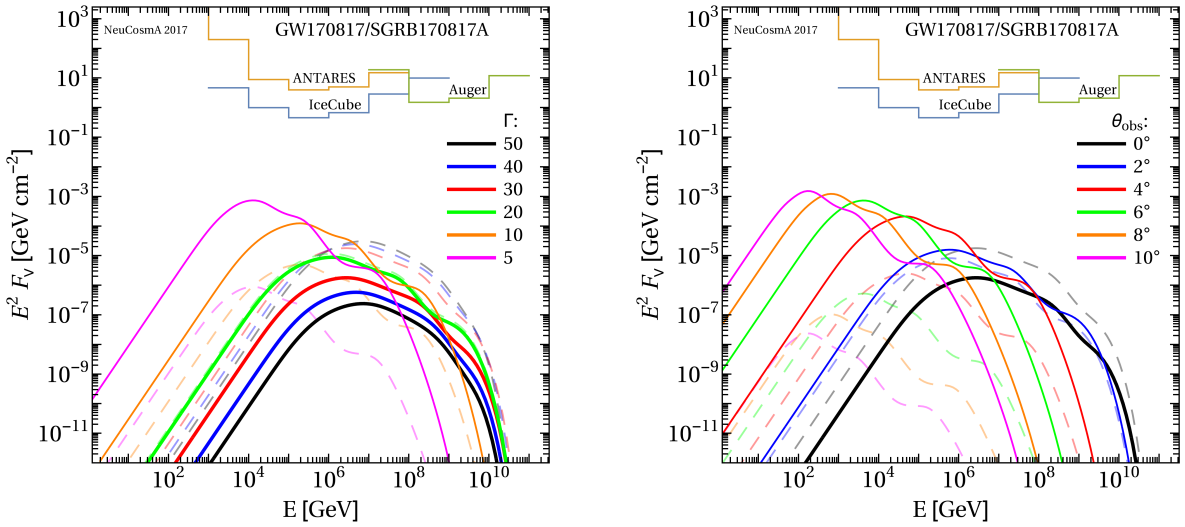

Figure 6.3: Neutrino fluence ($\nu_\mu + \bar{\nu}_m u$) for SGRB 170817A for different values of Γ for a structured jet (left) and for different values of $\theta_{\rm obs}$ for an off-axis jet (right, $\Gamma = 30$ fixed). We assume pure proton injection and the same parameters as in Fig. 6.2. For the solid curves, the baryonic loading is fixed to $\xi_A = 100$, with thick (thin) curves corresponding to super-photospheric (sub-photospheric) collisions. The dashed curves show maximized baryonic loading such that $R_{\rm coll} > R_{\rm ph}$. Taken from [277].

Compared to the original calculation, we assume a slightly different efficiency ε which leads to a slightly larger allowed region in our plot that is highlighted in white. Compared to this constraint, if we assume the typical baryonic loading of 10 frequently used in the literature, the photospheric limit provides already stronger constraints with $\theta_{\rm obs} \lesssim 3^\circ$ and $\Gamma \gtrsim 12$.

In the right panel of Fig. 6.4, we show all possible neutrino fluences allowed by the photospheric limit in the parameter range of the scan. For each point in the parameter space, the fluence has been computed and re-scaled according to the maximum possible baryonic loading in order to obtain the maximum possible fluence of neutrinos. Any combination of parameters will generate a fluence which lies within the blue shaded uncertainty band. It will not exceed $\sim 5 \times 10^{-5}$ GeV cm^{-2} and is therefore about a factor of 10^{-4} below the sensitivity of neutrino telescopes. It is now clear that since the event was observable in gamma-rays, it is highly unlikely to see any neutrinos from the prompt phase of this SGRB. We also show three explicit example fluences, which occupy different regions of the allowed band. The larger the observation angle, the more the peak is suppressed and the peak energy shifts to lower energies. For the on-axis case, the fluence is the highest, while for intermediate values of Γ and $\theta_{\rm obs}$ the fluence is in-between those extremes. We further show the examples for proton (solid) and iron injection (dashed), which almost give the same result apart from a different cut-off. Note that re-scaling with the

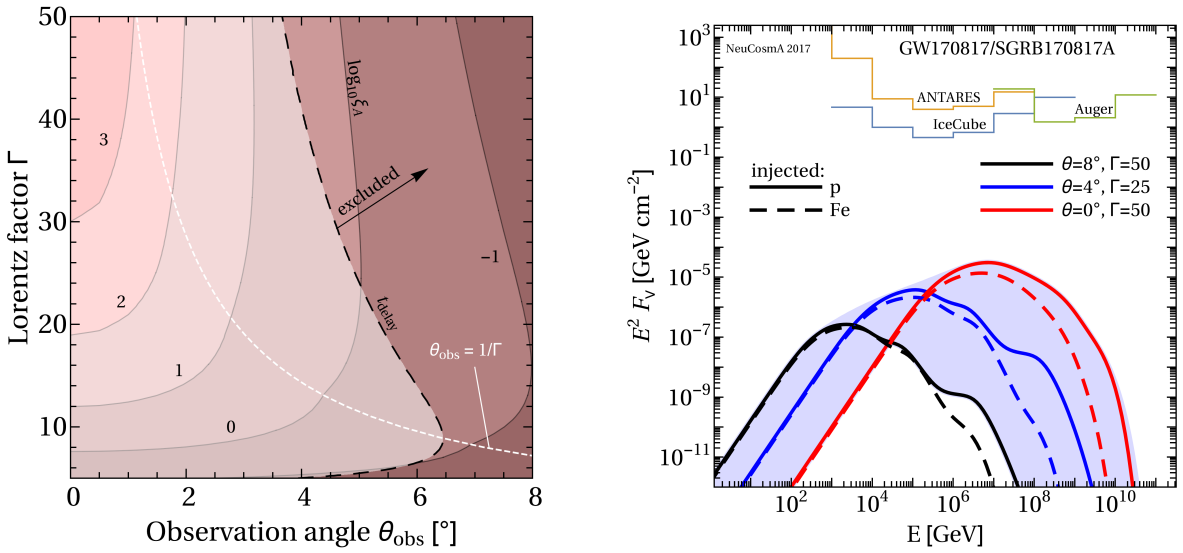

Figure 6.4: Maximum baryonic loading $\xi_{A,\mathrm{max}}$ such that the emission is still super-photospheric as a function of θ_{obs} and Γ (left) and resulting muon neutrino fluence expected in this region of the parameter space (right). In the left panel, it is assumed that $\theta_{\mathrm{jet}} \simeq 1/\Gamma$, *i.e.*, the off-axis scaling changes along the white dashed curve. The black dashed curve indicates the excluded region of the arrival time constraint [284]. In the right panel, solid curves refer to protons and dashed curves to iron injection. Three particular examples for low, intermediate and high fluence are shown according to the legend, all other parameter combinations are contained in the blue shaded band. The individual curves have been re-scaled with the maximum baryonic loading for each parameter set. Taken from [277].

maximum baryonic loading implies super-photospheric collisions. If this constraint is omitted, *e.g.*, in a sub-photospheric extrapolation, the neutrino fluence would increase drastically, since smaller radii lead to much higher radiation densities. However, as indicated by the thin lines in Fig. 6.3, this would still not be enough to reach the sensitivity of any detector.

In conclusion, if GW170817 is a typical neutron star merger, it is highly unlikely that neutrinos will be detected during the prompt emission phase. Nevertheless, certain source properties can be constrained by multi-messenger observations, *e.g.*, the baryonic loading. The jet scenario is still disputed: In the beginning, the situation was very unclear, and low-luminosity jets, off-axis jets, choked jets, or cocoon emission were among the considered scenarios. Some models claim that the radio light curve shows no signature of an off-axis jet afterglow and rather assign the observed gamma-ray emission to cocoon emission [281]. However, recent observations seem to favor the off-axis jet scenario again [290, 291, 292], but overall the situation is still uncertain and will only be clarified by further observations. See also [293, 294] for recent discussions.

6.2 Cosmic rays from binary neutron star merger remnants

After the prompt emission, a relatively bright electromagnetic counterpart, also called EM170817, was discovered in the optical bands [295, 296, 297, 298, 299]. This emission is associated to the remnant of the neutron star merger, in which subsequent non-thermal observations in the radio and X-ray bands indicated particle acceleration [270, 77, 268, 300]. The emission was observed to brighten as a power law in time up to about ~ 160 days, recently followed by an apparent dimming of the source [301, 302]. The outflowing kinetic energy released in the blast wave can be estimated from the gravitational binding energy and is of the order of 10^{50-52} erg. A value of 10^{51} erg would for instance be consistent with an estimated mass of $10^{-2} M_\odot$ and an ejecta velocity of $\beta = 0.2$. In this case, the total number of electrons in the outflow is approximately $N_e \approx 10^{55}$, such that at late time scales of about 100 days the average density of material in the outflow is estimated to be $\bar{n} \simeq 2 \times 10^4$ cm^{-3}. With these numbers, the outflow is expected to become optically thin to its own radiation after about 2 days and the brightening is expected to cease on a time scale of ~ 100 days, depending on the mean ambient density.

The late-time acceleration of cosmic rays was anticipated in [303], including $\sim$ mG magnetic fields , an outflow mass of $10^{-2} M_\odot$ and a non-relativistic shock speed, leading to a maximum proton energy of $\sim 10^{17}$ eV up to a deceleration time scale of about 1 year. Here, we present the results of our work [278] on this topic, where we focus on electron and nuclei acceleration and subsequent energy losses and emission. My main contributions were the considerations about nuclei and potential interactions that accelerated nuclei undergo with the target photons of the source. To do so, we first place some constraints on the magnetic fields and discuss the radiation field of the source in the weak and strong magnetic field scenario. We find a bottleneck period of a few days to weeks for the photo-disintegration of nuclei in strong magnetic fields and conclude that this source class can support cosmic rays up to the ankle.

6.2.1 Spectral energy distribution from non-thermal electron losses

The presence of a non-relativistic outflow is supported by photospheric velocity measurements of the remnant EM170817 [304]. The non-thermal emission of this outflow brightens with time in both, the radio and X-ray bands [300, 281]. If the emission is assumed to be synchrotron emitted by an electron population with a spectrum $dN/dE_e \propto E_e^{-2}$, the lack of a cooling feature in the observed spectrum can be used to constrain the maximum magnetic field strength of the source. The synchrotron cooling time of mono-energetic electrons is

$$t_e^{\rm syn} = \frac{9 m_e t_{\rm Lar}}{8\pi\alpha E_\gamma^{\rm syn}} = 2 \times 10^3 \left(\frac{10 \text{ keV}}{E_\gamma^{\rm syn}} \right) t_{\rm Lar} \quad , \tag{6.12}$$

with the Larmor time $t_{\rm Lar}$ and the characteristic energy of synchrotron photons $E_\gamma^{\rm syn}$. The non-observation of a cooling feature in the spectrum constrains now the cooling time of the electrons as $t_{\rm dyn} < t_e^{\rm syn}(E_\gamma^{\rm syn} = 10\ {\rm keV})$, leading to the constraint $t_{\rm Lar} > 4 \times 10^{-4} t_{\rm dyn}$. On the other hand, a limit on the minimum magnetic field is placed from a consideration of the acceleration time scale $t_{\rm acc} = t_{\rm Lar}/\beta^2$, such that the requirement $t_{\rm acc} < t_{\rm dyn}$ translates into $t_{\rm Lar} > 4 \times 10^{-2} t_{\rm dyn}$. With a dynamical time scale $t_{\rm dyn} \sim 100$ days and the Larmor time $t_{\rm Lar} \propto E_e^3/E_\gamma^{\rm syn}$, the maximum electron energy E_e and the corresponding magnetic field is limited to $0.03\ {\rm mG} < B < 2\ {\rm mG}$. For a value of 2 mG, cosmic ray protons can already reach maximum energies between 10^{15-16} eV, *i.e.*, addressing the energy range between the knee and the ankle. This is interesting due to the indications for an onset of an additional source component [305] bridging the gap between the iron knee [99] and the ankle. Constraints on the dipole anisotropy at such cosmic ray energies strongly support the idea of such an extragalactic component [306, 307].

The observed luminosity of the synchrotron emission can be explained by such a magnetic field if the electron energy density is much higher than the magnetic energy density. The observed X-ray emission is dominated by synchrotron emission of electrons with energy

$$E_e^{\text{X-ray}} = 30 \left(\frac{E_\gamma}{10\ {\rm keV}} \right)^{1/2} \left(\frac{B}{2\ {\rm mG}} \right)\ {\rm TeV} \quad . \tag{6.13}$$

In this monochromatic approximation, the total X-ray luminosity emitted by a population of electrons is given by

$$L_{\rm syn}^{\text{X-ray}} \approx c\sigma_T \left(\frac{E_e^{\text{X-ray}}}{m_e c^2} \right)^2 u_B N_e^{\text{X-ray}} \quad , \tag{6.14}$$

where $N_e^{\text{X-ray}}$ is the total number of electrons emitting X-rays. Using an approximate value of $L_{\rm syn}^{\text{X-ray}} = 4 \times 10^{39}$ erg s^{-1} at 10 keV (110 days after the merger [268]), Eq. (6.14) yields a total number of $N_e^{\text{X-ray}} = 3 \times 10^{46}$. The total number of accelerated electrons is dominated by the lowest energies as the number of non-thermal electron follows $E_e dN/dE_e \propto E_e^{-1}$, *i.e.*,

$$N_e^{\rm radio} = \frac{E_e^{\text{X-ray}}}{E_e^{\rm radio}} N_e^{\text{X-ray}} \quad . \tag{6.15}$$

This results in a number of radio-emitting electrons of $N_e^{\rm radio} = 3 \times 10^{51}$ ($E_\gamma = 10^{-6}$ eV). For this number, the low energy cut-off of the population is important, as the total electron population could otherwise reach a number close to the maximum possible number of swept-up and injected electrons $\sim 10^{55}$. As already mentioned, this scenario requires a much higher electron energy density compared to the magnetic energy density, which is $u_e \approx 10^7 u_B$ assuming a spherically expanding volume with $\beta = 0.2$ after 110 days. Note that also the high energy cut-off may be

higher than the energy which dominates X-ray production. If the acceleration is limited by the age of the remnant, a cut-off at $E_e^{\max} = 700$ TeV is expected at 110 days. A cooling break is not expected since synchrotron losses are sub-dominant in the relevant energy range.

There is a second, alternative scenario in which a strong magnetic field is present in order to boost the synchrotron production. Such a magnetic field could be supported by cosmic ray-driven magnetic field amplification [308], which could drive the field strength up to a saturation value of 2 G (see [278] for details). This is at the limit where the shock can still efficiently accelerate cosmic rays, but higher values are excluded as the shock would become sub-Alfvenic. However, this violates the constraint from the lack of a cooling feature, but there are two ways to circumvent it. The first option is that the electron spectrum is accelerated to a much harder spectrum than expected by diffusive shock acceleration, *e.g.*, by stochastic acceleration [309]. In such a strong magnetic field case, the entire population of non-thermal electrons would be cooled to a E^{-2} spectrum, producing the observed synchrotron emission. The second way to avoid violating the constraint is if the emitted radiation originates from electrons accelerated near the edge of the outflow. The number of picked up electrons increases with volume as the remnant expands. At the same time, the magnetic field strength may decrease linearly with time, implying that synchrotron emission is dominated by freshly accelerated electrons. If they dominate in number, the constraint on the synchrotron cooling efficiency of the source is relaxed. The magnetic field cannot be arbitrarily high as the observation of radio emission constrains the efficiency of synchrotron self-absorption in the remnant and with that the magnetic field to a maximum of 10 G. For strong magnetic fields of about 2 G, we find analogously $E_e^{\text{X-ray}} \approx 400 GeV$ with a number of high energy electrons $N_e^{\text{X-ray}} \approx 3 \times 10^{42}$ to account for the observed X-ray luminosity. This yields a number of radio-emitting electrons of 3×10^{47}, meaning that the total number of swept-up electrons cannot be reached even if the population extends to lower energies. The energy densities are related by $u_e \approx 10^{-7} u_B$ in this case.

This population of non-thermal particles embedded in the ambient radiation field inevitably gives rise to inverse Compton emission. If the observed synchrotron emission dominates the ambient photon field seen by the electrons, inverse Compton emission will be mainly produced via synchrotron self-Compton scattering (SSC). Significant SSC emission is expected for cases with $u_e \gg u_B$ [313]. The evolution of the non-thermal radiation field needed to calculate the inverse Compton emission is described as a power-law extrapolated from the X-ray luminosity observed at 9, 15 and 110 days after the merger [268, 300, 269] as

$$L_{\text{X-ray}} = 2 \times 10^{39} (t/110 \text{ days})^{0.6} \text{ erg s}^{-1} \quad . \tag{6.16}$$

At times $t < 15$ d, a bump is visible in the optical range of the spectral energy distribution with

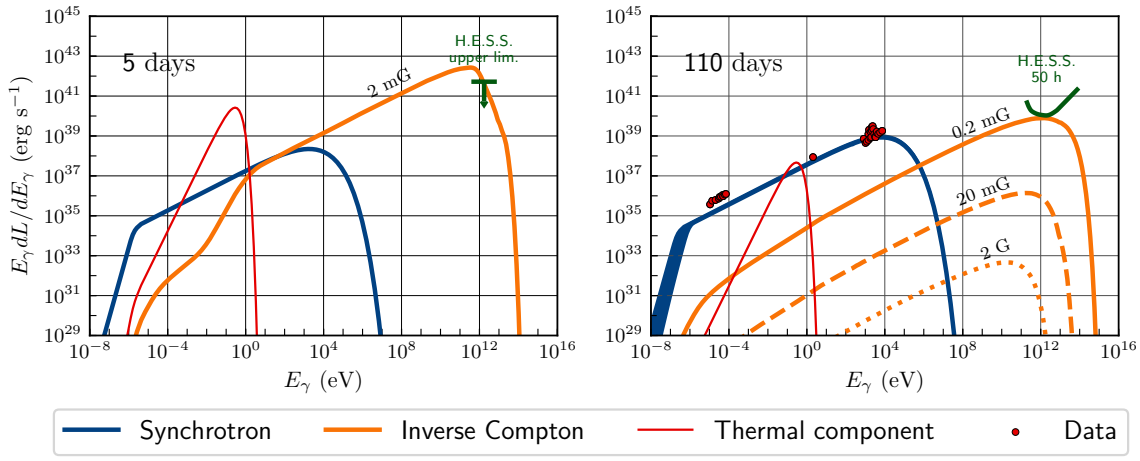

Figure 6.5: Spectrum produced by electrons via synchrotron emission (blue, including synchrotron self-absorption) and inverse Compton scattering (yellow) at five days (left) and 110 days (right) after the merger as a function of the observed energy. The thermal component is shown by the red curve. In the case of 110 days, we show predictions for three different values of the magnetic field. Optical [310], radio and X-ray [78] data is shown in red. At 5 days, the limit on the TeV luminosity [311] is shown in green, while at 110 days, the H.E.S.S. sensitivity (from [312]) translates into an upper limit on the source gamma-ray luminosity. Taken from [278].

a shape consistent with thermal emission [268]. The thermal bump decreases with time, which we model as

$$L_{\rm th} = 4 \times 10^{40} (t/7 \text{ days})^{-2.3} \text{ erg s}^{-1} \quad (t > 7 \text{ days}) \tag{6.17}$$

based on observations [314]. For $t < 7$ d, we assume that the luminosity of the thermal bump is constant.

Fig. 6.5 shows the resulting spectral energy distribution produced by the remnant at 5 days (left) and 110 days (right) after the merger. The low energy cut-on of the synchrotron component (blue curves) is due to synchrotron self-absorption, which we include in our computation following [315]. On the left hand side, we show the case of a 2 mG magnetic field at 5 days after the merger. At these early times, the thermal bump (red curve) provides the dominant target for inverse Compton emission (yellow curve). Furthermore, we show the H.E.S.S. upper limit in the energy range 0.5 – 6 TeV at 5.2 days [311], where we ensured that the inverse Compton emission does not overshoot the upper limit by adopting a high enough magnetic field. The sharp cut-off of the inverse Compton spectrum is introduced due to pair production on the thermal bump, which is included following [316]. The high level of inverse Compton emission for low magnetic fields indicates that a lower limit on the magnetic field may be placed at late time scales by

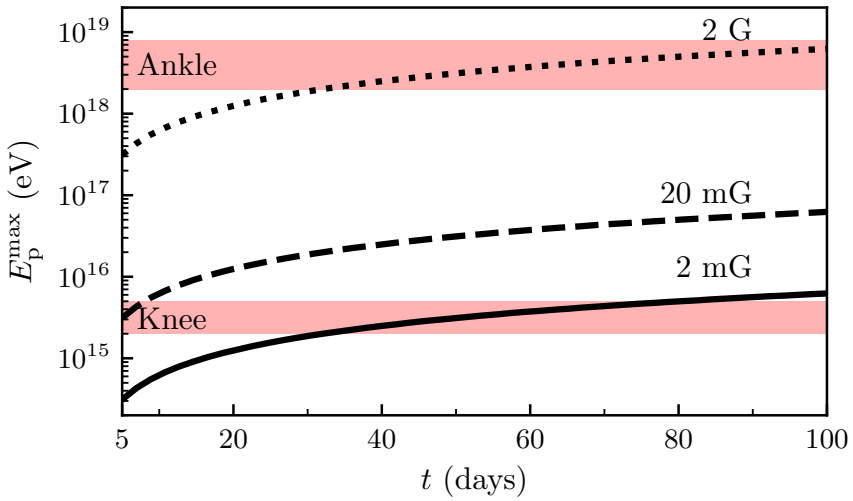

Figure 6.6: Maximum energy of accelerated protons as a function of the time since the merger for three different values of the magnetic field. The maximum energy is limited by the age of the remnant in every case, as photo-hadronic interactions are not efficient for protons. Taken from [278].

follow-up TeV observations. In the right panel, we show the result at 110 days with the inverse Compton component for three different magnetic fields for which the synchrotron radiation now provides the target. Data in radio, optical and X-ray are shown as red points [310, 78]. For the weakest magnetic field $B = 0.2$ mG, the luminosity in inverse Compton is the highest and the predicted gamma-ray luminosity is 10^{40} erg s^{-1} peaking at 1 TeV. This emission is at the level of the H.E.S.S. 50h sensitivity (green curve [312]) which indicates that it is sensitive enough to place a lower limit on the magnetic field strength. However, for high magnetic fields, the low electron density results in a gamma-ray power of only 3×10^{32} erg s^{-1} with a peak at 10 GeV.

6.2.2 Maximum cosmic ray energies and interaction rates

Acceleration and interaction processes for cosmic rays depend on the adopted strength of the magnetic field. In the following, we focus on the high magnetic field scenario, as low magnetic fields would otherwise increase the acceleration time, meaning that acceleration to high energies and photo-nuclear interactions would be rendered impossible. The maximum energy achieved by protons is always limited by the age of the remnant. We show the evolution of the maximum proton energy with time in Fig. 6.6 for three different, constant values of the magnetic field. In the weak magnetic field scenario, the source accelerates cosmic rays up to energies just beyond

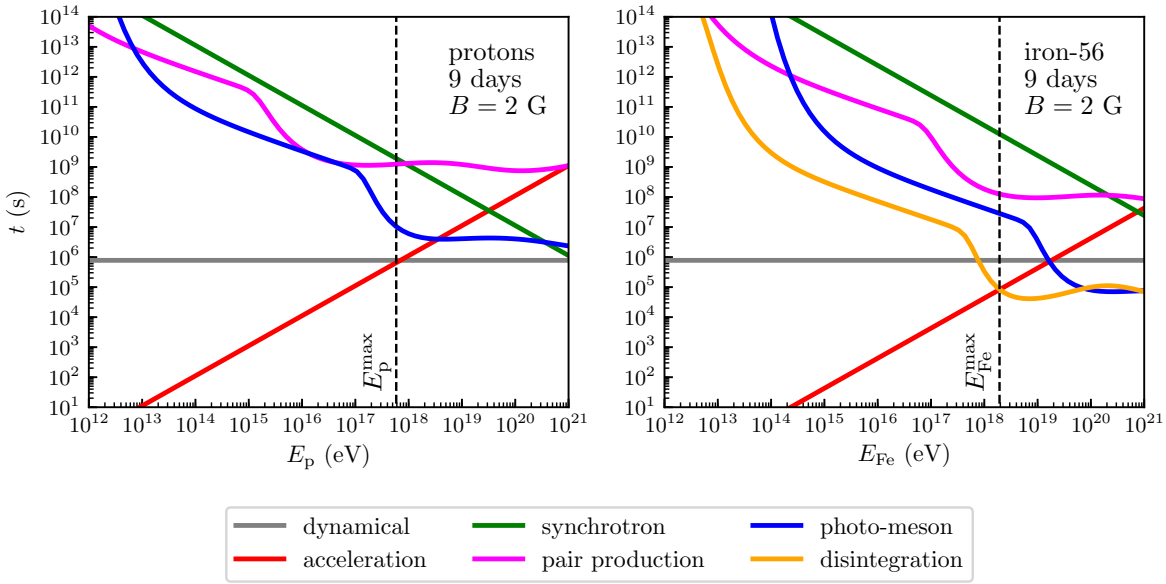

Figure 6.7: Interaction times for protons (left) and iron (right) 9 days after the merger in the high magnetic field scenario as a function of the energy in the observer's frame. Note that for the pair production and synchrotron processes, energy loss time scales are shown. Taken from [278].

the knee, whereas the strong magnetic field case supports cosmic ray energies up to the ankle.

Nuclei accelerated by the source interact with the ambient target photon field as well. At early times, considerable photo-disintegration can be expected in the source due to the thermal bump in the optical wavelength band. In Fig. 6.7, we show the interaction time scales as obtained by using *Neucosma* for different processes in the case of protons (left) and iron (right) at 9 days after the merger. For protons, the energy gain through acceleration (red line) is limited by the dynamical time scale, *i.e.*, the age of the remnant (gray line). Photo-meson production (blue curve) is inefficient and pair production (magenta curve) is sub-dominant but contributes considerably to the electron population. However, iron can efficiently disintegrate due to the bright optical radiation at 9 days, as shown by the yellow curve, with an optical thickness ~ 10 at 2 EeV. As the luminosity of the thermal component decreases, photo-disintegration becomes inefficient at later times, such that the maximum energy is also limited by the age of the remnant.

The temporal evolution of the optical thickness, defined as $\tau_{\rm int} = t_{\rm dyn}/t_{\rm int}$ at the maximum energy, is depicted in Fig. 6.8 for different isotopes. Additionally, we show the optical thickness to photo-meson production for protons. As fewer particles can escape for higher optical depths, it provides a measure for the fraction of accelerated particles that escape from the source. The optimal time for photo-disintegration is therefore within a few days to weeks after the

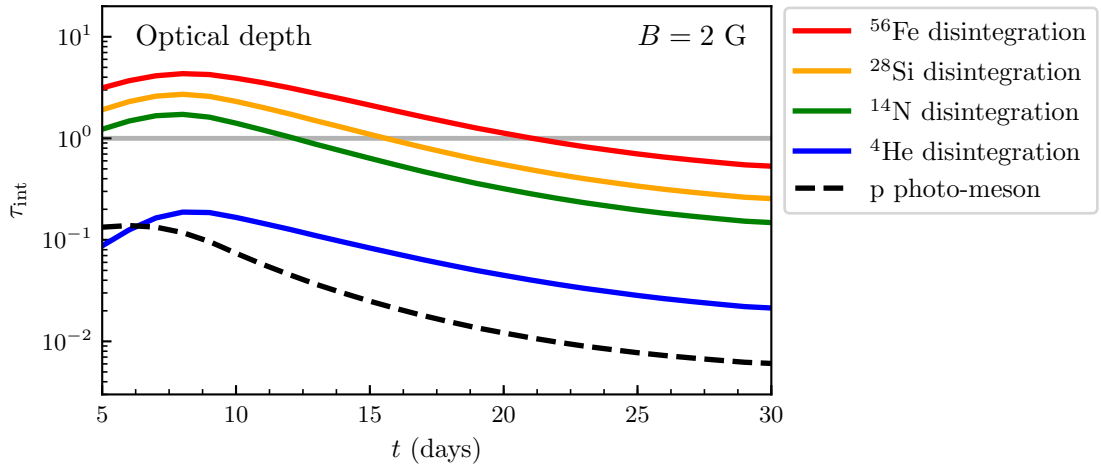

Figure 6.8: Optical depth to photo-disintegration of different isotopes (solid curves) and photo-meson production of protons (dashed curve) in the high magnetic field scenario as a function of the time since the merger. The horizontal gray line indicates the transition from the remnant being transparent to opaque. Taken from [278].

merger, due to the competition between dropping thermal photon field densities and rising maximum achievable energies in the expanding object. Because of effects of the nuclear cascade, the escaping cosmic rays can have different chemical composition with respect to the injected primary isotope. However, we did not explicitly calculate the spectra in this work.

Now we assume that the event EM170817 is representative for a whole population of identical sources which could accelerate cosmic ray nuclei. In order to support the cosmic ray spectrum at Earth with the observed abundance [193], a local emissivity of a few $\times 10^{44}$ erg Mpc^{-3} yr^{-1} is required. Together with the local rate of binary neutron star mergers of 1540^{+3200}_{-1220} inferred from the event [62], we estimate the energy input in cosmic rays in each merger event to be $E_{\rm CR} \approx 2 \times 10^{50}$ erg. This estimate is roughly consistent if we assume a fraction of $\sim 10\%$ of the released outflowing kinetic energy is dissipated in cosmic rays. With this, we can estimate the total neutrino fluence produced by the source as well. While the optical thickness is around $\tau_{p\gamma} = 0.1$ at 9 days, it diminishes due to the dimming of the thermal component and the expansion of the source. If we take an average optical thickness $\tau_{p\gamma} = 5 \times 10^{-3}$ from 5 to 160 days, we expect a neutrino fluence of $E_{\rm CR}\kappa_{p\gamma}\langle\tau_{p\gamma}\rangle/(4\pi d^2) \approx 5 \times 10^{-4}$ GeV cm^{-2} with the inelasticity $\kappa_{p\gamma} = 0.15$ and $d = 40$ Mpc the distance to the source. The normalization of this fluence is provided by the cosmic ray energy input, which carries notable uncertainties, mainly due to the uncertainties on the local rate. However, it can be compared to the current upper limits on the neutrino flux from EM170817 [289], showing that it would be challenging to detect with present instruments like IceCube.

Chapter 7

Conclusion and outlook

Multi-messenger astronomy is a powerful, rather new way to explore the Universe by combining information from disparate messenger particles arriving at Earth. Promising progress has been made especially recently with the observation of binary neutron star merger GW170817 electromagnetically and in gravitational waves as well as potentially the first correlated neutrino event from blazar TXS0506+056. However, many questions remain unsolved, of which the origin of the diffuse astrophysical neutrino flux and cosmic rays at ultra-high energies are two of the most profound. In this dissertation, we studied nuclear cascades in astrophysical objects and their impact on neutrino and cosmic ray production in order to contribute to solving these questions and to identify potential sources.

We use numerical models to compute the nuclear cascade, which is a full, self-consistent description of all relevant interactions in the source and thus goes one step further than most of the models used in the literature. Based on generic assumptions on the progenitor, jet formation and particle acceleration, radiation densities are provided which control the development of the nuclear cascade and, with that, cosmic ray and neutrino production. Up to about 500 different nuclear species up to ^{56}Fe and a total of around 50,000 competing interaction channels are included in the cascade, introducing a high level of complexity. The source model is then coupled to a cosmic ray propagation code in order to calculate the corresponding spectra at Earth, taking into account specific cosmological evolution scenarios. Our efficient combined source-propagation model enables us to study whether cosmic ray observations can be addressed depending on the injection composition, which is a key novelty in the field.

As we are able to compute the neutrino flavor composition within our source model, we showed that contrary to popular belief, the Glashow resonance is not suited for serving as a discriminator between pp and $p\gamma$ sources. This is due to the excess of π^+ in realistic pp interactions and the unavoidable contamination by π^- from multi-pion processes in photo-hadronic interactions. The latter effect gets even worse if the source is optically thick or heavier nuclei are present because of neutron interactions. On the other hand, high magnetic field strengths can lead to muon damping which can partially counteract this loss of discrimination power again. However, we

demonstrated that next generation neutrino telescopes such as IceCube-Gen2 can potentially constrain source properties and that the Glashow resonance can serve as a smoking gun signature for heavy nuclei in the sources.

Within this framework, we studied gamma-ray bursts and showed that, based on the development of the nuclear cascade, three different regimes can be identified in the parameter space. These are called Empty Cascade, Populated Cascade and Optically Thick Case for low, intermediate and high rate of interactions, respectively. In the Empty and Populated Cascade region, neutrinos are produced mainly off nuclei rather than secondary nucleons produced by disintegration, for which the uncertainties in the cross-section can lead to less reliable results in the fluxes. On the other hand, we demonstrated that the total neutrino flux weakly depends on the injected composition, such that the neutrino stacking limits remain valid even for heavy nuclei in the source. In order to accomodate the GRB-UHECR paradigm at least a moderate level of interactions in the source is needed, indicating that in-source interactions are not negligible. This is especially true when the ankle region has to be described, as secondary protons and neutrons naturally provide a soft low energy component. However, this is somewhat degenerate with the redshift evolution, as interactions during propagation also feed this light component. Although we studied only pure compositions in the first approach, we find that intermediate masses best describe the observations. The composition observables can however always be improved on by injecting a mixed composition. Our work is the first one doing such extensive parameter space scans taking into account the nuclear cascade and we can therefore strongly constrain gamma-ray bursts as treated in the one-zone model as sources of UHECRs. Despite finding viable solutions in the mixed composition ankle model, the corresponding neutrino fluxes are close to being excluded.

As GRBs are among the most studied and most constrained source candidates, they are suitable objects to test improved interaction models. It has been shown that the lack of cross-section measurements for photo-disintegration can lead to large uncertainties in the predicted neutrino fluxes, as nuclear interaction models do not always predict the cross-sections very accurate. Following this idea, we investigated the impact of improved photo-meson models in a GRB example with a maximum photon energy cut-off due to synchrotron self-absorption. As a consequence of different cross-section scalings and more nuclear channels than the conventional (superposition) model, neutrinos may be produced mainly by nucleons already in the Populated Cascade. However, the overall picture does not change dramatically with improved interaction models.

Our results on conventional GRBs point already towards low luminosity objects. In fact, low-luminosity gamma-ray bursts are an interesting alternative, as the stacking limits do not apply due to their dimness. The low luminosity is compensated by much larger durations, such that the

total energy output is of the same order as for conventional GRBs. Applying a similar procedure, we find that cosmic ray observations and neutrino data can be described simultaneously with a much lower baryonic loading as in the conventional case because of their higher event rate. While high-luminosity GRBs required a baryonic loading of $10^4 - 10^5$, we conclude that a loading of 10 is sufficient for LLGRBs, which is a typical value quoted in the literature. Furthermore, cosmic ray observations can be described across the ankle region if we include a residual galactic component following a power law in addition to the light extragalactic sub-ankle component from photo-hadronic interactions. Also in this case, a moderate level of interactions is needed in order to optimize the fit, a criterion which all investigated sources have in common. We explicitly showed how the nuclear cascade links the flux of the sub-ankle component and source neutrinos. In the best fit scenario, we arrive at an almost perfect description of the observations and predict the observation of cosmogenic neutrinos in next generation neutrino detectors.

While in the one-zone model a static burst is assumed with all emission regions being alike, a multi-zone approach allows for a dynamical evolution of the burst. Shells which are emitted from a central engine propagate with different Lorentz factors until they collide and form shocks where particle acceleration and interactions take place. This leads to GRBs which can provide both, heavy cosmic ray compositions and efficient neutrino production, as they are produced at different radii in the jet. The distribution of collisions over distance from the central emitter largely depends on the initial Lorentz factor distribution but the individual collisions scale as in the one-zone case. Thus, if the engine behaviour leads for instance mostly to collisions at small radii, large neutrino fluxes and a light composition is expected. Due to the complexity of the model, we invested a large amount of time in cross checks and understanding similarities and differences compared to the literature. At this point, we are able to reproduce the main results in the literature and compute fireballs efficiently, such that even in this model we are able to perform parameter space scans. For the methods presented in this thesis, many different applications exist already. In an ongoing work, we study the GRB-UHECR paradigm in the multi-zone context including a fit of the injected composition for different engines. This work will be the first of its kind, as it was not possible to fit the injection composition so far even in the one-zone model due to the complexity of the models. However, the multi-zone model faces difficulties because of the large amount of parameters, which especially for the engine are poorly constrained. This leads to a certain degeneracy of the results, such that further studies and observations are highly needed in order to get a clearer picture. Even if these degeneracies are taken into account, the GRB-UHECR paradigm is probably close to be excluded by neutrino stacking limits in the multi-zone picture as well.

From the behaviour of the engine, the light curve of the burst can be obtained in different energy bands. In the case of a disciplined engine where the stochastic spread in Lorentz factor is

small, a smooth light curve with a single bump is expected, while a high variability is expected for stochastic engines. This could be potentially interesting to correlate them to certain progenitor scenarios and classify events based on the light curves. Prompt gamma-ray emission is likely to be re-processed in the source by cascades, but we checked that for example in LLGRBs, even the observed spectrum can peak at TeV energies, which would be interesting for CTA for example. In fact, based on our work on LLGRBs as an additional motivation to search for these objects, a preliminary study of LLGRBs was initiated within the CTA collaboration and could be added to the CTA science case. Thus, it would be natural to continue studying the cascaded prompt emission, but also to apply the multi-zone framework on LLGRBs and other sources like TDEs and AGNs. More sophisticated composition models could be studied, *e.g.*, models where the composition depends on the radius of the shell. This can be motivated by the onion-like structure of collapsing stars, but unfortunately the literature on the expected injected composition depending on the progenitor scenario is sparse.

As an alternative source candidate, we studied stars that are tidally disrupted by black holes. This is a scenario which also provides enough energy to power UHECRs, yet at the same time is unconstrained by neutrino stacking analyses. This is due to their intrinsically low luminosity over large time scales, in addition to which they can potentially be obscured by dust. The required intermediate to heavy injection composition is supported by supermassive black holes disrupting main sequence stars or intermediate mass black holes disrupting carbon-oxygen white dwarfs. The cosmological distribution of TDEs is assumed to be negative, *i.e.*, local sources dominate, which has strong implications on the results: As the distance covered by cosmic rays during propagation is relatively small, less nucleons and cosmogenic neutrinos are expected with respect to a more positive (GRB-like) evolution. We find that, indeed, TDEs can describe both, cosmic rays at ultra-high energies as well as PeV neutrino data. Compared to LLGRBs, an important distinction is that TDEs are unlikely to be detected in cosmogenic neutrinos even in future instruments, mainly due to the negative source evolution. In contrast to other models in the literature, our work predicts that sizeable PeV neutrino fluxes can be obtained together with the UHECRs. In addition to the fact that most of the other models do not take into account interactions in the source up to this level of detail, we perform parameter space scans to test whether there are simultaneous solutions. In our models, solutions which fit only cosmic rays and provide a sub-dominant contribution to the neutrino flux exist as well, however we are able to identify a common description for both messengers.

In the TDE scenario, we expect a baryonic loading of about 500, which is consistent with current observations. Nevertheless, there are strong constraints from the non-observation of neutrino multiplets, which will eventually test the model. These constraints cannot be avoided by enhancing the baryonic loading, as energetics are violated and Swift J1644+57 should have been

visible in neutrinos otherwise. On the other hand, decreasing the luminosity while increasing the rate is in tension with X-ray observations. Thus, we computed the probability to obtain a multiplet based on our best fit flux, yielding a chance of 20% – 50%, which is on the verge of being in tension with data. Hence, the results will be tested in the near future and updated data sets are required to determine the viability of this scenario. A dedicated analysis which also uses the fluxes predicted from our model is in preparation by the IceCube collaboration. Cross-correlating neutrino events with observed TDEs in time and position could establish an association of neutrinos with TDEs. Precision measurements of jetted TDEs would greatly help to build more realistic models, as most of them are based on one particular event at the moment. By an increased sample size, the population model could also be improved, having direct implications on the baryonic loading and with that on the viability of TDEs as sources of UHECRs. If the redshift evolution turns out to be less negative than assumed, it would be also difficult to avoid constraints from the diffuse gamma-ray background. Obvious follow-up projects cover time dependent neutrino fluxes from TDEs, which our code can compute as well, or adapting the model to treat similar sources as X-ray flashes or fast radio bursts for example.

The detection of gravitational wave event GW170817 associated with a binary neutron star merger was awarded the Breakthrough of the Year in 2017. It triggered a multi-messenger observation campaign of unprecedented extent which revealed emission across several wavelength bands. However, no neutrinos were detected correlated to this event, and due to the low luminosity of the emission, it was speculated about alternative jet scenarios. We showed that neither in a structured low luminosity jet nor in an off-axis scenario significant neutrino production is expected, although the de-boosted luminosity may be much higher in the on-axis frame. Furthermore, we constrain the maximum possible neutrino fluences by demanding super-photospheric collisions, as otherwise no electromagnetic radiation would have been observed. Our constraints on the observation angle and the Lorentz factor are the most stringent for a typical baryonic loading of 10. After the prompt phase, the long time evolution of the light curve seemed to disfavor off-axis emission and prefer choked jets or cocoon scenarios. Recently, off-axis jets seem to be preferred again by data, however only further observations will lead to a definitive answer. It is expected that a distinction between different jet models is possible after 1–2 years. The contribution of such events to the diffuse flux is unknown, yet the contribution seems to be rather small as the event itself is short in duration, given that GW170817 is a representative case. On the other hand, the rate of neutron star mergers is highly uncertain and they also play a role in the production of heavy elements by the associated kilonova.

The spectral energy distribution of the remnant of this object was measured thoroughly in different wavelengths. From that, we discuss several magnetic field scenarios based on the lack of cooling features in the photon distribution. We explicitly show that in the case of a strong

magnetic field, late time acceleration of cosmic rays can provide energies reaching up to the ankle. Therefore, the population of neutron star merger remnants is potentially interesting as a component to bridge the gap between iron knee and ankle. We find a bottle-neck for the photo-disintegration of heavy nuclei within the first days to weeks after the merger, which is due to the thermal radiation of the kilonova that quickly fades while the other components are brightening. On the other hand, the remnant is optically thin to photo-meson production of nucleons at all times. Thus, we do not expect to detect any neutrinos from the remnant either. In order to improve on the estimated contribution of such objects to the cosmic ray and neutrino fluxes, improved measurements on the rate are required.

Multi-messenger astronomy is a modern, quickly evolving research field. It benefits more and more from the lively interactions across different expertises, between experimentalists and theorists as well as among different collaborations. Especially recently, major success stories were written along quotes stating that the multi-messenger era finally begun. New experiments such as CTA, IceCube Gen-2, GRAND, AugerPrime, Advanced LIGO and many more will record data with even better sensitivity and greatly increase our knowledge about any messenger and the Universe as a whole. For the future of the field, it is important that statistics increase such that cosmological models can be improved, while precision measurements of particular events reveal more about their true nature. Model components which are only poorly constrained by now, such as engines and their behaviour for example, would be of special interest. Theoretical models and their growing complexity can only be constrained by more sophisticated observations and a better understanding of the underlying physics. Moreover, improved alert systems will enable us to collect more diverse data of certain events, such that our task is to draw a consistent picture from that. However, not only data from new detectors is needed, but also measurements on nuclear data is for instance urgently needed in order to refine state-of-the-art models and theories. Such experiments are already in reach and would be greatly appreciated by the astroparticle physics community. Therefore, stronger collaborations with the nuclear physics community should be established. Astroparticle physics will profit from any advance in fundamental research such as physics beyond the Standard Model of particle physics. Vice versa, next generation instruments will also be able to test the Standard Model in unique astrophysical environments not accessible with terrestrial experiments. These co-dependences and correlations across various disciplines and approaches makes multi-messenger astrophysics a successful research field. Exciting times lie ahead which, thanks to the steady advances achieved as a collective effort of the community, will eventually be rewarded with the solution to the origin of ultra-high energy cosmic rays.

Appendix A

Efficient calculation of nuclear processes

In Eq. (3.2), the injection rate of particles of species i and energy E_i from the decay or interaction of a parent particle j can be approximated by

$$Q'_{j\to i}(E_i) = \int \frac{dx}{x} N'_j(E'_j)\Gamma'_j(E'_j)\frac{dn_{j\to i}}{dx}(x,\sqrt{s}) \quad , \tag{A.1}$$

where Γ'_j is the interaction rate, $x = E'_i/E'_j$ is the fraction of primary energy taken by the secondary and $\sqrt{s}$ is the center-of-mass energy. The distribution of secondaries of type i per final state energy interval dx is described by the function

$$\frac{dn_{j\to i}}{dx}(x,\sqrt{s}) \simeq M_{j\to i}(\sqrt{s}) p_{j\to i}(x,\sqrt{s}) \tag{A.2}$$

with the probability distribution $p_{j\to i}$ normalized to one, such that the integrated function yields the average number of secondaries $M_{j\to i}$ produced per interaction, *i.e.*, the multiplicity. The simplest approximation for the re-distribution function $p_{j\to i}$ is the δ-distribution $\delta(x - \chi_{j\to i})$. The function $\chi_{j\to i}$ describes the (mean) fraction of parent energy deposited in the secondary, which in the case for a secondary nucleus is $\chi_{j\to i} \simeq A_i/A_j$ assuming Lorentz factor conservation. The injection of secondary nuclei due to beta decays and spontaneous emission is therefore simply given by

$$Q'_{j\to i}(E_i) = N'_j\left(\frac{E'_j}{\chi_{j\to i}}\right)\Gamma'_j\left(\frac{E'_j}{\chi_{j\to i}}\right)\frac{M_{j\to i}}{\chi_{j\to i}} \tag{A.3}$$

with the interaction rate $\Gamma'_j = m_j/(E'_j\tau_{0,j})$. For β^{pm} decays, $\chi_{j\to i} \simeq 1$ and $M_{j\to i}$ is the branching ratio into the corresponding channel. We use refined computations for the neutrino spectrum of beta decays from relativistic ions, for which we take the peak value of $\chi_{j\to\nu}$ of the re-distribution function extracted from [317].

For photo-hadronic interactions, the interaction rate depends on the target photon field and is given by

$$\Gamma'_j(E'_j) = \int d\varepsilon' \int_{-1}^{+1} \frac{d\cos\theta'_{A\gamma}}{2}(1-\cos\theta'_{A\gamma}) n'_\gamma(\varepsilon')\sigma_j^{\rm abs}(\epsilon_r) \tag{A.4}$$

for isotropic photon densities $n'_\gamma(\varepsilon')$. In this equation, ε' represents the photon energy and $\theta'_{A\gamma}$ is the pitch angle between the momenta of the photon and the nucleus. The absorption cross section for species j is $\sigma_j^{\mathrm{abs}}(\epsilon_r)$ with

$$\epsilon_r = \frac{E'_j \varepsilon'}{m_A}(1 - \cos\theta'_{A\gamma}) \tag{A.5}$$

the photon energy in the parent rest frame (PRF) in the limit $\beta'_A \approx 1$. It corresponds to the available center-of-mass energy $\sqrt{s}$ of the interaction as $s = m_A^2 + 2m_A\epsilon_r$. Defining

$$f_j(y') = \frac{1}{2y'^2}\int_0^{2y'} d\epsilon_r \epsilon_r \sigma_j^{\mathrm{abs}}(\epsilon_r) \tag{A.6}$$

with $y' = E'_j\varepsilon'/m_A$ as the "typical" center-of-mass energy, the interaction rate can be written as an integral over the photon density

$$\Gamma'_j(E'_j) = \int d\varepsilon' n'_\gamma(\varepsilon') f_j(y') \quad . \tag{A.7}$$

The function $f_j(y')$ is an integral over the cross section (which is zero below the threshold ϵ_{th} by definition), which can be interpreted as pitch angle averaged cross section. The advantage is that it can be pre-computed, such that the interaction rate in Eq. (A.7) can be obtained by only a single integral. For the secondary nuclei injection, we can then write

$$Q'_{j\to i}(E_i) = N'_j\left(\frac{E'_j}{\chi_{j\to i}}\right)\frac{m_A}{E'_i}\int dy' n'_\gamma\left(\frac{m_{A_j} y' \chi_{j\to i}}{E'_i}\right) g_{j\to i}(y') \tag{A.8}$$

with $\chi_{j\to i} = A_i/A_j$ and the function

$$g_{j\to i}(y') = \frac{1}{2y'^2}\int_{\epsilon_{\mathrm{th}}}^{2y'} d\epsilon_r \epsilon_r \sigma_j^{\mathrm{abs}}(\epsilon_r) M_{j\to i}(\epsilon_r) \quad . \tag{A.9}$$

Here, the re-injection can still be obtained with a single integral as the function $g_{j\to i}$ can be pre-computed as well, taking into account that the secondary multiplicity strongly depends on the center-of-mass energy. The procedure further simplifies in the case of a constant target photon spectrum, as in this work, enabling us to efficiently perform these calculations.

The pre-computation of the values for $f(y')$ and $g_{j\to i}(y')$ are produced from disintegration models such as TALYS [175]. The quantity $g_{j\to i}(y')/f_j(y')$ thus describes the secondary multiplicity as a function of y', including the pitch angle averaging in the isotropic target photon field. In Fig. A.1, this is illustrated for three different isotopes for $y' = 50$ MeV (slightly above the GDR). In all cases, nucleons as well as light nuclei are produced in the process. Residual nuclei

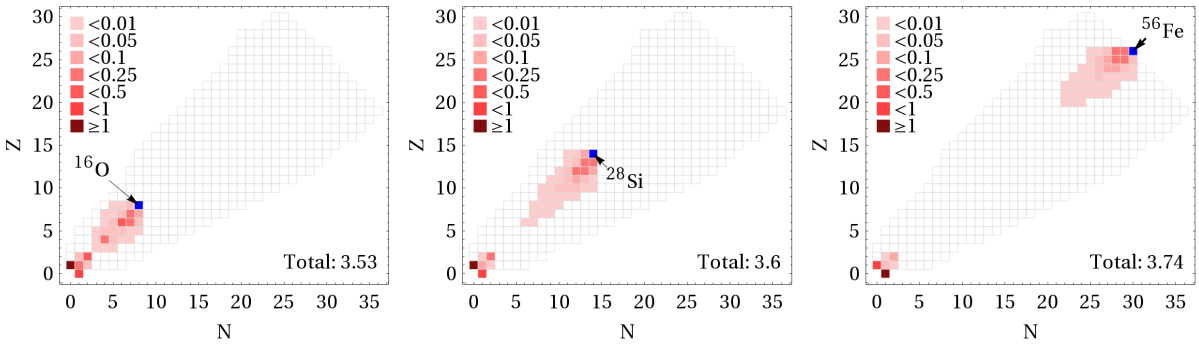

Figure A.1: Isotope chart illustrating secondary multiplicities for the disintegration of ^{16}O (left), ^{28}Si (center) and ^{56}Fe (right) for the TALYS disintegration model [175]. The color-coding indicates the average number of secondary nuclei $g_{j\to i}(y')/f_j(y')$ averaged over the pitch angle for $y' = 50$ MeV (injected isotopes are marked in blue). The total number of secondaries produced per interaction is (on average) shown in the lower right corner of each panel. Taken from [159].

tend to populate the main diagonal, however, compared to one-dimensional disintegration models such as the PSB model [185], the isotope chart will be populated in two dimensions, not only along the main diagonal but also perpendicular to it due to unstable isobars. The importance of using a sufficiently sophisticated disintegration model has been demonstrated in [24].

The interaction rate for photo-meson production can be calculated in a similar fashion, with the main difference that the re-distribution functions of secondary mesons should be taken into account. The methods in this work are a further advancement of [6]. If the re-distribution of secondaries is to be described, it is difficult to avoid double integrals in the injection function, which is the bottle-neck for efficient computations, and brute-force sampling methods sampling methods of interaction models often do not take this into account. The original idea in [6] is to discretize one of these integrals into a small number of interaction types by a physics-motivated splitting into t-channel production, resonances and multi-pion production. These interaction types could be evaluated similar to Eq. (A.8) while having different characteristics in terms of their inelasticities and multiplicities. We use a different method here, allowing for the automatic definition of interaction types for many isotopes, which will be even more efficient and precise as [6] despite being based in similar principles. By re-writing and discretizing one of the integrals in terms of x, the injection of secondaries can be written as

$$Q'_{j\to i}(E'_i) = \sum_{k=1}^{T} \Delta\tilde{x}_k N'_j \left(\frac{E'_i}{x_k}\right) \frac{m_{A_j}}{E'_i} \int dy' n'_\gamma \left(\frac{m_{A_j} y' x_k}{E'_i}\right) h_{j\to i}(\tilde{x}_k, y') \tag{A.10}$$

for T such interactions types. In this equation, we use $\tilde{x} = \log_{10}(x)$ and define a new re-

distribution function

$$h_{j\to i}(\tilde{x}_k, y') = \frac{1}{2y'^2}\int_{\epsilon_{\rm th}}^{2y'} d\epsilon_r \epsilon_r \frac{d\sigma_{j\to i}^{\rm incl}}{d\tilde{x}}(\tilde{x}_k, \epsilon_r) \quad , \tag{A.11}$$

in which we identified $\sigma_j^{\rm abs} dn_{j\to i}/d\tilde{x}$ with the differential inclusive cross section $d\sigma_{j\to i}^{\rm incl}/d\tilde{x}$. Now, the function $h_{j\to i}$ can again be directly compiled from the inclusive cross sections once an appropriate splitting in x is defined. In order to calculate the secondary injection, only a single integral has to be computed, which has to be summed over several discrete values of $\tilde{x}_k$. Note that

$$g_{j\to i}(y') = \sum_{k=1}^{T} \Delta\tilde{x}_k h_{j\to i}(\tilde{x}_k, y') \quad , \tag{A.12}$$

which implies that the re-distribution function for the secondaries has to add up to yield the secondary multiplicity, and the interaction types should be chosen accordingly. The simplest example which is often used in the literature is $T = 1$ and $dn_{j\to i}/d\tilde{x}(\tilde{x}_1, y') = M_{j\to i}$ with $\tilde{x}_1 = \log_{10}\chi_{j\to i}$ such that $h_{j\to i} = g_{j\to i}$. Using several such interaction types will lead to more precise results at the expense of computation time. We have tested several splittings in $\tilde{x}$ and found that $T = 4$ with $\tilde{x}_1 = -1.4$, $\tilde{x}_2 = -1.0$, $\tilde{x}_3 = -0.6$ and $\tilde{x}_4 = -0.2$ give reasonable results while being computationally efficient. We have also tested alternatives with eight and 17 values of $\tilde{x}$, which did not provide a significant gain in precision.

Appendix B

Photosphere and two-photon annihilation

Photons can be inhibited from escaping the source by Thomson scattering, which is the elastic scattering of electromagnetic radiation by free charged particles. The photosphere is the radius, measured as distance from the central engine, at which the optical depth to Thomson scattering equals unity. It can be deduced from collision parameters starting from the electron density, which is assumed to be equal to the proton density as shells are on average electrically neutral. Thus,

$$n'_e \simeq \frac{M}{m_p V_{\rm iso}} \quad , \tag{B.1}$$

where m_p is the proton mass, M is the mass of the shell and $V_{\rm iso} = 4\pi R^2 \Delta d$ is the isotropic volume as a function of the collision radius R and shell widh Δd. This implicitly assumes that pair production processes do not significantly increase electron and positron densities. The optical depth to Thomson scattering is then

$$\tau'_{\rm Th} \simeq \frac{1}{n'_e \sigma_{\rm Th} \Delta d} \tag{B.2}$$

with the Thomson cross section $\sigma_{\rm Th} \approx 66.52$ fm^2. The mass of the shell can be expressed as the ratio of its kinetic energy $E_{\rm kin}$ and the corresponding Lorentz factor Γ, which is related to the isotropic energy $E_{\rm iso}$ by the baryonic loading ξ_A and a conversion efficiency parameter ϵ, *i.e.*,

$$Mc^2 = \frac{E_{\rm kin}}{\Gamma} = \frac{\epsilon \xi_A E_{\rm iso}}{\Gamma} \quad . \tag{B.3}$$

In this equation, $E_{\rm iso}$ represents the isotropic equivalent energy in gamma-rays in the on-axis frame per shell. It can be rewritten in terms of luminosity as $E_{\rm iso} = L_\gamma t_v$, such that the photospheric radius is given by

$$R_{\rm ph} \simeq \sqrt{\frac{\xi_a L_\gamma t_v \sigma_{\rm Th}}{4\pi m_p \Gamma \epsilon}} \quad , \tag{B.4}$$

similar to Eq. (6.2). In case of a fixed observation off-axis, as it is the case in Sec. 6.1, an additional factor for boosting back in the on-axis frame enters according to Eq. (6.6). Furthermore, if only the total isotropic equivalent energy is available, an additional factor $N_{\rm sh} = T_{90}/t_v$ enters in order to convert it into the per-shell energy.

Thomson scattering is regarded as the low energy limit of Compton scattering. However, high energy gamma-rays can be produced by the decay of neutral pions as a by-product of photo-hadronic interactions for instance. If photons above TeV energies are able to leave the source, electromagnetic cascades on the CMB and EBL are initiated, processing them down to TeV energies. The gamma-ray background in this energy range is constrained by Fermi, challenging sources which are transparent to gamma-rays at these energies. The situation gets worse for negative source evolution, as most of the gamma-rays originate from close by sources, for which the cascades might not even fully develop. On the other hand, $p\gamma$ sources are in general optically thick to high energy gamma-rays due to intrasource cascades, *i.e.*, two-photon annihilation may inhibit the direct escape of gamma-rays in this range [318]. Especially the low energy target photon field is important for the behaviour of the optical depth, but often it is only poorly constrained by observations. Frequently used extrapolations are based on Swift data in the energy range 0.4 – 13.5 keV. In this work, we use broken power laws which are consistent with the measurements. Pair creation $\gamma + \gamma \to e^+ + e^-$ is the relevant process for high energy gamma-ray escape. The corresponding optical depth can be estimated according to [318] as

$$\tau_{\gamma\gamma}(\varepsilon_\gamma) \approx 0.1 \sigma_{\rm Th} \frac{R}{\Gamma} \varepsilon' \frac{dN}{d\varepsilon'}\Big|_{\varepsilon' = m_e^2 c^4/\varepsilon'_\gamma} \quad , \tag{B.5}$$

where ε_γ is the energy of the high energy photon and ε is the target photon energy. Primed quantities refer to the SRF, such that $\varepsilon' = \varepsilon/\Gamma$. The factor 0.1 originates from the weighting of different power law segments, which is set to typical, rather conservative value here for the sake of simplicity. For the TDE scenario as presented in Chapter 5, we find for example that the source is at the verge of being optically thick at gamma-ray energies around ~ 10 PeV. We want to stress that the behaviour of the target photon spectrum beyond the measurement is unknown. A second spectral break or a low energy thermal component could be further explanations for the non-observation of high energy photons. After all, the escape of PeV gamma-rays is speculative and $p\gamma$ sources tend in general to be rather optically thick.

Bibliography

[1] L. A. Anchordoqui. Ultra-High-Energy Cosmic Rays. 2018.

[2] W. F. Hanlon. *The energy spectrum of ultra high energy cosmic rays measured by the High Resolution Fly's Eye observatory in stereoscopic mode.* PhD thesis, Utah U., 2008. URL http://proquest.umi.com/pqdweb?sid=1&Fmt=2&clientId=79356&RQT=309&VName=PQD&did=1598931911.

[3] The pierre auger cosmic ray observatory. *Nucl. Instrum. Meth.*, 798:172 – 213, 2015. ISSN 0168-9002. doi: https://doi.org/10.1016/j.nima.2015.06.058. URL http://www.sciencedirect.com/science/article/pii/S0168900215008086.

[4] A. Aab et al. Combined fit of spectrum and composition data as measured by the Pierre Auger Observatory. *JCAP*, 1704(04):038, 2017. doi: 10.1088/1475-7516/2017/04/038.

[5] A. Aab et al. Depth of maximum of air-shower profiles at the Pierre Auger Observatory. I. Measurements at energies above $10^{17.8}$ eV. *Phys. Rev.*, D90(12):122005, 2014. doi: 10.1103/PhysRevD.90.122005.

[6] S. Hümmer et al. Simplified models for photohadronic interactions in cosmic accelerators. *Astrophys. J.*, 721:630–652, 2010. doi: 10.1088/0004-637X/721/1/630.

[7] J. F. Beacom et al. Measuring flavor ratios of high-energy astrophysical neutrinos. *Phys. Rev.*, D68:093005, 2003. Erratum-ibid.D72, 019901 (2005).

[8] M.G. Aartsen et al. Evidence for High-Energy Extraterrestrial Neutrinos at the IceCube Detector. *Science*, 342(6161):1242856, 2013. doi: 10.1126/science.1242856.

[9] M. G. Aartsen et al. All-sky Search for Time-integrated Neutrino Emission from Astrophysical Sources with 7 yr of IceCube Data. *Astrophys. J.*, 835(2):151, 2017. doi: 10.3847/1538-4357/835/2/151.

[10] I. Bartos and M. Kowalski. *Multimessenger Astronomy.* 2399-2891. IOP Publishing, 2017. ISBN 978-0-7503-1369-8. doi: 10.1088/978-0-7503-1369-8. URL http://dx.doi.org/10.1088/978-0-7503-1369-8.

[11] T. Piran. The physics of gamma-ray bursts. *Rev. Mod. Phys.*, 76:1143–1210, 2004. doi: 10.1103/RevModPhys.76.1143.

[12] F. W. Stecker et al. High-energy neutrinos from active galactic nuclei. *Phys. Rev. Lett.*, 66:2697–2700, 1991. doi: 10.1103/PhysRevLett.66.2697.

[13] E. Waxman and J. N. Bahcall. High-energy neutrinos from cosmological gamma-ray burst fireballs. *Phys. Rev. Lett.*, 78:2292–2295, 1997. doi: 10.1103/PhysRevLett.78.2292.

[14] R. Abbasi et al. An absence of neutrinos associated with cosmic-ray acceleration in γ-ray bursts. *Nature*, 484:351–353, 2012. doi: 10.1038/nature11068.

[15] D. Guetta et al. Neutrinos from individual gamma-ray bursts in the BATSE catalog. *Astropart. Phys.*, 20:429–455, 2004. doi: 10.1016/S0927-6505(03)00211-1.

[16] S. Hümmer, P. Baerwald, and W. Winter. Neutrino Emission from Gamma-Ray Burst Fireballs, Revised. *Phys. Rev. Lett.*, 108:231101, 2012. doi: 10.1103/PhysRevLett.108.231101.

[17] H.-N. He et al. Icecube non-detection of GRBs: Constraints on the fireball properties. *Astrophys. J.*, 752:29, 2012. doi: 10.1088/0004-637X/752/1/29.

[18] M. G. Aartsen et al. Extending the search for muon neutrinos coincident with gamma-ray bursts in IceCube data. *Astrophys. J.*, 843(2):112, 2017. doi: 10.3847/1538-4357/aa7569.

[19] M. Ahlers, M.C. Gonzalez-Garcia, and F. Halzen. GRBs on probation: testing the UHE CR paradigm with IceCube. *Astropart. Phys.*, 35:87–94, 2011. doi: 10.1016/j.astropartphys.2011.05.008.

[20] X.-Y. Wang, S. Razzaque, and P. Meszaros. On the Origin and Survival of UHE Cosmic-Ray Nuclei in GRBs and Hypernovae. *Astrophys. J.*, 677:432–440, 2008. doi: 10.1086/529018.

[21] L. A. Anchordoqui et al. High-energy neutrinos from astrophysical accelerators of cosmic ray nuclei. *Astropart. Phys.*, 29:1–13, 2008. doi: 10.1016/j.astropartphys.2007.10.006.

[22] K. Murase et al. High-energy cosmic-ray nuclei from high- and low-luminosity gamma-ray bursts and implications for multi-messenger astronomy. *Phys.Rev.*, D78:023005, 2008. doi: 10.1103/PhysRevD.78.023005.

[23] N. Globus et al. UHECR acceleration at GRB internal shocks. *Mon. Not. Roy. Astron. Soc.*, 451(1):751–790, 2015. doi: 10.1093/mnras/stv893.

[24] D. Boncioli, A. Fedynitch, and W. Winter. Nuclear Physics Meets the Sources of the Ultra-High Energy Cosmic Rays. *Scientific Reports*, 7:4882, 2017.

[25] K.-H. Kampert et al. CRPropa 2.0 – a Public Framework for Propagating High Energy Nuclei, Secondary Gamma Rays and Neutrinos. *Astropart. Phys.*, 42:41–51, 2013. doi: 10.1016/j.astropartphys.2012.12.001.

[26] P. Baerwald, M. Bustamante, and W. Winter. Are gamma-ray bursts the sources of ultra-high energy cosmic rays? *Astropart. Phys.*, 62:66, 2015.

[27] M. Unger, G. R. Farrar, and L. A. Anchordoqui. Origin of the ankle in the ultrahigh energy cosmic ray spectrum, and of the extragalactic protons below it. *Phys. Rev.*, D92 (12):123001, 2015. doi: 10.1103/PhysRevD.92.123001.

[28] R. Aloisio et al. A dip in the UHECR spectrum and the transition from galactic to extragalactic cosmic rays. *Astropart.Phys.*, 27:76–91, 2007. doi: 10.1016/j.astropartphys.2006.09.004.

[29] J. Heinze et al. Cosmogenic Neutrinos Challenge the Cosmic Ray Proton Dip Model. *Astrophys. J.*, 825(2):122, 2016. doi: 10.3847/0004-637X/825/2/122.

[30] A. D. Supanitsky. Implications of gamma-ray observations on proton models of ultrahigh energy cosmic rays. *Phys. Rev.*, D94(6):063002, 2016. doi: 10.1103/PhysRevD.94.063002.

[31] V. Berezinsky, A. Gazizov, and O. Kalashev. Cascade photons as test of protons in UHECR. *Astropart. Phys.*, 84:52–61, 2016. doi: 10.1016/j.astropartphys.2016.08.007.

[32] N. Globus, D. Allard, and E. Parizot. A complete model of the cosmic ray spectrum and composition across the Galactic to extragalactic transition. *Phys. Rev.*, D92(2):021302, 2015. doi: 10.1103/PhysRevD.92.021302.

[33] N. Globus et al. Probing the Extragalactic Cosmic Rays origin with gamma-ray and neutrino backgrounds. *Astrophys. J.*, 839(2):L22, 2017. doi: 10.3847/2041-8213/aa6af0.

[34] D. Guetta and M. Della Valle. On the Rates of Gamma Ray Bursts and Type Ib/c Supernovae. *Astrophys. J.*, 657:L73–L76, 2007. doi: 10.1086/511417.

[35] E. Liang, B. Zhang, and Z. G. Dai. Low Luminosity Gamma-Ray Bursts as a Unique Population: Luminosity Function, Local Rate, and Beaming Factor. *Astrophys. J.*, 662: 1111–1118, 2007. doi: 10.1086/517959.

[36] F. Virgili, E. Liang, and B. Zhang. Low-Luminosity Gamma-Ray Bursts as a Distinct GRB Population:A Monte Carlo Analysis. *Mon. Not. Roy. Astron. Soc.*, 392:91, 2009. doi: 10.1111/j.1365-2966.2008.14063.x.

[37] H. Sun, B. Zhang, and Z. Li. Extragalactic High-energy Transients: Event Rate Densities and Luminosity Functions. *Astrophys. J.*, 812(1):33, 2015. doi: 10.1088/0004-637X/812/1/33.

[38] K. Murase et al. High Energy Neutrinos and Cosmic-Rays from Low-Luminosity Gamma-Ray Bursts? *Astrophys. J.*, 651:L5–L8, 2006. doi: 10.1086/509323.

[39] R.-Y. Liu, X.-Y. Wang, and Z.-G. Dai. Nearby low-luminosity GRBs as the sources of ultra-high energy cosmic rays revisited. *Mon. Not. Roy. Astron. Soc.*, 418:1382, 2011. doi: 10.1111/j.1365-2966.2011.19590.x.

[40] N. Senno, K. Murase, and P. Meszaros. Choked Jets and Low-Luminosity Gamma-Ray Bursts as Hidden Neutrino Sources. *Phys. Rev.*, D93(8):083003, 2016. doi: 10.1103/PhysRevD.93.083003.

[41] I. Tamborra and S. Ando. Inspecting the supernova–gamma-ray-burst connection with high-energy neutrinos. *Phys. Rev.*, D93(5):053010, 2016. doi: 10.1103/PhysRevD.93.053010.

[42] B. T. Zhang et al. Low-luminosity gamma-ray bursts as the sources of ultrahigh-energy cosmic ray nuclei. *Phys. Rev.*, D97(8):083010, 2018. doi: 10.1103/PhysRevD.97.083010.

[43] J. G. Hills. Possible power source of seyfert galaxies and qsos. *Nature*, 254(5498):295–298, 03 1975. URL `http://dx.doi.org/10.1038/254295a0`.

[44] J. H. Lacy, C. H. Townes, and D. J. Hollenbach. The nature of the central parsec of the Galaxy. *Astrophys. J.*, 262:120–134, November 1982. doi: 10.1086/160402.

[45] M. J. Rees. Tidal disruption of stars by black holes of 10 to the 6th-10 to the 8th solar masses in nearby galaxies. *Nature*, 333:523–528, 1988. doi: 10.1038/333523a0.

[46] G. R. Farrar and A. Gruzinov. Giant AGN Flares and Cosmic Ray Bursts. *Astrophys. J.*, 693:329–332, 2009. doi: 10.1088/0004-637X/693/1/329.

[47] G. R. Farrar and T. Piran. Tidal disruption jets as the source of Ultra-High Energy Cosmic Rays. 2014.

[48] X.-Y. Wang et al. Probing the tidal disruption flares of massive black holes with high-energy neutrinos. *Phys. Rev.*, D84:081301, 2011. doi: 10.1103/PhysRevD.84.081301.

[49] K. Murase and K. Ioka. TeV-PeV Neutrinos from Low-Power Gamma-Ray Burst Jets inside Stars. 2013.

[50] D. N. Burrows et al. Discovery of the Onset of Rapid Accretion by a Dormant Massive Black Hole. *Nature*, 476:421, 2011. doi: 10.1038/nature10374.

[51] S. B. Cenko et al. Swift J2058.4+0516: Discovery of a Possible Second Relativistic Tidal Disruption Flare. *Astrophys. J.*, 753:77, 2012. doi: 10.1088/0004-637X/753/1/77.

[52] G. C. Brown et al. Swift J1112.2-8238: a candidate relativistic tidal disruption flare. *Mon. Not. Roy. Astron. Soc.*, 452(4):4297–4306, 2015. doi: 10.1093/mnras/stv1520.

[53] J. S. Bloom et al. A relativistic jetted outburst from a massive black hole fed by a tidally disrupted star. *Science*, 333:203, 2011. doi: 10.1126/science.1207150.

[54] R. Alves Batista and J. Silk. Ultra-high-energy cosmic rays from tidally-ignited stars. 2017.

[55] J. H. Krolik and T. Piran. Swift J1644+57: A White Dwarf Tidally Disrupted by a $10^4 M_\odot$ Black Hole? *Astrophys. J.*, 743:134, 2011. doi: 10.1088/0004-637X/743/2/134.

[56] X.-Y. Wang and R.-Y. Liu. Tidal disruption jets of supermassive black holes as hidden sources of cosmic rays: explaining the IceCube TeV-PeV neutrinos. *Phys. Rev.*, D93(8): 083005, 2016. doi: 10.1103/PhysRevD.93.083005.

[57] L. Dai and K. Fang. Can tidal disruption events produce the IceCube neutrinos? *Mon. Not. Roy. Astron. Soc.*, 469:1354, 2017. doi: 10.1093/mnras/stx863.

[58] N. Senno, K. Murase, and P. Meszaros. High-energy Neutrino Flares from X-Ray Bright and Dark Tidal Disruption Events. *Astrophys. J.*, 838(1):3, 2017. doi: 10.3847/1538-4357/aa6344.

[59] C. Lunardini and W. Winter. High Energy Neutrinos from the Tidal Disruption of Stars. *Phys. Rev.*, D95(12):123001, 2017. doi: 10.1103/PhysRevD.95.123001.

[60] B. T. Zhang et al. High-energy cosmic ray nuclei from tidal disruption events: Origin, survival, and implications. *Phys. Rev.*, D96(6):063007, 2017. doi: 10.1103/PhysRevD.96.063007,10.1103/PhysRevD.96.069902.

[61] C. Guépin et al. Ultra-High Energy Cosmic Rays and Neutrinos from Tidal Disruptions by Massive Black Holes. *Astron. Astrophys.*, 616:A179, 2018. doi: 10.1051/0004-6361/201732392.

[62] B. P. Abbott et al. GW170817: Observation of Gravitational Waves from a Binary Neutron Star Inspiral. *Phys. Rev. Lett.*, 119(16):161101, 2017. doi: 10.1103/PhysRevLett.119.161101.

[63] B. P. Abbott et al. Gravitational Waves and Gamma-rays from a Binary Neutron Star Merger: GW170817 and GRB 170817A. *Astrophys. J.*, 848(2):L13, 2017. doi: 10.3847/2041-8213/aa920c.

[64] M. G. Aartsen et al. Multimessenger observations of a flaring blazar coincident with high-energy neutrino IceCube-170922A. *Science*, 361(6398):eaat1378, 2018. doi: 10.1126/science.aat1378.

[65] J. Aasi et al. Advanced LIGO. *Class. Quant. Grav.*, 32:074001, 2015. doi: 10.1088/0264-9381/32/7/074001.

[66] M. Actis et al. Design concepts for the Cherenkov Telescope Array CTA: An advanced facility for ground-based high-energy gamma-ray astronomy. *Exper. Astron.*, 32:193–316, 2011. doi: 10.1007/s10686-011-9247-0.

[67] J. Alvarez-Muñiz et al. The Giant Radio Array for Neutrino Detection (GRAND): Science and Design. 2018.

[68] J. van Santen. IceCube-Gen2: the next-generation neutrino observatory for the South Pole. *PoS*, ICRC2017:991, 2018. doi: 10.22323/1.301.0991.

[69] G. Cataldi. AugerPrime: the upgrade program of the Pierre Auger Observatory. *PoS*, EPS-HEP2017:005, 2017. doi: 10.22323/1.314.0005.

[70] M. Spurio. *Particles and Astrophysics: A Multi-Messenger Approach.* Astronomy and Astrophysics Library. Springer International Publishing, 2014. ISBN 9783319080512. URL `https://books.google.de/books?id=4P67BAAAQBAJ`.

[71] K. Hirata et al. Observation of a Neutrino Burst from the Supernova SN 1987a. *Phys. Rev. Lett.*, 58:1490–1493, 1987. doi: 10.1103/PhysRevLett.58.1490.

[72] R. M. Bionta et al. Observation of a Neutrino Burst in Coincidence with Supernova SN 1987a in the Large Magellanic Cloud. *Phys. Rev. Lett.*, 58:1494, 1987. doi: 10.1103/PhysRevLett.58.1494.

[73] E. N. Alekseev et al. Possible Detection of a Neutrino Signal on 23 February 1987 at the Baksan Underground Scintillation Telescope of the Institute of Nuclear Research. *JETP Lett.*, 45:589–592, 1987.

[74] M. R. Drout et al. Light Curves of the Neutron Star Merger GW170817/SSS17a: Implications for R-Process Nucleosynthesis. *Science*, 358:1570–1574, 2017. doi: 10.1126/science.aaq0049.

[75] P. A. Evans et al. Swift and NuSTAR observations of GW170817: detection of a blue kilonova. *Science*, 358:1565, 2017. doi: 10.1126/science.aap9580.

[76] D. Haggard et al. A Deep Chandra X-ray Study of Neutron Star Coalescence GW170817. *Astrophys. J.*, 848(2):L25, 2017. doi: 10.3847/2041-8213/aa8ede.

[77] K. D. Alexander et al. The Electromagnetic Counterpart of the Binary Neutron Star Merger LIGO/VIRGO GW170817. VI. Radio Constraints on a Relativistic Jet and Predictions for Late-Time Emission from the Kilonova Ejecta. *Astrophys. J.*, 848(2):L21, 2017. doi: 10.3847/2041-8213/aa905d.

[78] R. Margutti et al. The Binary Neutron Star Event LIGO/Virgo GW170817 160 Days after Merger: Synchrotron Emission across the Electromagnetic Spectrum. *Astrophys. J.*, 856 (1):L18, 2018. doi: 10.3847/2041-8213/aab2ad.

[79] R. Chornock et al. The Electromagnetic Counterpart of the Binary Neutron Star Merger LIGO/VIRGO GW170817. IV. Detection of Near-infrared Signatures of r-process Nucleosynthesis with Gemini-South. *Astrophys. J.*, 848(2):L19, 2017. doi: 10.3847/2041-8213/aa905c.

[80] S. Ansoldi et al. The blazar TXS 0506+056 associated with a high-energy neutrino: insights into extragalactic jets and cosmic ray acceleration. *Astrophys. J. Lett.*, 2018. doi: 10.3847/2041-8213/aad083.

[81] S. Gao et al. Modelling the coincident observation of a high-energy neutrino and a bright blazar flare. *Nat. Astron.*, 3(1):88–92, 2019. doi: 10.1038/s41550-018-0610-1.

[82] P. Antonioli et al. SNEWS: The Supernova Early Warning System. *New J. Phys.*, 6:114, 2004. doi: 10.1088/1367-2630/6/1/114.

[83] M. W. E. Smith et al. The Astrophysical Multimessenger Observatory Network (AMON). *Astropart. Phys.*, 45:56–70, 2013. doi: 10.1016/j.astropartphys.2013.03.003.

[84] M. C. Malley. *Radioactivity: A History of a Mysterious Science*. EBSCO ebook academic collection. Oxford University Press, USA, 2011. ISBN 9780199766413. URL https://books.google.de/books?id=yvtjtKSfX54C.

[85] T. Wulf. About the radiation of high penetration capacity contained in the atmosphere. *Physikalische Zeitschrift*, 5:152–157, 1910.

[86] D. Pacini. Penetrating Radiation at the Surface of and in Water. *Nuovo Cim.*, 8:93–100, 1912. doi: 10.1007/BF02957440.

[87] V. F. Hess. Über Beobachtungen der durchdringenden Strahlung bei sieben Freiballonfahrten. *Phys. Z.*, 13:1084–1091, 1912.

[88] J. Clay. Penetrating Radiation. *Proceedings of the Royal Academy of Sciences Amsterdam*, 5:1115–1127, 1927.

[89] B. Rossi. On the magnetic deflection of cosmic rays. *Phys. Rev.*, 36:606–606, Aug 1930. doi: 10.1103/PhysRev.36.606. URL https://link.aps.org/doi/10.1103/PhysRev.36.606.

[90] B. Rossi. Misure sulla distribuzione angolare di intensita della radiazione penetrante all'Asmara. *Ricerca Scientifica*, 5:579–589, 1934.

[91] P. Auger et al. Extensive cosmic-ray showers. *Rev. Mod. Phys.*, 11:288–291, Jul 1939. doi: 10.1103/RevModPhys.11.288. URL https://link.aps.org/doi/10.1103/RevModPhys.11.288.

[92] H. J. Bhabha and W. Heitler. The passage of fast electrons and the theory of cosmic showers. *Proceedings of the Royal Society of London. Series A - Mathematical and Physical Sciences*, 159(898):432–458, 1937. doi: 10.1098/rspa.1937.0082.

[93] J. Linsley. Evidence for a primary cosmic-ray particle with energy 10^{20} ev. *Phys. Rev. Lett.*, 10:146–148, Feb 1963. doi: 10.1103/PhysRevLett.10.146. URL https://link.aps.org/doi/10.1103/PhysRevLett.10.146.

[94] M. N. Dyakonov et al. The use of cherenkov detectors at the yakutsk cosmic ray extensive air shower array. *Nucl. Instrum. Meth.*, 248(1):224 – 226, 1986. ISSN 0168-9002. doi: https://doi.org/10.1016/0168-9002(86)90518-8. URL http://www.sciencedirect.com/science/article/pii/0168900286905188.

[95] R. M. Tennent. The haverah park extensive air shower array. *Proceedings of the Physical Society*, 92(3):622, 1967. URL http://stacks.iop.org/0370-1328/92/i=3/a=315.

[96] N. Chiba et al. Akeno giant air shower array (agasa) covering 100 km2 area. *Nucl. Instrum. Meth.*, 311(1):338 – 349, 1992. ISSN 0168-9002. doi: https://doi.org/10.1016/0168-9002(92)90882-5. URL http://www.sciencedirect.com/science/article/pii/0168900292908825.

[97] N. Budnev et al. The taiga experiment: from cosmic ray to gamma-ray astronomy in the tunka valley. *Journal of Physics: Conference Series*, 718(5):052006, 2016. URL http://stacks.iop.org/1742-6596/718/i=5/a=052006.

[98] A. Tamburro. Measurements of Cosmic Rays with IceTop/IceCube: Status and Results. *Mod. Phys. Lett.*, A27:1230038, 2012. doi: 10.1142/S0217732312300388.

[99] W. D. Apel et al. Kneelike structure in the spectrum of the heavy component of cosmic rays observed with KASCADE-Grande. *Phys. Rev. Lett.*, 107:171104, 2011. doi: 10.1103/PhysRevLett.107.171104.

[100] D. Fuhrmann et al. KASCADE-Grande measurements of energy spectra for elemental groups of cosmic rays. In *Proceedings, 33rd International Cosmic Ray Conference (ICRC2013): Rio de Janeiro, Brazil, July 2-9, 2013*, page 0531, 2013. URL http://www.cbpf.br/%7Eicrc2013/papers/icrc2013-0531.pdf.

[101] A. Aab et al. The Pierre Auger Cosmic Ray Observatory. *Nucl. Instrum. Meth.*, A798: 172–213, 2015. doi: 10.1016/j.nima.2015.06.058.

[102] C. C. H. Jui and the Telescope Array Collaboration. Cosmic ray in the northern hemisphere: Results from the telescope array experiment. *Journal of Physics: Conference Series*, 404(1):012037, 2012. URL http://stacks.iop.org/1742-6596/404/i=1/a=012037.

[103] M. Casolino. The Pamela Cosmic Ray Space Observatory: Detector, Objectives and First Results. *Frascati Phys. Ser.*, 47:19–48, 2008.

[104] E. C. Stone et al. Voyager 1 observes low-energy galactic cosmic rays in a region depleted of heliospheric ions. *Science*, 341(6142):150–153, 2013. ISSN 0036-8075. doi: 10.1126/science.1236408. URL http://science.sciencemag.org/content/341/6142/150.

[105] E. S. Seo et al. Cosmic Ray Energetics And Mass for the International Space Station (ISS-CREAM). *Adv. Space Res.*, 53:1451–1455, 2014. doi: 10.1016/j.asr.2014.01.013.

[106] M. Aguilar et al. Antiproton flux, antiproton-to-proton flux ratio, and properties of elementary particle fluxes in primary cosmic rays measured with the alpha magnetic

spectrometer on the international space station. *Phys. Rev. Lett.*, 117:091103, Aug 2016. doi: 10.1103/PhysRevLett.117.091103. URL `https://link.aps.org/doi/10.1103/PhysRevLett.117.091103`.

[107] S. Thoudam et al. Cosmic-ray energy spectrum and composition up to the ankle: the case for a second galactic component. *A&A*, 595:A33, 2016. doi: 10.1051/0004-6361/201628894. URL `https://doi.org/10.1051/0004-6361/201628894`.

[108] M. Lemoine. Extra-galactic magnetic fields and the second knee in the cosmic-ray spectrum. *Phys. Rev.*, D71:083007, 2005. doi: 10.1103/PhysRevD.71.083007.

[109] V. Berezinsky, A. Z. Gazizov, and S. I. Grigorieva. Dip in UHECR spectrum as signature of proton interaction with CMB. *Phys. Lett.*, B612:147–153, 2005. doi: 10.1016/j.physletb.2005.02.058.

[110] K. Greisen. End to the cosmic ray spectrum? *Phys. Rev. Lett.*, 16:748–750, 1966. doi: 10.1103/PhysRevLett.16.748.

[111] G. T. Zatsepin and V. A. Kuzmin. Upper limit of the spectrum of cosmic rays. *JETP Lett.*, 4:78–80, 1966. [Pisma Zh. Eksp. Teor. Fiz.4,114(1966)].

[112] F. Fenu. The cosmic ray energy spectrum measured using the Pierre Auger Observatory. pages 9–16, 2017. doi: 10.22323/1.301.0486. [PoSICRC2017,486(2018)].

[113] A. Aab et al. Observation of a Large-scale Anisotropy in the Arrival Directions of Cosmic Rays above 8×10^{18} eV. *Science*, 357(6537):1266–1270, 2017. doi: 10.1126/science.aan4338.

[114] J. Bellido. Depth of maximum of air-shower profiles at the Pierre Auger Observatory: Measurements above $10^{17.2}$ eV and Composition Implications. *PoS*, ICRC2017:506, 2018. doi: 10.22323/1.301.0506.

[115] T. Pierog et al. EPOS LHC: Test of collective hadronization with data measured at the CERN Large Hadron Collider. *Phys. Rev.*, C92(3):034906, 2015. doi: 10.1103/PhysRevC.92.034906.

[116] E.-J. Ahn et al. Cosmic ray interaction event generator SIBYLL 2.1. *Phys. Rev.*, D80:094003, 2009. doi: 10.1103/PhysRevD.80.094003.

[117] S. Ostapchenko. Monte Carlo treatment of hadronic interactions in enhanced Pomeron scheme: I. QGSJET-II model. *Phys. Rev.*, D83:014018, 2011. doi: 10.1103/PhysRevD.83.014018.

[118] W. F. Hanlon. Telescope Array Hybrid Composition and Auger-TA Composition Comparison. In *20th International Symposium on Very High Energy Cosmic Ray Interactions (ISVHECRI 2018) Nagoya, Japan, May 21-25, 2018*, 2018.

[119] R. Abbasi et al. Report of the Working Group on the Composition of Ultra High Energy Cosmic Rays. *JPS Conf. Proc.*, 9:010016, 2016. doi: 10.7566/JPSCP.9.010016.

[120] A. Aab et al. Large-scale cosmic-ray anisotropies above 4 EeV measured by the Pierre Auger Observatory. *Astrophys. J.*, 868(1):4, 2018. doi: 10.3847/1538-4357/aae689.

[121] L. M. Brown. The idea of the neutrino. *Physics Today*, 31(9):23, 1978.

[122] C. L. Cowan et al. Detection of the free neutrino: a confirmation. *Science*, 124(3212):103–104, 1956. ISSN 0036-8075. doi: 10.1126/science.124.3212.103. URL `http://science.sciencemag.org/content/124/3212/103`.

[123] B. T. Cleveland et al. Measurement of the solar electron neutrino flux with the homestake chlorine detector. *The Astrophysical Journal*, 496(1):505, 1998. URL `http://stacks.iop.org/0004-637X/496/i=1/a=505`.

[124] G. Danby et al. Observation of high-energy neutrino reactions and the existence of two kinds of neutrinos. *Phys. Rev. Lett.*, 9:36–44, Jul 1962. doi: 10.1103/PhysRevLett.9.36. URL `https://link.aps.org/doi/10.1103/PhysRevLett.9.36`.

[125] K. Kodama et al. Observation of tau neutrino interactions. *Phys. Lett.*, B504:218–224, 2001. doi: 10.1016/S0370-2693(01)00307-0.

[126] Q. R. Ahmad et al. Measurement of the rate of $\nu_e + d \rightarrow p + p + e^-$ interactions produced by ^8B solar neutrinos at the Sudbury Neutrino Observatory. *Phys. Rev. Lett.*, 87:071301, 2001. doi: 10.1103/PhysRevLett.87.071301.

[127] Y. Fukuda et al. Measurements of the solar neutrino flux from Super-Kamiokande's first 300 days. *Phys. Rev. Lett.*, 81:1158–1162, 1998. doi: 10.1103/PhysRevLett.81.1158,10.1103/PhysRevLett.81.4279. [Erratum: Phys. Rev. Lett.81,4279(1998)].

[128] V.M. Lobashev et al. Direct search for neutrino mass and anomaly in the tritium beta-spectrum: Status of "troitsk neutrino mass" experiment. *Nuclear Physics B - Proceedings Supplements*, 91(1):280 – 286, 2001. ISSN 0920-5632. doi: https://doi.org/10.1016/S0920-5632(00)00952-X. URL `http://www.sciencedirect.com/science/article/pii/S092056320000952X`. Neutrino 2000.

[129] C. Kraus et al. Final results from phase II of the Mainz neutrino mass search in tritium beta decay. *Eur. Phys. J.*, C40:447–468, 2005. doi: 10.1140/epjc/s2005-02139-7.

[130] S. Mertens. Status of the katrin experiment and prospects to search for kev-mass sterile neutrinos in tritium β-decay. *Physics Procedia*, 61:267 – 273, 2015. ISSN 1875-3892. doi: https://doi.org/10.1016/j.phpro.2014.12.043. URL `http://www.sciencedirect.com/science/article/pii/S1875389214006567`. 13th International Conference on Topics in Astroparticle and Underground Physics, TAUP 2013.

[131] R. A. Battye and A. Moss. Evidence for Massive Neutrinos from Cosmic Microwave Background and Lensing Observations. *Phys. Rev. Lett.*, 112(5):051303, 2014. doi: 10.1103/PhysRevLett.112.051303.

[132] F. Capozzi et al. Neutrino masses and mixings: Status of known and unknown 3ν parameters. *Nuclear Physics B*, 908:218 – 234, 2016. ISSN 0550-3213. doi: https://doi.org/10.1016/j.nuclphysb.2016.02.016. URL `http://www.sciencedirect.com/science/article/pii/S0550321316000602`. Neutrino Oscillations: Celebrating the Nobel Prize in Physics 2015.

[133] M. Agostini et al. Background-free search for neutrinoless double-β decay of ^{76}Ge with GERDA. 2017. doi: 10.1038/nature21717. [Nature544,47(2017)].

[134] M. Drewes. The Phenomenology of Right Handed Neutrinos. *Int. J. Mod. Phys.*, E22:1330019, 2013. doi: 10.1142/S0218301313300191.

[135] S. Fukuda et al. The super-kamiokande detector. *Nucl. Instrum. Meth.*, 501(2):418 – 462, 2003. ISSN 0168-9002. doi: https://doi.org/10.1016/S0168-9002(03)00425-X. URL `http://www.sciencedirect.com/science/article/pii/S016890020300425X`.

[136] M. Ageron et al. ANTARES: the first undersea neutrino telescope. *Nucl. Instrum. Meth.*, A656:11–38, 2011. doi: 10.1016/j.nima.2011.06.103.

[137] R. Wischnewski et al. The amanda neutrino detector. *Nuclear Physics B - Proceedings Supplements*, 75(1):412 – 414, 1999. ISSN 0920-5632. doi: https://doi.org/10.1016/S0920-5632(99)00309-6. URL `http://www.sciencedirect.com/science/article/pii/S0920563299003096`.

[138] J. Ahrens et al. Icecube: The next generation neutrino telescope at the south pole. *Nucl. Phys. Proc. Suppl.*, 118:388–395, 2003.

[139] S. Adrian-Martinez et al. Letter of intent for KM3NeT 2.0. *J. Phys.*, G43(8):084001, 2016. doi: 10.1088/0954-3899/43/8/084001.

[140] A. V. Olinto et al. POEMMA: Probe Of Extreme Multi-Messenger Astrophysics. *PoS*, ICRC2017:542, 2018. doi: 10.22323/1.301.0542. [35,542(2017)].

[141] M.G. Aartsen et al. IceCube-Gen2: A Vision for the Future of Neutrino Astronomy in Antarctica. 2014.

[142] F. Halzen. The highest energy neutrinos: first evidence for cosmic origin. *Nuovo Cim.*, C037(03):117–132, 2014. doi: 10.1393/ncc/i2014-11772-8,10.1002/asna.201412058. [Astron. Nachr.335,507(2014)].

[143] P. Allison et al. Design and Initial Performance of the Askaryan Radio Array Prototype EeV Neutrino Detector at the South Pole. *Astropart. Phys.*, 35:457–477, 2012. doi: 10.1016/j.astropartphys.2011.11.010.

[144] S. W. Barwick. Development of telescopes for extremely energetic neutrinos: Amanda, anita, and arianna. *Nucl. Instrum. Meth.*, 602(1):279–284, 2009.

[145] K. Fang et al. The Giant Radio Array for Neutrino Detection (GRAND): Present and Perspectives. *PoS*, ICRC2017:996, 2017.

[146] B. Follin et al. First detection of the acoustic oscillation phase shift expected from the cosmic neutrino background. *Phys. Rev. Lett.*, 115:091301, Aug 2015. doi: 10.1103/PhysRevLett.115.091301. URL `https://link.aps.org/doi/10.1103/PhysRevLett.115.091301`.

[147] I. Tamborra and K. Murase. Neutrinos from Supernovae. *Space Sci. Rev.*, 214(1):31, 2018. doi: 10.1007/s11214-018-0468-7.

[148] K. Møller et al. Measuring the supernova unknowns at the next-generation neutrino telescopes through the diffuse neutrino background. *JCAP*, 1805(05):066, 2018. doi: 10.1088/1475-7516/2018/05/066.

[149] M. Ahlers. High-energy cosmogenic neutrinos. *Physics Procedia*, 61:392 – 398, 2015. ISSN 1875-3892. doi: https://doi.org/10.1016/j.phpro.2014.12.080. URL `http://www.sciencedirect.com/science/article/pii/S1875389214006932`. 13th International Conference on Topics in Astroparticle and Underground Physics, TAUP 2013.

[150] R. Abbasi et al. The Design and Performance of IceCube DeepCore. *Astropart. Phys.*, 35:615–624, 2012. doi: 10.1016/j.astropartphys.2012.01.004.

[151] C. Kopper. Observation of Astrophysical Neutrinos in Six Years of IceCube Data. *PoS*, ICRC2017:981, 2018. doi: 10.22323/1.301.0981.

[152] M.G. Aartsen et al. Energy Reconstruction Methods in the IceCube Neutrino Telescope. *JINST*, 9:P03009, 2014. doi: 10.1088/1748-0221/9/03/P03009.

[153] S. L. Glashow. Resonant Scattering of Antineutrinos. *Phys. Rev.*, 118:316–317, 1960. doi: 10.1103/PhysRev.118.316.

[154] A. Palladino and W. Winter. A Multi-Component Model for the Observed Astrophysical Neutrinos. 2018. doi: 10.3204/PUBDB-2018-01376.

[155] M. G. Aartsen et al. The contribution of Fermi-2LAC blazars to the diffuse TeV-PeV neutrino flux. *Astrophys. J.*, 835(1):45, 2017. doi: 10.3847/1538-4357/835/1/45.

[156] M. G. Aartsen et al. Multiwavelength follow-up of a rare IceCube neutrino multiplet. *Astron. Astrophys.*, 607:A115, 2017. doi: 10.1051/0004-6361/201730620.

[157] S. S. Kimura, K. Murase, and P. Mészáros. Super-Knee Cosmic Rays from Galactic Neutron Star Merger Remnants. *Astrophys. J.*, 866(1):51, 2018. doi: 10.3847/1538-4357/aadc0a.

[158] B. T. Zhang and K. Murase. Ultrahigh-energy cosmic-ray nuclei and neutrinos from engine-driven supernovae. 2018.

[159] D. Biehl et al. Cosmic-Ray and Neutrino Emission from Gamma-Ray Bursts with a Nuclear Cascade. *Astron. Astrophys.*, 611:A101, 2018. doi: 10.1051/0004-6361/201731337.

[160] D. Biehl et al. Astrophysical Neutrino Production Diagnostics with the Glashow Resonance. *JCAP*, 1701:033, 2017. doi: 10.1088/1475-7516/2017/01/033.

[161] NASA Goddard's Scientific Visualization Studio. Jet Shockwaves Produce Gamma Rays. . URL `https://svs.gsfc.nasa.gov/cgi-bin/details.cgi?aid=11407`. Accessed 18.01.19.

[162] P. Meszaros and E. Waxman. TeV neutrinos from successful and choked gamma-ray bursts. *Phys. Rev. Lett.*, 87:171102, 2001. doi: 10.1103/PhysRevLett.87.171102.

[163] E. Ramirez-Ruiz, A. Celotti, and M. J. Rees. Events in the life of a cocoon surrounding a light, collapsar jet. *Mon. Not. Roy. Astron. Soc.*, 337:1349, 2002. doi: 10.1046/j.1365-8711.2002.05995.x.

[164] P. Meszaros and M. J. Rees. Delayed GeV emission from cosmological gamma-ray bursts: Impact of a relativistic wind on external matter. *Mon. Not. Roy. Astron. Soc.*, 269:L41, 1994. doi: 10.1093/mnras/269.1.41L.

[165] P. Meszaros and M. J. Rees. Optical and long wavelength afterglow from gamma-ray bursts. *Astrophys. J.*, 476:232–237, 1997. doi: 10.1086/303625.

[166] M. J. Rees and P. Meszaros. Dissipative photosphere models of gamma-ray bursts and x-ray flashes. *Astrophys. J.*, 628:847–852, 2005. doi: 10.1086/430818.

[167] D. Giannios. Prompt GRB emission from gradual energy dissipation. *Astron. Astrophys.*, 480:305, 2008. doi: 10.1051/0004-6361:20079085.

[168] M. Lyutikov, V. I. Pariev, and R. D. Blandford. Polarization of prompt GRB emission: Evidence for electromagnetically - dominated outflow. *Astrophys. J.*, 597:998–1009, 2003. doi: 10.1086/378497.

[169] B. Zhang and H. Yan. The Internal-Collision-Induced Magnetic Reconnection and Turbulence (ICMART) Model of Gamma-Ray Bursts. *Astrophys. J.*, 726:90, 2011. doi: 10.1088/0004-637X/726/2/90.

[170] L. O. Drury. An introduction to the theory of diffusive shock acceleration of energetic particles in tenuous plasmas. *Rept. Prog. Phys.*, 46:973–1027, 1983. doi: 10.1088/0034-4885/46/8/002.

[171] R. Schlickeiser. *Cosmic Ray Astrophysics*. Astronomy and Astrophysics Library. Springer Berlin Heidelberg, 2002. ISBN 9783540664659. URL `https://books.google.de/books?id=0JaLQqQcPzIC`.

[172] P. Baerwald, M. Bustamante, and W. Winter. UHECR escape mechanisms for protons and neutrons from GRBs, and the cosmic ray-neutrino connection. *Astrophys. J.*, 768:186, 2013. doi: 10.1088/0004-637X/768/2/186.

[173] P. Baerwald, S. Hümmer, and W. Winter. Systematics in the Interpretation of Aggregated Neutrino Flux Limits and Flavor Ratios from Gamma-Ray Bursts. *Astropart. Phys.*, 35:508–529, 2012.

[174] M. Goldhaber and E. Teller. On nuclear dipole vibrations. *Phys. Rev.*, 74:1046–1049, 1948. doi: 10.1103/PhysRev.74.1046.

[175] A. J. Koning, S. Hilaire, and M. C. Duijvestijn. TALYS 1.0. In *Proceedings, International Conference on Nuclear Data for Science and Tecnology*, pages 211–214, 2007.

[176] A. Mucke et al. SOPHIA: Monte Carlo simulations of photohadronic processes in astrophysics. *Comput. Phys. Commun.*, 124:290–314, 2000. doi: 10.1016/S0010-4655(99)00446-4.

[177] D. Biehl et al. Astrophysical neutrino production and impact of associated uncertainties in photo-hadronic interactions of UHECRs. In *20th International Symposium on Very High Energy Cosmic Ray Interactions (ISVHECRI 2018) Nagoya, Japan, May 21-25, 2018*, 2018.

[178] J. P. Rachen. *Interaction Processes and Statistical Properties of the Propagation of Cosmic Rays in Photon Backgrounds.* PhD thesis, MPIfR Bonn, Germany, 1996.

[179] G.R. Blumenthal. Energy loss of high-energy cosmic rays in pair-producing collisions with ambient photons. *Phys. Rev.*, D 1:1596–1602, 1970. doi: 10.1103/PhysRevD.1.1596.

[180] S. Hümmer, M. Maltoni, W. Winter, and C. Yaguna. Energy dependent neutrino flavor ratios from cosmic accelerators on the Hillas plot. *Astropart. Phys.*, 34:205–224, 2010. doi: 10.1016/j.astropartphys.2010.07.003.

[181] P. Lipari, M. Lusignoli, and D. Meloni. Flavor Composition and Energy Spectrum of Astrophysical Neutrinos. *Phys. Rev.*, D75:123005, 2007. doi: 10.1103/PhysRevD.75.123005.

[182] Y. Ohira, K. Murase, and R. Yamazaki. Escape-limited Model of Cosmic-ray Acceleration Revisited. *Astron. Astrophys.*, 513:A17, 2010. doi: 10.1051/0004-6361/200913495.

[183] R. Alves Batista, D. Boncioli, A. di Matteo, A. van Vliet, and D. Walz. Effects of uncertainties in simulations of extragalactic UHECR propagation, using CRPropa and SimProp. *JCAP*, 1510(10):063, 2015. doi: 10.1088/1475-7516/2015/10/063.

[184] R. Aloisio, D. Boncioli, A. F. Grillo, S. Petrera, and F. Salamida. SimProp: a Simulation Code for Ultra High Energy Cosmic Ray Propagation. *JCAP*, 1210:007, 2012. doi: 10.1088/1475-7516/2012/10/007.

[185] J. L. Puget, F. W. Stecker, and J. H. Bredekamp. Photonuclear Interactions of Ultrahigh-Energy Cosmic Rays and their Astrophysical Consequences. *Astrophys. J.*, 205:638–654, 1976. doi: 10.1086/154321.

[186] F. W. Stecker and M. H. Salamon. Photodisintegration of ultrahigh-energy cosmic rays: A New determination. *Astrophys. J.*, 512:521–526, 1999. doi: 10.1086/306816.

[187] R. C. Gilmore, R. S. Somerville, J. R. Primack, and A. Dominguez. Semi-analytic modeling of the EBL and consequences for extragalactic gamma-ray spectra. *Mon. Not. Roy. Astron. Soc.*, 422:3189, 2012. doi: 10.1111/j.1365-2966.2012.20841.x.

[188] A. M. Hopkins and J. F. Beacom. On the normalisation of the cosmic star formation history. *Astrophys. J.*, 651:142, 2006. doi: 10.1086/506610.

[189] M. D. Kistler et al. The Star Formation Rate in the Reionization Era as Indicated by Gamma-ray Bursts. *Astrophys. J.*, 705:L104–L108, 2009. doi: 10.1088/0004-637X/705/2/L104.

[190] H. Yuksel et al. Revealing the High-Redshift Star Formation Rate with Gamma-Ray Bursts. *Astrophys. J.*, 683:L5–L8, 2008. doi: 10.1086/591449.

[191] E. Waxman. Cosmological origin for cosmic rays above 10^{19} eV. *Astrophys. J.*, 452:L1–L4, 1995. doi: 10.1086/309715.

[192] B. Katz, R. Budnik, and E. Waxman. The energy production rate & the generation spectrum of UHECRs. *JCAP*, 0903:020, 2009. doi: 10.1088/1475-7516/2009/03/020.

[193] T. K. Gaisser, T. Stanev, and S. Tilav. Cosmic Ray Energy Spectrum from Measurements of Air Showers. *Front. Phys.(Beijing)*, 8:748–758, 2013. doi: 10.1007/s11467-013-0319-7.

[194] M. Tanabashi et al. Review of particle physics. *Phys. Rev. D*, 98:030001, Aug 2018. doi: 10.1103/PhysRevD.98.030001. URL `https://link.aps.org/doi/10.1103/PhysRevD.98.030001`.

[195] P. F. Harrison, D. H. Perkins, and W. G. Scott. Tri-bimaximal mixing and the neutrino oscillation data. *Phys. Lett.*, B530:167, 2002. doi: 10.1016/S0370-2693(02)01336-9.

[196] B. Pontecorvo. Inverse beta processes and nonconservation of lepton charge. *Sov. Phys. JETP*, 7:172–173, 1958. [Zh. Eksp. Teor. Fiz.34,247(1957)].

[197] Z. Maki, M. Nakagawa, and S. Sakata. Remarks on the unified model of elementary particles. *Prog. Theor. Phys.*, 28:870–880, 1962. doi: 10.1143/PTP.28.870. [,34(1962)].

[198] M. G. Aartsen et al. Observation and Characterization of a Cosmic Muon Neutrino Flux from the Northern Hemisphere using six years of IceCube data. *Astrophys. J.*, 833(1):3, 2016. doi: 10.3847/0004-637X/833/1/3.

[199] M. G. Aartsen et al. A combined maximum-likelihood analysis of the high-energy astrophysical neutrino flux measured with IceCube. *Astrophys. J.*, 809(1):98, 2015. doi: 10.1088/0004-637X/809/1/98.

[200] I. Esteban et al. Updated fit to three neutrino mixing: exploring the accelerator-reactor complementarity. *JHEP*, 01:087, 2017. doi: 10.1007/JHEP01(2017)087.

[201] W. Winter. Photohadronic Origin of the TeV-PeV Neutrinos Observed in IceCube. *Phys.Rev.*, D88:083007, 2013. doi: 10.1103/PhysRevD.88.083007.

[202] M. M. Reynoso and G. E. Romero. Magnetic field effects on neutrino production in microquasars. *Astron. Astrophys.*, 493:1–11, 2009.

[203] M. G. Aartsen et al. The IceCube Neutrino Observatory - Contributions to ICRC 2015 Part II: Atmospheric and Astrophysical Diffuse Neutrino Searches of All Flavors. In *Proceedings, 34th International Cosmic Ray Conference (ICRC 2015): The Hague, The Netherlands, July 30-August 6, 2015*, 2015.

[204] R. W. Klebesadel, I. B. Strong, and R. A. Olson. Observations of Gamma-Ray Bursts of Cosmic Origin. *Astrophys. J.*, 182:L85–L88, 1973. doi: 10.1086/181225.

[205] J.T. Bonnell (NASA/GSFC). Gamma-Ray Burst Light Curves. URL `https://heasarc.gsfc.nasa.gov/docs/cgro/images/epo/gallery/grbs/`. Accessed 28.01.19.

[206] M. S. Briggs et al. Batse observations of the large scale isotropy of gamma-ray bursts. *Astrophys. J.*, 459:40, 1996. doi: 10.1086/176867.

[207] C. Kouveliotou et al. Identification of two classes of gamma-ray bursts. *Astrophys. J.*, 413: L101–104, 1993. doi: 10.1086/186969.

[208] A. J. Levan et al. A new population of ultra-long duration gamma-ray bursts. *Astrophys. J.*, 781:13, 2013. doi: 10.1088/0004-637X/781/1/13.

[209] M. Boer, B. Gendre, and G. Stratta. Are Ultra-long Gamma-Ray Bursts different? *Astrophys. J.*, 800(1):16, 2015. doi: 10.1088/0004-637X/800/1/16.

[210] E. Berger. Short-Duration Gamma-Ray Bursts. *Ann. Rev. Astron. Astrophys.*, 52:43–105, 2014. doi: 10.1146/annurev-astro-081913-035926.

[211] J. Hjorth and J. S. Bloom. The Gamma-Ray Burst - Supernova Connection. *CAPS*, 51: 169–190, 2012.

[212] L. Piro. BeppoSAX overview. In C. D. Dermer, M. S. Strickman, and J. D. Kurfess, editors, *Proceedings of the Fourth Compton Symposium*, volume 410 of *American Institute of Physics Conference Series*, pages 1485–1492, May 1997. doi: 10.1063/1.53959.

[213] G. Chincarini. Gamma ray bursts: recent results obtained by the swift mission. In *Proceedings, 3rd Workshop on Science with the New Generation of High Energy Gamma-ray Experiments (SciNeGHE 2005): Cividale del Friuli, Italy, May 30-June 1, 2005*, 2005.

[214] S. Zhu et al. Fermi-LAT Observations of the Gamma-ray Burst GRB 130427A. *Science*, 343:42, 2014. doi: 10.1126/science.1242353.

[215] R. Mirzoyan. First time detection of a GRB at sub-TeV energies; MAGIC detects the GRB 190114C. *The Astronomer's Telegram*, 12390, January 2019.

[216] D. Boncioli, D. Biehl, and W. Winter. On the common origin of cosmic rays across the ankle and diffuse neutrinos at the highest energies from low-luminosity Gamma-Ray Bursts. *Astrophys. J.*, 872:110, 2019. doi: 10.3847/1538-4357/aafda7.

[217] A. M. Hillas. The Origin of Ultrahigh-Energy Cosmic Rays. *Ann. Rev. Astron. Astrophys.*, 22:425–444, 1984. doi: 10.1146/annurev.aa.22.090184.002233.

[218] E. Waxman and J. N. Bahcall. High energy neutrinos from astrophysical sources: An upper bound. *Phys. Rev.*, D59:023002, 1999. doi: 10.1103/PhysRevD.59.023002.

[219] I. Valiño et al. The flux of ultra-high energy cosmic rays after ten years of operation of the Pierre Auger Observatory. PoS(ICRC2015)271, 2015.

[220] A. di Matteo. Combined fit of spectrum and composition data as measured by the Pierre Auger Observatory. *PoS*, ICRC2015:249, 2016. doi: 10.22323/1.236.0249.

[221] M. G. Aartsen et al. Constraints on Ultrahigh-Energy Cosmic-Ray Sources from a Search for Neutrinos above 10 PeV with IceCube. *Phys. Rev. Lett.*, 117(24):241101, 2016. doi: 10.1103/PhysRevLett.117.241101.

[222] A. Porcelli et al. Measurements of $X_{\max}$ above 10^{17} eV with the fluorescence detector of the Pierre Auger Observatory. PoS(ICRC2015)420, 2015.

[223] J. C. Joshi, W. Winter, and N. Gupta. How Many of the Observed Neutrino Events Can Be Described by Cosmic Ray Interactions in the Milky Way? *MNRAS*, 439:3414, 2014. doi: 10.1093/mnras/stu189.

[224] K.-H. Kampert and M. Unger. Measurements of the Cosmic Ray Composition with Air Shower Experiments. *Astropart. Phys.*, 35:660–678, 2012. doi: 10.1016/j.astropartphys.2012.02.004.

[225] A. D. Vlasov et al. Neutrino-heated winds from millisecond protomagnetars as sources of the weak r-process. *Mon. Not. Roy. Astron. Soc.*, 468(2):1522–1533, 2017. doi: 10.1093/mnras/stx478.

[226] S. Woosley and A. Heger. The Progenitor stars of gamma-ray bursts. *Astrophys. J.*, 637:914–921, 2006. doi: 10.1086/498500.

[227] M.-A. Aloy, C. F. Cuesta-Martínez, and M. Obergaulinger. On the existence of a luminosity threshold of GRB jets in massive stars. 2018. doi: 10.1093/mnras/sty1212.

[228] Y. Suwa and K. Ioka. Can Gamma-Ray Burst Jets Break Out the First Stars? *Astrophys. J.*, 726:107, 2011. doi: 10.1088/0004-637X/726/2/107.

[229] B.-B. Zhang et al. How Long does a Burst Burst? *Astrophys. J.*, 787:66, 2014. doi: 10.1088/0004-637X/787/1/66.

[230] T. Matsumoto and S. S. Kimura. Delayed jet breakouts from binary neutron star mergers. *Astrophys. J.*, 866(2):L16, 2018. doi: 10.3847/2041-8213/aae51b.

[231] O. Bromberg, E. Nakar, and T. Piran. Are low luminosity GRBs generated by relativistic jets? *Astrophys. J.*, 739:L55, 2011. doi: 10.1088/2041-8205/739/2/L55.

[232] H.-N. He et al. Neutrinos from Choked Jets Accompanied by Type-II Supernovae. *Astrophys. J.*, 856(2):119, 2018. doi: 10.3847/1538-4357/aab360.

[233] A. Haungs et al. Latest Results of KASCADE-Grande. *PoS*, ICRC2017:545, 2018. doi: 10.22323/1.301.0545.

[234] R. Aloisio, V. Berezinsky, and P. Blasi. Ultra high energy cosmic rays: implications of Auger data for source spectra and chemical composition. *JCAP*, 1410(10):020, 2014. doi: 10.1088/1475-7516/2014/10/020.

[235] C. Kopper et al. Observation of Astrophysical Neutrinos in Six Years of IceCube Data. PoS(ICRC2017)981, 2017.

[236] R. Alves Batista et al. Cosmogenic photon and neutrino fluxes in the Auger era. *JCAP*, 1901(01):002, 2019. doi: 10.1088/1475-7516/2019/01/002.

[237] K. Møller, P. B. Denton, and I. Tamborra. Cosmogenic Neutrinos Through the GRAND Lens Unveil the Nature of Cosmic Accelerators. 2018.

[238] B. S. Acharya et al. *Science with the Cherenkov Telescope Array.* WSP, 2018. ISBN 9789813270084. doi: 10.1142/10986.

[239] S. Kobayashi, T. Piran, and R. Sari. Can internal shocks produce the variability in GRBs? *Astrophys. J.*, 490:92–98, 1997. doi: 10.1086/512791.

[240] F. Daigne and R. Mochkovitch. Gamma-ray bursts from internal shocks in a relativistic wind: temporal and spectral properties. *Mon. Not. Roy. Astron. Soc.*, 296:275, 1998. doi: 10.1046/j.1365-8711.1998.01305.x.

[241] M. Bustamante et al. Multi-messenger light curves from gamma-ray bursts in the internal shock model. *Astrophys. J.*, 837(1):33, 2017. doi: 10.3847/1538-4357/837/1/33.

[242] J. Heinze et al. A new view on Auger data and cosmogenic neutrinos in light of different nuclear disintegration and air-shower models. 2019.

[243] S. Kobayashi and R. Sari. Ultra efficient internal shocks. *Astrophys. J.*, 551:934, 2001. doi: 10.1086/320249.

[244] K. Fang and K. Murase. Linking High-Energy Cosmic Particles by Black Hole Jets Embedded in Large-Scale Structures. *Phys. Lett.*, 14:396, 2018. doi: 10.1038/s41567-017-0025-4. [Nature Phys.14,no.4,396(2018)].

[245] M. Kachelrieß, O. Kalashev, S. Ostapchenko, and D. V. Semikoz. Minimal model for extragalactic cosmic rays and neutrinos. *Phys. Rev.*, D96(8):083006, 2017. doi: 10.1103/PhysRevD.96.083006.

[246] E. S. Phinney. Manifestations of a Massive Black Hole in the Galactic Center. In M. Morris, editor, *The Center of the Galaxy*, volume 136 of *IAU Symposium*, page 543, 1989.

[247] NASA Goddard's Media Studio. Swift J1644+57: Onset of a relativistic jet. . URL `https://svs.gsfc.nasa.gov/10807`. Accessed 11.02.19.

[248] D. Biehl et al. Tidally disrupted stars as a possible origin of both cosmic rays and neutrinos at the highest energies. *Sci. Rep.*, 8(1):10828, 2018. doi: 10.1038/s41598-018-29022-4.

[249] G.E. Romero and G.S. Vila. *Introduction to Black Hole Astrophysics.* Lecture Notes in Physics. Springer Berlin Heidelberg, 2013. ISBN 9783642395963. URL `https://books.google.de/books?id=sCm6BQAAQBAJ`.

[250] H. Shiokawa et al. General Relativistic Hydrodynamic Simulation of Accretion Flow from a Stellar Tidal Disruption. *Astrophys. J.*, 804(2):85, 2015. doi: 10.1088/0004-637X/804/2/85.

[251] L. Dai, J. C. McKinney, and M. C. Miller. Soft X-ray Temperature Tidal Disruption Events from Stars on Deep Plunging Orbits. *Astrophys. J.*, 812(2):L39, 2015. doi: 10.1088/2041-8205/812/2/L39.

[252] C. S. Kochanek. Tidal disruption event demographics. *Mon. Not. Roy. Astron. Soc.*, 461 (1):371–384, 2016. doi: 10.1093/mnras/stw1290.

[253] F. Shankar, D. H. Weinberg, and J. Miralda-Escude. Self-Consistent Models of the AGN and Black Hole Populations: Duty Cycles, Accretion Rates, and the Mean Radiative Efficiency. *Astrophys. J.*, 690:20–41, 2009. doi: 10.1088/0004-637X/690/1/20.

[254] N. C. Stone and B. D. Metzger. Rates of Stellar Tidal Disruption as Probes of the Supermassive Black Hole Mass Function. *Mon. Not. Roy. Astron. Soc.*, 455(1):859–883, 2016. doi: 10.1093/mnras/stv2281.

[255] A. Fialkov and A. Loeb. Jetted Tidal Disruptions of Stars as a Flag of Intermediate Mass Black Holes at High Redshifts. *Mon. Not. Roy. Astron. Soc.*, 471(4):4286–4299, 2017. doi: 10.1093/mnras/stx1755.

[256] T. W. S. Holoien et al. Six months of multiwavelength follow-up of the tidal disruption candidate ASASSN-14li and implied TDE rates from ASAS-SN. *Mon. Not. Roy. Astron. Soc.*, 455(3):2918–2935, 2016. doi: 10.1093/mnras/stv2486.

[257] M. Kowalski. Status of High-Energy Neutrino Astronomy. *J. Phys. Conf. Ser.*, 632(1): 012039, 2015. doi: 10.1088/1742-6596/632/1/012039.

[258] M. Ahlers and F. Halzen. Pinpointing Extragalactic Neutrino Sources in Light of Recent IceCube Observations. *Phys. Rev.*, D90(4):043005, 2014. doi: 10.1103/PhysRevD.90.043005.

[259] K. Murase and E. Waxman. Constraining High-Energy Cosmic Neutrino Sources: Implications and Prospects. *Phys. Rev.*, D94(10):103006, 2016. doi: 10.1103/PhysRevD.94.103006.

[260] A. Aab et al. The Pierre Auger Observatory: Contributions to the 33rd International Cosmic Ray Conference (ICRC 2013). In *Proceedings, 33rd International Cosmic Ray*

Conference (ICRC2013): Rio de Janeiro, Brazil, July 2-9, 2013, 2013. URL http://lss.fnal.gov/archive/2013/conf/fermilab-conf-13-285-ad-ae-cd-td.pdf.

[261] S. Wu, E. R. Coughlin, and C. Nixon. Super-Eddington accretion in tidal disruption events: the impactof realistic fallback rates on accretion rates. *Mon. Not. Roy. Astron. Soc.*, 478(3):3016–3024, 2018. doi: 10.1093/mnras/sty971.

[262] V. Barger et al. Glashow resonance as a window into cosmic neutrino sources. *Phys.Rev.*, D90(12):121301, 2014. doi: 10.1103/PhysRevD.90.121301.

[263] I. Taboada. A View of the Universe with the IceCube and ANTARES Neutrino Telescopes, June 2018. URL https://doi.org/10.5281/zenodo.1286919.

[264] M. Chianese, G. Miele, and S. Morisi. Interpreting icecube 6-year hese data as an evidence for hundred tev decaying dark matter. *Physics Letters B*, 773:591 – 595, 2017. ISSN 0370-2693. doi: https://doi.org/10.1016/j.physletb.2017.09.016. URL http://www.sciencedirect.com/science/article/pii/S0370269317307141.

[265] E. Waxman and A. Loeb. Constraints on the local sources of ultra high-energy cosmic rays. *Journal of Cosmology and Astroparticle Physics*, 2009(08):026–026, aug 2009. doi: 10.1088/1475-7516/2009/08/026. URL https://doi.org/10.1088%2F1475-7516%2F2009%2F08%2F026.

[266] K. Ioka, K. Hotokezaka, and T. Piran. Are Ultra-Long Gamma-Ray Bursts Caused by Blue Supergiant Collapsars, Newborn Magnetars, or White Dwarf Tidal Disruption Events? *Astrophys. J.*, 833(1):110, 2016. doi: 10.3847/1538-4357/833/1/110.

[267] T. Alexander and B. Bar-Or. A universal minimal mass scale for present-day central black holes. *Nature Astronomy*, 1:0147, August 2017. doi: 10.1038/s41550-017-0147.

[268] R. Margutti et al. The Electromagnetic Counterpart of the Binary Neutron Star Merger LIGO/VIRGO GW170817. V. Rising X-ray Emission from an Off-Axis Jet. *Astrophys. J.*, 848(2):L20, 2017. doi: 10.3847/2041-8213/aa9057.

[269] E. Troja et al. The X-ray counterpart to the gravitational wave event GW 170817. *Nature*, 2017. doi: 10.1038/nature24290.

[270] G. Hallinan et al. A Radio Counterpart to a Neutron Star Merger. *Science*, 358:1579, 2017. doi: 10.1126/science.aap9855.

[271] P. S. Cowperthwaite et al. The Electromagnetic Counterpart of the Binary Neutron Star Merger LIGO/Virgo GW170817. II. UV, Optical, and Near-infrared Light Curves and Comparison to Kilonova Models. *Astrophys. J.*, 848(2):L17, 2017. doi: 10.3847/2041-8213/aa8fc7.

[272] M. Nicholl et al. The Electromagnetic Counterpart of the Binary Neutron Star Merger LIGO/VIRGO GW170817. III. Optical and UV Spectra of a Blue Kilonova From Fast Polar Ejecta. *Astrophys. J.*, 848(2):L18, 2017. doi: 10.3847/2041-8213/aa9029.

[273] S. J. Smartt et al. A kilonova as the electromagnetic counterpart to a gravitational-wave source. *Nature*, 551(7678):75–79, 2017. doi: 10.1038/nature24303.

[274] D. Kasen et al. Origin of the heavy elements in binary neutron-star mergers from a gravitational wave event. 2017. doi: 10.1038/nature24453.

[275] B. P. Abbott et al. Multi-messenger Observations of a Binary Neutron Star Merger. *Astrophys. J.*, 848(2):L12, 2017. doi: 10.3847/2041-8213/aa91c9.

[276] B. D. Metzger. Welcome to the Multi-Messenger Era! Lessons from a Neutron Star Merger and the Landscape Ahead. 2017.

[277] D. Biehl, J. Heinze, and W. Winter. Expected neutrino fluence from short Gamma-Ray Burst 170817A and off-axis angle constraints. *Mon. Not. Roy. Astron. Soc.*, 476(1):1191–1197, 2018. doi: 10.1093/mnras/sty285.

[278] X. Rodrigues et al. Binary neutron star merger remnants as sources of cosmic rays below the "Ankle". *Astropart. Phys.*, 106:10–17, 2019. doi: 10.1016/j.astropartphys.2018.10.007.

[279] P. B. Denton and I. Tamborra. Exploring the Properties of Choked Gamma-ray Bursts with IceCube's High-energy Neutrinos. *Astrophys. J.*, 855(1):37, 2018. doi: 10.3847/1538-4357/aaab4a.

[280] P. B. Denton and I. Tamborra. The Bright and Choked Gamma-Ray Burst Contribution to the IceCube and ANTARES Low-Energy Excess. *JCAP*, 1804(04):058, 2018. doi: 10.1088/1475-7516/2018/04/058.

[281] K. P. Mooley et al. A mildly relativistic wide-angle outflow in the neutron star merger GW170817. *Nature*, 554:207, 2018. doi: 10.1038/nature25452.

[282] A. Goldstein et al. An Ordinary Short Gamma-Ray Burst with Extraordinary Implications: Fermi-GBM Detection of GRB 170817A. *Astrophys. J.*, 848(2):L14, 2017. doi: 10.3847/2041-8213/aa8f41.

[283] J. Granot et al. Off-Axis Emission of Short GRB Jets from Double Neutron Star Mergers and GRB 170817A. 2017.

[284] O. S. Salafia et al. Interpreting GRB170817A as a giant flare from a jet-less double neutron-star merger. *Astron. Astrophys.*, 619:A18, 2018. doi: 10.1051/0004-6361/201732259.

[285] F. Daigne and R. Mochkovitch. The Expected thermal precursors of gamma-ray bursts in the internal shock model. *Mon. Not. Roy. Astron. Soc.*, 336:1271–1280, 2002. doi: 10.1046/j.1365-8711.2002.05875.x.

[286] A. M. Beloborodov. On the efficiency of internal shocks in gamma-ray bursts. *Astrophys. J.*, 539:L25–L28, 2000. doi: 10.1086/312830.

[287] K. Ioka and T. Nakamura. Can an Off-axis Gamma-Ray Burst Jet in GW170817 Explain All the Electromagnetic Counterparts? *Submitted to: PTEP*, 2017.

[288] O. S. Salafia et al. Light curves and spectra from off-axis gamma-ray bursts. *Mon. Not. Roy. Astron. Soc.*, 461(4):3607–3619, 2016. doi: 10.1093/mnras/stw1549.

[289] A. Albert et al. Search for High-energy Neutrinos from Binary Neutron Star Merger GW170817 with ANTARES, IceCube, and the Pierre Auger Observatory. 2017.

[290] K. D. Alexander et al. A Decline in the X-ray through Radio Emission from GW170817 Continues to Support an Off-Axis Structured Jet. *Astrophys. J.*, 863(2):L18, 2018. doi: 10.3847/2041-8213/aad637.

[291] G. P. Lamb, I. Mandel, and L. Resmi. Late-time Evolution of Afterglows from Off-Axis Neutron-Star Mergers. 2018. doi: 10.1093/mnras/sty2196.

[292] K. P. Mooley et al. Superluminal motion of a relativistic jet in the neutron-star merger GW170817. *Nature*, 561(7723):355–359, 2018. doi: 10.1038/s41586-018-0486-3.

[293] E. Troja et al. The outflow structure of GW170817 from late-time broad-band observations. *Mon. Not. Roy. Astron. Soc.*, 478(1):L18–L23, 2018. doi: 10.1093/mnrasl/sly061.

[294] J. Zrake, X. Xie, and A. MacFadyen. Radio sky maps of the GRB 170817A afterglow from simulations. *Astrophys. J.*, 865(1):L2, 2018. doi: 10.3847/2041-8213/aaddf8.

[295] I. Arcavi et al. Energetic eruptions leading to a peculiar hydrogen-rich explosion of a massive star. 2017. doi: 10.1038/nature24030.

[296] D. A. Coulter et al. Swope Supernova Survey 2017a (SSS17a), the Optical Counterpart to a Gravitational Wave Source. *Science*, 2017. doi: 10.1126/science.aap9811. [Science358,1556(2017)].

[297] V. M. Lipunov et al. MASTER Optical Detection of the First LIGO/Virgo Neutron Star Binary Merger GW170817. *Astrophys. J.*, 850(1):L1, 2017. doi: 10.3847/2041-8213/aa92c0.

[298] M. Soares-Santos et al. The Electromagnetic Counterpart of the Binary Neutron Star Merger LIGO/Virgo GW170817. I. Discovery of the Optical Counterpart Using the Dark Energy Camera. *Astrophys. J.*, 848(2):L16, 2017. doi: 10.3847/2041-8213/aa9059.

[299] S. Valenti et al. The discovery of the electromagnetic counterpart of GW170817: kilonova AT 2017gfo/DLT17ck. *Astrophys. J.*, 848(2):L24, 2017. doi: 10.3847/2041-8213/aa8edf.

[300] J. J. Ruan et al. Brightening X-Ray Emission from GW170817/GRB 170817A: Further Evidence for an Outflow. *Astrophys. J.*, 853(1):L4, 2018. doi: 10.3847/2041-8213/aaa4f3.

[301] P. D'Avanzo et al. The evolution of the X-ray afterglow emission of GW 170817/ GRB 170817A in XMM-Newton observations. *Astron. Astrophys.*, 613:L1, 2018. doi: 10.1051/0004-6361/201832664.

[302] M. Nynka et al. Fading of the X-Ray Afterglow of Neutron Star Merger GW170817/GRB 170817A at 260 Days. *Astrophys. J.*, 862(2):L19, 2018. doi: 10.3847/2041-8213/aad32d.

[303] H. Takami, K. Kyutoku, and K. Ioka. High-Energy Radiation from Remnants of Neutron Star Binary Mergers. *Phys. Rev.*, D89(6):063006, 2014. doi: 10.1103/PhysRevD.89.063006.

[304] A. L. Piro and J. A. Kollmeier. Evidence for Cocoon Emission from the Early Light Curve of SSS17a. *Astrophys. J.*, 855(2):103, 2018. doi: 10.3847/1538-4357/aaaab3.

[305] A. M. Hillas. Where do 10^{19} eV cosmic rays come from? *Nucl. Phys. Proc. Suppl.*, 136: 139–146, 2004. doi: 10.1016/j.nuclphysbps.2004.10.004. [,139(2004)].

[306] G. Giacinti et al. Cosmic Ray Anisotropy as Signature for the Transition from Galactic to Extragalactic Cosmic Rays. *JCAP*, 1207:031, 2012. doi: 10.1088/1475-7516/2012/07/031.

[307] P. Abreu et al. Constraints on the origin of cosmic rays above 10^{18} eV from large scale anisotropy searches in data of the Pierre Auger Observatory. *Astrophys. J.*, 762:L13, 2012. doi: 10.1088/2041-8205/762/1/L13.

[308] A. R. Bell. Turbulent amplification of magnetic field and diffusive shock acceleration of cosmic rays. *Monthly Notices of the Royal Astronomical Society*, 353(2):550–558, 2004.

[309] F. C. Jones. A theoretical review of diffusive shock acceleration. *Astrophys. J.*, 90:561–565, feb 1994. doi: 10.1086/191875.

[310] J. D. Lyman et al. The optical afterglow of the short gamma-ray burst associated with GW170817. *Nat. Astron.*, 2(9):751–754, 2018. doi: 10.1038/s41550-018-0511-3.

[311] H. Abdalla et al. TeV gamma-ray observations of the binary neutron star merger GW170817 with H.E.S.S. *Astrophys. J.*, 850(2):L22, 2017. doi: 10.3847/2041-8213/aa97d2.

[312] M. Holler et al. Observations of the Crab Nebula with H.E.S.S. Phase II. *PoS*, ICRC2015: 847, 2016. doi: 10.22323/1.236.0847.

[313] C. Fransson and C.-I. Björnsson. Modeling the radio and x-ray emission of SN 1993J and SN 2002ap. *Springer Proc. Phys.*, 99:59–69, 2005. doi: 10.1007/3-540-26633-X_8.

[314] V. A. Villar et al. *SpitzerSpaceTelescope* Infrared Observations of the Binary Neutron Star Merger GW170817. *Astrophys. J.*, 862(1):L11, 2018. doi: 10.3847/2041-8213/aad281.

[315] M. S. Longair. *High energy astrophysics. Volume 2. Stars, the Galaxy and the interstellar medium.* 1994.

[316] R. J. Gould and G. P. Schreder. Pair Production in Photon-Photon Collisions. *Phys. Rev.*, 155:1404–1407, 1967. doi: 10.1103/PhysRev.155.1404.

[317] J. Burguet-Castell et al. Neutrino oscillation physics with a higher gamma beta beam. *Nucl. Phys.*, B695:217–240, 2004. doi: 10.1016/j.nuclphysb.2004.06.021.

[318] K. Murase, D. Guetta, and M. Ahlers. Hidden Cosmic-Ray Accelerators as an Origin of TeV-PeV Cosmic Neutrinos. *Phys. Rev. Lett.*, 116(7):071101, 2016. doi: 10.1103/PhysRevLett.116.071101.